Title
Modeling and simulations of electrical energy storage in electrochemical capacitors

Author
Wang, Hainan

Publication Date
2013

Peer reviewed|Thesis/dissertation

University of California

Los Angeles

Modeling and Simulations of Electrical Energy Storage in Electrochemical Capacitors

A dissertation submitted in partial satisfaction

of the requirements for the degree

Doctor of Philosophy in Mechanical Engineering

by

Hainan Wang

2013

Abstract of the Dissertation

Modeling and Simulations of Electrical Energy Storage in Electrochemical Capacitors

by

Hainan Wang

Doctor of Philosophy in Mechanical Engineering

University of California, Los Angeles, 2013

Professor Laurent G. Pilon, Chair

The present study investigates transport and electrochemical phenomena in electrochemical capacitors (ECs) for electrical energy storage applications. Modeling of such systems is made difficult by the complex multidimensional and multiscale porous electrode structures along with the coupled physical phenomena and redox reactions. This study is unique in that it presents rigorous development of physical models for electric double layers and redox reactions in ECs. These models were used to gain insights into the coupled transport and electrochemical phenomena involved. Finally, the results were used to identify the dominant design parameters.

First, this study identified the important physical phenomena that must be accounted for when simulating electric double layer capacitors (EDLCs). It established that the Stern and diffuse layers, the finite ion sizes, and the field-dependent electrolyte permittivity must all be accounted for. To account for the Stern layer for 3D electrode structures along with all the other phenomena, a new set of boundary conditions was derived. In fact, this study presents the first simulations of EDLCs with 3D electrode structures including (i) ordered mesoporous carbon sphere arrays and (ii) ordered bimodal mesoporous carbons, respectively. The model and numerical tools were validated successfully against experimental data.

Second, this study derives a scaling law for the integral areal capacitance of carbon-based EDLCs supported by rigorous analysis and experimental data for various mesoporous carbon electrodes with different electrolytes. It establishes that the integral areal capacitance of porous electrodes can be expressed as the product of the capacitance of planar electrodes and a semi-empirical function to correct for the porous electrode morphology. To maximize the integral areal capacitance, the electrolyte should have small ion effective diameter and large dielectric constant. The electrode pore diameter should be tailored as monodispersed as possible to match the ion diameter.

Third, this study presents dynamic modeling of EDLCs accounting for charge transport in both the electrode and electrolyte. It provides rigorous physical interpretations of experimental observations from electrochemical impedance spectroscopy and cyclic voltammetry (CV) experiments based on physics-based numerical simulations. Moreover, a generalized modified Poisson-Nernst-Planck (GMPNP) model was derived from first principles to simulate electric double layer dynamics valid for asymmetric electrolytes and/or in the presence of multiple ion species. For the first time, a self-similar behavior was identified for the electric double layer integral capacitance estimated from CV measurement simulations.

Finally, this study presents dynamic modeling of asymmetric supercapacitors in CV measurements by rigorously and simultaneously accounting for electric double layers and redox reactions as well as ion insertion in the electrode. It establishes that in CV measurements of pseudocapacitive materials: (i) the capacitive current varies linearly with scan rate v and (ii) the Faradaic current is proportional to $v^{1/2}$.

The models and results could help develop the optimum electrode architecture to achieve maximum energy and power densities. Moreover, these models will also be useful for simulating and designing various practical electrochemical, colloidal, and biological systems for a wide range of applications.

The dissertation of Hainan Wang is approved.

Bruce S. Dunn

Pirouz Kavehpour

Christopher S. Lynch

Laurent G. Pilon, Committee Chair

University of California, Los Angeles

2013

This thesis is dedicated to my parents and my wife.

Table of Contents

List of Figures

List of Tables

Acknowledgments

I would like to express my gratitude to my advisor Professor Laurent Pilon for his guidance, support, and encouragement during my doctoral study. I have improved significantly in both academic and non-academic aspects thanks to his supervision. I would like to thank Professor Bruce Dunn, Professor Pirouz Kavehpour, and Professor Christopher Lynch for their constructive comments and guidance as well as serving in my doctoral committee.

I would also like to thank all my collaborators in the EFRC at UCLA for their advice and help. Special thanks go to Prof. Bruce Dunn, Dr. Zheng Chen, Dr. Veronica Augustyn, Dr. Fei Zhou, and Dr. Emilie Perre. I thank all my lab members including Jin Fang, Thomas Coquil, Ashcon Navid, Euntaek Lee, Hiep Nguyen, Ian McKinley, Dr. Hong Qi, Anna d'Entremont, Alexander Thiele, and Henri-Louis Girard, just to name a few. I am also grateful to all my friends who have made my life enjoyable during my study at UCLA. Their kindness and friendship have encouraged me during my doctoral study.

I would like to dedicate this thesis to my wife Yanjun Xia for her love, encouragement, and understanding. I could not get through the difficult time without her. This thesis is also dedicated to my parents for their endless love, patience, and encouragement in all my life.

Vita

2003	B.S. Thermal Science and Energy Engineering, University of Science and Technology of China, Hefei, Anhui, China
2006	M.S. Thermal Science and Energy Engineering, University of Science and Technology of China, Hefei, Anhui, China
2007	M.S. Aerospace and Mechanical Engineering, University of Notre Dame, South Bend, IN, USA
2013	Ph.D. Mechanical and Aerospace Engineering, University of California, Los Angeles, CA, USA

Publications

1. **H. Wang**, A. Thiele, and L. Pilon, 2013, Simulations of cyclic voltammetry for electric double layers with asymmetric electrolytes: A generalized modified Poisson-Nernst-Planck model, *Journal of Physical Chemistry C*, vol.117, no.36, pp.18286-18297.

2. **H. Wang**, J. Fang, and L. Pilon, 2013, Scaling laws for carbon-based electric double layer capacitors, *Electrochimica Acta*, vol.109, pp.316-321.

3. **H. Wang** and L. Pilon, 2013, Mesoscale modeling of electric double layer capacitors with three-dimensional ordered structures, *Journal of Power Sources*,

vol.221, pp.252-260.

4. **H. Wang** and L. Pilon, 2012, Physical interpretation of cyclic voltammetry for measuring electric double layer capacitances, *Electrochimica Acta*, vol.64, pp.130-139.

5. **H. Wang** and L. Pilon, 2012, Intrinsic limitations of impedance measurements in determining electric double layer capacitances, *Electrochimica Acta*, vol.63, pp.55-63.

6. **H. Wang** and L. Pilon, 2011, Accurate simulations of electric double layer capacitance of ultramicroelectrodes, *Journal of Physical Chemistry C*, vol.115, no.33, pp.16711-16719.

7. J. Varghese, **H. Wang**, and L. Pilon, 2011, Simulating electric double layer capacitance of mesoporous electrodes with cylindrical pores, *Journal of Electrochemical Society*, vol.158, no.10, pp.1-9.

8. **H. Wang**, J. Varghese, and L. Pilon, 2011, Simulation of electric double layer capacitors with mesoporous electrodes: Effects of morphology and electrolyte permittivity, *Electrochimica Acta*, vol.56, no.17, pp.6189-6197.

9. **H. Wang** and M. Sen, 2009, Analysis of 3omega method for thermal conductivity measurement, *International Journal of Heat and Mass Transfer*, vol.52, no.7-8, pp.2102-2109.

10. J. Wang, **H. Wang**, J. Sun, and J. Wang, 2007, Numerical simulation of control ablation by transpiration cooling, *Heat and Mass Transfer*, vol.43, no.5,

pp.275-284.

11. J. Wang and **H. Wang**, 2006, A discussion of transpiration cooling problems through an analytical solution of local thermal non-equilibrium model, *ASME Journal of Heat Transfer*, vol.128, no.10, pp.1093-1098.

12. **H. Wang** and J. Wang, 2006, An investigation of analytical solutions for one-dimensional steady non-equilibrium transpiration cooling, *Journal of Aerospace Power*, in Chinese, vol.21, no.1, pp.77-82.

CHAPTER 1

Introduction

This chapter presents the motivations and objectives of the present study and the scope of this Ph.D. thesis. First, an overview of electrochemical capacitors is provided. Then, the physical phenomena and materials in electrochemical capacitors are introduced. Finally, this chapter describes the objectives of the present research and concludes with the organization of the document.

1.1 Motivations of The Present Study

Electrical energy storage systems (EES) have been the subject of intense study as they constitute an essential element in the development of sustainable energy technologies. Electrical energy generated from renewable resources such as solar radiation or wind provides great potential to meet our energy needs in a sustainable manner. It would reduce not only our dependence on fossil fuel but also pollutant emission responsible for global warming [1, 17–20]. However, these renewable energy technologies generate electricity intermittently and thus require efficient and reliable electrical energy storage (EES) methods [1, 21]. For commercial and residential grid applications, electricity must be reliably available at any time of the day. In fact, second-to-second fluctuations can cause major disruptions with costs estimated to be in the tens of billions of dollars annually [1]. Thus, the development of new EES systems will be critical in the use of large-scale solar- or wind-based electricity generation [1, 22]. Moreover, greatly improved EES systems are required to enable the widespread use of hybrid electrical vehicles (HEV),

plug-in hybrids, and all-electric vehicles [1, 23, 24]. Figures 1.1a and 1.1b show a gasoline/electric hybrid bus and a diesel/electric hybrid gantry crane equipped with an electrochemical capacitor energy storage system to harvest and store kinetic energy of the bus or potential energy of the crane during load lowering [1,2]. Furthermore, improvements in ESS performance, reliability, and efficiency are needed in the development of modern portable electronic devices such as laptops and smart phones [1].

(a) **(b)**

Figure 1.1: (a) A gasoline/electric hybrid bus (taken from Ref. [1]) and (b) hybrid diesel/electric rubber-tired gantry crane (taken from Ref. [2]) equipped with electrochemical capacitor energy storage systems.

The performances of electrical energy storage devices can be assessed by comparing their energy density (in Wh/kg) and power density (in W/kg). Figure 1.2 shows the so-called Ragone chart plotting the energy density versus the power density of different electrical energy storage devices. Batteries and fuel cells have relatively high energy density but low power density due to the slow kinetics of the chemical reactions taking place. In comparison, capacitors have high power density but low energy density because they store or deliver electric charges very rapidly but in limited amount.

Alternatively, electrochemical capacitors (ECs) can operate in a wide range of energy and power densities. This versatility is a key feature for energy storage,

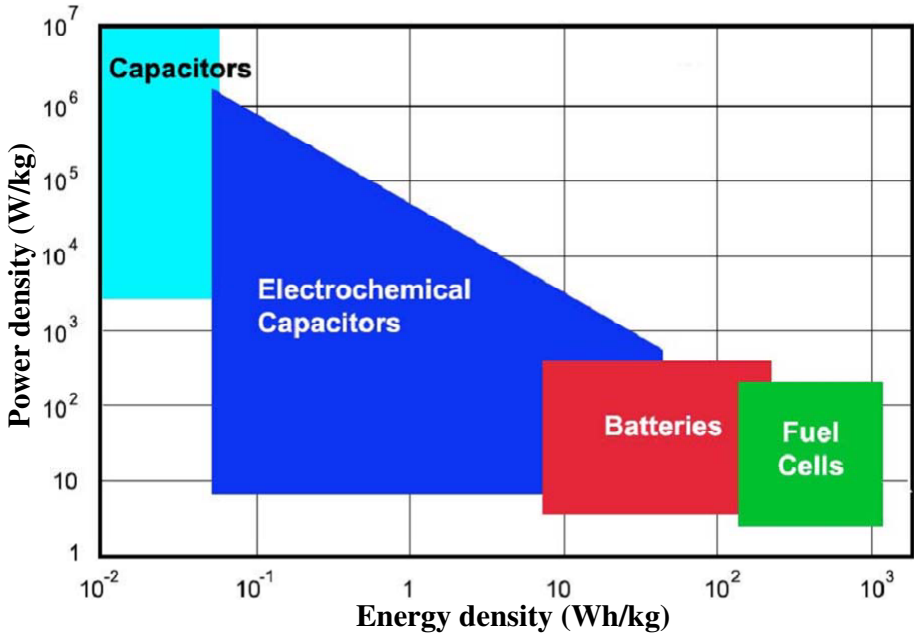

Figure 1.2: Energy density and power density of different electrical energy storage systems (taken from Ref. [1]).

energy harvesting, and energy regeneration applications [1]. For example, ECs are suitable in various applications where high charging/discharging rates are needed such as (i) instant restart of electronic equipments, (ii) powering up a computer CPU from energy-saving sleep mode to full operation, and (iii) powering hybrid electronic vehicles (HEVs) or electronic vehicles (EVs) [1, 2, 25].

1.2 Electrochemical Capacitors

Electrochemical capacitors (ECs), also known as supercapacitors or ultracapacitors, are typically classified into two categories based on their different energy storage mechanisms as shown in Figure 1.3. First, electric double layer capacitors (EDLCs) store charges physically (i.e., without chemical reactions) in electric double layers forming near the electrode/electrolyte interfaces. Thus, the process

is highly reversible and the cycle life is essentially infinite [1, 26]. On the other hand, pseudocapacitors store energy via not only electric double layer such as that in EDLCs but also fast surface oxidation-reduction (redox) reactions as well as possible ion intercalation in the electrode [1, 25, 27–30].

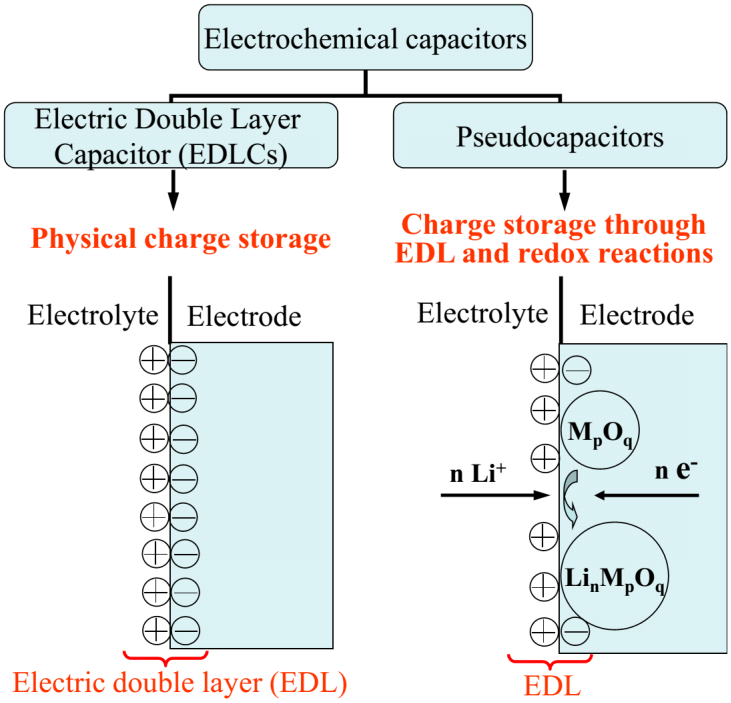

Figure 1.3: Schematics for electrical double layer capacitors and pseudocapacitors.

1.2.1 Electric Double Layer Capacitors

Electric double layer capacitors (EDLCs) have attracted significant attention in recent years due to their promises as electrical energy storage devices for high power applications such as hybrid electric vehicles [27, 31–34]. EDLCs store electric charges physically in the electric double layer forming at electrode/electrolyte interfaces accessible to ions present in the electrolyte [27, 31–34]. Figure 1.4 shows a schematic of the electric double layer structure forming near a positively charged electrode. Solvated anions of diameter a migrate and adsorb to the electrode surface due to electrostatic forces while the cations are repelled [8, 9, 35, 36]. The

Stern layer is defined as the compact layer or inner layer near the electrode surface [8,9,35,36]. Note that there are no free charges within the Stern layer [8,9,35]. Beyond the Stern layer is the so-called diffuse layer where anions and cations are mobile under the coupled influence of electrostatic forces and diffusion [8,9,35,36].

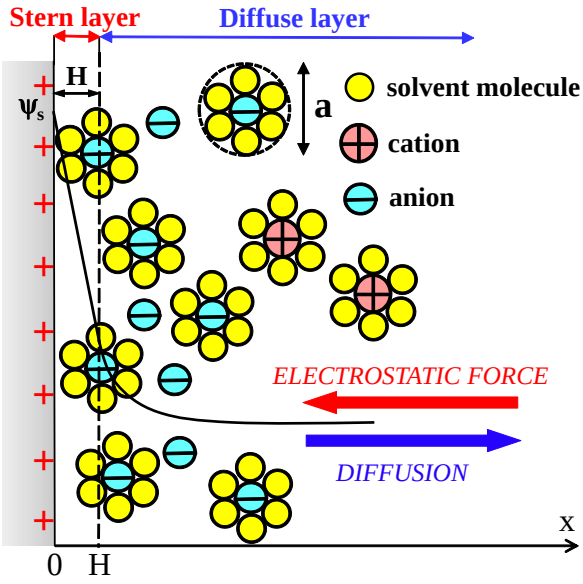

Figure 1.4: A schematic of the electric double layer structure showing solvated anions and cations arrangement near the electrode/electrolyte interface in the Stern and diffuse layers.

In practice, EDLCs' electrodes are made of nanoporous or mesoporous carbons featuring large surface area to enhance the capacitance and stored energy. Moreover, the pore size distribution also significantly affects the performance of EDLCs. It has been established that micropores with size less than 2 nm contribute greatly to the formation of electrical double layer [37–39]. The pores smaller than the ions usually do not contribute to the double layer capacitance [27, 40]. On the other hand, porous electrodes must also be electrochemically accessible for ions. Therefore, the mesopores with diameter ranging from 2 to 50 nm are necessary for fast dynamic charge thanks to the easier accessibility to ions [33, 40–43].

1.2.2 Pseudocapacitors and Asymmetric Supercapacitors

Pseudocapacitors differ from EDLCs in that their electrodes are made of pseudocapacitive materials such as transition metal oxides (M_pO_q). Their capacitance and energy density are greatly enhanced thanks to the Faradaic redox reactions between the redox active ion species (e.g., Li^+) and pseudocapacitive materials M_pO_q according to [1, 44–47],

$$M_pO_q + nLi^+ + ne^- \rightleftharpoons Li_nM_pO_q \tag{1.1}$$

Moreover, another type of supercapacitors, named asymmetric supercapacitors or hybrid supercapacitors, has emerged in recent years by combining pseudocapacitors and EDLCs [27, 48–59]. In asymmetric (hybrid) supercapacitors, one carbon-based electrode stores charges physically in electric double layers while the other electrode is redox-active and store charges via reversible chemical reactions [27, 48–59]. Here, the pseudocapacitive electrode serves as the energy source and the carbon-based electrode serves as the power source [27, 48–59].

Understanding the electrochemical behaviors of pseudocapacitive materials are essential for designing these electrochemical capacitors and improving their performances. Modeling of such systems is made difficult by the complex multidimensional and multiscale porous electrode structures along with the different and coupled physical phenomena and redox reactions.

1.3 Materials of Electrochemical Capacitors

The performance of electrochemical capacitors is determined by the combination of the electrode material and electrolyte used. There are three main categories of electrode materials used for ECs [25, 28, 47], namely (1) carbon-based materials, (2) transition metal oxides, and (3) conductive polymers. Similarly, three types of electrolyte materials are used for ECs including [27,28,47] (1) aqueous electrolytes,

(2) organic electrolytes, and (3) ionic liquids. The following subsections discuss the different electrode materials and electrolytes in details.

1.3.1 Electrode Materials

Various carbon-based materials have been considered for electrodes of ECs including activated carbon, carbon nanotubes, templated carbons, and carbon aerogels [32–34, 40]. Carbon materials are attractive for electrodes due to their versatility, easy processability, non-toxicity, high chemical stability, low density, good electrical conductivity, high surface area, and relatively low cost [28, 33, 40]. The design of electrodes using carbon materials requires [18, 28, 33, 40] (i) high specific surface area to ensure high capacitance, (ii) optimum pore size and pore distribution in order to permit easy access of ions to the electrode surface, and (iii) small electrical resistance.

Transition metal oxides, composed of transition metal elements (e.g. Ru, Mn, Ti, Ni, Nb, Mo, V, W, Ce, Co) and oxygen, have been used extensively as electrodes for pseudocapacitors [1, 25, 28, 60]. Among various transition metal oxides, ruthenium oxide (RuO_2) has been the most widely investigated and commercially used materials for ECs, especially for aerospace and military applications [1, 27, 61, 62]. RuO_2 has a number of attractive features including (i) high specific capacitance, (ii) long cycle life, (iii) high electrical conductivity, and (iv) good electrochemical reversibility [1, 25, 28]. However, the scarcity and high cost of the precious metal Ru greatly impede the wide use of RuO_2 for commercial applications [26, 28, 60].

Moreover, the conductive polymers, such as polypyrrole, have also been investigated as ECs' electrodes [28,63–66]. They have been used as modified membrane coated on the electrically-conductive materials such as activated carbon to reduce resistance [28, 66]. Conductive polymers are usually inexpensive and have fast

doping-undoping process. These materials can also be easily manufactured into ECs but they showed poor long-term stability during cycling [28].

Finally, nanostructured porous materials feature large surface area and provide great potential as electrode materials for improving energy density of EES. Moreover, advances in nanotechnologies have made the assembly of nanoporous or mesoporous materials possible with controlled morphology using repeatable and inexpensive synthesis routes [67–71]. However, current understanding of the mechanisms determining the performances of supercapacitors is still limited due to (i) the complex geometry of the porous structures and (ii) the complex transport and electrochemical phenomena occurring at mesoscale and nanoscale [26].

1.3.2 Electrolyte Materials

The performance of electrochemical capacitors also strongly depends on the electrolyte used. The ideal electrolytes for ECs should have the following features [1,72]: (i) large ionic conductivity and mobility for very fast charge/discharge rates (< 1 s), (ii) large chemical and electrochemical stability resulting in a large potential window and long device lifetime, (iii) excellent temperature stability to deliver high power and energy at both low (-30 °C) and high (100 °C) temperatures, and (iv) low volatility, flammability, and toxicity for high safety. The operating voltage of ECs is determined by the electrochemical stability window (voltage) of the electrolytes [1, 10]. Above that voltage, electrolysis of the electrolyte occurs resulting in potential system failure and destruction. Both the energy and power densities of ECs increase quadratically with the maximum operating potential window. Thus, electrolytes with a large electrochemical operational window are desirable [1, 10].

Two frequently used aqueous electrolytes are KOH and H_2SO_4 [28, 47]. Both of them have high electrical conductivity resulting in lower device impedance and

faster response time [1]. However, the maximum operating voltage of aqueous electrolyte solutions is typically limited to 1 V due to the electrochemical stability window of water (1.23 V) [1, 25, 34].

In comparison, organic electrolytes can reach a potential window larger than 2 V [25, 34]. Organic electrolytes used in commercial ECs generally consist of 1 mol/L acetonitrile or propylene carbonate solutions with tetraethylammonium tetrafluoroborate Et_4NBF_4 or Et_3MeNBF_4 [1]. However, major issues associated with organic electrolytes include their (i) high cost, (ii) low electrical conductivity compared with aqueous electrolytes, (iii) low dielectric constant leading to smaller capacitance, (iv) complex purification procedure, as well as (v) safety concerns due to the flammability and toxicity of organic solvents [34].

Finally, ionic liquids (ILs) are attractive candidates as electrolytes because of their (i) high thermal stability, (ii) high decomposition voltage (> 3 V), (iii) low volatility, (iv) non-flammability, and (v) variety of combination choices of cations and anions [1, 33, 34]. However, due to their relatively low conductivity, the power density of ECs using ILs is lower than that achieved using organic electrolytes [1, 33, 34].

1.4 Objectives of The Present Study

The present study focuses on modeling transport and electrochemical phenomena in electrochemical capacitors (ECs). It aims not only to develop the rigorous physical modeling approach for electrochemical capacitors but also to identify the dominant physical phenomena and the design parameters. It is useful in understanding the coupled transport and electrochemical phenomena involved in ECs and in providing design rules for ECs.

1.4.1 Equilibrium Modeling of EDLCs With 3D Electrode Structures

First, the present study aims to develop equilibrium multiscale and multiphysics simulation tools and use them to identify dominant design parameters of mesoporous electrodes in order to improve the performances of EDLCs. In this area, the specific objectives of the study are as follows,

1. To identify the important physical phenomena that must be accounted for in simulating EDLCs under equilibrium conditions.

2. To develop an equilibrium continuum model of EDLCs validated against experimental data accounting for three-dimensional ordered electrode structures.

3. To assess the effects of electrode morphology on the performance of EDLCs under equilibrium conditions.

4. To formulate design rules for the porous electrode morphology and for the electrolyte by identifying scaling laws governing the equilibrium capacitance of carbon-based EDLCs.

1.4.2 Dynamic Modeling of ECs' Charging/Discharging

Dynamic modeling of electrochemical capacitors is imperative for understanding and optimizing their performance under charging/discharging conditions. In this area, the specific objectives of the study are as follows,

1. To develop physical models for simulating ECs valid for practical conditions with large ion concentrations and large potential and for electrolytes with asymmetric properties and/or in the presence of multiple ion species.

2. To provide rigorous physical interpretation of experimental observations

from electrochemical impedance spectroscopy and cyclic voltammetry measurements based on physics-based numerical simulations.

3. To formulate design and operating rules for the electrodes and electrolytes affecting the charging/discharging dynamics of EDLCs by identifying the scaling law of cyclic voltammetry for measuring EDLCs.

4. To establish a rigorous approach for analyzing the capacitance of pseudocapacitive materials using cyclic voltammetry measurements based on physics-based numerical simulations.

1.5 Organization of the Document

Figure 1.5 summarizes the organization of the document including the equilibrium and dynamic modeling and simulations of EDLCs and asymmetric supercapacitors. Specifically, Chapter 2 provides an overview of fundamental concepts and existing models for electrochemical capacitors. Chapter 3 identifies dominant physical phenomena that must be accounted for in simulating EDLCs based on equilibrium simulations of a single spherical microelectrode. Chapters 4 and 5 present the equilibrium modeling of EDLCs with three-dimensional electrodes consisting of (i) ordered mesoporous carbon sphere arrays in periodic packings and (ii) ordered bimodal mesoporous carbons, respectively. Validations of the models against experimental data are also provided. Based on the model developed in Chapters 3 to 5, Chapter 6 presents scaling laws for the integral areal capacitance of carbon-based EDLCs and the resulting design rules. Chapters 7 and 8 present dynamic modeling of EDLCs in electrochemical impedance spectroscopy (EIS) and cyclic voltammetry (CV) measurements by accounting for the charge transport in both the electrode and the electrolyte. It also provides physical interpretations of observations from actual EIS and CV measurements. Chapter 9 presents a generalized dynamic model of EDLCs derived from first principles

valid for practical electrolytes with asymmetric properties and/or in the presence of multiple ion species. It also identifies the self-similar behavior of integral areal capacitance of EDLCs in CV measurements. Chapter 10 presents the dynamic modeling of asymmetric supercapacitors under CV measurements. It also rigorously establishes an approach widely used experimentally for discriminating between electric double layer and redox reaction contributions to the measured total current and for analyzing the capacitance of pseudocapacitive materials. Finally, Chapter 11 summarizes the key contributions of the present research and provides recommendations for future work.

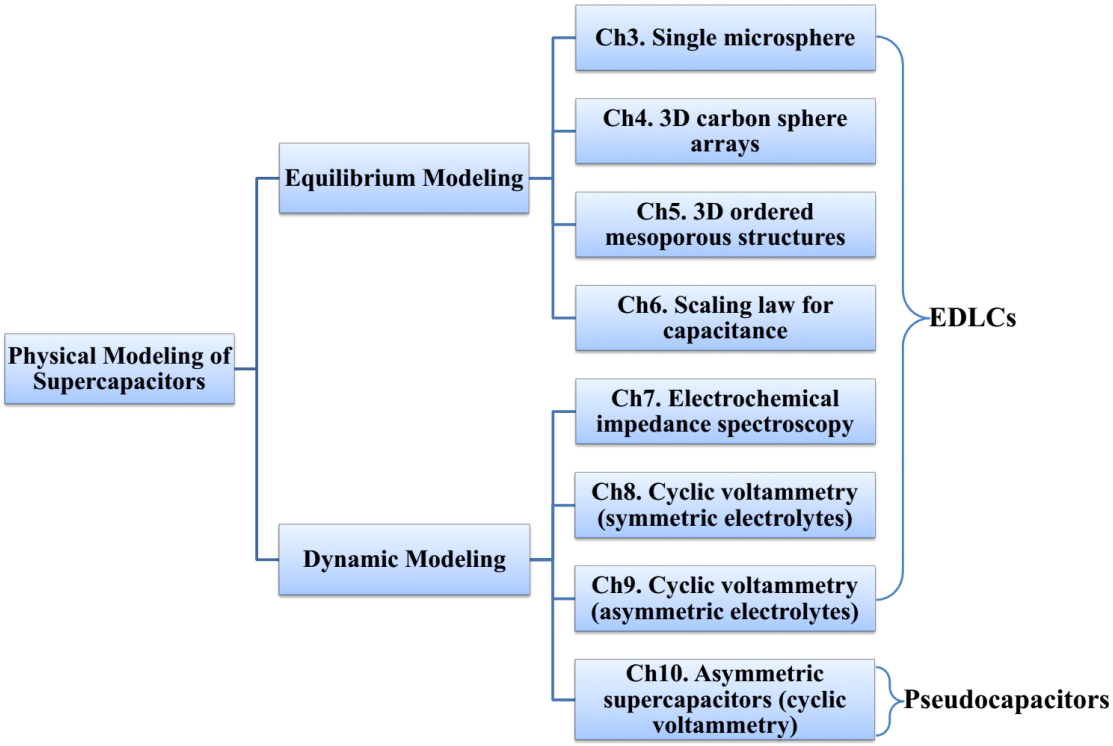

Figure 1.5: Flow chart illustrating the organization of the thesis including the modeling and simulations of EDLCs and asymmetric supercapacitors.

CHAPTER 2

Background

2.1 Integral and Differential Capacitances

2.1.1 Definitions

The areal differential capacitance C_{diff} and integral capacitance C_{int} (both in F/m^2) are respectively defined as [16],

$$C_{diff} = \frac{dq_s}{d\psi_s} \quad \text{and} \quad C_{int} = \frac{q_s}{\psi_s} \tag{2.1}$$

where q_s and ψ_s represent the surface charge density and the surface electric potential, respectively. Note that these definitions are independent of experimental measurements. Under very low electric potential, the surface charge density varies linearly with electrical potential and $C_{diff} = C_{int}$ [4].

2.1.2 Capacitances Measured Using Different Techniques

Electrochemical impedance spectroscopy (EIS) measures the differential capacitance through the following formula [9, 73],

$$C_{diff} = \frac{-1}{2\pi f Z''} \tag{2.2}$$

where f and Z'' are the frequency of the applied electric potential signal and the out-of-phase component of the measured impedance, respectively. In addition, the differential capacitance C_{diff} and integral capacitance C_{int} can be computed

from CV measurements according to [16],

$$C_{diff} = \frac{j_s}{v} \quad \text{and} \quad C_{int} = \frac{1}{\psi_{max} - \psi_{min}} \oint \frac{j_s}{2v} d\psi_s \tag{2.3}$$

where j_s and ψ_s represent the measured current density and the imposed surface electric potential, respectively. The scan rate is denoted by v while ψ_{max} and ψ_{min} are the maximum and minimum values of the imposed electric potential ψ_s, respectively.

Similarly, the galvanostatic charge/discharge method can be used to measure both differential and integral capacitances through [16],

$$C_{diff} = \frac{j_s}{d\psi_s/dt} \quad \text{and} \quad C_{int} = \frac{j_s \Delta t}{\psi_{max} - \psi_{min}} \tag{2.4}$$

where Δt is the time for varying the electric potential from ψ_{min} to ψ_{max} or vice versa under imposed current j_s. Note that in galvanostatic measurements, the differential and integral capacitances calculated using Equations (2.4) are identical only when the measured electric potential varies strictly linearly with time. This condition could be met near zero surface potential [4]. It is also important to note that the integral capacitance rather than the differential capacitance is typically reported for supercapacitors when using galvanostatic charge/discharge method [74–80]. This may be due to two reasons: (i) the integral capacitance directly represents the total charge storage performance of supercapacitors and (ii) ψ_s in Equation (2.4) is the variable directly measured in the galvanostatic method unlike $d\psi_s/dt$. Table 2.1 summarizes whether the EIS, CV, and galvanostatic charge/discharge methods can measure the differential and integral capacitances and gives the associated expressions.

Table 2.1: Calculation formula of the differential or integral capacitances using EIS, CV, and galvanostatic charge/discharge methods [16]. (N/A: not available)

Capacitance	**EIS**	**CV**	**Galvanostatic**
C_{diff}	$\frac{-1}{2\pi f Z"}$	$\frac{j_s}{v}$	$\frac{j_s}{d\psi_s/dt}$
C_{int}	N/A	$\frac{\oint \frac{j_s}{2v} d\psi_s}{\psi_{max} - \psi_{min}}$	$\frac{j_s \Delta t}{\psi_{max} - \psi_{min}}$

2.2 Equilibrium Models

2.2.1 Helmholtz Model

Helmholtz [81] was the first to propose the concept of electric double layer. He realized that charged electrodes immersed in electrolyte solutions will repel the co-ions while attracting counter-ions to their surfaces. The two compact layers of charges forming at the electrode/electrolyte interfaces were called the electric double layer (EDL). Figure 2.1a shows a schematic of the electric double layer structure formed near the surface of a positively charged electrode as envisioned by Helmholtz [9, 35, 36, 81, 82]. In the Helmholtz model, all the counter-ions were assumed to be adsorbed at the electrode surface [9, 81, 82]. This structure is analogous to that of conventional dielectric capacitors with two planar electrodes separated by a distance H [9, 81, 82]. Therefore, the capacitance per unit surface area (or specific capacitance) of the Helmholtz double layer denoted by C_s^H and expressed in F/m^2 is given by [83–87],

$$C_s^H = \begin{cases} \dfrac{\epsilon_0 \epsilon_r}{H} & \text{for planar electrode} \quad (2.5a) \\ \dfrac{\epsilon_0 \epsilon_r}{R_0 \log(1 + H/R_0)} & \text{for cylindrical electrode of radius } R_0 \quad (2.5b) \\ \dfrac{\epsilon_0 \epsilon_r}{H} \left(1 + \dfrac{H}{R_0}\right) & \text{for spherical electrode of radius } R_0 \quad (2.5c) \end{cases}$$

where ϵ_0 and ϵ_r are the free space permittivity and the relative permittivity of the electrolyte solutions, respectively. The thickness H of the Helmholtz double layer can be approximated as the radius of solvated ions [9, 35, 36]. Note that Equations

(2.5b) and (2.5c) reduce to the asymptotic expression given by Equation (2.5a) when the electrode radius is large enough, i.e., $R_0 \gg H$.

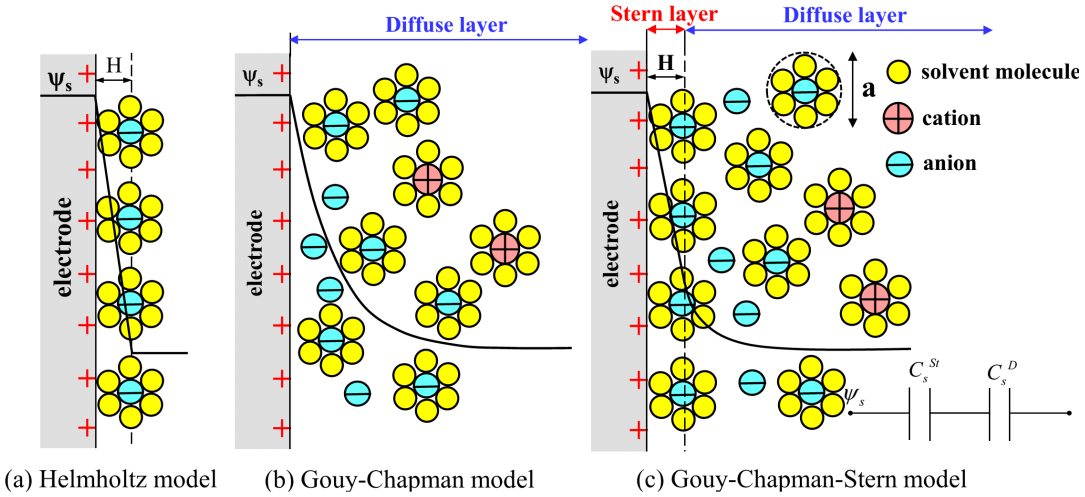

Figure 2.1: Schematics of the electric double layer structure showing the arrangement of solvated anions and cations near the electrode/electrolyte interface. (a) Helmholtz model, (b) Gouy-Chapman model, and (c) Gouy-Chapman-Stern model.

2.2.2 Gouy-Chapman Model

Gouy [88] and Chapman [89] developed an electric double layer model accounting for the fact that the ions are mobile in the electrolyte solutions and are driven by the coupled influences of diffusion and electrostatic forces [9, 35, 82]. This results in the so-called diffuse layer shown in Figure 2.1b. In this model, the ions are treated as point-charges and the equilibrium concentration c_i of ion species "i" is given by the Boltzmann distribution as [8, 9, 35, 36, 82, 90, 91],

$$c_i = c_{i\infty} \exp\left(\frac{-z_i e\psi}{k_B T}\right) \tag{2.6}$$

where z_i and $c_{i\infty}$ are the valency and bulk molar concentration of ion species "i", respectively. The absolute temperature is denoted by T, e is the elementary charge, while k_B is the Boltzmann constant ($k_B = 1.381 \times 10^{-23}$ m^{2}kgK^{-1}s^{-2}). In

the Gouy-Chapman model, the local electric potential ψ in the diffuse layer is determined by the Poisson-Boltzmann (PB) equation assuming constant electrolyte permittivity [8,9,35,36,82,90,91]. For binary symmetric electrolytes, $z_1 = -z_2 = z$ and $c_{1\infty} = c_{2\infty} = c_\infty$. Then, the PB equation is expressed as [8,9,35,36,82,90,91],

$$\nabla \cdot (\epsilon_0 \epsilon_r \nabla \psi) = 2zeN_A c_\infty \sinh\left(\frac{ze\psi}{k_B T}\right) \tag{2.7}$$

where N_A is the Avogadro's number ($N_A = 6.022 \times 10^{23}$ mol^{-1}).

For planar electrodes and constant electrolyte properties, the exact solution of Equation (2.7) exists subject to the following boundary conditions (i) $\psi(0) = \psi_D$, and (ii) $\psi(\infty) = 0$. Then, the specific capacitance corresponding to the diffuse layer C_s^D is given by [8, 9, 35, 36, 82, 90, 91],

$$C_s^D = \frac{q_s}{\psi_D} = \frac{4zeN_A c_\infty \lambda_D}{\psi_D} \sinh\left(\frac{ze\psi_D}{2k_B T}\right) \tag{2.8}$$

where q_s is the surface charge density and λ_D is the Debye length for symmetric electrolytes defined as $\lambda_D = (\epsilon_0 \epsilon_r k_B T / 2e^2 z^2 N_A c_\infty)^{1/2}$ [8, 9, 35, 36, 82, 90, 91].

For spherical electrodes, the exact solution of Equation (2.7) exists provided that the Debye-Hückel approximation requiring $z_i e\psi / k_B T \ll 1$ is satisfied [8, 35, 90, 91]. Then, the diffuse layer specific capacitance is given by [8, 35, 90, 91],

$$C_s^D = \frac{\epsilon_0 \epsilon_r}{\lambda_D}\left(1 + \frac{\lambda_D}{R_0}\right) \tag{2.9}$$

Equations (2.8) and (2.9) reduce to the same asymptotic expression of $C_s^D = \epsilon_0 \epsilon_r / \lambda_D$ when the Debye-Hückel approximation and the thin double layer approximation assuming $\lambda_D / R_0 \ll 1$ are satisfied [8, 35, 90, 91].

2.2.3 Gouy-Chapman-Stern Model

Stern [92] combined the Helmholtz model and the Gouy-Chapman model and described the electric double layer as two layers (Figure 2.1c), namely: (i) the Stern layer (or Helmholtz layer), referring to the compact layer of immobile ions

strongly adsorbed to the electrode surface, and (ii) the diffuse layer where the ions are mobile and the Gouy-Chapman model [Equation (2.7)] applies [8, 9, 35, 36, 82, 90, 91]. Note that there are no free charges within the Stern layer [8, 9, 35, 82]. The total electric double layer capacitance consists of the Stern layer and diffuse layer capacitances in series [8,9,82,90]. Mathematically, the Gouy-Chapman-Stern (GCS) model for symmetric electrolytes is expressed as [8, 93, 94],

$$\nabla \cdot (\epsilon_0 \epsilon_r \nabla \psi) = \begin{cases} 0 & \text{in the Stern layer} \quad (2.10a) \\ 2zeN_A c_\infty \sinh\left(\dfrac{ze\psi}{k_B T}\right) & \text{in the diffuse layer} \quad (2.10b) \end{cases}$$

2.2.4 Modified Poisson-Boltzmann Models

The point-charge assumption associated with the Poisson-Boltzmann equation [Equations (2.7) and (2.10b)] is only valid for very low ion concentration c_∞ and low electric potential [9, 82, 90]. In reality, the ions have finite size and thus a maximum ion concentration $c_{\max}$ exists corresponding to the closed packing of ions. It is given by $c_{\max} = 1/(N_A a^3)$ corresponding to simple cubic packing of ions with effective diameter a [4,95]. Therefore, the ion concentration given by the Boltzmann distribution [Equation (2.6)] should not exceed $c_{\max}$. This corresponds to a maximum surface potential ψ_{max} given by [4, 95],

$$\psi_{max} = -\frac{k_B T}{ze} \log(N_A a^3 c_\infty) \tag{2.11}$$

The magnitude of the local electric potential $|\psi|$ in the diffuse layer should not exceed ψ_{max} for the Gouy-Chapman and Gouy-Chapman-Stern models [Equations (2.7) and (2.10b)] to be valid. For example, $\psi_{max} = 0.04$ V for the typical values of $T = 298$ K, $z = 1$, $c_\infty = 1$ mol/L, and $a = 0.66$ nm [85–87, 94].

Numerous studies have been reported in the literature to account for the effect of finite ion size in the electrolyte solution [4, 95–102]. Among them, the modified Poisson-Boltzmann (MPB) models based on the local-density and mean-field approximations are relatively convenient both mathematically and numer-

ically [4, 95–102]. For example, Bikerman [96] developed the first equilibrium modified Poisson-Boltzmann (MPB) model accounting for finite ion size. This model applies to electrolytes with anions and cations having different volumes but symmetric valency. Borukhov *et al.* [97,98] and Silalahi *et al.* [103] developed MPB models valid for binary electrolytes with asymmetric valency but identical ion diameters. Their model was later extended to binary asymmetric electrolytes with unequal ion diameters [104, 105]. Biesheuvel and co-workers [99, 106, 107] and Alijó *et al.* [108] developed more general MPB models valid for asymmetric electrolytes and/or multiple ion species with different ion sizes and valencies. This was accomplished by incorporating an excess chemical potential term based on the Boublik-Mansoori-Carnahan-Starling-Leland equation-of-state. It directly relates the excess chemical potential to the local ion concentrations, ions' effective diameters, and their exclusion volumes [99,106–108]. Moreover, Tresset [109] developed a generalized Poisson-Fermi model for asymmetric electrolytes and multiple ion species based on the lattice gas approach by considering ions in discrete cells of different volumes. In addition, Li and co-workers [110–112] developed a model for asymmetric electrolytes based on the variational principle while accounting for the finite sizes of both ions and solvent molecules. Alternatively, Horno and co-workers [113–119] developed a MPB model for asymmetric electrolytes by directly applying a "Langmuir-type" correction to the equilibrium ion concentration given by the Boltzmann distribution.

For binary and symmetric electrolytes, the MPB models reduce to [4,95–97,99],

$$\nabla \cdot (\epsilon_0 \epsilon_r \nabla \psi) = \frac{2zeN_A c_\infty \sinh\left(\frac{ze\psi}{k_B T}\right)}{1 + 2\nu_p \sinh^2\left(\frac{ze\psi}{2k_B T}\right)} \tag{2.12}$$

where the packing parameter is defined as $\nu_p = 2a^3 N_A c_\infty = 2c_\infty / c_{max}$ [4,95–97,99]. From here on, the term "MPB model" will be used to refer to Equation (4.1). For vanishing ion diameter such that $a = 0$ nm and $\nu_p = 0$, the MPB model reduces

to the Gouy-Chapman model given by Equation (2.7). For planar electrodes and constant electrolyte properties, the surface charge density and diffuse layer specific capacitance are given by [4, 95, 102],

$$C_s^D = \frac{q_s}{\psi_D} = \frac{2zeN_A c_\infty \lambda_D}{\psi_D} \sqrt{\frac{2}{\nu_p} \log\left[1 + 2\nu_p \sinh^2\left(\frac{ze\psi_D}{2k_B T}\right)\right]} \tag{2.13}$$

Note that when $\psi_D = 0$, Equation (2.13) predicts an extremum for the diffuse layer capacitance, i.e., $C_s^D = \epsilon_0 \epsilon_r / \lambda_D$. This capacitance could be either a maximum or a minimum value depending on the packing parameter ν_p as discussed in Refs. [4, 95, 99, 102].

2.3 Dynamic Models

2.3.1 Equivalent RC Rircuit and Transmission Line Models

The equivalent RC circuit models and more complex transmission line models [120–127] have been used to investigate the performance of supercapacitors. However, the equivalent RC circuit models require prior knowledge of macroscopic parameters such as the resistance and capacitance of the device which are typically determined experimentally or by other methods. In fact, these models are typically used to fit the experimental data [120–127] rather than predict the performances of supercapacitors. Moreover, the classical RC circuit models inherently neglects ion diffusion and non-uniform ion concentration in the electrolyte [128–130]. Thus, Thus, these models may not be valid for supercapacitors under large electric potential and electrolyte concentration [128–131].

2.3.2 Homogeneous Models

Homogeneous models were also developed to investigate the charging/discharging dynamics of supercapacitors [132–145]. These models treat the heterogeneous microstructure of the electrodes as homogeneous with some effective macroscopic

properties determined from effective medium approximations and depending on porosity and specific area [132–145]. Therefore, they cannot account for the detailed three-dimensional electrode morphology. Moreover, homogeneous models typically impose specific area capacitance or volumetric capacitance rather than predict them [132–145].

2.3.3 Poisson-Nernst-Planck Model

The classical Poisson-Nernst-Planck (PNP) model governs the transient electric potential and ion concentration profiles in the diffuse layer [8, 9, 35, 90, 132, 146]. It is expressed as [8, 9, 35, 90, 132, 146],

$$\nabla \cdot (\epsilon_0 \epsilon_r \nabla \psi) = -\sum_{i=1}^{N} z_i e N_A c_i \tag{2.14a}$$

$$\frac{\partial c_i}{\partial t} = \nabla \cdot \left(\underbrace{D_i \nabla c_i}_{\text{Diffusion}} + \underbrace{\frac{z_i D_i}{R_u T} F c_i \nabla \psi}_{\text{Migration}} - \underbrace{c_i \mathbf{u}}_{\text{Advection}} \right) \tag{2.14b}$$

where t is time and c_i is the molar concentration for ion species i, respectively. Here, D_i is the mass diffusion coefficient of ion species i (m^2/s), $F = eN_A = 9.65 \times 10^4$ C/mol is the Faraday constant, $R_u = k_B N_A = 8.314$ J/(K·mol) is the universal gas constant and $\mathbf{u}$ is the velocity vector of ions' bulk motion. The three terms in the mass conservation equation given by Equation (2.14b) correspond to [9,82,132]: (1) ions' diffusion to their concentration gradient, (2) ions' migration due to electrostatic force, and (3) advection in the electrolyte due to the bulk motion of ion species, respectively. Note that the Poisson-Nernst-Planck model [Equation 2.14] reduces to the Gouy-Chapman model in steady state and when advection is negligible [35, 147].

The PNP model neglects the finite size of ions and treat ions as point-charges [95, 130, 146, 148, 149]. This assumption breaks down when either the electrolyte concentration c_∞ or the electric potential is large [95, 146, 149]. Therefore, the PNP model is invalid for practical EDLCs with typical electrolyte concentration

larger than 1 mol/L and potential window larger than 1 V.

2.3.4 Modified Poisson-Planck Models

Recent efforts have been made to account for the effect of finite ion size in modeling ion transport in concentrated electrolyte solutions and/or under large electric potential [95, 130, 146, 150–162]. For example, Kilic *et al.* [146] derived a modified Poisson-Nernst-Planck (MPNP) model valid for binary and symmetric electrolytes under large electrolyte concentration and electric potential. The authors added an excess term accounting for the entropic contribution due to finite-size ions in the expression of the Helmholtz free energy. This resulted in an excess term in the expressions of the chemical potentials and mass fluxes [95,130,146,151]. Assuming identical diffusion coefficient $D_1 = D_2 = D$ and negligible advection effect, the MPNP model is expressed as [95, 130, 146, 151],

$$\nabla \cdot (\epsilon_0 \epsilon_r \nabla \psi) = e N_A z (c_1 - c_2) \tag{2.15a}$$

$$\frac{\partial c_i}{\partial t} = \nabla \cdot \left(\underbrace{D \nabla c_i}_{\text{Diffusion}} + \underbrace{\frac{z_i D}{R_u T} F c_i \nabla \psi}_{\text{Migration}} + \underbrace{\frac{D N_A a^3 c_i \nabla (c_1 + c_2)}{1 - N_A a^3 (c_1 + c_2)}}_{\text{Correction due to finite ion size}} \right) \tag{2.15b}$$

This MPNP model reduces to the PNP model [Equation (2.14)] for vanishing ion diameter, i.e., for $a = 0$. Moreover, the MPNP model reduces to the MPB model [Equation (2.12)] in steady state [4]. Note that this MPNP model does not apply to asymmetric electrolytes or to multiple ion species [95, 130, 146, 148–152].

Alternatively, several authors [153–155] incorporated the finite ion size in ion mass fluxes using the activity coefficient to account for the deviation from ideal electrolyte solutions. However, these studies [153–155] were limited to binary and symmetric electrolytes. Note that the MPNP model developed by Kilic *et al.* [146] [Equation (2.15)] can be also formulated in a form equivalent to that based on the activity coefficient [95, 119, 130].

Davidson and Goulbourne [156] extended the MPNP model to multiple ion

species but with symmetric ion diameter and valency. Eisenberg and co-workers [157–159] developed a MPNP model for binary asymmetric electrolytes based on the variation principle. Horng *et al.* [160] later extended this model [157–159] for asymmetric electrolytes with multiple ion species. However, these MPNP models [157–160] were expressed as integral-differential equations, thus making the numerical solution procedure highly involved particularly for three-dimensional geometries.

Lu and Zhou [161,162] extended the expression of chemical potential developed in Refs. [97,98] and proposed a "size-modified" Poisson-Nernst-Planck (SMPNP) model for asymmetric electrolytes and multiple ion species. In their model [161, 162], they introduced a parameter "$k_i = a_i/a_0$" representing the ratio of ion diameter a_i and the diameter of solvent molecules a_0. The authors considered different cases for $k_i > 1$ and justified that the model successfully constrained the ion concentrations below their maximum values. However, this SMPNP model breaks down when neglecting the size of solvent molecules and as $k_i \to \infty$ since the excess term accounting for finite ion sizes approaches infinity.

2.4 Conclusions

The present chapter first summarized the definitions of integral and differential capacitances as well as their calculation formula in different experimental techniques. Then, it presented an overview of the existing models in the literature for equilibrium and transient simulations of supercapacitors. Limitations associated with these models were also discussed. Simulations of supercapacitors will be performed based on new numerical tools capable of capturing important electrochemical and transport phenomena in supercapacitors and will also be validated with experimental data. Scaling laws governing the performances of EDLCs will also be presented by performing dimensional analysis of the physics-based continuum modeling. Note that more detailed background and current state of knowledge on

specific topics will be introduced in the subsequent chapters.

CHAPTER 3

Accurate Simulations of EDLCs of Microspheres

This chapter presents the modeling and simulations of electric double layer capacitance of spherical microelectrodes. It aims to clarify the drawbacks of existing models and to identify the dominant physical phenomena that must be accounted for in predicting the electric double layer capacitance.

3.1 Introduction

Microelectrodes and ultramicroelectrodes (UMEs) have been the subjects of intense studies in electrochemical sensing [163–171] and in electrical energy storage and conversion [18, 27, 70, 72, 172–179]. Microelectrodes and ultramicroelectrodes refer to electrodes with characteristic size less than 25 μm [165–168]. These electrodes have been used extensively in different scanning probe microscopy techniques [180–186]. For example, scanning electrochemical potential microscopy (SECPM) was developed to directly measure the equilibrium electric potential profile in the electric double layer forming near electrode surfaces [182–186]. It also provides information on the local charge distribution and electric field in the electrolyte. The size and geometry of UMEs are critical parameters determining the spatial and temporal resolutions of the measurements [180–186].

Moreover, electrodes with nanostructures and tailored morphology hold great promise to enhance the energy and power densities of electrical energy storage devices [18, 27, 70, 72, 172–179]. For example, Pech *et al.* [31] synthesized onion-like carbon spheres $6 - 7$ nm in diameter and used them to synthesize electrodes for

electric double layer capacitors (EDLCs) using electrophoretic deposition. The volumetric power density of their EDLC devices was comparable to that of conventional electrolytic capacitors while the volumetric energy density was one order of magnitude larger [31]. This was attributed to the electrode's fully accessible surface area [31].

In all the above mentioned applications, understanding the electric double layer structure is of great importance for the rational and optimum design of the electrode morphology [27, 70, 175, 176, 183–186]. For this purpose, numerical simulations can facilitate the design of electrodes in a more systematic and efficient way than a trial-and-error approach. They can also account for various and complex phenomena and identify the dominant processes governing the capacitance behavior of the electrode. This chapter aims to develop rigorous and accurate numerical tools for simulating electric double layer formed near ultramicroelectrodes. It also assesses the validity of analytical expressions for the capacitance of ultramicroelectrodes.

3.2 Background

The equilibrium models for electric double layers were reviewed in Section 2.2 and therefore need not be repeated here. This section presents a review of existing simulations of electric double layer near ultramicroelectrodes.

3.2.1 Simulations of Electric Double Layer Near Ultramicroelectrodes

The models discussed in Section 2.2 have been used extensively to investigate the electric double layer near ultramicroelectrodes despite their inherent limitations. Huang *et al.* [85–87] used the Helmholtz model [Equation (2.5)] to predict the specific capacitance of EDLCs based on single spherical and cylindrical electrode carbon particles as well as single cylindrical pore. Their models predicted that the

total specific capacitance decreases with increasing electrode radius larger than 2 nm. However, the electrolyte permittivity was used as an empirical parameter to match the specific capacitance predicted by Equation (2.5) with experimental data [85–87].

Compton and co-workers [187,188] investigated the effect of the electrode curvature on the diffuse layer formed at the surface of single hemispherical and cylindrical nanoelectrodes. The authors solved the Gouy-Chapman model [Equation (2.7)] numerically for electrode radius ranging from 2 nm to 100 μm. The surface electric potential ψ_s was less than 0.25 V and the electrolyte concentration c_∞ was less than 0.1 mol/L. They observed significantly enhanced surface charge density for sphere radius less than 50 nm and attributed this phenomenon to the "nonclassical behavior" caused by the large electrode curvature [187,188]. However, it should be noted that this trend could be readily predicted by the exact solution given by Equation (2.9). Moreover, the Gouy-Chapman model used in Refs. [187,188] is limited to very low ion concentrations and electric potentials.

Huang *et al.* [94] used the Gouy-Chapman-Stern model to investigate the effects of the shape and geometry of a single nanopore on the specific capacitance. They explored "slit" and cylindrical pores with diameter ranging from 2 to 16 nm. The dielectric permittivity $\epsilon_r = 9.73$ was imposed in the Stern layer based on the values previously fitted in Refs. [85,86] while $\epsilon_r = 36$ in the diffuse layer [94]. The electrolyte concentration was $c_\infty = 1.0$ mol/L and the electrode surface potential was $\psi_s = 1$ V. However, the Gouy-Chapman-Stern model breaks down for such concentration and potential as ions can no longer be treated as point-charges [**?**,4].

Hamou *et al.* [185,186] numerically investigated the electric potential profile near the probe apex in SECPMs by simulating planar and spherical electrodes. Their model accounted for both the Stern layer and the finite size of ions and solved the MPB model given by Equation (4.1). The electrolyte concentration c_∞ ranged from 10^{-5} to 10^{-2} mol/L while the surface potential ψ_s varied from 0.2

to 0.4 V [185, 186]. The authors investigated the effects of the shape and size of the probe on the electric potential profile in the electrolyte. They found that a sharper apex resulted in (i) higher electric field and surface charge density at the probe vertex, as well as (ii) better resolution of the electric potential in the lateral direction [185, 186].

In nearly all the above mentioned references, the electrolyte dielectric permittivity was assumed to be constant and sometimes was treated as a fitting parameter. However, the relative permittivity ϵ_r of polar electrolytes is known to significantly decrease as the electric field increases [3, 189–195]. In fact, the individual electrolyte molecules become highly oriented under large electric field. Therefore, further orientation of the molecules can hardly provide more polarization and the relative permittivity decreases [191–193]. Booth derived the following model to account for the dependency of electrolyte dielectric permittivity on the local electric field [189–191],

$$\epsilon_r(E) = n^2 + \left(\epsilon_r(0) - n^2\right) \frac{3}{\beta E} \left[\coth(\beta E) - \frac{1}{\beta E}\right] \text{ for } E \geq 10^7 \text{ V/m} \quad (3.1a)$$

$$\epsilon_r = \epsilon_r(0) \text{ for } E < 10^7 \text{ V/m} \quad (3.1b)$$

where $E = |-\nabla\psi|$ is the norm of the local electrical field vector, $\epsilon_r(0)$ is the relative permittivity at zero electric field, and n is the index of refraction of the electrolyte at zero electric field frequency. Results of molecular dynamics simulations for different electrolytes [3, 193, 194] have verified that the Booth model accurately predicts the electrolyte permittivity for high electric fields up to 4 V/nm typically encountered in EDLCs [3, 10]. Moreover, the Booth model has been combined with Poisson equation in Refs. [196–198] to investigate the repulsion between two charged planar surface electrodes due to hydration forces in aqueous electrolyte solutions. Hamou *et al.* [186] investigated the effect of field-dependent electrolyte permittivity using the Booth model in the simulations of SECPM. However, they did not observe significant changes in the dielectric permittivity and in electric potential profiles [186].

More recently, Wang *et al.* [199] utilized the MPB and Booth models to predict the specific capacitance of closely packed monodispersed sphere arrays with different packing morphologies and sphere diameter. The numerical results established that the diffuse layer specific capacitance of the sphere arrays significantly decreased when the field-dependent electrolyte permittivity was accounted for [199]. However, the Stern layer capacitance was predicted using the Helmholtz model [Equation (2.5a)], rather than by simulating the complete electric double layer structure consisting of both the Stern and diffuse layers.

This chapter aims to clarify the dominant physical phenomena that must be accounted for in simulating electric double layer formed near ultramicroelectrodes. It also assesses the validity of the Helmholtz model. An equilibrium model based on continuum theory was developed to predict the specific capacitance of a single spherical electrode particle with various radius. To the best of our knowledge, the present study is the first to simulate the electric double layer capacitance of ultramicroelectrodes by simultaneously accounting for (1) the Stern and diffuse layers, (2) finite size of ions, and (3) field-dependent dielectric permittivity. Note that the double layer capacitances also significantly depend on surface electric potential [4, 95], electrolyte concentration [99, 102] and temperature [Equation (2.12)]. This has been explored extensively in the literature and need not be repeated.

3.3 Analysis

3.3.1 Schematics and Assumptions

Figure 3.1 shows the schematic of the computational domain simulated in the present study. A spherical electrode of radius R_0 was immersed in an electrolyte solution. The region of electrolyte solution consists of two layers corresponding to (1) a Stern layer of thickness H near the electrode surface and (2) a diffuse

layer beyond. By virtue of symmetry, the problem was one-dimensional in the radial direction and was solved in spherical coordinates. The electric potential was prescribed as positive at the electrode surface and was zero far away from the electrode surface. The length of the overall computational domain was specified to be $L = 80$ nm for all cases simulated. Increasing this length to 160 nm was found to have no effect on the predicted electric potential profile and on the specific capacitance.

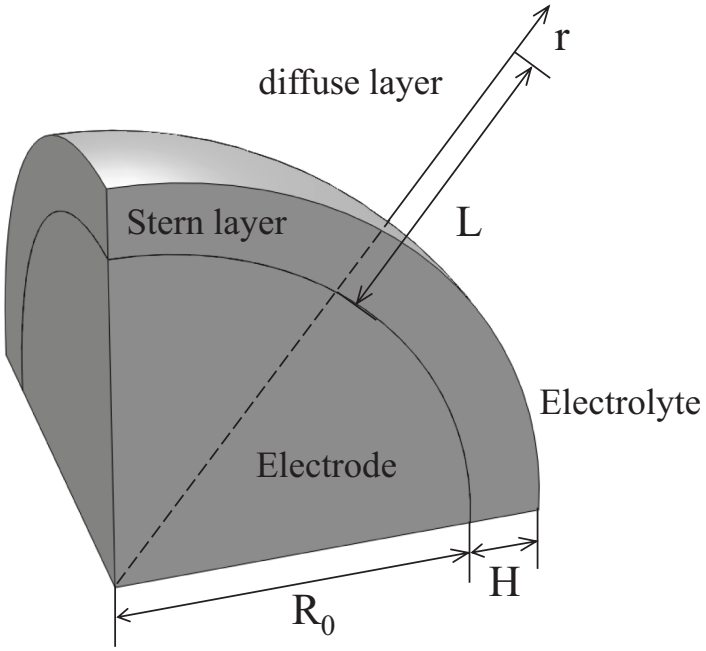

Figure 3.1: Schematic and coordinate system of the simulated computational domain consisting of the Stern layer and the diffuse layer. The problem is one-dimensional in spherical coordinates by virtue of symmetry.

To make the problem mathematically tractable, the following assumptions were made: (1) the electric potential and ion concentration were invariant with time (steady state) and reached their equilibrium states, (2) anions and cations had the same and constant effective diameter [4, 95, 200] independent of the electrolyte concentrations, (3) isothermal conditions prevailed throughout the electrode and electrolyte, (4) advection of the electrolyte was assumed to be negli-

gible, (5) the ions could only accumulate at the electrode surface and could not diffuse into the electrode particle, i.e., there was no ion insertion.

3.3.2 Governing Equation and Boundary Conditions

The local steady-state and equilibrium electric potential in the electrolyte solution denoted by $\psi(r)$ was computed by solving (i) Equation (2.10a) in the Stern layer and (ii) Equation (2.12) in the diffuse layer. In addition, the coordinate transformation $R = r - R_0$ was used to simplify the governing equation to,

$$\frac{1}{(R+R_0)^2}\frac{d}{dR}\left(\epsilon_0\epsilon_r(R+R_0)^2\frac{d\psi}{dR}\right)$$

$$= \begin{cases} 0 & 0 \leq R < H \quad (3.2a) \\ \dfrac{2zeN_Ac_\infty \sinh\left(\dfrac{ze\psi}{k_BT}\right)}{1+2\nu_p \sinh^2\left(\dfrac{ze\psi}{2k_BT}\right)} & R \geq H \quad (3.2b) \end{cases}$$

where R represents the distance from the electrode surface.

The associated boundary conditions were given by [8, 90],

$$\psi = \psi_s, \text{ at } R = 0 \quad (3.3a)$$

$$\psi\big|_{R=H^-} = \psi\big|_{R=H^+} \quad \text{and} \quad \epsilon_0\epsilon_r\frac{d\psi}{dR}\bigg|_{R=H^-} = \epsilon_0\epsilon_r\frac{d\psi}{dR}\bigg|_{R=H^+}, \text{ at } R = H \quad (3.3b)$$

$$\psi = 0, \text{ at } R = L \quad (3.3c)$$

Equation (3.3b) states that the electric potential and displacement were continuous across the Stern/diffuse layers interface located at $R = H$ [8, 90]. Cases when $H = 0$ in Equations (3.2) and (3.3) correspond to simulations without the Stern layer as performed in Refs. [4, 95–97, 99].

3.3.3 Constitutive Relations

In order to solve Equations (3.2) and (3.3), the electrolyte properties ϵ_r, z, c_∞ and a along with the temperature T are needed. Here, the Booth model [189–191]

given by Equation (3.1) was used to account for the effects of the electric field on electrolyte relative permittivity. The present study focuses on aqueous binary symmetric electrolyte solution at room temperature ($T = 298$ K) characterized by the following properties: $\epsilon_r(0) = 78.5$ [82], $n = 1.33$, and $\beta = 1.41 \times 10^{-8}$ V/m [196–198]. The effective ion diameter was taken as $a = 0.66$ nm and the valency was $z = 1$ corresponding to solvated ions such as K^+, OH^-, and Cl^- in aqueous solutions [200], for example. The electrolyte concentration was chosen as $c_\infty = 1.0$ mol/L corresponding to the typical values in EDLCs.

Finally, the Stern layer thickness H was approximated as the solvated ion radius, i.e., $H = a/2 = 0.33$ nm [9, 35, 36]. In reality, the Stern layer thickness may be larger than the solvated ion radius due to the specific adsorption of solvent molecules or anions near the electrode surface [8, 9, 36, 82, 90]. This is typically caused by non-electrostatic forces [8, 9, 36, 82, 90]. A parametric study was also carried out for different values of Stern layer thickness $H = 0,\ 0.33$ and 1.0 nm.

3.3.4 Method of Solution And Data Processing

Equation (3.2) was solved using the commercial finite element solver COMSOL 3.5a, along with the boundary conditions given by Equation (3.3). The model was solved for constant permittivity $\epsilon_r(0)$ or field-dependent permittivity $\epsilon_r(E)$ given by Equation (3.1). The specific capacitances of the Stern and diffuse layers were computed by dividing the surface charge density [35, 201, 202] $q_s(R) = \epsilon_0\epsilon_r E(R)$ by their respective potential difference as [9, 82, 90],

$$C_s^{St} = \frac{q_s(0)}{\psi_s - \psi_D} = \frac{\epsilon_0\epsilon_r E(0)}{\psi_s - \psi_D} \quad \text{and} \quad C_s^D = \frac{q_s(H)}{\psi_D} = \frac{\epsilon_0\epsilon_r E(H)}{\psi_D} \tag{3.4}$$

where $E(R) = |-d\psi/dR|(R)$ is the norm of the local electric field at location R while $\psi_D = \psi(H)$ is the electric potential computed at the Stern/diffuse layers interface. Then, total specific capacitance C_s was calculated using the series

formula as [9, 82, 90],

$$\frac{1}{C_s} = \frac{1}{C_s^{St}} + \frac{1}{C_s^{D}} \tag{3.5}$$

Numerical convergence was assessed based on the surface charge densities $q_s(R)$ at $R = 0$ and at $R = H$. The convergence criterion was chosen such that the maximum relative difference in both $q_s(0)$ and $q_s(H)$ was less than 1% when multiplying the total number of finite elements by two. The total number of finite elements required to obtain a converged solution was less than 400 for all cases simulated in the present study.

3.3.5 Validation

The numerical tool was validated against (i) the exact solutions of Gouy-Chapman model for planar electrodes [Equation (2.8)] and spherical electrodes [Equation (2.9)] for $\epsilon_r = 78.5$, $c_\infty = 0.01$ mol/L and $\psi_D = 0.01$ V, and (ii) the numerical results of MPB model [Equation (2.12)] for planar electrodes reported in Ref. [4] for a wide range of packing parameter ν_p and dimensionless potential ($ze\psi_D/k_BT$). Excellent agreement was found in all cases considered.

Figure 3.2 shows the numerically predicted diffuse layer specific capacitance C_s^D as a function of sphere radius R_0 ranging from 1 nm to 100 μm. It was obtained by solving Equation (3.2) with $H = 0$ assuming constant permittivity $\epsilon_r = 78.5$, $c_\infty = 0.01$ mol/L, $a = 0.66$ nm (i.e., $\nu_p = 0.0035$) and $\psi_D = 0.01$ V. Figure 3.2 also shows the exact solutions for planar and spherical electrodes respectively given by Equations (2.8) and (2.9). The numerical predictions agreed quite well with the exact solutions for all values of electrode radius considered. It is evident that C_s^D decreased with increasing sphere radius. It also reached the asymptotic value of planar electrodes [Equation (2.8)] for sphere radius larger than 100 nm. This can be attributed to the fact that smaller sphere radius results in larger surface electric field [202] and thus larger surface charge and specific capacitance.

These results are similar to the trend predicted numerically in Refs. [187,188] for spherical and cylindrical nanoelectrodes using $\psi_s = 0.25$ V and $c_\infty = 0.1$ mol/L. However, the observed trend is not due to "nonclassical behavior" but based on classical continuum theory.

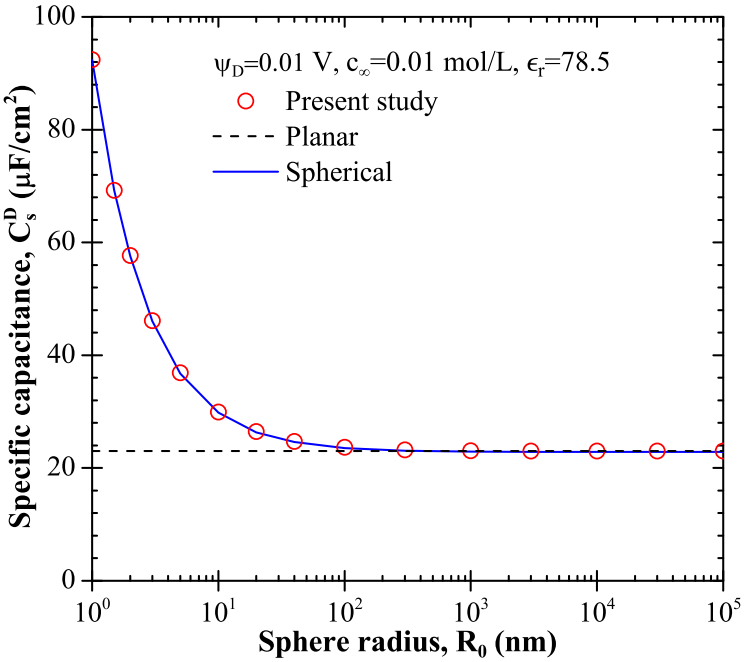

Figure 3.2: Predicted diffuse layer specific capacitance C_s^D obtained by numerically solving Gouy-Chapman model [Equation (2.7)] assuming constant permittivity $\epsilon_r = 78.5$, $c_\infty = 0.01$ mol/L, and $\psi_D = 0.01$ V, along with the exact solutions for planar and spherical electrodes [Equations (2.8) and (2.9)].

3.4 Results and Discussions

3.4.1 Revisiting Gouy-Chapman-Stern Model

Figure 3.3 shows the numerically predicted Stern, diffuse, and total specific capacitances as a function of sphere radius R_0 ranging from 1 nm to 100 μm as well as the predictions using Helmholtz model [Equation (2.5c)]. Results were obtained by solving the Gouy-Chapman-Stern model [Equation (2.10)] assuming constant

permittivity $\epsilon_r = 78.5$, $c_\infty = 1$ mol/L, $H = 0.33$ nm, and $\psi_s = 0.5$ V. The specific capacitances C_s^{St}, C_s^D, and C_s were computed using Equations (3.4) and (3.5). Figure 3.3 indicates that the predicted C_s^{St} decreased while C_s^D increased slightly with increasing sphere radius and reached a plateau for R_0 larger than 100 nm. In addition, the Stern layer specific capacitance C_s^{St} was much smaller than C_s^D. Thus, the total specific capacitance C_s was dominated by C_s^{St} according to Equation (3.5).

Furthermore, Figure 3.3(a) indicates that the predictions of Helmholtz model [Equation (2.5c)] were identical to the computed Stern layer specific capacitance C_s^{St}. This can be attributed to the fact that in both models, the electric potential is governed by Poisson's equation [Equation (2.10a)] assuming constant permittivity [83, 84]. Thus, the electric potential profile for planar electrodes is linear in both the Helmholtz model and the solution of the Gouy-Chapman-Stern model in the Stern layer [8, 9, 36, 82, 90]. Consequently, both models predict the same specific capacitance, i.e., C_s^H=C_s^{St}. This also establishes that the Helmholtz model predicts the Stern layer capacitance rather than the total double layer capacitance as sometimes assumed in the literature for large electrolyte concentrations [85–87].

Figure 3.3(b) shows the predicted electric potential ψ_D at the diffuse layer boundary ($R = H = 0.33$ nm) as a function of sphere radius R_0, as well as the maximum potential ψ_{max} given by Equation (2.11) for $\epsilon_r = 78.5$, $c_\infty = 1$ mol/L, $H = 0.33$ nm, and $\psi_s = 0.5$ V. It indicates that the computed diffuse layer potential ψ_D was larger than the maximum potential $\psi_{max} = 0.04$ V for all values of sphere radius considered. Therefore, the Gouy-Chapman-Stern model [Equation (2.10)] was not valid for computing the diffuse layer capacitance C_s^D for such high concentration as the results do not satisfy the point-charge assumption.

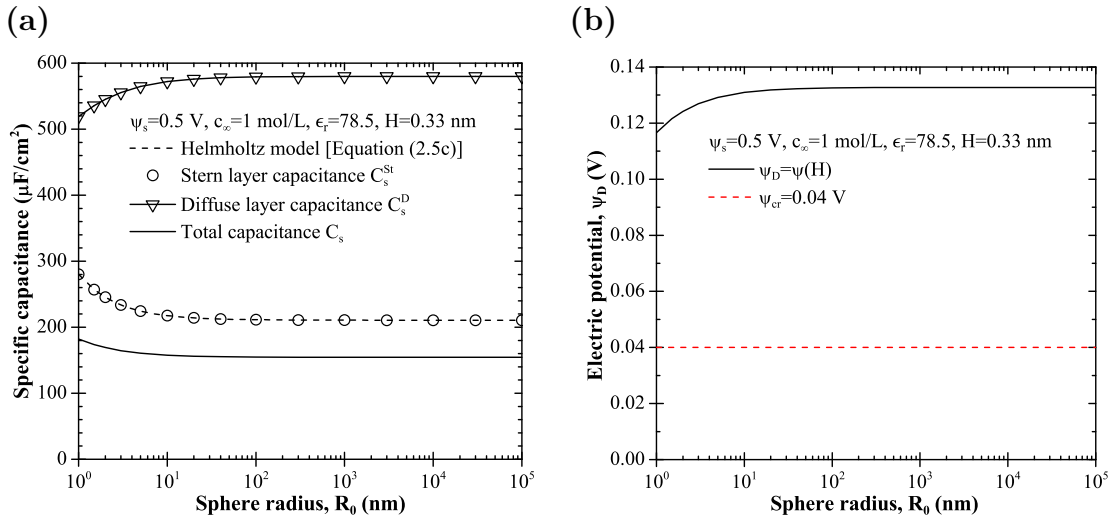

Figure 3.3: Predicted (a) Stern layer, diffuse layer, and total specific capacitances, and (b) electric potential ψ_D at the diffuse layer boundary ($R = H = 0.33$ nm) obtained by numerically solving Gouy-Chapman-Stern model [Equation (2.10)] assuming constant electrolyte permittivity $\epsilon_r = 78.5$, $c_\infty = 1$ mol/L, and $\psi_s = 0.5$ V.

3.4.2 Effect of Finite Size of Ions

Figure 3.4 shows the numerically predicted specific capacitances C_s^{St}, C_s^D, and C_s as a function of sphere radius R_0 obtained by solving the MPB model with Stern layer [Equations (3.2) and (3.3)]. The model accounted for both the Stern layer and the finite ion size in the diffuse layer with effective ion diameter $a = 0.66$ nm. The other parameters were identical to those used to generate Figure 3.3, i.e., $\epsilon_r = 78.5$, $c_\infty = 1$ mol/L, $H = a/2 = 0.33$ nm, and $\psi_s = 0.5$ V. Here again, the Stern layer specific capacitance C_s^{St} was identical to the predictions of (i) the Helmholtz model C_s^H [Equation (2.5c)] and (ii) of the Gouy-Chapman-Stern model (Figure 3.3) for all values of sphere radius. However, the predicted diffuse layer specific capacitance C_s^D decreased with increasing sphere radius by contrast with predictions from the Gouy-Chapman-Stern model shown in Figure 3.3. Moreover, C_s^D was about four times smaller than that plotted in Figure 3.3.

Then, the total specific capacitance C_s was no longer dominated by the Stern layer specific capacitance and was about half of that predicted by the Gouy-Chapman-Stern model (Figure 3.3). These results demonstrate that the finite size of ions has a significant effect on the specific capacitance and must be accounted for in simulating electric double layer for large electrolyte concentration and large electric potential. Here again, the Helmholtz model cannot be used to predict the total specific capacitance.

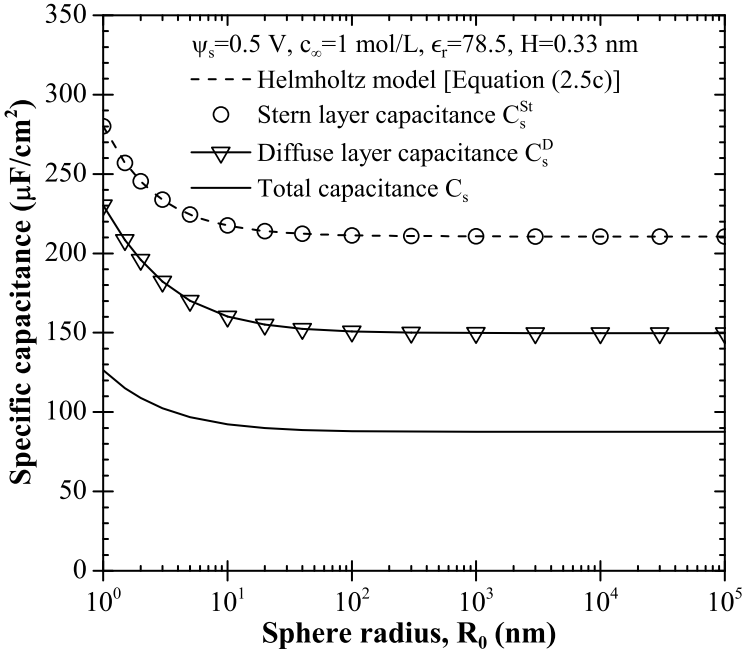

Figure 3.4: Predicted specific capacitances obtained by numerically solving the MPB model with Stern layer [Equations (3.2) and (3.3)] assuming constant electrolyte permittivity $\epsilon_r = 78.5$, $c_\infty = 1$ mol/L, and $\psi_s = 0.5$ V, while $H = a/2 = 0.33$ nm.

3.4.3 Effect of Field-dependent Dielectric Permittivity

Figure 3.5 shows the numerically predicted specific capacitances C_s^{St}, C_s^D, and C_s as a function of R_0 accounting for field-dependent permittivity. Results were

obtained by solving the MPB model with Stern layer [Equations (3.2) and (3.3)] with $c_\infty = 1$ mol/L, $H = a/2 = 0.33$ nm, $\psi_s = 0.5$ V, and ϵ_r given by Equation (3.1). It also shows the predictions by the Helmholtz model [Equation (2.5c)] using $\epsilon_r = \epsilon_r(E_s)$ based on the local electric field computed at the electrode surface $E_s = E(R = 0)$.

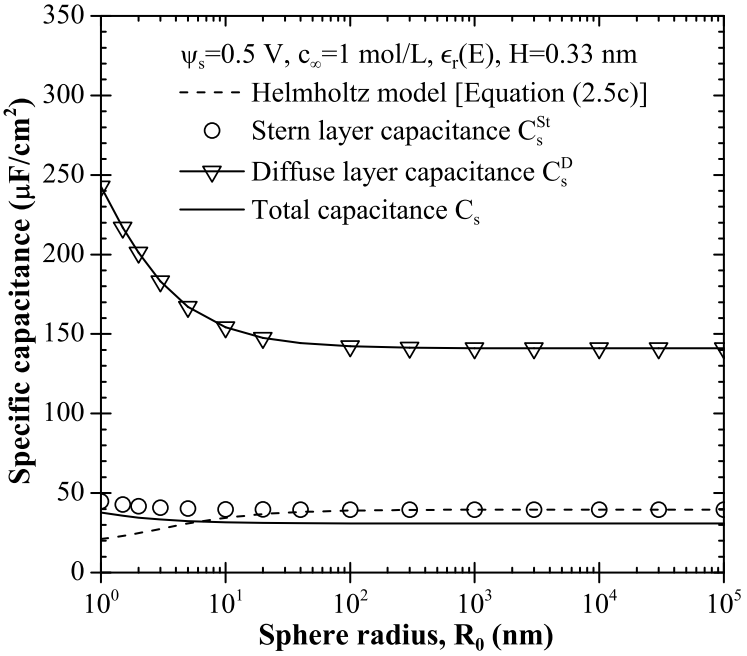

Figure 3.5: Predicted specific capacitances obtained by numerically solving the MPB model with Stern layer [Equations (3.2) and (3.3)] using field-dependent electrolyte permittivity [Equation (3.1)] with $c_\infty = 1$ mol/L, $\psi_s = 0.5$ V and $H = a/2 = 0.66$ nm.

Figure 3.5 indicates that the predicted Stern layer specific capacitance C_s^{St} using field-dependent permittivity $\epsilon_r(E_s)$ differed significantly from that obtained assuming constant permittivity (Figure 3.4). First, the numerical predictions assuming constant permittivity overestimated C_s^{St} by a factor of 4. Second, the predicted value of C_s^{St} was now in the range of $40 - 45$ μF/cm^2 and was about 4 to 5 times smaller than C_s^D. Third, the predicted Stern layer capacitance C_s^{St} was found to be nearly independent of the sphere radius. This can be attributed to

the facts that a smaller sphere radius resulted in larger surface electric field and thus smaller electrolyte permittivity. Overall, these competing effects balanced each other so that the surface charge density, given by $q_s = \epsilon_0 \epsilon_r(E_s) E_s$, and the specific capacitance C_s^{St} given by Equation (3.4) did not change significantly as sphere radius varied.

By contrast, the Helmholtz model predicted that the specific capacitance decreased with decreasing sphere radius less than 40 nm due to the significant decrease of electrolyte permittivity. In fact, the Helmholtz model underestimated the Stern layer capacitance for sphere radius less than 40 nm when accounting for field-dependent permittivity. Figure 3.5 also demonstrates that the predicted diffuse layer specific capacitance C_s^D using field-dependent permittivity $\epsilon_r(E)$ was nearly the same as the predictions assuming constant permittivity $\epsilon_r(0)$ shown in Figure 3.4. Note that the electrolyte relative permittivity and the Stern layer thickness (or solvated ion radius) could be adjusted arbitrarily in order to achieve good agreement between Helmholtz model and experimental data as performed in Refs. [85–87]. However, the effects of electrolyte concentration and electrode potential cannot be predicted explicitly by this approach. In other words, such an approach lacks rigor and thus cannot be used for the systematic optimization of EDLCs.

Overall, the total capacitance $C_s = 31 - 37$ μF/cm^2 was about half of that predicted assuming constant permittivity (Figure 3.4). It was dominated by the Stern layer capacitance as shown in Figure 3.5. This is consistent with the hypothesis typically made for concentrated electrolyte solutions [85–87]. Moreover, the electrode curvature had no effect on the predicted specific capacitance C_s^{St}, C_s^D, and C_s for sphere radius larger than 40 nm instead of 100 nm when assuming constant permittivity (Figure 3.4).

In summary, these results demonstrate that the Stern layer as well as the finite ion size and field-dependent electrolyte permittivity need to be accounted for in

simulating EDLCs. This is particularly true when the electrode sphere radius is small and less than 40 nm for aqueous electrolytes.

Note that Hamou *et al.* [186] investigated the effect of field-dependent electrolyte permittivity in the simulation of SECPMs using the Booth model. Unfortunately, the parameters used in the Booth model were not reported in Ref. [186]. Unlike the present study, the authors did not observe significant change in the dielectric permittivity and in electric potential profiles [186]. This may be attributed to the following two reasons. First, the electrolyte concentration and the surface potential considered in Ref. [186] were $c_\infty = 10^{-5} - 10^{-3}$ mol/L and $\psi_s = 0.2 - 0.4$ V. These values were lower than $c_\infty = 1$ mol/L and $\psi_s = 0.5$ V used in the present study. Second, electric double layers between the working electrode and the probe overlapped in the simulations of SECPMs [186]. This could significantly reduce the local electric field making the dependency of the electrolyte permittivity on the electric field negligible [199].

3.4.4 Effect of Stern Layer Thickness

Figure 3.6 shows the diffuse layer specific capacitance C_s^D as a function of R_0 obtained by solving Equations (3.2) and (3.3) using field-dependent permittivity for Stern layer thickness $H = 0$, 0.33 and 1.0 nm. The case of $H = 0$ nm corresponds to the simulation of the diffuse layer without Stern layer. The other parameters were identical to those used to produce Figure 3.5. Figure 3.6 shows that C_s^D decreased with decreasing Stern layer thickness for all particle radius R_0. The predicted C_s^D significantly decreased with increasing sphere radius R_0 for finite Stern layer thickness H. However, in the limiting case of $H = 0$ nm (i.e., without Stern layer), C_s^D remained nearly independent of R_0.

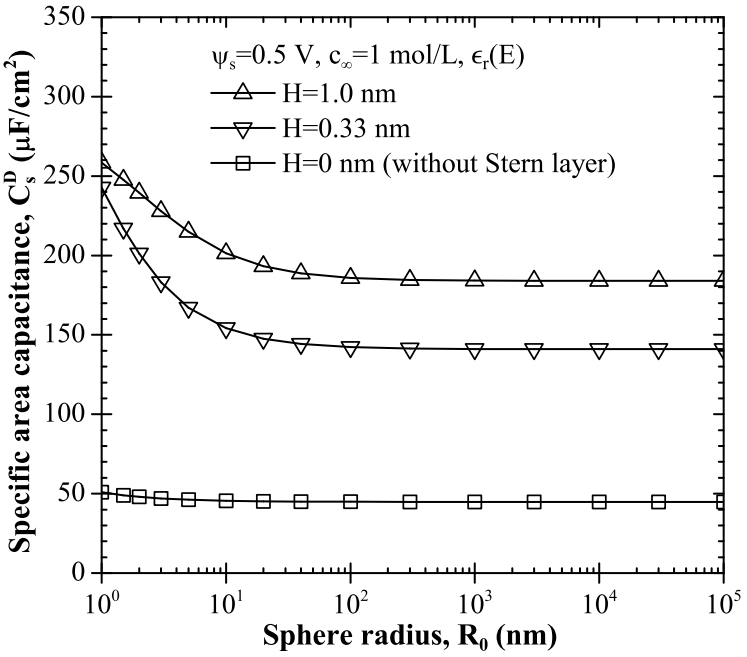

Figure 3.6: Predicted diffuse layer specific capacitance C_s^D obtained by numerically solving Equations (3.2) and (3.3) using field-dependent electrolyte permittivity [Equation (3.1)] for Stern layer thickness $H = 0,\ 0.33$ and 1.0 nm. Electrolyte concentration was set to be $c_\infty = 1$ mol/L and surface potential was $\psi_s = 0.5$ V while $a = 0.66$ nm.

3.5 Conclusions

This chapter presented numerical simulations of the electric double layer near the surface of a spherical ultramicroelectrode particle immersed in aqueous electrolyte solution. The model accounted for (i) the Stern and diffuse layers, (ii) the finite size of ions in both layers, as well as (iii) the field-dependent electrolyte permittivity. The effect of electrode curvature was also investigated by varying the particle radius from 1 nm to 100 μm. The following conclusions can be drawn:

1. The field-dependent permittivity $\epsilon_r(E)$ significantly affects predictions of the Stern layer and total specific capacitances for all particle radius considered.

2. The finite size of ions and the Stern layer need to be accounted for in predict-

ing the electric double layer capacitance for large electric potential ($\sim$ 0.5 V) and electrolyte concentration ($\sim$ 1 mol/L).

3. The electrode curvature has negligible effect on the Stern layer and diffuse layer specific capacitances for sphere radius larger than 40 nm for both constant and field-dependent permittivity.

4. The Stern layer capacitance dominates the total capacitance when the electrolyte concentration and surface potential are large ($c_\infty \geq 1$ mol/L and $\psi_s \geq 0.5$ V).

5. The Helmholtz model predicts the Stern layer capacitance C_s^{St} of a sphere if the electrolyte permittivity is assumed to be constant or if the sphere radius is larger than 40 nm.

6. The Helmholtz model significantly underestimates C_s^{St} for sphere radius less than 40 nm when accounting for field-dependent permittivity.

These conclusions will be useful in accurately simulating ultramicroelectrodes for electrochemical sensors and EDLCs with more complex geometries.

CHAPTER 4

Equilibrium Simulations of EDLCs with Carbon Sphere Arrays

The previous chapter identified the dominant physical phenomena that must be accounted for in modeling EDLCs based on the simulations of a single spherical microelectrode. Electrodes of actual EDLCs are made of mesoporous materials with three-dimensional morphology. This chapter extends the tool developed in the previous chapter and presents the modeling and simulations of EDLCs with three-dimensional electrode morphology.

4.1 Introduction

Electrodes in EDLCs are typically made of materials featuring both micropores and mesopores offering large surface area [1, 27, 28, 32–34, 40]. Research efforts have focused on increasing the energy density of EDLCs by increasing the surface area of porous electrodes and tailoring their morphology or pore size distribution [1, 27, 28, 32–34, 40]. For example, Liu *et al.* [5] synthesized highly ordered mesoporous carbon spheres arranged in a face-centered cubic structure and used them as electrodes for EDLCs. Mesopores with hexagonal cross-section existed in the carbon spheres and aligned toward the sphere center [5]. The diameters of the mesoporous carbon spheres and their mesopores were 250 nm and 10.4 nm, respectively while the total specific surface area was reported to be 601 m^2/g [5]. The electrolyte was $(C_2H_5)_4NBF_4$ in propylene carbonate non-aqueous solution [5]. The capacitance of the mesoporous carbon spheres was measured using both cyclic

voltammetry and galvanostatic charge/discharge. The capacitance measured by cyclic voltammetry at low scan rate (1 mV/s) was identical to results obtained using galvanostatic method [5]. The authors reported the specific area capacitance of 10.8, 12.6, and 14.0 μF/cm^2 under voltage of 1.5 V for the electrolyte concentrations of 0.3, 0.5, and 1.0 mol/L, respectively [5].

Numerous experimental studies have been devoted to characterizing the performances of EDLCs and their dependence on the material, morphology, and pore size of the porous electrodes, as well as on the ion size and solvent of the electrolyte [37,39,42,43,203–212]. It is believed that the optimal electrode morphology should provide both large surface area and "appropriate pore size" [1, 33]. However, it remains unclear how the electrode morphology affects the capacitance of EDLCs [1, 85, 86].

The equivalent RC circuit models [122, 124, 125, 127] and homogeneous models [132–145] have been used to numerically predict and investigate the performance of EDLCs. However, the equivalent RC circuit models require prior knowledge of macroscopic parameters such as the resistance and capacitance of the device which are typically determined experimentally or by other methods. Moreover, the classical RC circuit models may not be valid for EDLCs since this approach inherently neglects ion diffusion and non-uniform ion concentration in the electrolyte [128–130]. Alternatively, homogeneous models were also developed to investigate the charging/discharging dynamics of EDLCs. These models treat the heterogeneous microstructure of the electrodes as homogeneous with some effective macroscopic properties determined from effective medium approximations and depending on porosity and specific area [133–145]. In addition, they typically impose specific area capacitance or volumetric capacitance rather than predict them [133–145]. In addition, none of the RC and homogeneous models mentioned accounts for the detailed mesoporous electrode morphology.

Moreover, Yang *et al.* [213] performed molecular dynamics (MD) simulations

of EDLCs made of 390 single-wall carbon nanotubes with diameter of 0.67 nm. Their results showed that the capacitance increases "modestly" with decreasing pore diameter larger than 2 nm. This qualitatively supported the experimental results reported for mesoporous carbide-derived carbon electrodes [37]. However, MD simulations are inadequate to perform extensive and systematic study of EDLCs due to their computational cost and time requirement.

This chapter aims to clarify the fundamental physical mechanisms to be accounted for in simulating EDLCs. Three-dimensional (3D) equilibrium and heterogeneous model based on continuum theory was developed to predict the specific area capacitance of electrodes made of closely-packed spheres and of cylindrical mesopores immersed in an electrolyte. It is unique in that it accounts for (i) the accurate electrode morphology, (ii) the non-uniform ion concentration and electric potential distribution in the electrolyte, as well as (iii) the dependency of the electrolyte dielectric permittivity on the electric field.

4.2 Analysis

4.2.1 Schematics and Assumptions

The actual geometry of the mesoporous carbon electrodes synthesized in Ref. [5] was quite complex. In order to simplify the simulations while accurately accounting for the electrode morphology, the problem was divided in two uncoupled problems simulating (1) non-porous (i.e. dense) carbon spheres arranged in periodic packing, and (2) a single mesopore inside a carbon matrix. This approach is supported by the following facts: (i) under equilibrium conditions, the electric potential is uniform across all the electrode particles. Thus, the electric potentials at the outer surface of the carbon spheres and the inner pore walls were identical. (ii) The electric potential in the electrolyte solution decreased rapidly to zero away from the electrode surface as discussed in Section 4.3.2. Therefore,

it suffices to consider the dense spheres and mesopores separately while imposing the same potential at the sphere or mesopore surface and zero potential far-away in the electrolyte solution.

Figure 4.1 shows the schematic of a representative computational domain of closely-packed dense spheres. Only the domain consisting of the electrodes and the electrolyte solution was considered thus, ignoring the current collector. The electrodes consisted of dense monodispersed carbon spheres arranged in simple cubic (SC), body-centered cubic (BCC), and face-centered cubic (FCC) packings. Due to the periodicity, only a representative region of the entire electrode was considered with the width and height equal to that of one unit cell. Moreover, only a quadrant of a lattice unit cell was simulated by virtue of symmetry (Figure 4.1). Figures 4.1a through c illustrate the computational domain corresponding to five unit cells with SC, BCC and FCC packings, respectively. The distance separating the anode and cathode (separator) was always specified as 100 nm. Increasing the distance to 200 nm was found to have no effect on the predicted equilibrium capacitance. Note, however, that this distance would have a significant effect on transient simulations of the EDLC devices [139, 140, 214]. In addition, it is sufficient to simulate only half of the entire device and consider only the anode, for example, due to antisymmetry in the electric potential.

Moreover, Figure 4.2 shows the schematic of the computational domain of one mesopore in a mesoporous carbon sphere. Assuming the electric potential to be the same across the solid phase of the mesoporous spheres, it suffices to simulate only one mesopore. Mesopores with either hexagonal or circular cross-section were simulated. The length of the mesopore was denoted by L and varied from 50 to 250 nm since its exact length remained unknown [5]. An additional electrolyte region was specified on one end of the mesopore with $L < 250$ nm corresponding to the space between adjacent carbon spheres (Figure 4.2b). Due to symmetry, the length of this region was specified as 30 nm corresponding to half of the

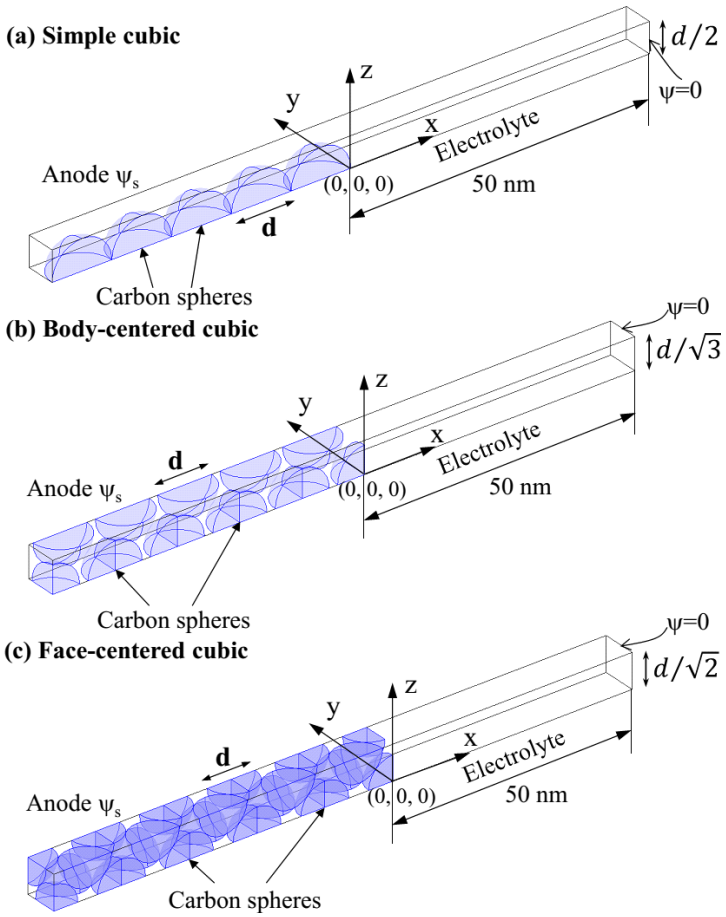

Figure 4.1: Schematic, dimensions, and coordinate system of the computational domain simulated for carbon spheres with (a) SC, (b) BCC, and (c) FCC packings. Shaded areas represent carbon spheres of diameter d. Five unit cells are shown here for illustration purposes.

"interconnected window" between carbon spheres of 250 nm in diameter [5]. For mesopores going through the entire sphere ($L = 250$ nm), a 30 nm thick electrolyte region was specified at both ends of the pore (Figure 4.2c).

To make the problem mathematically tractable, the following assumptions were made: (1) the electric potential and ion concentration were invariant with time (steady state) and reached their equilibrium states, (2) all the electrode particles were at the same potential since there is no electric current under equilibrium

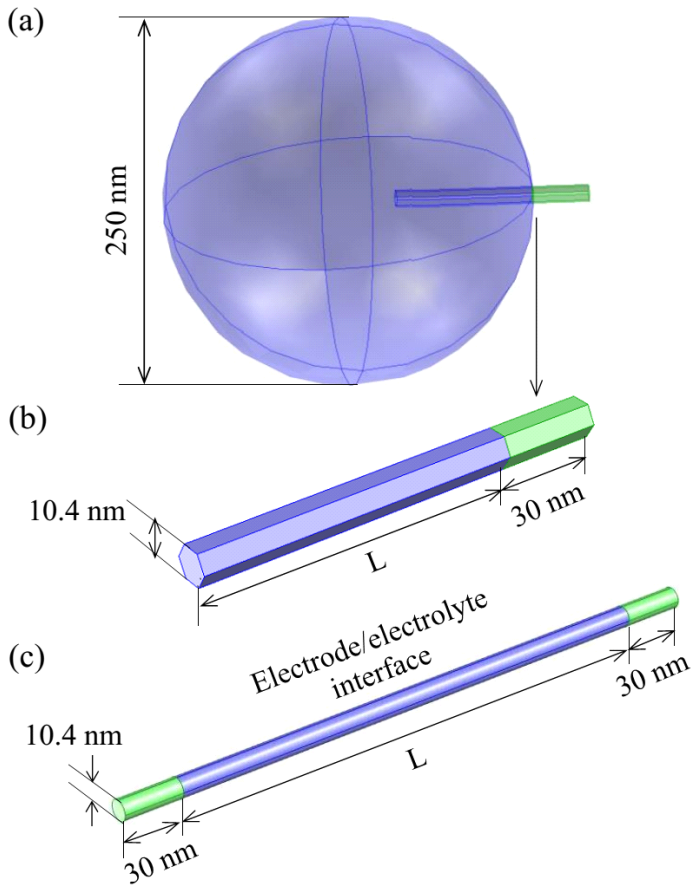

Figure 4.2: Schematic and dimensions of the computational domain simulated for (a) one mesopore within a carbon sphere of (b) hexagonal cross-section with pore length $L < 250$ nm, and (c) circular cross-section with pore length $L = 250$ nm.

conditions, (3) anions and cations had the same effective diameter [4, 95–97], (4) isothermal conditions were assumed throughout the electrolyte solution and the carbon spheres, (5) advection of the electrolyte was assumed to be negligible, (6) the ions could only accumulate at the electrode surfaces and could not diffuse into the solid phase of carbon particles constituting the electrodes. In fact, in the cyclic voltammetry experiments reported in Ref. [5], no pseudocapacitive peak was observed in the C-V curves. Therefore, ion insertion contribution to the electrode capacitance was considered negligible [9, 10], and (7) the continuum theory was assumed to be valid for all the cases considered in this study. Its validity has

been examined in the literature [215–218] and is typically accepted when the pore diameter is larger than $3 - 5$ nm [215–218].

4.2.2 Governing Equation and Boundary Conditions

Based on assumptions (2) and (6), the governing equations only need to be solved within the electrolyte solution. The local steady-state and equilibrium electric potential in the diffuse layer, denoted by $\psi(x, y, z)$, can be found by solving the modified Poisson-Boltzmann (MPB) model accounting for the finite size of the ions [4, 95–97, 99]. Among different MPB models, Bikerman's model was the simplest developed for symmetric electrolytes and was expressed as [4, 95–97, 99],

$$\nabla \cdot (\epsilon_0 \epsilon_r \nabla \psi) = zeN_A c_\infty \frac{2 \sinh\left(\dfrac{ze\psi}{k_B T}\right)}{1 + 2\nu_p \sinh^2\left(\dfrac{ze\psi}{2k_B T}\right)} \tag{4.1}$$

where ϵ_0 and ϵ_r are the free space permittivity and relative permittivity of the electrolyte, respectively. The valency of the symmetric electrolyte is denoted by z, while T is the absolute temperature, c_∞ is the bulk molar concentration of electrolyte, e is the elementary charge, N_A and k_B are the Avogadro constant and Boltzmann constant, respectively. The packing parameter is defined as $\nu_p = 2a^3 N_A c_\infty$ where a is the effective ion diameter. It represents the ratio of the total bulk ion concentration to the maximum ion concentration assuming a simple cubic ion packing [4, 95, 102, 130]. Therefore, it should not be larger than unity for the model to be physically acceptable [102, 130].

The boundary conditions associated with Equation (4.1) correspond to experimental conditions where the electric potential was set to be constant and equal to ψ_s and $-\psi_s$ at the anode and cathode, respectively. By virtue of symmetry of the geometry and antisymmetry in the electric potential, only half of the entire domain was simulated (Figure 4.1). Then, the boundary conditions can be written

as,

$$\psi(\mathbf{r}_a) = \psi_s \quad \text{and} \quad \psi(\mathbf{r}_s) = 0 \tag{4.2}$$

where $\mathbf{r}_a$ and $\mathbf{r}_s$ denote the position vectors of the electrode/electrolyte interfaces for the anode and the center plane of the separator, respectively. In addition, symmetric conditions were imposed at all the other boundaries.

4.2.3 Constitutive Relations

In order to solve Equations (4.1) and (4.2), the electrolyte properties ϵ_r, z, c_∞ and a are needed. The relative permittivity ϵ_r of polar electrolytes may significantly decrease as the electric field increases [189–193]. In fact, the individual electrolyte molecules become highly oriented under large electric field. Therefore, further orientation of the molecules can hardly provide more polarization and the relative permittivity decreases [191–193]. Here, the Booth model [189–191] was used to account for the effects of the electric field on electrolyte relative permittivity. It is expressed as [189–191],

$$\epsilon_r(E) = n^2 + \left(\epsilon_r(0) - n^2\right) \frac{3}{\beta E} \left[\coth(\beta E) - \frac{1}{\beta E}\right] \text{ for } E \geq 10^7 \text{ V/m} \tag{4.3a}$$

$$\epsilon_r = \epsilon_r(0) \text{ for } E < 10^7 \text{ V/m} \tag{4.3b}$$

where $E = |-\nabla\psi|$ is the norm of the local electric field vector, $\epsilon_r(0)$ is the relative permittivity at zero electric field, and n is the index of refraction of the electrolyte at zero electric field frequency.

The Booth model was combined with Poisson equation in Refs. [196–198] to investigate the repulsion between two charged planar surface electrodes due to hydration forces in aqueous electrolyte solutions. However, to the best of our knowledge, the present study is the first to combine field-dependent permittivity and Poisson equation for simulating EDLCs. It focuses on $(C_2H_5)_4NBF_4$ electrolyte in propylene carbonate solution at room temperature characterized by the

following properties: $\epsilon_r(0) = 64.4$ [219], $n = 1.42$ [220], and $z = 1$. Moreover, the parameter β in Equation (4.3a) was determined by least-square fitting for the relative permittivity of propylene carbonate reported in Ref. [3] and obtained by MD simulations. Figure 4.3 shows the relative permittivity of propylene carbonate predicted by the Booth model with $\beta = 1.314 \times 10^{-8}$ m/V along with the predictions from MD simulations [3]. The maximum relative difference was found to be less than 7% for electric field between 0 and 4×10^9 V/m.

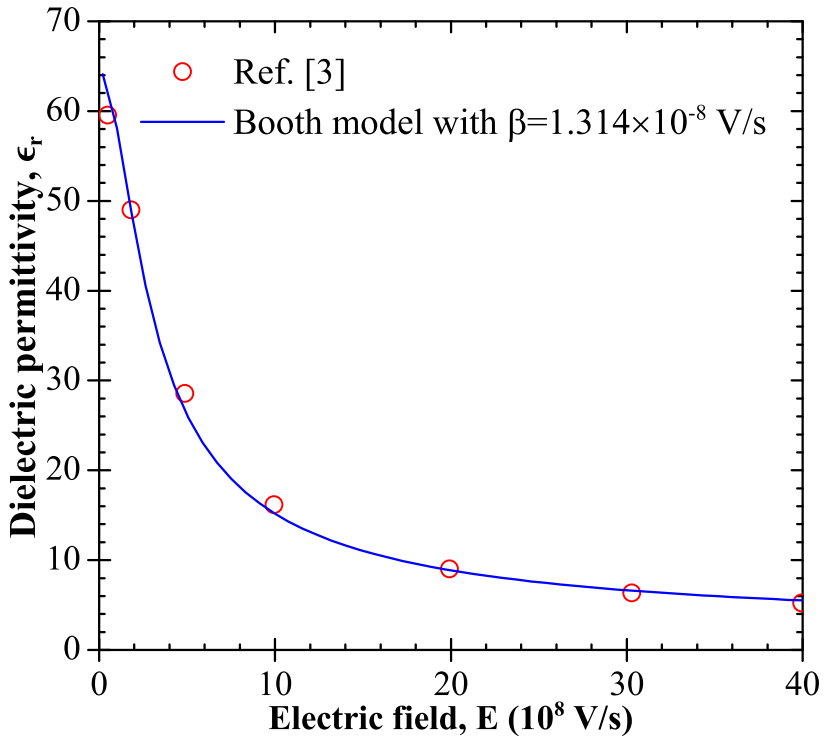

Figure 4.3: Comparison of the relative permittivity of propylene carbonate electrolyte predicted by Booth model [Equation (4.3)] with $\beta = 1.314 \times 10^{-8}$ m/V with predictions from MD simulations reported in Ref. [3]. The maximum relative difference was less than 7%.

Finally, the values of electrolyte concentration c_∞ used in the simulation were the same as those used in Ref. [5], i.e., $c_\infty = 1.0$ mol/L. The ion diameter of non-solvated $(C_2H_5)_4N^+$ and BF_4^- ions was reported to be $a_{\min} = 0.68$ nm and

0.33 nm [37, 221], respectively. However, as discussed in Ref. [95, 222], "Smaller bare ions tend to be more heavily solvated and therefore have larger effective diameters". Here, the effective ion diameters of $(C_2H_5)_4N^+$ and BF_4^- were assumed to be equal. In addition, when the electrolyte concentration decreases, the dissolved electrolyte ions are more solvated, i.e., they are surrounded by more solvent molecules [5, 223–226]. Consequently, the effective diameter a of the ions may decrease with increasing electrolyte concentration [5, 224, 226]. Considering the fact that the solubility of $(C_2H_5)_4NBF_4$ in propylene carbonate is about 1 mol/L at room temperature [227], the effective ion diameter a was assumed to be equal to $a = 0.68$ nm. The other parameters needed to perform the simulations were also chosen to be consistent with those used experimentally, i.e., $T = 298$ K, and $2\psi_s = 1.5$ V [5].

4.2.4 Method of Solution And Data Processing

Equation (4.1) was solved using the commercial finite element solver COMSOL 3.5a, along with the boundary conditions given by Equation (4.2). The model was solved for constant permittivity $\epsilon_r(0)$ or field-dependent permittivity $\epsilon_r(E)$ given by Equation (4.3). The simulations were run on a Dell workstation Precision 690 with two 2.66 GHz Quad-Core Intel Xeon CPUs and 40 GB of RAMs.

The total amount of charges Q stored at the anode was computed by integrating the surface charge density ($\epsilon_0\epsilon_r\mathbf{E}\cdot\mathbf{n}$) along the anode/electrolyte interfaces as [35, 201],

$$Q = \int_{A_a} \epsilon_0\epsilon_r\mathbf{E}\cdot\mathbf{n}\; dA \tag{4.4}$$

where $\mathbf{E} = -\nabla\psi$ is the electric field vector, $\mathbf{n}$ is the local outward normal unit vector at the anode/electrolyte interfaces. The interfacial surface area A_a of dense sphere packings was the sum of the surface area of the carbon spheres and of the current collector. For the single pore simulations, A_a was the surface area

of the mesopore. The absolute amount of charges computed at the anode and cathode were identical due to symmetry in geometry and to the anti-symmetry of the electric potential. The capacitance of the diffuse layer of the simulated EDLC from single electrode was estimated as $C^D = Q/\psi_s$ while its specific area capacitance C_s^D was given by,

$$C_s^D = \frac{C^D}{A_a} = \frac{Q}{\psi_s A_a} = \frac{1}{\psi_s A_a} \int_{A_a} \epsilon_0 \epsilon_r \mathbf{E} \cdot \mathbf{n} \, dA \tag{4.5}$$

Moreover, the total specific area capacitance of electric double layer, denoted by C_s, consists of the Stern layer capacitance and of the diffuse layer capacitance in series. It is expressed as [9, 10, 36],

$$\frac{1}{C_s} = \frac{1}{C_s^{St}} + \frac{1}{C_s^D} \tag{4.6}$$

where C_s^{St} is the Stern layer specific area capacitance which can be estimated as [9, 10, 36],

$$C_s^{St} = \frac{\epsilon_0 \overline{\epsilon}_r}{H} \tag{4.7}$$

where H is the thickness of the Stern layer. It can be approximated as the radius of the solvated ions [9, 35, 36, 92] while $\overline{\epsilon}_r$ is the average dielectric permittivity along electrode surface defined as,

$$\overline{\epsilon}_r = \frac{1}{A_a} \int_{A_a} \epsilon_r(E) \, dA \tag{4.8}$$

Here, $\epsilon_r(E)$ is determined by Equation (4.3) based on the local electric field at the electrode surface computed numerically. Note that here, the potential drop in the Stern layer was neglected. The same approach was used by Bazant *et al.* [95] to predict the differential double layer capacitance of Ag electrode in KPF_6 aqueous electrolyte solution. Nevertheless, Wang and Pilon [228] found that the predicted diffuse layer specific area capacitance vs. electrode diameter without Stern layer featured the same trend as that accounting for potential drop in the Stern layer.

Finally, numerical convergence was assessed based on the total amount of charges Q accumulated at the electrode/electrolyte interfaces. For the simulation of packed carbon spheres, the convergence criterion was chosen such that the maximum relative difference in Q was less than 2% and 6% for constant permittivity and field-dependent permittivity, respectively, when multiplying the total number of finite elements by at least two. For the simulation of mesopores, this convergence criterion was chosen to be 2.5% for both constant and field-dependent dielectric permittivity. The tetrahedral elements were used in all the meshes generated. Mesh refinement was required near the electrode surfaces where the large potential gradient was large. The maximum element size to reach a converged solution was about $0.08 - 0.2$ nm at all electrode surfaces. The total number of finite elements depended on the electrode morphology (SC, BCC, FCC) and on the number of unit cells simulated, as well as on the model used for ϵ_r. The number of finite elements was on the order of 10^5 to 10^6 in the simulations of densely packed spheres when assuming constant ϵ_r. It was one order of magnitude larger for field-dependent ϵ_r predicted by Equation (4.3) due to larger potential gradient near the electrode surfaces as discussed in Section 4.3.3. In addition, the number of elements was on the order of 10^5 to 10^6 for the single-pore simulations depending on the pore length and for both constant and field-dependent ϵ_r.

4.3 Results and Discussions

4.3.1 Effect of Electrode Thickness On Diffuse Layer Capacitance

The effect of the number of unit cells on the diffuse layer specific area capacitance C_s^D was first investigated for SC, BCC, and FCC packings and for electrode spheres with diameter equal to 5, 10, 20, 40, 60, 80 and 100 nm. For each packing morphology and sphere diameter, the number of unit cells was increased from 1 to 5. The diffuse layer specific area capacitance C_s^D computed when assuming

constant electrolyte permittivity decreased slightly when increasing the number of unit cells and rapidly reached a plateau (not shown). The effect of the number of unit cells simulated on C_s^D was smaller for large particle diameter. In fact, for particle diameter $d = 20$ nm, the relative difference in C_s^D between 2 and 5 unit cells was found to be less than 2%.

In cases when ϵ_r dependency on electric field was accounted for through Equation (4.3), this difference was less than 3% for all sphere diameters and packing morphologies considered. Therefore, the diffuse layer capacitance C_s^D computed for mesoporous electrodes can be assumed to be independent of the number of unit cells simulated.

4.3.2 Effect of Electrode Morphology

Figure 4.4 shows the computed electric potential contours in two representative cross-sections perpendicular to the x-axis in the computational domain for the SC packing with five spheres of diameter $d = 10$ nm. Their x-coordinates were (a) $x = -d/2$, and (b) $x = -d$, respectively. Results were obtained assuming constant permittivity ($\epsilon_r = 64.4$), $c_\infty = 1$ mol/L, $a = 0.68$ nm and $\psi_s = 0.75$ V. Figure 4.4 demonstrates that the electric potential decreased rapidly to zero away from the electrode surface. Note that the nearly identical contours were observed periodically along the x-axis for $-5d < x < 0$ (Figure 4.1a).

Figure 4.5 shows the computed diffuse layer specific area capacitance C_s^D for sphere diameter ranging from 5 to 100 nm obtained assuming constant permittivity ($\epsilon_r = 64.4$), $c_\infty = 1$ mol/L, and $a = 0.68$ nm for SC, BCC, and FCC packings. It is evident that C_s^D increased with particle diameter for all three morphologies simulated and rapidly reached a plateau. This can be attributed to the fact that (i) the electric potential ψ in the electrolyte solution was maximum at the electrode surface and decreased rapidly away from it, (ii) the electric double layer of

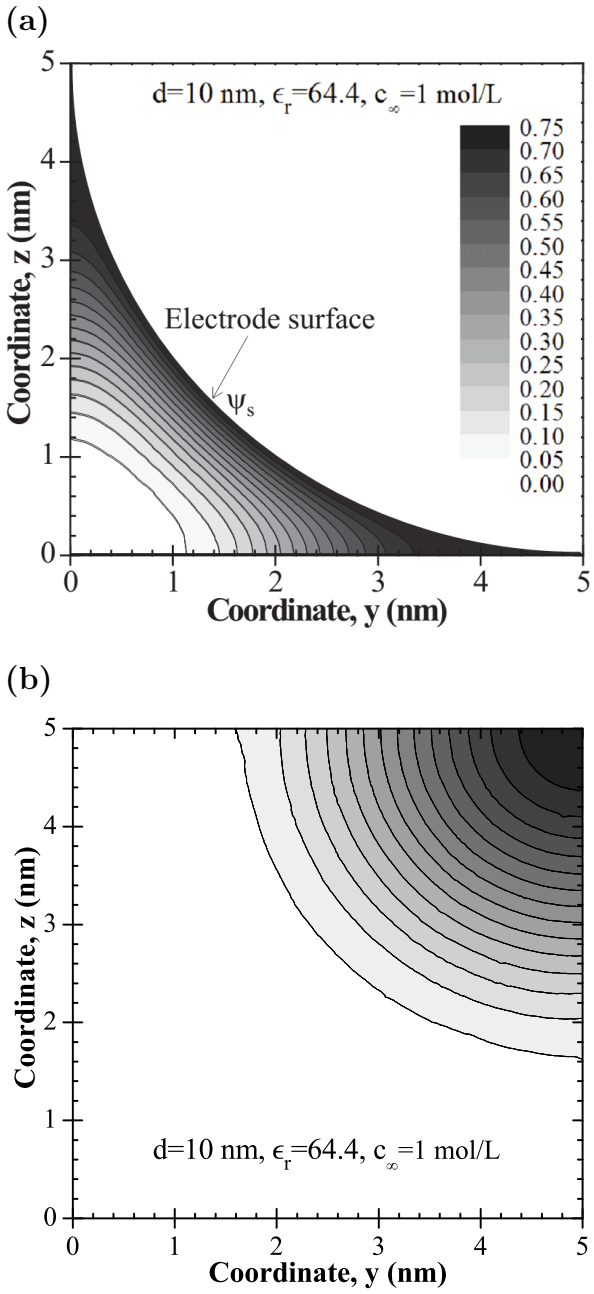

Figure 4.4: Numerically predicted electric potential contours at two representative cross-sections perpendicular to the x-axis for the SC packing with five spheres with diameter of $d = 10$ nm. Their x-coordinates were (a) $x = -d/2$, and (b) $x = -d$. Electrolyte concentration was set as $c_\infty = 1.0$ mol/L, electrolyte permittivity was assumed to be constant ($\epsilon_r = 64.4$), $a = 0.68$ nm and $\psi_s = 0.75$ V.

adjacent spheres started overlapping as the particles got closer to one another, and (iii) the distance between surfaces of adjacent electrode particles increased with particle diameter. Overall, larger electrode particle diameter resulted in larger electric field ($\mathbf{E} = -\nabla\psi$) at the electrode surface and thus larger C_s^D, according to Equation (4.5). The asymptotic value of C_s^D, represented by the solid line in Figure 4.5, corresponds to that of planar electrodes assuming constant electrolyte permittivity and given by [4, 95, 102],

$$C_s^D = \frac{2zeN_Ac_\infty\lambda_D}{\psi_s}\sqrt{\frac{2}{\nu_p}\log\left[1+2\nu_p\sinh^2\left(\frac{ze\psi_s}{2k_BT}\right)\right]} \tag{4.9}$$

where λ_D is the Debye length for symmetric electrolyte defined as $\lambda_D = (\epsilon_0\epsilon_r k_BT/2e^2z^2N_Ac_\infty)^{1/2}$ [4, 35, 95]. For the cases considered in Figure 4.5, Equation (4.9) predicts $C_s^D = 85.4\ \mu\text{F/cm}^2$. In addition, the specific area A_s of the mesoporous electrode is defined as the total surface area A_a divided by the mass of the electrode and is expressed in m^2/g. It decreases with increasing particle diameter. Therefore, the numerical predictions in Figure 4.5 were consistent with the experimental results reported in Ref. [205] showing that the total specific area capacitance C_s decreased with increasing specific area.

Moreover, for a given particle diameter, SC packing featured the largest diffuse layer specific area capacitance C_s^D and FCC packing the lowest (Figure 4.5). Indeed, SC packing has the largest electrolyte volume fraction, thus it provides the largest inter-particle distance through which the electric potential decreases. This results in larger electric field and surface charge density at the electrode/electrolyte interfaces and consequently, larger diffuse layer specific area capacitance C_s^D compared with other packings. On the contrary, FCC packing has the lowest electrolyte volume fraction. Thus, it features the lowest electric field, surface charge density and diffuse layer specific area capacitance. To confirm this physical interpretation, Figures 4.6a and 4.6b respectively show the numerical predictions of the local electric potential and the norm of electric field vector along a straight

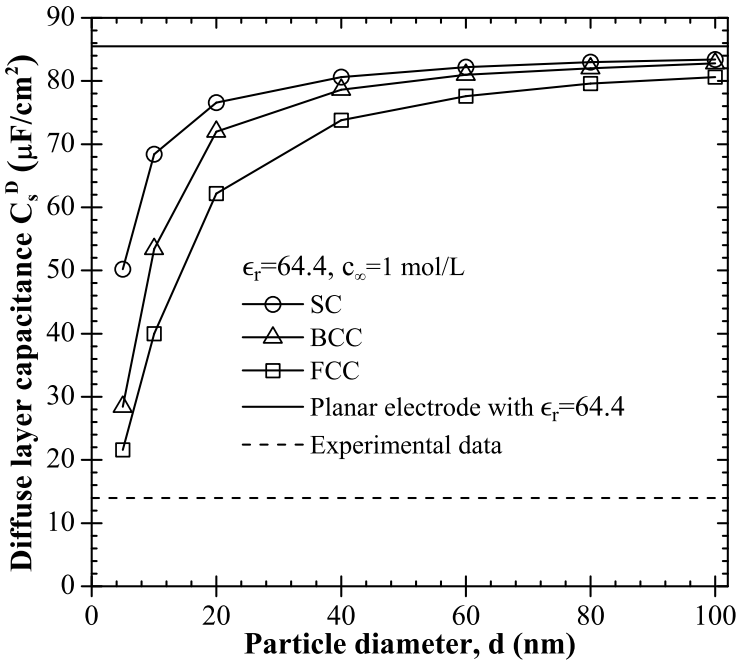

Figure 4.5: Numerically predicted diffuse layer specific area capacitance C_s^D for SC, BCC, and FCC packings. Electrolyte concentration was set as $c_\infty = 1.0$ mol/L, electrolyte permittivity was assumed to be constant ($\epsilon_r = 64.4$) and $a = 0.68$ nm. Solid line represents the theoretical value of C_s^D for planar electrodes given by Equation (4.9) [4]. Dashed line shows experimental data reported for identical electrolyte and mesoporous carbon spheres with 250 nm in diameter in a FCC packing [5].

line passing through SC, BCC, and FCC packings with five unit cells for sphere diameter $d = 5$ nm. For each packing morphology, the straight line was chosen such that it was parallel to the x-axis and touched the surface of the spheres. More specifically, the (y, z) coordinates of each plotting line were given by (i) $[(d/2)\cos 45°, (d/2)\sin 45°]$ for SC packing, (ii) $[d/2, 0]$ for BCC packing, and (iii) $[(d/2)\cos 45°, (d/2)\sin 45°]$ for FCC packing. The maximum value of the electric potential shown in Figure 4.6a was 0.75 V corresponding to ψ_s at the surface of the electrode particles. Figure 4.6a establishes that the electric potential varied significantly from 0.18 to 0.75 V between electrode spheres for SC packing while

it oscillated only between 0.67 and 0.75 V for FCC packing. Consequently, the electric field was the largest between spheres with SC packing and the smallest between those with FCC packing as shown in Figure 4.6b. Note also that the electric potential and electric field in the electrolyte decreased rapidly to zero away from the boundary of mesoporous electrodes located in the plane $x = 0$. Further increasing the separator thickness did not affect the electric potential profile at the electrode surface. Thus the predicted specific area capacitance C_s^D was independent of the separator thickness.

Furthermore, Figure 4.5 demonstrates that the difference in diffuse layer specific area capacitance C_s^D among the three morphologies decreased with increasing particle diameter. In fact, C_s^D reached nearly the same value for all morphologies for particle diameter larger than 100 nm. This establishes that the packing of the electrode spheres has no significant effect on diffuse layer specific area capacitance for the electrode particle diameter larger than 100 nm when assuming constant electrolyte permittivity. However, note that the diffuse layer gravimetric capacitance C_g^D $(= C_s^D A_s)$ decreased with increasing particle diameter for all packing morphologies (not shown) due to the decrease in specific area. This is also consistent with experimental data for the total gravimetric capacitance reported in the literature [32, 33, 203, 205–207, 211].

4.3.3 Effect of Electric Field On Dielectric Permittivity

Figures 4.6c and 4.6d respectively show the electric potential and the norm of the electric field along the same lines as those previously discussed for SC, BCC, FCC structures. Here, the results were obtained using field-dependent dielectric permittivity given by Equation (4.3) while all other parameters including $a = 0.68$ nm were identical to those used for results shown in Figures 4.6a and 4.6b. The local electric potential and the norm of the electric field followed the same trend as that shown in Figures 4.6a and 4.6b. However, the norm of electric field

plotted in Figure 4.6d was almost one order of magnitude larger than that obtained assuming constant electrolyte permittivity (Figure 4.6b). This can be explained by examining Equation (4.1). The term on the right-hand side was constant at the electrode/electrolyte interfaces where $\psi = \psi_s$. Therefore, the electric field ($\mathbf{E} = -\nabla\psi$) at the electrode/electrolyte interfaces, appearing on the left-hand side must increase to compensate for the decrease in dielectric permittivity ϵ_r at large electric field (Figure 4.3).

Figure 4.7 shows the computed diffuse layer specific area capacitance C_s^D obtained as a function of electrode particle diameter using field-dependent permittivity [Equation (4.3)] as well as $c_\infty = 1$ mol/L and $a = 0.68$ nm for SC, BCC and FCC packings. The computed capacitance C_s^D followed the same trend as the results predicted assuming constant permittivity (Figure 4.5) for all morphologies and particle diameters. However, it was significantly smaller when using field-dependent permittivity. In addition, C_s^D reached a plateau for smaller particle diameter around 40 nm instead of 100 nm when assuming constant permittivity. The asymptotic value of C_s^D, represented by the solid line in Figure 4.7, corresponds to the diffuse layer specific area capacitance of a planar electrode. It was found to be 30.8 μF/cm^2 by using Equation (4.5) after solving Equation (4.1) combined with field-dependent permittivity [Equation (4.3)]. For $d = 40$ nm, the maximum relative difference in C_s^D for the three morphologies was less than 6%. Here also, the effect of electrode packing morphology on the diffuse layer specific capacitance can be neglected as the electrode particle diameter increases. Moreover, the value of C_s^D predicted for FCC packing of carbon spheres larger than 40 nm was found to be 27.6 μF/cm^2.

Figure 4.8 shows the computed diffuse layer specific area capacitance C_s^D of a mesopore with hexagonal or circular cross-section as a function of pore length obtained using constant and field-dependent electrolyte permittivity. It indicates that C_s^D slightly increased with pore length. Changing the pore cross-section from

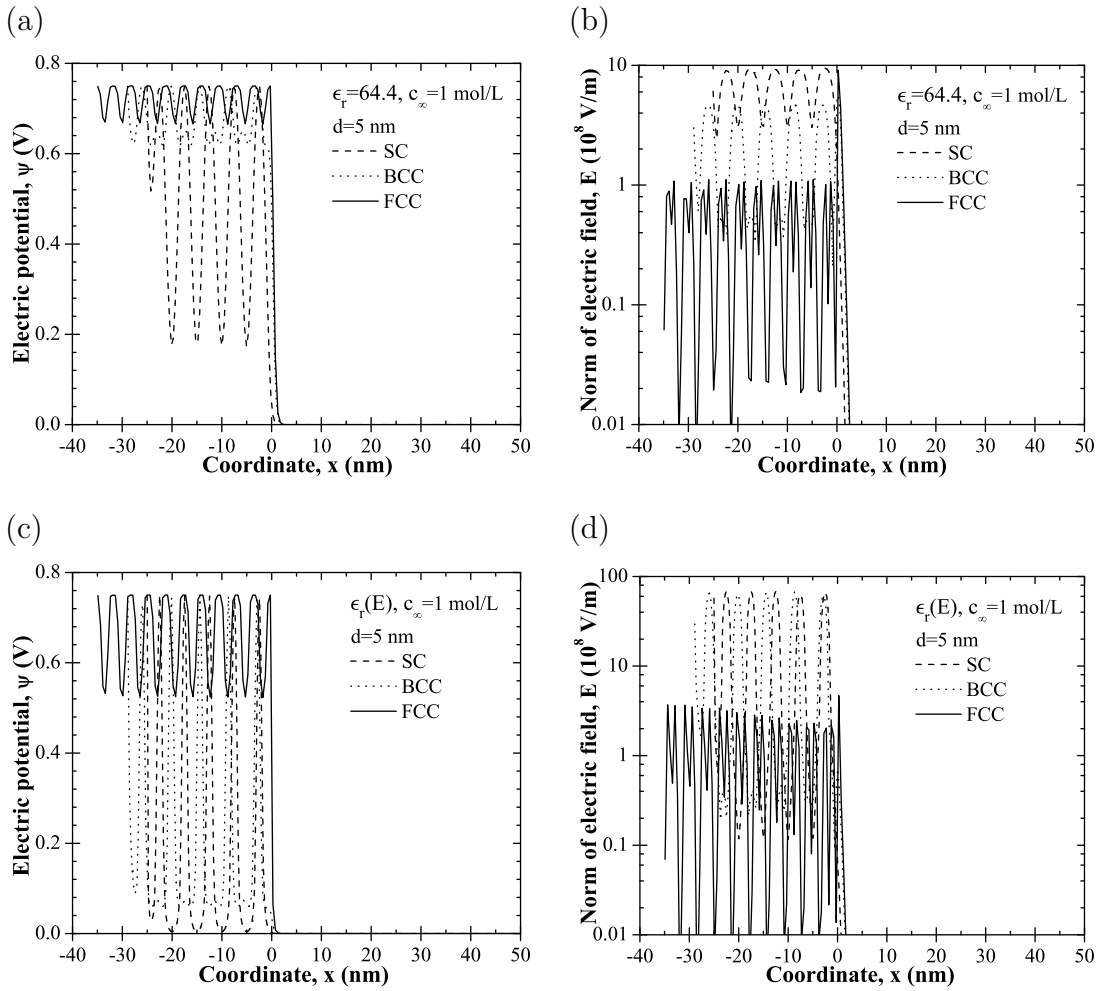

Figure 4.6: Numerically predicted electric potential ψ and norm of electric field ($E = |-\nabla\psi|$) as a function of x along a straight line for SC, BCC, and FCC packings with five unit cells and spheres of 5 nm in diameter. Results were obtained using (a, b) constant permittivity ($\epsilon_r = 64.4$), and (c, d) field-dependent permittivity given by Equation (4.3) with electrolyte concentration $c_\infty = 1.0$ mol/L, and $a = 0.68$ nm.

hexagonal to circular resulted in minor differences in C_s^D. This difference decreased with increasing pore length and was insignificant for pore longer than 100 nm. The diffuse layer capacitance of hexagonal and circular pores predicted using field-dependent permittivity ranged from 26.0 to 29.8 μF/cm^2. This was consistent

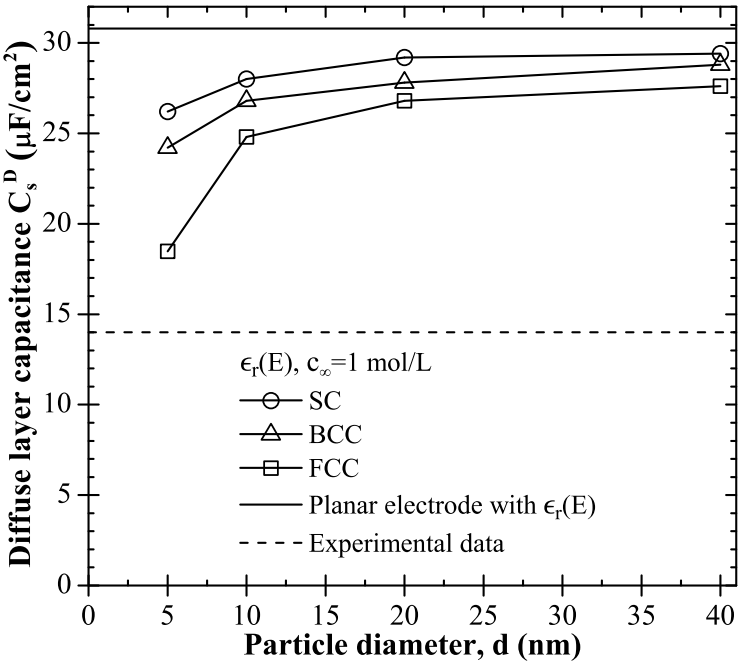

Figure 4.7: Numerically predicted diffuse layer specific area capacitance C_s^D for SC, BCC, and FCC packings. Electrolyte concentration was set as $c_\infty = 1.0$ mol/L, electrolyte permittivity was given by Equation (4.3) and $a = 0.68$ nm. Dashed line shows experimental data (14.0 μF/cm^2) reported for identical electrolyte and mesoporous carbon spheres with 250 nm in diameter in a FCC packing [5].

with the diffuse layer specific area capacitance of 27.6 μF/cm^2 predicted for carbon spheres arrays without mesopores arranged in FCC packing (Figure 4.7). Here again, the numerical predictions assuming constant permittivity were significantly larger than the predictions using field-dependent permittivity. The solid line in Figure 4.8 is the same asymptotic value of $C_s^D = 30.8$ μF/cm^2 for planar electrodes shown in Figure 4.7. This demonstrates that the closely-packed dense spheres and the mesopores feature the same diffuse layer specific area capacitance when the diameters of the electrode particles and of the mesopores are large enough regardless of the morphology and porosity.

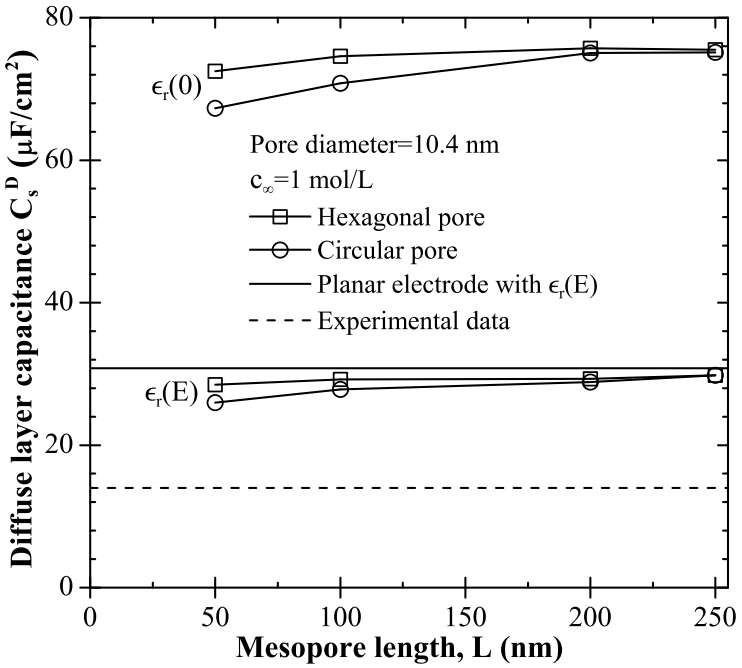

Figure 4.8: Numerically predicted diffuse layer specific area capacitance C_s^D for one mesopore as a function of mesopore length assuming hexagonal and circular cross-section with diameter 10.4 nm. Electrolyte concentration was set as $c_\infty = 1.0$ mol/L, and $a = 0.68$ nm. Dashed line shows experimental data (14.0 μF/cm^2) reported for identical electrolyte and mesoporous carbon spheres with 250 nm in diameter in a FCC packing [5].

4.3.4 Comparison With Experimental Data

The capacitance measured from cyclic voltammetry at small scan rate (e.g. < 10 mV/s) is analogous to the equilibrium capacitance [5,214]. Therefore, the equilibrium capacitance computed using Equation (4.6) can be directly compared with experimental results reported in Ref. [5] for the scan rate of 1 mV/s. In addition, previous discussion (Section 4.3.1) established that predicted total specific area capacitance of mesoporous electrodes with more than two unit cells can be compared with actual experimental data where electrodes were thick (> 20 μm [39,207,208]) and typically consisted of a large number of unit cells [5].

For FCC packing of dense spheres with diameter of 40 nm, Equation (4.8) yields $\bar{\epsilon}_r = 7.8$. Using $H = a/2 = 0.34$ nm as the Stern layer thickness, Equation (4.7) predicted $C_s^{St} = 20.3\ \mu\text{F/cm}^2$ while $C_s^D = 27.6\ \mu\text{F/cm}^2$. Thus, the total specific area capacitance was $C_s = 11.8\ \mu\text{F/cm}^2$. This value is similar to experimental measurements reporting $C_s = 14.0\ \mu\text{F/cm}^2$ for mesoporous carbon spheres [5]. This demonstrates that the Stern layer capacitance needs to be accounted for in predicting the capacitance of EDLCs with large electrolyte concentrations and electric potentials such that $c_\infty \geq 1$ mol/L and $\psi_s \geq 0.5$ V.

Finally, one should be careful in extending the conclusions drawn from the present simulations to micropores with diameter less than 2 nm for the following two reasons: (i) the diffuse layer may not exist in such small pores and (ii) the continuum theory and the Bikerman model [Equation (4.1)] may not be valid. In fact, Chmiola *et al.* [37] observed an anomalous increase in capacitance for the pore diameter less than 1 nm. This phenomenon was explained by the adsorption of desolvated ions in micropores [37,39]. In these conditions, atomistic simulations may be more appropriate such as that performed in Ref. [213].

4.4 Conclusion

This chapter presented numerical simulations of EDLCs with electrodes made of closely-packed monodispersed mesoporous spheres. For the first time, 3D heterogeneous mesostructures were modeled based on continuum theory to investigate the capacitance of EDLCs while accounting for the accurate electrode morphology and the effect of electric field on electrolyte permittivity. To simplify the problem, both dense carbon spheres in SC, BCC, and FCC packings and a single mesopore with hexagonal and circular cross-sections in a carbon sphere were simulated. The following conclusions can be drawn:

1. The field-dependent permittivity $\epsilon_r(E)$ significantly affects the predicted

diffuse and Stern layer capacitances of EDLCs.

2. The Stern layer capacitance needs to be accounted for in order to find good agreement between the predicted and experimental specific area capacitance [5] for high electrolyte concentrations and electric potentials typically encountered in EDLCs.

3. For a given sphere packing, the diffuse layer specific area capacitance increased with increasing diameter. Larger spheres provided more space for the electric potential to decrease resulting in larger electric field at the electrode surface, and therefore larger diffuse layer specific area capacitance.

4. The electrode morphology (SC, BCC, FCC) was found to have no significant effect on the diffuse layer specific area capacitance for sphere diameter larger than 40 nm.

5. SC packing featured the largest diffuse layer specific area capacitance compared with BCC and FCC packings due to larger electric field at the electrode surface for sphere diameter smaller than 40 nm.

6. The diffuse layer specific area capacitance of closely-packed dense spheres and mesopores reached the same asymptotic value corresponding to that of planar electrodes when sphere and pore diameter was larger than 40 and 10 nm, respectively.

CHAPTER 5

Equilibrium Modeling of EDLCs With 3D Ordered Mesoporous Structures

The previous chapter presented the first simulation of EDLCs with three-dimensional electrode morphology. However, the simulation of carbon spheres and cylindrical mesopores as well as the computation of Stern and diffuse layer capacitances were separated due to the complex electrode structures. This chapter presents a generalized approach to simulate EDLCs with three-dimensional ordered structures while rigorously and simultaneously accounting for the Stern and diffuse layers as well as the field-dependent electrolyte permittivity.

5.1 Introduction

Electrodes in actual EDLCs are typically made of mesoporous materials offering large surface area. Research efforts have focused on increasing the energy and power densities of supercapacitors by increasing the surface area of porous electrodes and tailoring their morphology or pore size distribution [27, 31–34]. In particular, electrodes with three-dimensional ordered structures [5, 6, 42, 204, 229–242] have attracted significant attentions due to [176, 204, 239–243] (1) their small ion transport resistance, (2) their uniform pore connection leading to short ion diffusion length, and (3) their continuous electron transport framework. For example, Woo *et al.* [6] synthesized highly-ordered mesoporous carbon films as electrodes for EDLCs. These carbon films had ordered "bimodal" structure featuring both interconnected macropores and mesopores. In particular, their "CP204-S15" car-

bon film had specific surface area of $S_{BET} = 1003$ m^2 g^{-1} [6]. The radius of the macropores and mesopores was reported to be 95 nm and 7 nm [6], respectively. The surface area due to micropores with diameter around or less than 2 nm was less than 6% [6]. From the FE-SEM image (Figure 3a in Ref. [6]), the radius of the channels between macropores in "CP204-S15" carbon film was estimated to be 20 nm while the carbon wall thickness was about 2 nm. The electrolyte was 1 mol L^{-1} $(C_2H_5)_4NBF_4$ (or $TEABF_4$) in propylene carbonate while the potential window was 2 V. The capacitances were measured using galvanostatic charge/discharge at low current density 40 mA g^{-1} using the three-electrode method [6]. Finally, the areal and gravimetric capacitances for the "CP204-S15" carbon film were reported to be $C_s = 9.4$ μF cm^{-2} and $C_g = 95$ F g^{-1}, respectively [6].

Numerous experimental studies have been devoted to characterizing the performances of EDLCs and assessing the effects of electrode morphology as well as of the physical or electrochemical properties of electrodes and electrolytes [5, 6, 27, 31–34, 42, 204, 229–242]. Experimental approaches are typically time consuming and costly. They also rely on trial and errors in order to optimize EDLCs. On the contrary, accurate and reliable numerical tools can facilitate the design and optimization of the electrode morphology in a more systematic and efficient way. Moreover, they can be used to understand the electrochemical and transport processes involved in EDLCs [148, 149]. For example, they can predict the local electric potential and ion concentrations throughout the mesoporous electrodes [199, 228, 244] which cannot be measured experimentally. However, such numerical simulations are complicated by the multi-scales (from subnanometer to micron) and multi-physics nature of the problem. They should also be validated against experimental data.

The present chapter aims to develop a three-dimensional (3D) model based on continuum theory for simulating EDLCs with ordered mesoporous electrode structures. For the first time, the model simultaneously and rigorously accounts

for (1) 3D electrode morphology, (2) finite ion size, (3) Stern and diffuse layers, and (4) the dependency of the electrolyte dielectric permittivity on the local electric field. First, a new set of boundary conditions was derived to account for the Stern layer without simulating it in the electrolyte domain. The model was then used to simulate faithfully the electrode morphology of CP204-S15 mesoporous carbon EDLC synthesized and characterized by Woo *et al.* [6].

5.2 Background

5.2.1 Traditional Modeling Approaches

The Helmholtz model [85–87] and Gouy-Chapman-Stern (GCS) model [94] are frequently used to simulate EDLCs with one- or two-dimensional electrode structure. In these models, the electrolyte dielectric permittivity is either assumed to be constant [87, 94] or treated as a fitting parameter [85–87]. However, the relative permittivity ϵ_r of polar electrolytes is known to significantly decrease as the electric field increases [189–191]. In addition, the GCS model neglects the finite size of ions and treat ions as point-charges [4, 95, 199, 228, 244]. This assumption breaks down when either the electrolyte concentration c_∞ or the electric potential is large [4, 95, 148, 149, 199, 228, 244]. Therefore, the GCS model is invalid for practical EDLCs with typical electrolyte concentration larger than 1 mol L^{-1} and potential window larger than 1 V [228].

Due to their intrinsic limitations, none of the above-mentioned models can account for the three-dimensional mesoporous electrode morphology of practical EDLCs. The first equilibrium simulations of EDLCs with three-dimensional electrode morphology were reported by Pilon and co-workers [199, 244]. These simulations also accounted for finite ion size as well as the dependency of the electrolyte dielectric permittivity on the local electric field [199, 244]. However, the computations of the Stern and diffuse layer capacitances were decoupled due to

the complex electrode structures [199, 244]. Our recent study indicated that the Stern and diffuse layer need to be simulated simultaneously in order to predict accurately the electric double layer capacitances [228]. In the previous literature, the Stern and diffuse layers have been simultaneously simulated only for one- or two-dimensional electrode structures such as planar electrodes [148, 149] and a single cylindrical or spherical electrode particle or pore [85–87, 94, 228].

Under equilibrium conditions, the local electric potential $\psi(\mathbf{r})$ at location $\mathbf{r}$ in the electrolyte can be found by solving the modified Poisson-Boltzmann (MPB) model with a Stern layer accounting for the finite ion size and expressed as [4, 7, 95, 228],

$$\nabla \cdot (\epsilon_0 \epsilon_r \nabla \psi) = \begin{cases} 0 & \text{in the Stern layer} \quad (5.1a) \\ \dfrac{2 z_0 e N_A c_\infty \sinh\left(\dfrac{z_0 e \psi}{k_B T}\right)}{1 + 2\nu_p \sinh^2\left(\dfrac{z_0 e \psi}{2 k_B T}\right)} & \text{in the diffuse layer} \quad (5.1b) \end{cases}$$

Then, the local ion concentration $c(\mathbf{r})$ is given by [4, 7, 95]

$$c(\mathbf{r}) = \frac{c_\infty \exp\left(-z_0 e \psi / k_B T\right)}{1 + 2\nu_p \sinh^2\left(\dfrac{z_0 e \psi}{2 k_B T}\right)} \tag{5.2}$$

where ϵ_0 and ϵ_r are the free space permittivity ($\epsilon_0 = 8.854 \times 10^{-12}$ F m^{-1}) and the relative permittivity of the electrolyte solution, respectively. The valency of the symmetric electrolyte is denoted by z_0, while c_∞ is the bulk molar concentration of electrolyte, T is the absolute temperature, e is the elementary charge ($e = 1.602 \times 10^{-19}$ C), N_A and k_B are the Avogadro's number ($N_A = 6.022 \times 10^{23}$ mol^{-1}) and the Boltzmann constant ($k_B = 1.381 \times 10^{-23}$ m^{2}kg K^{-1}s^{-2}), respectively. The packing parameter is defined as $\nu_p = 2a^3 N_A c_\infty$ where a is the effective ion diameter. It represents the ratio of the total bulk ion concentration to the maximum ion concentration $c_{max} = 1/N_A a^3$ assuming a simple cubic ion packing [4, 95, 130]. Therefore, ν_p should not be larger than unity for the model to be physically acceptable.

5.2.2 Conventional Boundary Conditions

Boundary conditions are required to predict the electric potential and ion concentration profile in the electrolyte. The electric potential at the electrode/electrolyte interface is typically prescribed under equilibrium conditions [8, 9, 35, 36, 95, 146, 199, 228]. For a sphere or cylinder of radius R_0, it is given by

$$\psi(r = R_0) = \psi_s, \tag{5.3a}$$

In addition, the electric potential and displacement are continuous across the Stern/diffuse layer interface located at $r = R_0 + H$ so that [8, 90, 148, 149],

$$\begin{aligned} \psi(r = R_0 + H^-) &= \psi(r = R_0 + H^+) \quad \text{and} \\ \epsilon_0\epsilon_r \frac{d\psi}{dr}(r = R_0 + H^-) &= \epsilon_0\epsilon_r \frac{d\psi}{dr}(r = R_0 + H^+) \end{aligned} \tag{5.3b}$$

Far away from the electrode surface, the electric potential and ion concentration are constant such that [128, 148, 149, 199, 228, 244],

$$\psi(r = R_0 + L) = 0 \quad \text{and} \quad c_i(r = R_0 + L) = c_\infty \tag{5.3c}$$

In fact, the presence of the very thin Stern layer near the electrode surface causes several numerical challenges. First, the Stern layer complicates the computational domain by introducing an additional length scale which is significantly smaller than that of the diffuse layer. Therefore, the computational domain becomes extremely complicated and the number of meshes prohibitively large for simulating three-dimensional electrode structures. Second, the governing equations for the electric potential and ion concentrations in the Stern and diffuse layers are numerically solved separately and coupled through the boundary conditions [Equations (5.3b)]. These equations must be solved simultaneously thus requiring excessive computational time and resources. Therefore, the MPB model with a Stern layer [Equations (5.1)] and the conventional boundary conditions [Equations (5.3)] [94, 148, 149, 228] cannot be used to simulate three-dimensional structures such as those encountered in practical EDLCs.

Alternatively, the Stern layer forming near planar electrodes can also be accounted for via a modified boundary condition without simulating it explicitly in the electrolyte domain. In one-dimensional Cartesian coordinates, the corresponding boundary condition at the Stern/diffuse layer interface located at $x = H$ has been derived as [4, 95, 128, 130, 245–252],

$$\epsilon_0 \epsilon_r \frac{d\psi}{dx}(x = H) = C_s^{St}[\psi_s - \psi(x = H)] \tag{5.4}$$

where $C_s^{St} = \epsilon_0 \epsilon_r / H$ is the Stern layer capacitance for planar electrodes [4, 95, 128, 130, 245–252]. Then, Equations (5.3c) and (5.4) form a complete set of boundary conditions for the entire electric double layer while simulating only the diffuse layer from $x = H$ to $x = L$. To the best of our knowledge, no similar approach has been proposed for simulating electric double layers near electrodes in other geometries or coordinate systems.

5.3 Analysis

5.3.1 Schematics and Assumptions

Figure 5.4.1 shows the schematic representation of the ordered bimodal mesoporous carbon simulated in this study [7]. Here, the dimensions of the simulated electrode structure were identical to those of the bimodal mesoporous carbon "CP204-S15" reported in Ref. [6] as previously discussed. Note that the capacitances predicted by the MPB model with the Stern layer [Equations (5.1)] are identical for the positive and negative electrodes in binary and symmetric electrolytes [4, 95, 199, 228] such as those considered here. Therefore, it suffices to simulate only one electrode [4, 95, 199, 228]. In addition, the present study simulated one unit cell of the 3D porous electrode structure. Further increasing the number of unit cells was found to have no effect on the predicted areal and gravimetric capacitances under equilibrium conditions [199]. By virtue of symmetry, it suffices to simulate only 1/12th of one unit cell. Figure 5.4.1 shows the schematic

of the computational domain simulated in this study. The density of carbon materials is about $\rho = 1.8$ g cm^{-3} in its amorphous phase [253]. Then, the number of mesopores existing in the walls was adjusted so that the specific area of the simulated electrode matched that of the actual bimodal electrodes ranging from 492 to 1504 m^2 g^{-1} [6]. Overall, the specific area of the simulated structure [Figure 5.4.1] was adjusted to be 960 m^2 g^{-1} which falls within 5% of its experimental value of 1003 m^2 g^{-1} [6]. The thickness of the electrolyte region at the edge of the electrode was specified to be $L = 30$ nm. Increasing this thickness to $L = 60$ nm was found to have no effect on the predicted areal and gravimetric capacitances due to the rapid decrease of the electric potential from the electrode surface caused by the thin electric double layer [199, 228, 244].

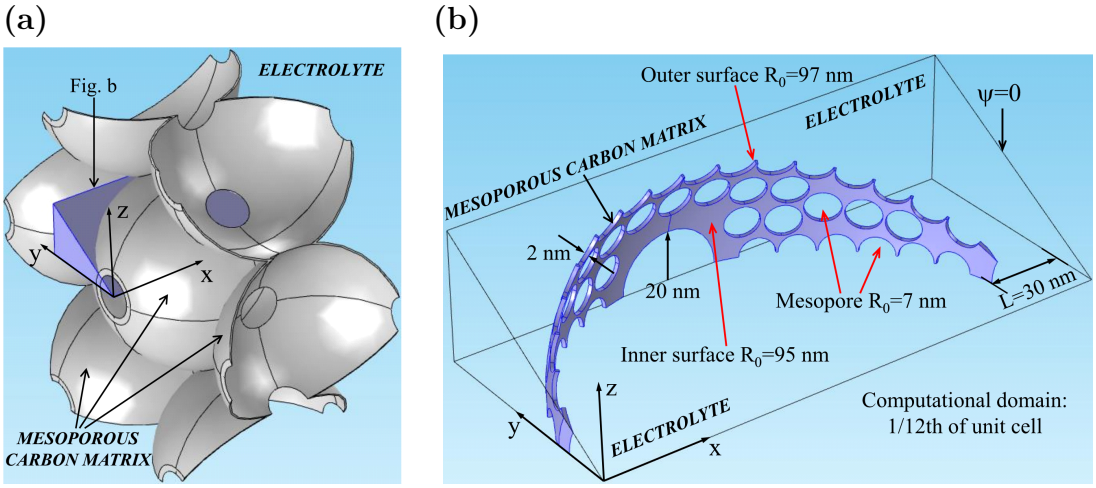

Figure 5.1: Schematic and coordinate systems of (a) ordered bimodal carbon electrodes as synthesized in Ref. [6] and (b) the computational domain along with the boundary conditions and coordinate system for the ordered bimodal carbon CP204-S15 simulated in the present study [7].

To make the problem mathematically tractable, the following assumptions were made: (1) the electric potential and ion concentrations reached their equilibrium states, (2) anions and cations had the same effective diameter assumed to be constant and independent of electrolyte concentration [4, 95, 200], (3) the

electrolyte relative permittivity was constant and uniform within the Stern layer. Note that the electrolyte relative permittivity is typically defined for media with characteristic length larger than 1 or 2 nm [254, 255], (4) isothermal conditions prevailed throughout the electrode and electrolyte, (5) advection of the electrolyte was assumed to be negligible, (6) the ions could only accumulate at the electrode surface and could not diffuse into the electrode, i.e., there was no ion insertion, and (7) the specific ion adsorption due to non-electrostatic forces were assumed to be negligible.

5.3.2 Constitutive Relations

In order to solve Equations (5.1) and (5.3), the electrolyte properties ϵ_r, z_0, c_∞, and a along with the temperature T and the surface potential ψ_s are needed. In the diffuse layer, the Booth model was used to account for the dependency of electrolyte dielectric permittivity on the local electric field [189–191, 199, 228],

$$\epsilon_r(E) = n^2 + \left(\epsilon_r(0) - n^2\right) \frac{3}{\beta E} \left[\coth(\beta E) - \frac{1}{\beta E}\right] \text{ for } E \geq 10^7 \text{ V/m} \quad (5.5a)$$

$$\epsilon_r = \epsilon_r(0) \text{ for } E < 10^7 \text{ V/m} \quad (5.5b)$$

where $E = |-\nabla\psi|$ is the norm of the local electrical field vector, $\epsilon_r(0)$ is the relative permittivity at zero electric field, and n is the index of refraction of the electrolyte at zero electric field frequency. In the Stern layer, the electrolyte dielectric permittivity was imposed as constant and uniform [assumption (3)]. Its value was evaluated using Equation (5.5) and the computed local electric field at the Stern/diffuse layer interface.

The electrolyte solution used in Ref. [6] was $TEABF_4$ in propylene carbonate solution at room temperature ($T = 298$ K) characterized by the following properties: $\epsilon_r(0) = 64.4$ [219], $n = 1.42$ [220], $\beta = 1.314 \times 10^{-8}$ m V^{-1} [199], and $z_0 = 1$. The ion diameter of non-solvated TEA^+ and BF_4^- ions are $a = 0.68$ and 0.34 nm [37], respectively. Their solvated ion diameters were reported to be $a = 1.36$

and 1.40 nm [256,257], respectively. The electrolyte concentration and the surface electric potential were chosen to be the same as those used in Ref. [6], namely, $c_\infty = 1.0$ mol L^{-1} and $\psi_s = 2$ V. In addition, the Stern layer thickness H was approximated as the radius of solvated ions, i.e., $H = a/2$ [9,35,36].

5.3.3 Derivation of Generalized Boundary Conditions

This section presents the derivation of a generalized boundary condition valid for cylindrical and spherical electrode particles or pores. Figure 5.2 shows a schematic of the electric double layer structure forming near a positively charged cylindrical/spherical electrode particle or pore.

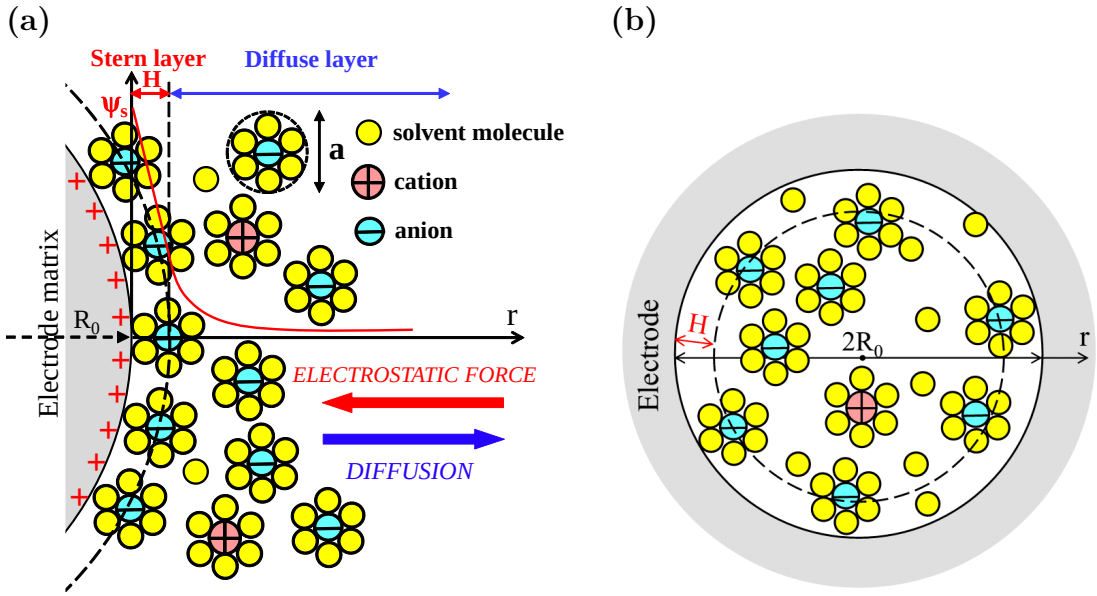

Figure 5.2: Schematic of the electric double layer structure illustrating the arrangement of solvated anions and cations as well as the Stern layer and the diffuse layer forming near (a) a cylindrical or spherical electrode particle [7–9] and (b) a cylindrical or spherical pore with radius R_0 and Stern layer thickness H [7–9].

For a cylindrical electrode of radius R_0 (Figure 5.2a), Equation (5.1a) in the

Stern layer is expressed as [94, 148, 149]

$$\frac{d}{dr}\left(\epsilon_0\epsilon_r r\frac{d\psi}{dr}\right) = 0 \quad \text{for} \quad R_0 \leq r < R_0 + H \tag{5.6}$$

where $\epsilon_r = \epsilon_r(E_H)$ is the uniform electrolyte relative permittivity within the Stern layer [assumption (3)]. Its value is evaluated at the Stern/diffuse layer interface located at $r_H = R_0 + H$ using Booth model [Equation (5.5)] based on the local electric field $E_H(r_H)$. Then, integrating Equation (5.6) twice with respect to r from $r = R_0$ to $r = R_0 + H$ using the boundary condition given by Equations (5.3a) and (5.3b) yields,

$$\psi(r) = -\left[\psi_s - \psi(r = R_0 + H)\right]\frac{\log(r/R_0)}{\log(1 + H/R_0)} + \psi_s \tag{5.7}$$

Differentiation of Equation (5.7) with respect to r yields the following boundary condition at the Stern/diffuse layer interface at $r = R_0 + H$,

$$\begin{aligned} &-\epsilon_0\epsilon_r(E_H)\frac{d\psi}{dr}(r = R_0 + H) \\ &= \frac{\epsilon_0\epsilon_r(E_H)}{R_0\log(1 + H/R_0)}\frac{R_0}{R_0 + H}\left[\psi_s - \psi(r = R_0 + H)\right] \end{aligned} \tag{5.8}$$

Equation (5.8) relates the local electric potential to its gradient at $r = R_0 + H$. It serves as a new boundary condition at the Stern/diffuse layer interface.

Similarly, for spherical electrodes, the boundary condition at the Stern/diffuse layer interface can be derived as,

$$\begin{aligned} &-\epsilon_0\epsilon_r(E_H)\frac{d\psi}{dr}(r = R_0 + H) \\ &= \frac{\epsilon_0\epsilon_r(E_H)}{H}\left(1 + \frac{H}{R_0}\right)\left(\frac{R_0}{R_0 + H}\right)^2\left[\psi_s - \psi(r = R_0 + H)\right] \end{aligned} \tag{5.9}$$

Note that Equations (5.4), (5.8), and (5.9) can be rewritten in a generalized form for planar, cylindrical, and spherical electrodes as,

$$-\epsilon_0\epsilon_r(E_H)\nabla\psi\cdot\left(\frac{\mathbf{r}_H}{r_H}\right) = C_s^H\left(\frac{R_0}{R_0 + H}\right)^p\left[\psi_s - \psi(\mathbf{r}_H)\right] \tag{5.10}$$

where $\mathbf{r}_H$ is the local position vector at the Stern/diffuse layer interface located at $r_H = R_0 + H$ for cylindrical and spherical electrodes. Note that $\mathbf{r}_H/r_H$ represents

the local outward normal unit vector at the Stern/diffuse layer interface. Here, C_s^H is the Stern layer capacitance predicted by the Helmholtz model assuming constant ϵ_r within the Stern layer and given by [84, 228],

$$C_s^H = \begin{cases} \dfrac{\epsilon_0 \epsilon_r(E_H)}{H} & \text{for planar electrode} \quad (5.11a) \\ \dfrac{\epsilon_0 \epsilon_r(E_H)}{R_0 \log(1 + H/R_0)} & \text{for cylindrical electrode of radius } R_0 \quad (5.11b) \\ \dfrac{\epsilon_0 \epsilon_r(E_H)}{H}\left(1 + \dfrac{H}{R_0}\right) & \text{for spherical electrode of radius } R_0 \quad (5.11c) \end{cases}$$

The value of p in Equation (5.10) is given by,

$$p = \begin{cases} 0 & \text{for planar electrodes} \quad (5.12a) \\ 1 & \text{for cylindrical electrodes} \quad (5.12b) \\ 2 & \text{for spherical electrodes} \quad (5.12c) \end{cases}$$

Moreover, for cylindrical and spherical pores of radius R_0 illustrated in Figure 5.2b, the new boundary condition at the Stern/diffuse layer interface located at $r_H = R_0 - H$ can be similarly derived as,

$$-\epsilon_0 \epsilon_r(E_H) \nabla\psi \cdot \left(\frac{\mathbf{r}_H}{r_H}\right) = C_s^H \left(\frac{R_0}{R_0 - H}\right)^p [\psi_s - \psi(\mathbf{r}_H)] \quad (5.13)$$

where $p = 1$ or 2 for cylindrical or spherical pores, respectively. Here also, the Stern layer capacitance C_s^H for cylindrical or spherical pores is given by the Helmholtz model assuming constant ϵ_r within the Stern layer and expressed as [84],

$$C_s^H = \begin{cases} \dfrac{\epsilon_0 \epsilon_r(E_H)}{R_0 \log\left(\dfrac{R_0}{R_0 - H}\right)} & \text{for cylindrical pores of radius } R_0 \quad (5.14a) \\ \dfrac{\epsilon_0 \epsilon_r(E_H)}{H}\left(\dfrac{R_0 - H}{R_0}\right) & \text{for spherical pores of radius } R_0 \quad (5.14b) \end{cases}$$

5.3.4 Method of Solution and Data Processing

Equation (5.1b) was solved using the commercial finite element solver COMSOL 4.2, along with the boundary conditions given by Equations (5.3c) and (5.10)

or (5.13) and field-dependent permittivity $\epsilon_r(E)$ given by Equation (5.5). The simulations were run on a Dell workstation Precision 690 with two 2.66 GHz Quad-Core Intel Xeon CPUs and 64 GB of RAMs.

Due to charge conservation [Equation (5.1a)], the total amount of charges Q stored near the electrode surfaces A_s is equal to that present at the Stern/diffuse layer interface denoted by A_d. Then, it can be computed by integrating the surface charge density ($\epsilon_0\epsilon_r\mathbf{E}\cdot\mathbf{n}$) along A_s or A_d and expressed as [35, 201],

$$Q = \int_{A_s} \epsilon_0\epsilon_r(E)\mathbf{E}\cdot\mathbf{n}\; dA = \int_{A_d} \epsilon_0\epsilon_r(E)\mathbf{E}\cdot\mathbf{n}\; dA \tag{5.15}$$

where $\mathbf{E} = -\nabla\psi$ is the local electric field vector, $\mathbf{n}$ is the local outward normal unit vector at the electrode surface A_s or at the electrode/electrolyte interface A_d. Then, the overall gravimetric capacitance was estimated as [244],

$$C_g = \frac{Q}{\rho V \psi_s} \tag{5.16}$$

where ρ and V are the density and volume of the amorphous carbon electrode, respectively. The diffuse layer areal capacitance C_s^D and the total areal capacitance C_s were respectively estimated as [199, 244],

$$C_s^D = \frac{Q}{\psi_d A_d} = \frac{1}{\psi_d A_d}\int_{A_d} \epsilon_0\epsilon_r(E)\mathbf{E}\cdot\mathbf{n}\; dA \quad \text{and} \quad C_s = \frac{Q}{\psi_s A_s} \tag{5.17}$$

Note that the total areal capacitance C_s can be also equivalently calculated using the one-dimensional series formula $1/C_s = 1/C_s^{St} + 1/C_s^D$ when the Stern layer thickness is much smaller than the electrode or pore diameter as considered here. In addition, the Stern layer areal capacitance C_s^{St} was given by the Helmholtz model [Equations (5.11) or (5.14)].

The numerical convergence criterion was defined such that the maximum relative differences in the predicted capacitances C_s^{St}, C_s^D, C_s, and C_g was less than 1.5% when decreasing the mesh size by a factor two. The mesh size was the smallest at the Stern/diffuse layer interface due to the large electric potential gradient

and then gradually increased. The maximum mesh size was specified to be about 0.1 nm at all Stern/diffuse layer interfaces and remained less than 2.5 nm anywhere else in the computational domain. The total number of finite elements was on the order of 10^7 for the simulations of bimodal ordered carbon CP204-S15 with 1/12th of one unit cell shown in Figure 5.4.1.

Finally, the numerical tool was validated based on two equilibrium cases reported in the literature. First, the equilibrium electric potential profile in the diffuse layer predicted by solving the MPB model was validated against the exact solution for planar electrodes [8, 35, 90] with $\epsilon_r = 78.5$, $c_\infty = 0.01$ and 0.001 mol L^{-1}, $\nu_p = 0$, and $\psi_D = 0.1$ V. Second, the computed capacitances for the Stern and diffuse layers obtained from the MPB model were validated against their theoretical formula assuming constant electrolyte permittivity [4, 95, 228] for $\psi_s = 2$ V, $c_\infty = 1$ mol L^{-1}, and $a = 0.68$ or 1.40 nm. Good agreement was obtained between our results and reported electric potential profiles [8, 35, 90] or capacitances [4, 95, 228] for all cases considered.

5.4 Results and Discussions

5.4.1 Validity of the New Boundary Conditions

The new boundary conditions [Equations (5.10) and (5.13)] were used to compute the capacitances for a single cylindrical electrode particle and a cylindrical pore by solving Equations (5.1b), (5.3c), and (5.10) or (5.13), respectively. The parameters were chosen such that $a = 0.68$ nm, $c_\infty = 1.0$ mol L^{-1}, and $\psi_s = 2$ V with field-dependent electrolyte permittivity $\epsilon_r(E)$ given by Equation (5.5). The results were compared with those obtained by simulating both the Stern and diffuse layers in the electrolyte domain using the conventional boundary conditions given by Equations (5.3). Figure 5.3 shows the Stern layer, diffuse layer, and total areal capacitances predicted using these two approaches as a function of particle or

pore radius R_0 ranging from 2.5 to 60 nm. The relative difference in the values of C_s^{St}, C_s^D, and C_s predicted using these two approaches was less than 0.2% for all cases considered here. In addition, it is evident that the predicted C_s^{St} was much smaller than C_s^D for all cases considered. Therefore, the double layer capacitance C_s was dominated by C_s^{St} which is consistent with the conclusion drawn in our previous study [228] when accounting for field-dependent electrolyte permittivity. Note that for particle or pore radius larger than 40 nm, the predicted capacitance reached a plateau of $C_s = 10.2$ μF cm^{-2} corresponding to that of planar electrodes as discussed in Refs. [86, 87, 199, 228, 244].

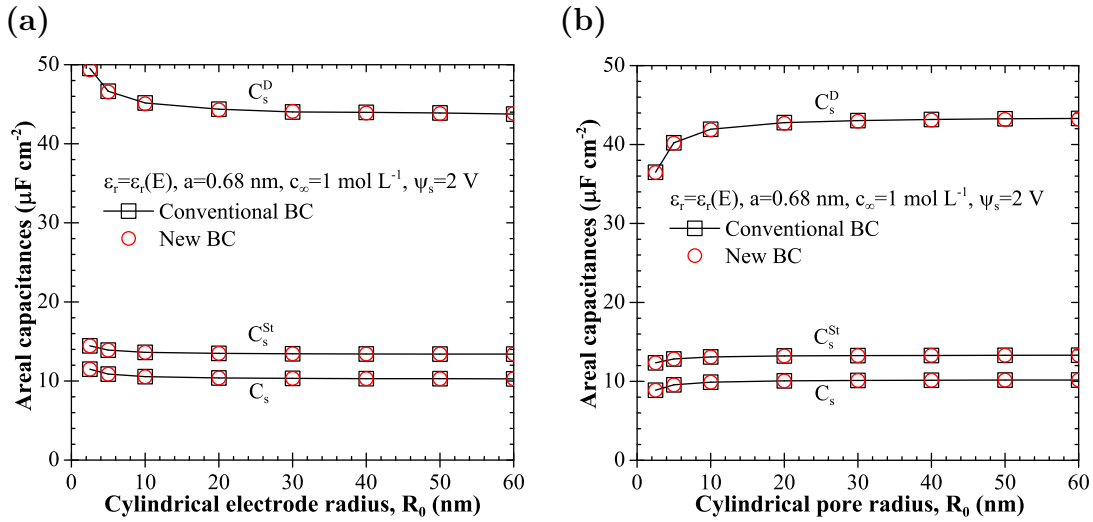

Figure 5.3: Predicted Stern layer C_s^{St}, diffuse layer C_s^D, and total C_s areal capacitances [7] for (a) a cylindrical electrode particle and (b) a cylindrical pore as a function of radius R_0 ranging from 2.5 to 60 nm. Results were obtained using conventional and our new boundary conditions (BC) with $a = 0.68$ nm, $c_\infty = 1$ mol L^{-1}, $\psi_s = 2$ V, and electrolyte permittivity given by Equation (5.5).

Similarly, the predicted capacitances C_s^{St}, C_s^D, and C_s using these two approaches were compared for a spherical electrode and a spherical pore with various radii ranging from 2.5 to 60 nm. Excellent agreement was observed in all cases. Overall, these results demonstrate that the Stern layer can be accurately

accounted for by using the new boundary conditions given by Equations (5.10) or (5.13) for cylindrical and spherical electrodes or pores without explicitly simulating the Stern layer in the electrolyte domain. Note that the total number of finite elements decreased by about 30% to 60% when using the new boundary conditions for simulating a single cylindrical and spherical electrode or pore with radius ranging from 2.5 to 60 nm. The corresponding computational time was reduced by about $10\% - 30\%$. This reduction in finite elements and computational time became more significant with increasing radius and geometric complexity. This clearly demonstrates the advantage of the new boundary conditions.

5.4.2 Capacitances of Ordered Bimodal Carbons

The double layer capacitances C_s^{St}, C_s^D, and C_s of the ordered bimodal carbon shown in Figure 5.4.1 were predicted by solving Equation (5.1b) in the diffuse layer along with the new boundary conditions given by Equations (5.3c) and (5.10) or (5.13). The electrode surface was divided in three sections (i) the inner surface of the pores of radius 95 nm, (ii) the outer surface of radius 97 nm, and (iii) the mesopore with 7 nm in radius located in the walls separating the macropores. The boundary condition given by Equation (5.10) was imposed at the outer surfaces while Equation (5.13) was imposed at the mesopore and inner pore surfaces, respectively. Note that without these new boundary conditions, it was impossible to solve the coupled governing equations for such a complex domain due to (i) the difficulty in creating the geometry and (ii) an excessively large number of finite elements.

Table 5.1 summarizes the predicted Stern layer, diffuse layer, and total areal capacitances as well as the gravimetric capacitance at the inner, outer, and mesopore surfaces of the ordered bimodal carbon. Results were obtained based on the non-solvated effective ion diameter $a = 0.68$ nm [37] with field-dependent electrolyte permittivity $\epsilon_r(E)$ given by Equation (5.5). The areal capacitances

predicted for planar electrodes for the same parameters were also reported in Table 5.1 for comparison purposes.

Table 5.1: Predicted Stern layer, diffuse layer, and total areal capacitances as well as gravimetric capacitance C_g for the ordered bimodal carbon (Figure 5.1b) computed at the inner, outer, and mesopore surfaces. Results were obtained by solving Equations (5.1b), (5.3c), and (5.10) or (5.13) using non-solvated or solvated ion diameter $a = 0.68$ or $a = 1.40$ nm, respectively along with $c_\infty = 1$ mol L^{-1}, $\psi_s = 2$ V, and electrolyte permittivity given by Equation (5.5). Predictions for planar electrodes are also reported for comparison.

Ion diameter	**Capacitance**	**Planar electrode**	**Inner surface**	**Outer surface**	**Mesopores**
$a = 0.68$ nm	C_s^{St} (μ**F cm**$^{-2}$)	13.4	13.3	13.4	12.8
	C_s^{D} (μ**F cm**$^{-2}$)	43.2	44.6	43.8	47.3
	C_s (μ**F cm**$^{-2}$)	10.2	10.2	10.2	10.1
	C_g (**F g**$^{-1}$)	–	39.0	35.0	23.0
$a = 1.40$ nm	C_s^{St} (μ**F cm**$^{-2}$)	13.0	11.8	11.9	10.0
	C_s^{D} (μ**F cm**$^{-2}$)	17.7	21.4	20.7	28.5
	C_s (μ**F cm**$^{-2}$)	7.5	7.5	7.5	7.4
	C_g (**F g**$^{-1}$)	–	29.2	25.1	17.8

It is evident that the Stern layer areal capacitance C_s^{St} was about one-third smaller than the diffuse layer areal capacitance C_s^D at all surfaces. Thus, the total areal capacitance C_s was controlled by the Stern layer. In addition, the total areal capacitances C_s at the inner and outer surfaces were 10.2 μF cm^{-2} which was identical to that for planar electrodes. Indeed, electrodes with radius of curvature larger than 40 nm behave like planar electrodes as established in Refs. [199, 228] and also shown in Figure 5.3. Similarly, the areal capacitance C_s at mesopore surfaces was 10.1 μF cm^{-2} which fell within 1% of that of planar electrodes. In fact, it was found that the areal capacitance C_s of mesopores decreased with

increasing pore depth (or carbon wall thickness) (not shown). This was due to the confinement of the electric field in small pores leading to reduced surface charge density and capacitance as previously discussed [199, 244]. However, this effect appeared to be negligible for small pore depth (i.e., carbon wall thickness) of 2 nm such as those considered here. In addition, the mesopores contributed about 30% less to the gravimetric capacitance C_g than the inner and outer pore surfaces. This was due to the small carbon wall thickness and thus the relatively small mesopore surface area compared with those of inner and outer pore surfaces.

Table 5.1 also summarizes the predicted capacitances for the electrode structure shown in Figure 5.4.1 but using solvated ion diameter $a = 1.40$ nm [257]. It demonstrates that, for larger effective ion diameter, the Stern layer areal capacitance C_s^{St} had the same order of magnitude as the diffuse layer areal capacitance C_s^D at all surfaces. Consequently, the capacitances C_s^{St} and C_s^D contributed nearly equally to the total areal capacitance C_s. Here also, the inner and outer pore surfaces contributed slightly more to the gravimetric capacitance than mesopores. However, both the local areal and gravimetric capacitances decreased by about 30% when using the solvated ion diameter $a = 1.40$ nm instead of $a = 0.68$ nm. This was due to the associated reduction in the maximum ion concentration $c_{max} = 1/N_A a^3$ at the electrode surface as ion diameter a increases.

5.4.3 Comparison With Experimental Data

Table 5.2 shows the predicted overall areal and gravimetric capacitances C_s and C_g defined by Equations (5.16) and (5.17) and accounting for the contribution of all electrode surfaces. The experimental values reported in Ref. [6] are also reproduced for comparison. It is worth noting that the values of C_s and C_g predicted using non-solvated ion diameter $a = 0.68$ nm were about 8.5% and 3% larger than their respective experimental counterparts. On the other hand, C_s and C_g predicted using solvated ion diameter $a = 1.40$ nm underestimated the experimental

values by about 24%. In fact, the predictions using non-solvated and solvated ion diameters set the upper and lower bounds for the capacitances, respectively. The capacitances predicted using non-solvated ion diameter ($a = 0.68$ nm [37]) showed better agreement with experimental data. We speculate that these results could be attributed to two possible reasons. First, as the electrolyte concentration increases, the dissolved electrolyte ions become less solvated, i.e., they are surrounded by less solvent molecules [5, 224–226]. Consequently, the effective ion diameter decreases with increasing electrolyte concentration [5,224,226]. Note also that the solubility of $TEABF_4$ in propylene carbonate is about 1 mol L^{-1} at room temperature [227]. Second, the effective ion diameter of TEA^+ tends to decrease under large local electric field [258]. In fact, TEA^+ ions was found to become distorted and able to adsorb in pores with diameter even smaller than the non-solvated TEA^+ [213, 258, 259]. Thus, the effective ion diameter near the electrode surfaces approaches that of the non-solvated ions, i.e., $a = 0.68$ nm [213, 258, 259]. Overall, the predicted capacitances agreed well with experimental data. These results validate the numerical models, boundary conditions, and constitutive relationships developed here for simulating EDLCs with three-dimensional ordered structures. The new boundary conditions were essential in obtaining such results.

Table 5.2: Predicted [7] overall areal and gravimetric capacitances of the ordered bimodal carbon using (a) non-solvated ion diameter $a = 0.68$ nm and (b) solvated ion diameter $a = 1.40$ nm in comparison with experimental data reported in Ref. [6]. Results were obtained by solving Equations (5.3c), (5.1b), and (5.10) or (5.13) with $c_\infty = 1$ mol L^{-1} and $\psi_s = 2$ V.

	Specific area (m^2 g^{-1})	C_s **(μF cm^{-2})**	C_g **(F g^{-1})**
Measured [6]	1003	9.4	95
$a = 0.68$ **nm**	960	10.2	97.9
$a = 1.40$ **nm**	960	7.5	72.0

Thanks to this experimentally validated numerical model, it becomes possible to numerically explore the effects of the electrode architecture on its energy storage capabilities. Figure 5.4 shows the predicted gravimetric capacitance C_g of bimodal carbon structures as a function of their specific surface area ranging from 910 to 1030 $m^2\ g^{-1}$. Here, the specific surface area was varied by changing the inner pore radius R_0 from 50 to 150 nm while other geometric parameters such as the carbon wall thickness and mesopore radius remained identical to those of CP204-S15 carbon shown in Figure 5.4.1. The results were obtained by solving Equation (5.1b) subject to boundary conditions given by Equations (5.3c) and (5.10) or (5.13) using both solvated and non-solvated ion diameters, i.e., $a = 1.40$ nm and $a = 0.68$ nm, respectively. Other parameters were identical to those used to generate the results presented in Table 5.1. Figure 5.4 also shows the measured gravimetric capacitance of different bimodal carbon films [6] obtained using 1 mol L^{-1} $TEABF_4$ electrolyte. It is evident that predicted and experimentally measured gravimetric capacitance C_g increased linearly with increasing specific surface area. The slope of C_g vs. specific surface area corresponds to a constant areal capacitance of $C_s \approx 7.4$ or 10.2 $\mu F\ cm^{-2}$ when using solvated or non-solvated ion diameter, respectively. Note that this trend is consistent with experimental data reporting a linear relationship between gravimetric capacitance and specific surface area with an areal capacitance of 9.4 $\mu F\ cm^{-2}$ [6]. Overall, very good agreement was observed between experimental measurements and model predictions.

Finally, it is evident that the new boundary conditions [Equations (5.10) and (5.13)] developed here made possible the simulations of EDLCs with three-dimensional ordered electrode structures. These simulations can give detailed information such as the equilibrium local charge storage, electric potential, and ion concentrations within the electrolyte which cannot be measured experimentally. Note also that these boundary conditions [Equations (5.10) and (5.13)] can

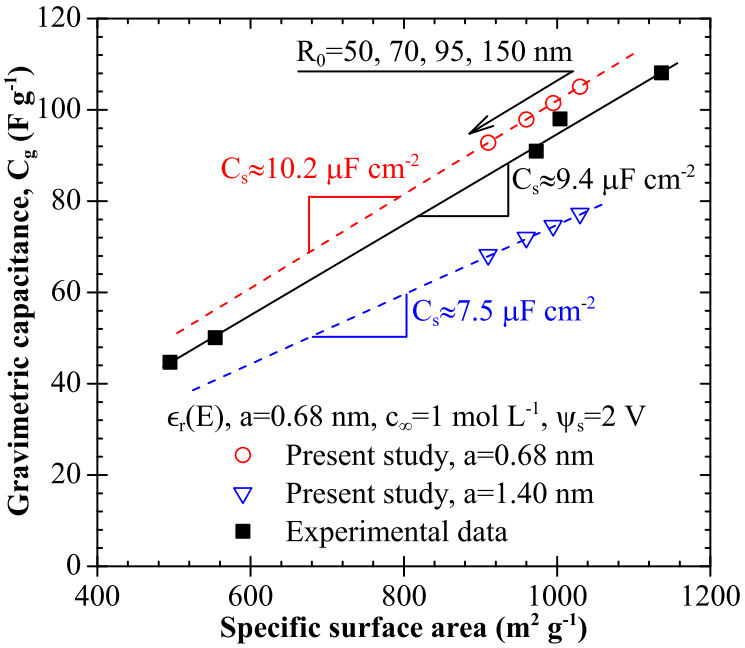

Figure 5.4: Predicted [7] and experimentally measured [6] gravimetric capacitance C_g for bimodal carbons as a function of their specific surface area. Numerical results were obtained by solving Equation (5.1b) using boundary conditions given by Equations (5.3c) and (5.10) or (5.13) with non-solvated ion diameter $a = 0.68$ nm, $c_\infty = 1$ mol L^{-1}, $\psi_s = 2$ V, and the electrolyte permittivity given by Equation (5.5). The inner pore radius R_0 was varied from 50 to 150 nm.

be readily employed to simulate the dynamic charging and discharging of EDLCs with ordered electrode structures. Then, the model could be used to identify the optimum electrode architecture and provide design rules to achieve maximum charging performance by EDLCs.

5.5 Conclusions

This chapter developed a three-dimensional equilibrium model based on continuum theory for simulating EDLCs with highly ordered electrode structures. For the first time, a new set of boundary conditions was derived to account for the

Stern layer forming near planar, cylindrical, and spherical electrodes as well as cylindrical and spherical pores [7]. They made possible the simulations of EDLCs with 3D ordered electrode structures while simultaneously and accurately accounting for [7] (i) both Stern and diffuse layers, (ii) finite ion size, and (iii) the dependency of electrolyte permittivity on the local electric field. The model was used to faithfully simulate an actual EDLC consisting of complex 3D ordered bimodal carbons in 1 mol L^{-1} $TEABF_4$/propylene carbonate electrolyte solution [6]. The predicted gravimetric capacitance of different bimodal carbon electrodes was found to increase linearly with increasing specific surface area corresponding to constant areal capacitance. Numerical predictions were in very good agreement with experimental data [6].

CHAPTER 6

Scaling Laws of Carbon-Based EDLCs

Chapters 3 to 5 presented physical modeling of EDLCs starting from a single microsphere to 3D ordered electrode structures. This chapter further extends the theory developed in previous chapters and presents a scaling law for the integral capacitance of carbon-based EDLCs.

6.1 Introduction

Electrodes of electric double layer capacitors (EDLCs) are typically made of porous carbon-based materials [27, 31, 34]. The porous structure increases the electrode surface area per unit volume available for EDL formation thus increasing energy density. However, the relationship between energy density and surface area is neither linear nor straightforward. The capacitance of EDLCs depends on a variety of parameters such as the electrode surface area, pore size, electrolyte properties, and the potential window [27,31,34]. General correlations relating the capacitance of EDLCs to the physical or electrochemical properties of the electrodes and electrolytes and accounting for the detailed structure of the electric double layer are not available. Instead, progress has been made mainly by trial and error informed by physical intuition and simplified EDLC models [85–87, 94].

This chapter aims to develop an experimentally-validated correlation relating the integral capacitance of EDLCs to these parameters. Such correlations would rationalize the design of EDLCs and provide rules for optimizing the porous architecture of EDLCs and for selecting the electrolyte.

6.2 Background

6.2.1 Equilibrium MPB Model - Planar Electrodes

The modified Poisson-Boltzmann (MPB) model for binary and symmetric electrolytes predicts the equilibrium electric potential ψ in the diffuse layer and accounts for the finite ion size [4, 95–99]. In one-dimensional Cartesian coordinates corresponding to a planar electrode, it is expressed as [4, 95–99],

$$\frac{\partial}{\partial x}\left(\epsilon_0\epsilon_r\frac{\partial\psi}{\partial x}\right)=\frac{2zeN_Ac_\infty\sinh\left(\dfrac{ze\psi}{k_BT}\right)}{1+4N_Aa^3c_\infty\sinh^2\left(\dfrac{ze\psi}{2k_BT}\right)}. \tag{6.1}$$

where ϵ_0 and ϵ_r are the free space permittivity ($\epsilon_0 = 8.854 \times 10^{-12}$ F/m) and the relative permittivity of the electrolyte solution, respectively. The Boltzmann constant is denoted by $k_B = 1.38\times10^{-23}$ J/K while T is the absolute temperature, z is the ion valency, $e = 1.602 \times 10^{-19}$ C is the elementary charge, and $N_A = 6.022 \times 10^{23}$ mol^{-1} is the Avogadro constant. The effect of the Stern layer can be accounted for via a boundary condition at the Stern/diffuse layer interface located at $x = H$ expressed as [245, 246],

$$-\frac{\partial\psi}{\partial x}(x=H)=\frac{\psi_s-\psi_D}{H} \tag{6.2}$$

where ψ_s is the surface potential and H is the Stern layer thickness corresponding to half of the effective ion diameter a, i.e., $H = a/2$, as illustrated in Figure 5.2. The potential at the Stern layer/diffuse layer interface located at $x = H$ is denoted by $\psi_D = \psi(H)$. The electric potential far away from the electrode was imposed as zero, i.e., $\psi(x = L) = 0$. Note that this boundary condition is valid for symmetric electrolytes but cannot be used for asymmetric electrolytes [260].

Solving Equations (6.1) and (6.2) yields expression for the equilibrium Stern and diffuse layer capacitances for planar electrodes in binary and symmetric electrolytes, denoted by C_s^{St} and C_s^D, respectively. Assuming constant electrolyte

properties and accounting for the finite ion size, they are expressed as [4,7,95,228]

$$C_s^{St} = \frac{\epsilon_0 \epsilon_r}{H} \quad \text{and} \quad C_s^D = \frac{2zeN_A c_\infty \lambda_D}{\psi_D} \sqrt{\frac{2}{\nu_p} \ln\left[1 + 2\nu_p \sinh^2\left(\frac{ze\psi_D}{2k_B T}\right)\right]} \tag{6.3}$$

where λ_D is the Debye length for symmetric electrolytes defined as $\lambda_D = \sqrt{\epsilon_0 \epsilon_r k_B T / 2e^2 z^2 N_A c_\infty}$ and corresponding to an estimate of the EDL thickness [9, 35]. The packing parameter ν_p is defined as $\nu_p = 2a^3 N_A c_\infty$. It represents the ratio of the total bulk ion concentration to the maximum ion concentration assuming a simple cubic ion packing [4,7,95,228]. By treating the Stern and diffuse layer capacitances in series, the total double layer integral capacitance $C_{s,planar}$ can be expressed as [7,9,90,149,228]

$$\frac{1}{C_{s,planar}} = \frac{1}{C_s^{St}} + \frac{1}{C_s^D} = \frac{a}{2\epsilon_0 \epsilon_r} + \frac{\psi_D}{2zeN_A c_\infty \lambda_D} \left\{ \frac{2}{\nu_p} \ln\left[1 + 2\nu_p \sinh^2\left(\frac{ze\psi_D}{2k_B T}\right)\right] \right\}^{-1/2} \tag{6.4}$$

6.2.2 Equilibrium MPB Model - Cylindrical and Spherical Pores

The MPB model with Stern layer for cylindrical or spherical pores (Figure 5.2b) is expressed as [7, 228],

$$\frac{1}{r^p} \frac{\partial}{\partial r}\left(\epsilon_0 \epsilon_r r^p \frac{\partial \psi}{\partial r}\right) = zeN_A c_\infty \frac{2\sinh\left(\frac{ze\psi}{k_B T}\right)}{1 + 4N_A a^3 c_\infty \sinh^2\left(\frac{ze\psi}{2k_B T}\right)} \tag{6.5}$$

where $p = 1$ or 2 for cylindrical or spherical pores, respectively. Here also, the effect of the Stern layer can be accounted for via the boundary condition at the Stern/diffuse layer interface, located at $r = R_0 - H$ (Figure 5.2b), expressed as [7],

$$\frac{\partial \psi}{\partial r}(r = R_0 - H) = \begin{cases} \dfrac{\psi_s - \psi_D}{(R_0 - H)\ln\left(\dfrac{R_0}{R_0 - H}\right)} & \text{for cylindrical pores.} \quad (6.6a) \\ \dfrac{\psi_s - \psi_D}{H} \dfrac{R_0}{R_0 - H} & \text{for spherical pores.} \quad (6.6b) \end{cases}$$

where ψ_D is the potential at the Stern layer/diffuse layer interface, i.e., $\psi_D = \psi(r = R_0 - H)$. Moreover, the gradient of electric potential at the center of the

spherical or cylindrical pore (at $r = 0$) was imposed as zero by virtue of symmetry, i.e.,

$$\frac{\partial \psi}{\partial r}(r = 0) = 0 \tag{6.7}$$

To the best of our knowledge, unlike for planar electrodes, no analytical expressions exist for the total and diffuse layer capacitances of cylindrical or spherical pores when accounting for the finite ion size.

This chapter aims to identify scaling laws governing the integral areal capacitance of actual EDLCs with porous carbon-based electrodes as a function of the dimensionless similarity parameters rigorously identified from scaling analysis of the governing equations for the electric potential and ion concentrations.

6.3 Analysis

6.3.1 Equilibrium MPB Model - Planar Electrodes

The dimensional analysis of the MPB model can be performed by scaling (i) the spatial coordinate by the Debye length λ_D and (ii) the local potential ψ by the thermal voltage $k_B T/ez$ representing the voltage that would induce a potential energy equivalent to the thermal energy of an ion of charge z so that [261],

$$x^* = \frac{x}{\lambda_D} \quad \text{and} \quad \psi^* = \frac{\psi}{k_B T/ez}. \tag{6.8}$$

Then, Equation (6.1) can be written in dimensionless form as

$$\frac{\partial^2 \psi^*}{\partial x^{*2}} = \frac{2 \sinh \psi^*}{1 + 2\nu_p \sinh^2(\psi^*/2)}. \tag{6.9}$$

Moreover, the dimensionless boundary conditions can be written as

$$-\frac{\partial \psi^*}{\partial x^*}(x^* = a^*/2) = \frac{\psi_s^* - \psi_D^*}{a^*/2} \quad \text{and} \quad \psi^*(x^* = L^*) = 0. \tag{6.10}$$

where $\psi_D^* = \psi_D/(k_B T/ez) = \psi^*(a^*/2)$ is the dimensionless diffuse layer potential. Four dimensionless similarity parameters arise from the scaling analysis of the

equilibrium MPB model with Stern layer for planar electrodes [Equations (6.9) and (6.10)] namely (i) the dimensionless surface potential $\psi_s^* = \psi_s/(k_BT/ze)$, (ii) the packing parameter $\nu_p = 2N_Aa^3c_\infty$, (iii) the dimensionless ion diameter $a^* = a/\lambda_D = 2H/\lambda_D$, and (iv) the dimensionless electrolyte layer thickness $L^* = L/\lambda_D$. Note that these four dimensionless numbers, or combination thereof, were also derived from the scaling analysis of the modified Poisson-Nernst-Planck (MPNP) model (Chapter 8). In the scaling analysis of the MPNP model, an additional dimensionless number was obtained corresponding to the dimensionless scan rate. The two approaches are equivalent if one considers low scan rates and imposes $\psi_s = (\psi_{max} - \psi_{min})/2$ where $\Delta\psi$ is the potential window used in cyclic voltammetry simulations [149].

Similarly, scaling the total integral capacitance of a planar electrode $C_{s,planar}$ [Equation 8.15b)] by the Stern layer capacitance $C_s^{St} = \epsilon_0\epsilon_r/H$ with $H = a/2$, results in the dimensionless total integral capacitance $C^*_{s,planar}$ expressed as,

$$\frac{1}{C^*_{s,planar}} = \frac{C_s^{St}}{C_{s,planar}} = 1 + \frac{2\psi_D^*}{a^*}\left\{\frac{2}{\nu_p}\ln\left[1 + 2\nu_p\sinh^2\left(\frac{\psi_D^*}{2}\right)\right]\right\}^{-1/2} \tag{6.11}$$

To the best of our knowledge, analytical expressions for the diffuse layer potential ψ_D or ψ_D^* do not exist when accounting for the finite ion size, i.e., when $\nu_p \neq 0$. Alternatively, they can be determined numerically by solving the equilibrium modified Poisson-Boltzmann (MPB) model with the Stern layer [Equations (6.1) and (6.2)]. If the above scaling analysis is correct, ψ_D^* should depend only on the four dimensionless numbers identified namely ν_p, a^*, L^*, and ψ_s^*.

6.3.2 Equilibrium MPB Model - Cylindrical and Spherical Pores

By employing the scaling parameters $r^* = r/\lambda_D$ and $\psi^* = \psi/(k_BT/ez)$, the MPB model with Stern layer [Equation (6.5) to (6.7)] for cylindrical and spherical pores

can be written in dimensionless form as

$$\frac{1}{r^{*p}}\frac{\partial}{\partial r^*}\left(r^{*p}\frac{\partial \psi^*}{\partial r^*}\right) = \frac{2\sinh\psi^*}{1+2\nu_p\sinh^2(\psi^*/2)}. \tag{6.12}$$

The dimensionless boundary conditions at the Stern/diffuse layer interface can be written as,

$$-\frac{\partial \psi^*}{\partial r^*}(r^* = R_0^* - a^*/2)$$

$$= \begin{cases} \dfrac{\psi_s^* - \psi_D^*}{(R_0^* - a^*/2)\ln\left(\dfrac{R_0^*}{R_0^* - a^*/2}\right)} & \text{for cylindrical pores} \quad (6.13a) \\ \dfrac{\psi_s^* - \psi_D^*}{a^*/2}\dfrac{R_0^*}{R_0^* - a^*/2} & \text{for spherical pores} \quad (6.13b) \end{cases}$$

where $\psi_D^* = \psi^*(R_0^* - a^*/2)$. The symmetry boundary condition at the center of the pore is given by,

$$\frac{\partial \psi^*}{\partial r^*}(r^* = 0) = 0. \tag{6.14}$$

Here also, four dimensionless numbers appeared in the dimensionless MPB model with Stern layer [Equations (6.12) to (6.14)] for cylindrical and spherical pores, namely (i) ψ_s^*, (ii) ν_p, (iii) a^*, and (iv) the dimensionless pore radius defined as $R_0^* = R_0/\lambda_D$. The only difference from the dimensionless numbers governing the integral capacitance of planar electrodes is the substitution of L^* by R_0^*.

6.4 Results and Discussions

6.4.1 Equilibrium Diffuse Layer Potential

6.4.1.1 Planar Electrodes

Figure 6.1 shows the dimensionless diffuse layer potential ψ_D^* as a function of the dimensionless surface potential window ψ_s^* ranging from 0.01 to 20 with L^* varying between 16 and 329, while ν_p ranged from 0.052 to 0.94, and a^* from 1.15 to 3.03. It was computed by numerically solving the equilibrium MPB model

with the Stern layer [Equations (6.9) and (6.10)]. It is evident that all curves nearly collapsed on a single line irrespective of the values of ν_p, a^*, and L^* so that ψ_D^* depended solely on ψ_s^*. The inter-electrolyte distance $2L$ did not affect ψ_D provided that the electric double layer on each electrode did not overlap the other, i.e., for $L \gg \lambda_D$ or $L^* \gg 1$. Then, the dimensionless diffuse layer potential ψ_D^* as a function of ψ_s^* was fitted with a power law to yield

$$\psi_D^* = 0.37\psi_s^{*1.16}. \tag{6.15}$$

The associated coefficient of determination was $R^2 = 0.98$. Predictions of C_s^D using Equation (8.15b) and the above expression for ψ_D^* fell within 1% of its value obtained using the numerically computed value of ψ_D^*.

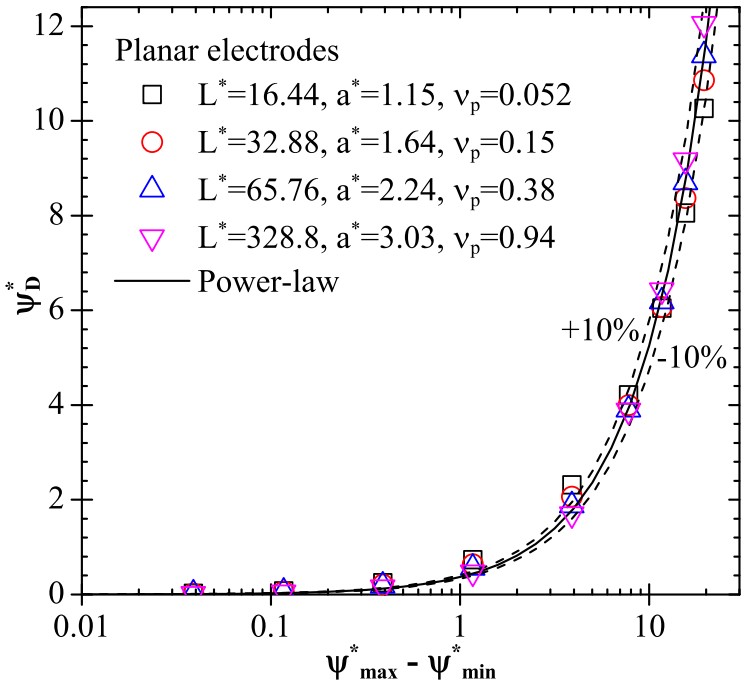

Figure 6.1: Dimensionless diffuse layer potential ψ_D^* as a function of dimensionless surface potential ψ_s^* ranging from 0.01 to 20 for different values of L^*, ν_p, and a^*.

6.4.1.2 Cylindrical and Spherical Pores

Figure 6.2 shows the predicted dimensionless diffuse layer potential ψ_D^* as a function of dimensionless surface potential window ψ_s^* ranging from 0.01 to 20 for (a) cylindrical and (b) spherical pores with dimensionless pore radius $R_0^* = 6.58$, 16.44, 65.76, and 328.8. These values correspond to surface potential ψ_s ranging from 0.001 to 0.5 V and R_0 equals to 2, 5, 20, and 100 nm, respectively. Here, ν_p ranged from 0.15 to 0.94 and a^* from 1.64 to 3.29. The dimensionless diffuse layer potential ψ_D^* for planar electrodes given by Equation (6.15) was also shown in Figure 6.2 for comparison. It is evident that ψ_D^* for cylindrical or spherical pores was nearly identical to that of planar electrodes for $R_0^* \geq 16$. For $R_0^* < 16$, the predicted ψ_D^* for cylindrical or spherical pores was larger than that of planar electrodes. The difference increased with increasing ψ_s^* and decreasing R_0^*. The maximum relative difference was less than 15% and 30% for cylindrical and spherical pores, respectively, for the range of R_0^* and ψ_s considered. Overall, these results demonstrate that the correlation for the equilibrium diffuse layer potential for planar electrodes [Equation (6.15)] may be applied to cylindrical or spherical pores with acceptable accuracy.

6.4.2 Equilibrium Integral Capacitance

Combining Equations (6.11) and (6.15), the dimensionless equilibrium integral capacitance $C_{s,planar}^*$ for planar electrodes can be expressed in terms of the three dimensionless numbers identified previously ψ_s^*, ν_p, and a^* as

$$\frac{1}{C_{s,planar}^*} = 1 + \frac{0.74\psi_s^{*1.16}}{a^*}\left\{\frac{2}{\nu_p}\ln\left[1 + 2\nu_p \sinh^2(0.185\psi_s^{*1.16})\right]\right\}^{-1/2} \tag{6.16}$$

Note that, under equilibrium conditions, $C_{s,planar}^*$ does not depend on L^* as also observed in CV simulations at low scan rates [149]. This analytical expression enables the prediction of the integral capacitance of planar electrodes without solving the MPB model.

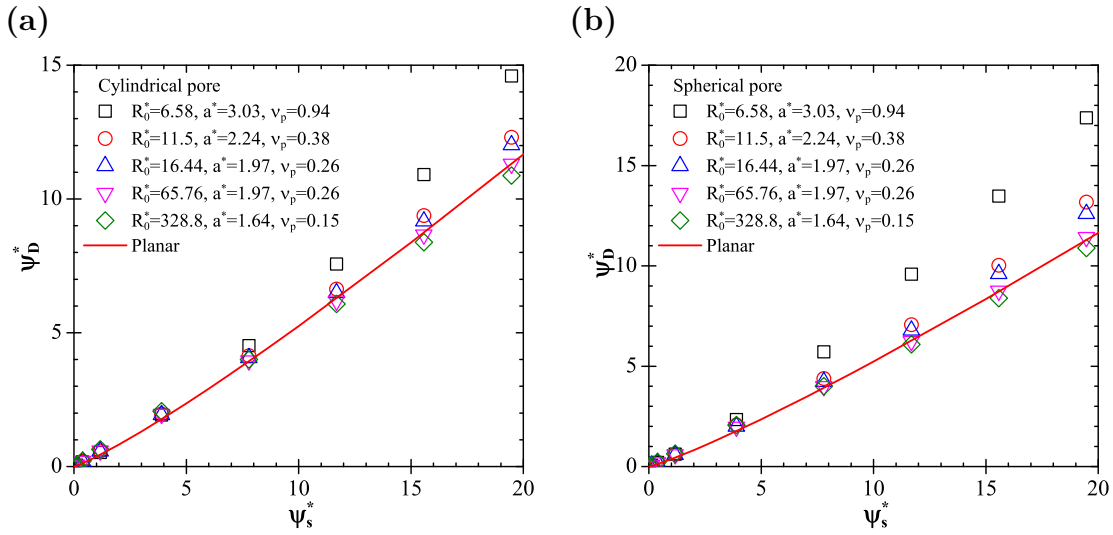

Figure 6.2: Predicted dimensionless diffuse layer potential ψ_D^* as a function of dimensionless surface potential ψ_s^* for (a) cylindrical and (b) spherical pores obtained from MPB model with Stern layer for different values of R_0^*, a^*, and ν_p.

6.4.3 Experimental Data

A wide range of experimental data was collected from the literature in order to assess the applicability of the above scaling analysis to actual carbon-based porous electrodes. Experimental data were selected to ensure that (i) the electrolytes were binary and symmetric such as KOH and $TEABF_4$, (ii) the reported capacitance was the integral areal capacitance and not the differential areal capacitance, and (iii) the integral areal capacitance was measured using either cyclic voltammetry at low scan rates or galvanostatic charge/discharge at low currents corresponding to the quasi-equilibrium regime. Then, the integral areal capacitances measured using these two techniques were identical as quasi-equilibrium conditions prevailed [16, 149]. It is convenient to consider the areal capacitance as it accounts for the possibility that electrodes might have different porosity and surface area per unit volume.

Table 6.1 summarizes the experimental data reported in the literature for

EDLCs with various electrolytes, electrode pore radii R_0, and potential windows $\Delta\psi = 2\psi_s$ along with the corresponding range of the experimentally-measured integral areal capacitance, denoted by $C_{s,exp}$ (in $\mu F/cm^2$). The electrodes consisted of various mesoporous carbons, namely (i) titanium carbide-derived carbon (TiC-CDC) [37], (ii) ordered mesoporous carbon (OMC) [237, 238, 262–264], (iii) highly-ordered mesoporous carbon (HOMC) [265], (iv) graphene nanosheet (GNS) and graphene nanosheet/carbon black composites (GNS/CB) [266], (v) free-standing mesoporous carbon thin films (FSMC) [236], (vi) cubic mesoporous carbon (CMK), (vii) acid-modified CMK (H-CMK) [239], (viii) carbon foams [267], (ix) ginkgo activated carbon shells (GAC) [268], and (x) hierarchical porous core-shell carbon structure (C-CS) [269]. The electrode average pore radius varied from 0.36 to 3.25 nm. Three different electrolytes were considered including aqueous KOH and $TEABF_4$ in propylene carbonate (PC) or acetonitrile (AN) at concentrations c_∞ between 1 and 6.88 M. Anion and cation effective diameters typically differ, at least slightly. For example, OH^- and TEA^+ ions are slightly larger than K^+ and BF_4^-, respectively. However, they were assumed to be identical. The non-solvated effective ion diameter a was taken as 0.35 nm for ions K^+ and OH^- in water. It was assumed to be 0.68 nm for TEA^+ and BF_4^- [37,200]. The potential window varied between 0.6 V and 2.3 V depending on the electrolyte. Overall, a total of 56 experimental data points were collected corresponding to dimensionless numbers in the ranges $23 \leq \Delta\psi^* = 2\psi_s^* \leq 90$, $0.1 \leq \nu_p \leq 0.57$, $1.6 \leq a^* \leq 4.05$ (based on non-solvated ion diameters), and $1.4 \leq R_0^* \leq 40.2$.

Figure 6.3a shows the reported integral areal capacitance $C_{s,exp}$ as a function of the reported average pore radius R_0 for the above-mentioned experimental data. As expected, these data are scattered and the capacitance varies from 5.5 to 47 $\mu F/cm^2$ due to the wide range of electrolytes, electrode morphologies, pore sizes, and potential windows considered. On the other hand, Figure 6.3b shows the same data plotted in terms of the ratio $C_{s,exp}/C_{s,planar}$ as a function of $R_0^* - a^*/2$.

Table 6.1: Summary of experimental data reported in the literature for various carbon electrodes, binary and symmetric electrolytes, potential window $\Delta\psi = 2\psi_s$, and average pore radius R_0 along with their integral capacitance $C_{s,exp}$ (in μF/cm^2).

Ref.	**Electrode**	R_0 **(nm)**	**Electrolyte**	$\Delta\psi = 2\psi_s$ **(V)**	$C_{s,exp}$ $(\mu F/\mathbf{cm}^2)$
[37]	TiC-CDC	0.68-1.09	1 M $TEABF_4$ in AN	2.3	6.0-13.6
[262]	OMC-M	2.15-4.25	6.88 M KOH	0.8	16.8-27.5
[262]	OMC-K	1.95-4.7	6.88 M KOH	0.8	12.0-22.5
[266]	GNS/CB	0.364-0.37	6 M KOH	1	28.3-46.6
[265]	HOMC	0.37-0.41	6 M KOH	1	8.2-11.2
[236]	FSMC	2.15	6 M KOH	0.6	19.4
[263]	OMC	1.35-3.0	6 M KOH	1	5.8-11.8
[263]	OMC	1.35-3.0	1 M $TEABF_4$ in AN	2	5.2-6.7
[237]	OMC	2.7-3.25	6.88 M KOH	0.89	11.9-15.0
[239]	CMK-8	2.39	2 M KOH	1	13.3
[239]	H-CMK-8	2.33	2 M KOH	1	20.2
[238]	OMC	2.25	6 M KOH	0.8	18.8
[270]	MC spheres	1.34	2 M KOH	1	11.1
[271]	MC	0.625-0.69	1 M $TEABF_4$ in AN	2	10.3-11.6
[264]	OMC	0.395-0.555	1 M $TEABF_4$ in PC	2	5.5-6.7
[267]	Carbon foam	1.9	6 M KOH	1	12.5
[272]	OMC	0.6	6 M KOH	0.8	14.1-19.6
[268]	GAC	0.245-0.26	6 M KOH	1	13.4-17.7
[269]	C-CS	1.95	6 M KOH	0.9	10.6-16

Note: solvent for KOH was water.

It indicates that $C_{s,exp}/C_{s,planar}$ decreased from 0.5 to about 0.1 when $R_0^* - a^*/2$ increases from 0 to 40. First, it is remarkable that the experimental capacitances of mesoporous carbon electrodes had the same order of magnitude as the theoretical capacitance for planar electrodes $C_{s,planar}$. It is also worth noting that plotting the data in terms of $C_{s,exp}/C_{s,planar}$ versus $R_0^* - a^*/2$ significantly reduced the

scatter compared to Figure 6.3a and described a consistent trend. The capacitance ratio $C_{s,exp}/C_{s,planar}$ increased as the dimensionless pore radius R_0^* decreased and approached the dimensionless ion radius $a^*/2$. As the pore radius increased, the capacitance ratio $C_{s,exp}/C_{s,planar}$ reached a plateau of around 0.08. Curve fitting of the experimental data led to the following correlation,

$$\frac{C_{s,pred}}{C_{s,planar}} = 0.08 + \frac{0.084}{\sqrt{R_0^* - a^*/2}}. \tag{6.17}$$

Figure 6.3b also shows curves with ±20% deviations. The scatter in the experimental data and the fact that $C_{s,exp}$ differs from $C_{s,planar}$ for large values of R_0 can be attributed to the following main reasons: (i) experimentally, the pores featured a nonuniform size distribution while the scaling analysis was based on the reported average pore radius, (ii) the relative permittivity ϵ_r was assumed to be constant while it may vary significantly under high the electric fields such as those encountered near the electrode surface [199, 228], (iii) the electrolytes were assumed to be symmetric while anions and cations may have different solvated and/or non-solvated ion diameters, and (iv) the simple cubic packing of ions near the electrode assumed in formulating the MPB model may be overly simplistic. Note that attempts to account for the field-dependent dielectric constant in the Stern layer did not yield a better correlation (not shown). In other words, the semi-empirical constant in Equation (6.17) overall accounted for this effect.

The scaling law given by Equation (6.17) indicates that the equilibrium integral capacitance of mesoporous carbons with binary and symmetric electrolytes can be expressed as

$$C_{s,pred} = f(R_0^* - a^*/2)C_{s,planar} \tag{6.18}$$

where $C_{s,planar}$ is the equilibrium areal capacitance of the planar electrode given by Equation (8.16) while $f(R_0^* - a^*/2)$ is a geometric function correcting for the fact that pore/electrolyte interfaces are not planar. It is constant in the limiting case when $R_0 \gg a/2$ or $R_0^* \gg a^*/2$ such that the effect of the pore curvature on

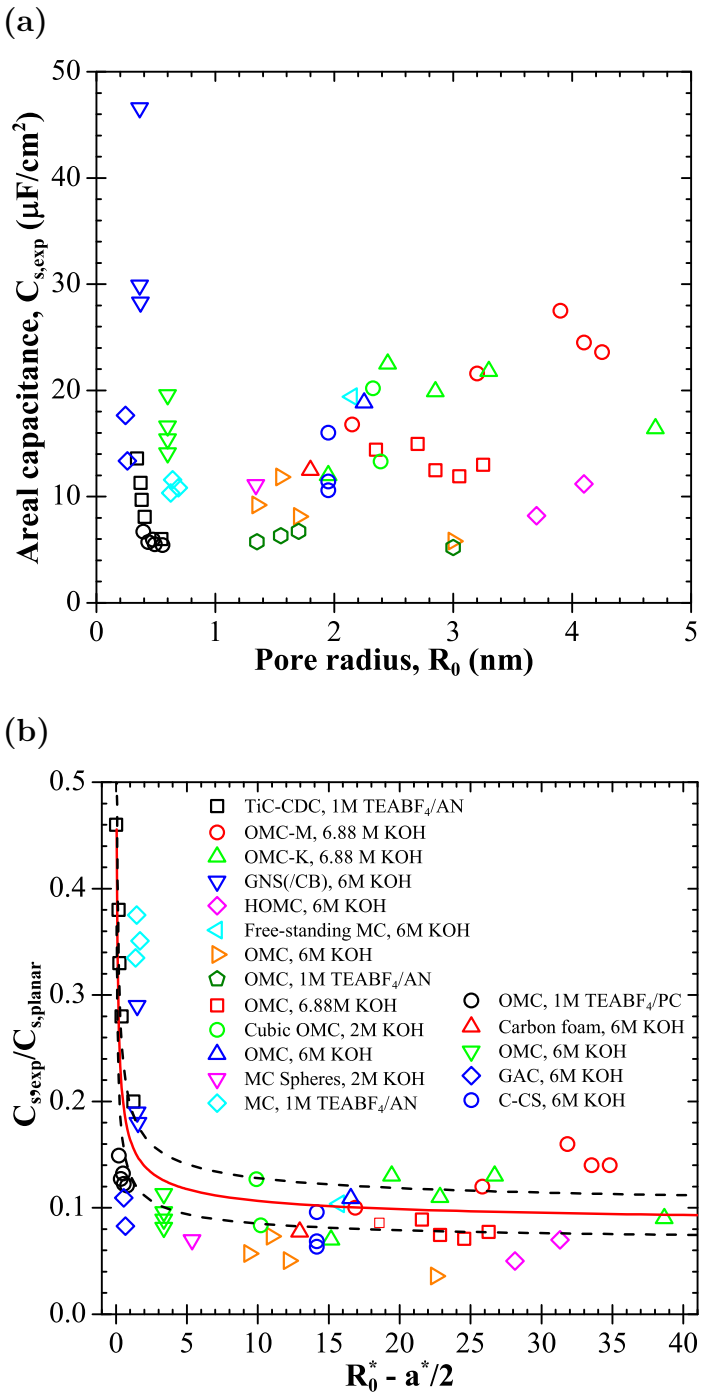

Figure 6.3: (a) Experimental data of integral capacitance $C_{s,exp}$ as a function of pore radius R_0 and (b) the ratio $C_{s,exp}/C_{s,planar}$ as a function of $R_0^* - a^*/2$ for EDLCs with various mesoporous carbon electrodes and binary symmetric electrolytes.

the areal capacitance is negligible.

Sensitivity analysis of this semi-empirical model was performed by randomly sampling it with 1300 sets of input parameters with electrolyte properties (i) a ranging from 0.1 to 1 nm, (ii) ϵ_r between 20 and 100, (iii) c_∞ from 1 to 6 M, and (iv) z with integer values between 1 and 3. The electrode properties were such that (v) R_0 ranged from 1 to 10 nm and (vi) ψ_s varied between 1 and 3 V. Scatter plots of $C_{s,pred}$ against each individual input variable indicates that the integral areal capacitance was most sensitive to the effective ion diameter a and the ion valency z followed by the electrolyte dielectric constant ϵ_r. This can be attributed to the fact that under large ion concentrations and potential windows, the total capacitance was dominated by the Stern layer capacitance expressed as $C_s^{St} = 2\epsilon_0\epsilon_r/a$. Interestingly, $C_{s,pred}$ was only weakly sensitive to the surface potential ψ_s. However, the fact that the total energy stored E (in J) is proportional to ψ_s, i.e., $E = C\psi_s^2/2$ confirms the importance of maximizing the potential window to maximize EDLCs' performance. Similarly, $C_{s,pred}$ was weakly sensitive to the pore radius R_0 except as R_0 approaches a, as suggested by Equation (6.17). Note that reducing the pore size also increases the interfacial area A_i between the electrode and the electrolyte and thus the total energy E and the capacitance C (in F) given by $C = C_{s,pred} \times A_i$.

6.5 Conclusions

This chapter presented scaling analysis of equilibrium MPB model for the electric double layer integral capacitance $C_{s,planar}$ for planar electrodes in binary and symmetric electrolytes. It was based on a power law correlation for the equilibrium diffuse layer potential. For the first time, a scaling law was derived to predict the integral areal capacitance $C_{s,pred}$ of porous electrodes as the product of an analytical expression [Equation (6.16)] and a semi-empirical function $f(R_0^* - a^*/2)$ accounting for the porous electrode morphology. The latter was obtained using

experimentally-measured integral areal capacitance $C_{s,exp}$ for EDLCs with various porous carbon electrodes and binary symmetric electrolytes. The scaling law indicates that the integral areal capacitance was most sensitive to the ions' effective diameter and valency and to the electrolyte dielectric constant. It was also sensitive to the pore radius R_0 only as R_0 approaches the ion radius $a/2$. Overall, to achieve large integral areal capacitance (i) the effective ion diameter a should be small, (ii) the electrolyte dielectric constant ϵ_r should be large, (iii) the pores should be as monodisperse as possible, and (iv) their radius R_0 should be tailored to match the ion diameter, i.e., $2R_0 \approx a$. Finally, (v) the ion valency z should be large. The total energy stored can be further enhanced by increasing the surface potential ψ_s or the potential window and the interfacial area between electrode and electrolyte.

CHAPTER 7

Physical Modeling of Electrochemical Impedance Spectroscopy for EDLCs

Chapters 3 to 6 presented equilibrium simulations of EDLCs. To better understand their charging/discharging performances, dynamic modeling of EDLCs is essential. This chapter presents physical modeling of charging/discharging dynamics of electric double layers during electrochemical impedance spectroscopy (EIS) measurements.

7.1 Introduction

Electrochemical impedance spectroscopy (EIS) is a powerful tool in the field of electrochemistry [9, 11–13, 273]. It has been used extensively to characterize the performance of various electrical energy storage devices such as electrochemical capacitors (also known as supercapacitors) [10, 14, 25, 31, 274–278], batteries [279–281], and fuel cells [13, 282]. In these applications, the charged electrodes are typically immersed in the electrolyte solution. Electric double layers form at the electrode/electrolyte interfaces which are accessible to ions present in the electrolyte.

EIS measurements consist of imposing a time harmonic electric potential with a certain frequency at the electrodes. This harmonic potential consists of two components: (i) a time-independent "DC potential" and (ii) a periodically oscillating potential with a small amplitude typically less than 10 mV [13, 31, 277].

The resulting electric current is recorded. Then, the magnitude of the electrochemical impedance can be defined as the ratio of the amplitudes of oscillating potential and current while its phase angle is the shift by which the current is ahead of the potential [9, 11–13]. A simple RC circuit consisting of a resistor and a capacitor in series is most commonly used to model pure electric double layers (i.e., without Faradic reaction) forming at an electrode as shown in Figure 8.1c [9, 11–14, 274–276]. The resistance and differential capacitance for a given frequency are retrieved from the in-phase and out-of-phase components of the measured electrochemical impedance, respectively [9,11–14,274–276]. The double layer differential capacitance measured by EIS is typically plotted as a function of frequency [12, 14, 25, 31, 43, 204, 274–276, 278, 283–290]. It is known to decrease with increasing frequency beyond a critical frequency due to the fact that the double layer is not ideally capacitive at large frequencies [287–290]. It has also been referred to as double layer impedance [288–291]. The capacitance retrieved from EIS measurements at low frequencies has been regarded as an estimate of the differential capacitance at the imposed DC potential [14, 31, 274, 292].

In comparison, cyclic voltammetry (CV) and galvanostatic charge/discharge techniques can measure both differential and integral capacitances as discussed in Section 2.1. EIS, CV, and galvanostatic charge/discharge methods have been extensively used to measure the capacitances of various electrical energy storage devices. However, the measured capacitances using these techniques have been frequently reported and compared without any discrimination between differential and integral capacitances in the literature [28, 43, 78, 79, 285, 286, 293–295]. For example, the differential capacitance of various supercapacitors estimated from EIS or CV measurements have been compared with their integral capacitance measured using CV or galvanostatic charge/discharge method in Refs. [43, 78, 79, 285, 286, 293, 294].

This study aims to clarify the confusion in the literature when comparing

the electric double layer capacitances measured using EIS and other techniques. The EIS measurements were simulated by modeling ion transport in electrolyte solutions as a function of frequency. The results were compared with the analytical expressions for integral and differential capacitances under equilibrium conditions.

7.2 Background

7.2.1 Electrochemical Impedance Spectroscopy

In EIS measurements, the electric potential $\psi_s(t)$ imposed at the electrode is a harmonic function of time t. This results in a harmonic current density j_s (in $\mathrm{A/m^2}$) provided that the amplitude of the harmonic potential is small enough (e.g., less than 10 mV). Using complex notations, the imposed electric potential and the corresponding current density can be expressed as [9, 11–13],

$$\psi_s(t) = \psi_{dc} + \psi_0 e^{i2\pi ft} \quad \text{and} \quad j_s(t) = j_{dc} + j_0 e^{i(2\pi ft - \phi)} \tag{7.1}$$

where ψ_{dc} and j_{dc} are time-independent DC potential and DC current density, respectively. Here, ψ_0 and j_0 are the amplitudes of the potential and current density around their DC components, respectively. The imaginary unit is denoted by i, f is the frequency expressed in Hz, while $\phi(f)$ is the frequency-dependent phase angle between the harmonic potential $\psi_s(t)$ and the current density $j_s(t)$. The complex electrochemical impedance Z is defined as [9, 11–13],

$$Z = \frac{\psi_0}{j_0} e^{i\phi} = Z' + iZ'' \tag{7.2}$$

where Z' and Z'' (expressed in $\Omega\mathrm{m^2}$) are the real and imaginary parts of the impedance, respectively. Based on the equivalent RC circuit shown in Figure 8.1c, the resistance and differential capacitance per unit surface area are given by [9, 11–14],

$$R_s^{EIS} = Z' \quad \text{and} \quad C_s^{EIS} = \frac{-1}{2\pi f Z''} \tag{7.3}$$

Equation (7.3) is the most commonly used formula to determine the differential capacitance of EDLCs from EIS measurements [14, 25, 43, 204, 274–276, 284–286, 293]. Alternatively, more complicated RC circuits [10,296,297] or transmission line models [10,298–303] have also been developed to represent electric double layers by introducing more resistor and capacitor components. Then, these models have to be fitted with experimental EIS data to retrieve the resistances and capacitances. However, these models suffer from other drawbacks as stated in Ref. [304]: *"First, it is possible for two different models to produce the same impedance response [...]. Second, the overall impedance expressions corresponding to most models give little or no direct information about the physical meaning of the elements for such models."* Note also that the fitted pseudocapacitance values based on complex RC circuits were also reported to underpredict those measured using other techniques [305–309].

7.2.2 Ion Transport in Electrolyte Solutions

It is well known that ion transport in dilute electrolyte solutions can be accurately described by the classical Poisson-Nernst-Planck (PNP) model [9,90,95,146]. The PNP model has been used extensively to investigate EIS and reaction kinetics of one-dimensional electrolytic cells [288–291, 310] and ion-exchange membranes [311–315]. However, the PNP model neglects the finite size of ions and treat ions as point-charges. This assumption is appropriate only when both the ion concentration c_∞ and the electric potential are small [95, 146].

Recently, efforts have been made to account for the effect of finite ion size in modeling ion transport in concentrated electrolyte solutions. Lim *et al.* [316, 317] used the classical Nernst-Planck model and accounted for the finite ion size by adding a Stern layer. Their model imposed linear potential profile and uniform ion concentrations in the Stern layer. However, it was limited to relatively low surface potential and electrolyte concentration, i.e., $\psi_s \leq 0.2$ V and $c_\infty \leq 0.01$

mol/L. Kilic *et al.* [146] derived a modified PNP (MPNP) model valid for binary and symmetric electrolytes under large electrolyte concentration and electric potential. They added an excess term in the expression of the electrochemical potential to account for the finite ion size. They solved the MPNP model numerically for a planar electrode and predicted the profiles of electric potential and ion concentrations in the diffuse layer [146]. Their results demonstrated that under large electrolyte concentration and electric potential, the predictions of PNP model deviated significantly from the MPNP model due to the point-charge assumption. Alternatively, Horno and co-workers [113, 153] accounted for the finite ion size in ion mass fluxes using the activity coefficient. It was later demonstrated that Kilic's model [146] can be formulated in a form equivalent to that based on activity coefficient [95, 130]. However, to the best of our knowledge, no studies have simulated EIS measurements under both large electrolyte concentrations and electric potential other than by using RC circuits [10, 14, 274] or transmission line models [10, 300–303].

This chapter aims to simulate the electric double layer dynamics and to predict electric double layer capacitances in EIS measurements. The transient double layer dynamics was simulated for the electric double layer formed near a planar electrode in aqueous electrolyte solutions. For low electrolyte concentrations, the classical Poisson-Nernst-Planck (PNP) model with or without the Stern layer was solved. Instead, for large electrolyte concentrations, a modified PNP model [146] was used accounting for the Stern layer.

7.3 Analysis

7.3.1 Schematics and Assumptions

Figure 7.1 shows the schematic of the computational domain simulating a planar electrode immersed in an electrolyte solution. The region of electrolyte solution

consists of two layers corresponding to (1) a Stern layer of thickness H near the electrode surface and (2) a diffuse layer beyond. A time-dependent electric potential $\psi_s(t)$ was prescribed at the electrode surface and was zero far away from the electrode surface. The length of the overall computational domain was specified to be (i) $L = 160$ nm for electrolyte concentration c_∞ less than 0.01 mol/L and (ii) $L = 80$ nm for c_∞=1 mol/L. Note that the electric double layer thickness decreases with increasing electrolyte concentration [35, 95, 146]. Increasing the value of L by a factor of two was found to have no effect on (i) the predicted integral capacitance C_s under equilibrium conditions and (ii) the differential capacitance C_s^{EIS} retrieved from EIS simulations at low frequency using Equation (7.3). However, the values of C_s^{EIS} predicted at large frequencies were found to decrease with increasing L. This can be attributed to the fact that the charge storage or charge relaxation took longer as the domain length L increased under large frequencies [128]. Then, the charge storage at large frequencies was limited as it could not follow the fast variation in the electric potential. Figure 8.1b shows the typical representation of an electric double layer capacitance with the Stern layer and diffuse layer capacitances in series [8–10, 36].

To make the problem mathematically tractable, the following assumptions were made: (1) anions and cations had the same effective diameter and diffusion coefficient which were assumed to be constant and independent of electrolyte concentration [4, 95, 200], (2) the electrolyte dielectric relative permittivity was constant, independent of frequency, and equals to that of water. Note that the relative permittivity of water at room temperature is known to significantly decrease for frequency larger than 5×10^9 Hz [253]. The frequency range considered here did not exceed this value except otherwise mentioned, (3) isothermal conditions prevailed throughout the electrode and electrolyte, (4) advection of the electrolyte was assumed to be negligible, (5) the ions could only accumulate at the electrode surface and could not diffuse into the electrode, i.e., there was no

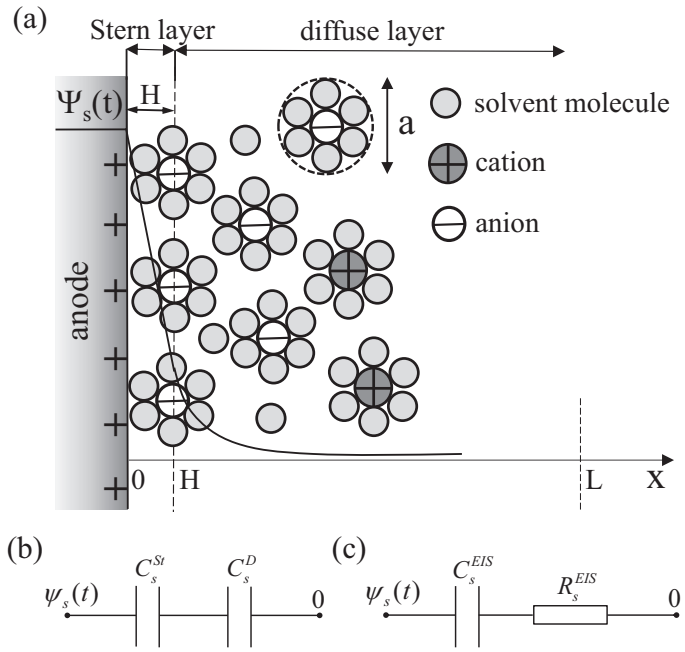

Figure 7.1: Schematic of (a) the electric double layer structure showing the arrangement of solvated anions and cations near an anode/electrolyte interface and the simulated computational domain consisting of the Stern layer and the diffuse layer, (b) the Stern and diffuse layer capacitances in series [8–10], and (c) the equivalent RC circuit used in EIS [9, 11–14].

ion insertion, and (6) the specific ion adsorption due to non-electrostatic forces were assumed to be negligible.

7.3.2 Governing Equation and Boundary Conditions

The local electric potential $\psi(x,t)$ and ion concentrations $c_i(x,t)$ in the electrolyte solution were computed by solving (i) the Poisson equation in the Stern and diffuse layers [8, 316, 317] and (ii) the PNP or MPNP model in the diffuse layer for small or large electrolyte concentration, respectively [95, 130, 146]. For binary and symmetric electrolytes, the valency is such that $z_1 = -z_2 = z$ and the bulk ion concentration is given by $c_{1\infty} = c_{2\infty} = c_\infty$. Then, assuming identical diffusion

coefficient $D_1 = D_2 = D$, the MPNP model with Stern layer can be written as [95, 130, 146],

$$\frac{\partial}{\partial x}\left(\epsilon_0\epsilon_r\frac{\partial\psi}{\partial x}\right) = \begin{cases} 0 & \text{for } 0 \le x < H \quad (7.4a) \\ eN_Az(c_1 - c_2) & \text{for } x \ge H \quad (7.4b) \end{cases}$$

$$\frac{\partial c_i}{\partial t} = \frac{\partial}{\partial x}\left(D\frac{\partial c_i}{\partial x} + \frac{z_iD}{R_uT}Fc_i\frac{\partial\psi}{\partial x} + \frac{\nu_pDc_i}{2c_\infty - \nu_p(c_1+c_2)}\frac{\partial(c_1+c_2)}{\partial x}\right) \quad \text{for } x \ge H \quad (7.4c)$$

where $c_i(x,t)$ is the local molar concentration of ion species "i" ($i = 1,\ 2$). The Cartesian coordinate is denoted by x while ϵ_0 and ϵ_r are the free space permittivity ($\epsilon_0 = 8.854 \times 10^{-12}$ F/m) and the relative permittivity of the electrolyte solution, respectively. The absolute temperature is denoted by T, e is the elementary charge ($e = 1.602 \times 10^{-19}$ C), N_A is the Avogadro's number ($N_A = 6.022 \times 10^{23}$ mol^{-1}) while F and R_u are the Faraday constant ($F = eN_A$ sA/mol) and the universal gas constant ($R_u = 8.314$ JK^{-1}mol^{-1}), respectively. The packing parameter is defined as $\nu_p = 2a^3N_Ac_\infty$ where a is the effective ion diameter. It represents the ratio of the total bulk ion concentration to the maximum ion concentration $c_m = 1/N_Aa^3$ assuming a simple cubic ion packing [95, 130, 146]. Therefore, ν_p should not be larger than unity for the model to be physically acceptable [95,130,146]. Equations (7.4b) and (7.4c) reduce to the classical Poisson-Nernst-Planck model when $\nu_p = 0$ [95, 130, 146]. Note that in Refs. [95, 130, 146], the Stern layer was accounted for via a boundary condition relating the potential drop across the Stern layer and the potential gradient at the Stern/diffuse layer interface. Here, the electric potential in the Stern layer was solved explicitly. In fact, these two approaches are equivalent for planar electrodes [130, 146, 228].

Moreover, the associated boundary and initial conditions were given by [8, 90,

146],

$$\psi(x=0,t)=\psi_s(t), \tag{7.5a}$$

$$\psi\big|_{x=H^-}=\psi\big|_{x=H^+} \quad \text{and} \quad \epsilon_0\epsilon_r\frac{d\psi}{dx}\bigg|_{x=H^-}=\epsilon_0\epsilon_r\frac{d\psi}{dx}\bigg|_{x=H^+}, \tag{7.5b}$$

$$D\frac{\partial c_i}{\partial x}+\frac{z_i D}{R_u T}Fc_i\frac{\partial\psi}{\partial x}+\frac{\nu_p D c_i}{2c_\infty-\nu_p(c_1+c_2)}\frac{\partial(c_1+c_2)}{\partial x}=0, \text{ at } x=H \tag{7.5c}$$

$$\psi(x=L,t)=0 \quad \text{and} \quad c_i(x=L,t)=c_\infty, \tag{7.5d}$$

$$\psi(x,t=0)=0 \quad \text{and} \quad c_i(x,t=0)=c_\infty, \text{ for } 0\le x\le L \tag{7.5e}$$

Note that the surface electric potential $\psi_s(t)$ in Equation (7.5a) was given by Equation (7.1). Equation (7.5b) states that the electric potential and displacement were continuous across the Stern/diffuse layer interface located at $x = H$ [8, 90]. Equation (7.5c) indicates that the mass fluxes vanish for both ion species at the electrode surface since there is no ion insertion [assumption (6)] [95, 146]. Note that, when $H = 0$ nm, Equations (7.4) and (7.5) correspond to simulations without the Stern layer.

7.3.3 Constitutive Relations

In order to solve Equations (7.4) and (7.5), the electrolyte properties ϵ_r, z, c_∞, a and D along with the temperature T and the surface potential $\psi_s(t)$ are needed. The present study focuses on aqueous electrolyte solution at room temperature ($T = 298$ K) with $\epsilon_r = 78.5$ [253]. Note that the electrolyte dielectric permittivity decreases at large local electric field [199, 228]. The electric double layer capacitance may decrease by a factor two or three when accounting for this effect [199, 228]. However, this is not expected to affect either the comparison between the capacitance under equilibrium conditions and that retrieved from EIS simulations or the qualitative conclusions of the present study.

The effective ion diameter and diffusion coefficient were taken as $a = 0.66$ nm [200] and $D = 2 \times 10^{-9}$ m^2/s [253], respectively, while the valency was $z =$

1. These values correspond to solvated ions such as K^+ and Cl^- in aqueous solutions. The diffusion coefficients of ions such as K^+ and Cl^- are known to decrease by about 10% when increasing the electrolyte concentration from 0 to 1 mol/L [318]. In addition, ion diffusion coefficients significantly decrease in the presence of charged obstacles [319] or porous electrodes [320]. Here, a parametric study was also carried out for other values of diffusion coefficient, namely, $D = 2 \times 10^{-8}$ and 2×10^{-10} m^2/s. The electrolyte concentration was chosen as (i) $c_\infty = 0.01$ and 0.001 mol/L so that the classical PNP model is valid and (ii) $c_\infty = 1.0$ mol/L corresponding to typical values in actual electrochemical capacitors. In addition, the Stern layer thickness H was approximated as the radius of solvated ions [9, 35, 36], i.e., $H = a/2 = 0.33$ nm.

Moreover, the DC potential component ψ_{dc} of the harmonic surface electric potential $\psi_s(t)$ was varied from 0.01 to 0.5 V. A DC potential of $\psi_{dc} = 0.5$ V corresponds to a typical potential difference of 1 V between the anode and the cathode for aqueous electrochemical capacitors. The amplitude of the potential oscillation was taken as (i) $\psi_0 = 0.001$ V for $\psi_{dc} \leq 0.1$ V and (ii) $\psi_0 = 0.005$ V for $\psi_{dc} > 0.1$ V. Decreasing ψ_0 by up to a factor five was found to have no effect on the predicted impedance and capacitance.

Finally, note that for low electrolyte concentrations $c_\infty = 0.001 - 0.01$ mol/L, the frequency range explored in the present study was $f = 10 - 10^7$ Hz. It was similar to the range $f = 1 - 10^7$ Hz in the experiments used for planar electrodes of gold platted stainless steel in $0.001 - 0.01$ mol/L KCl and $BaCl_2$ electrolyte solutions [321]. For $c_\infty = 1$ mol/L, frequency ranged from 10^3 to 10^9 Hz due to the significant decrease in the electrical resistance to ion transport when increasing electrolyte concentration [311, 322] as discussed in Section 7.4.2. However, these frequency ranges were several orders of magnitude larger than those encountered in typical EIS measurements for electrochemical capacitors with mesoporous electrodes where the frequency typically ranges from 10^{-3} to 10^5

Hz [31, 43, 274–277]. The difference is due to the fact that the electrode was not simulated in the present study. The electrical resistance of the mesoporous electrodes is significantly larger than that of planar electrodes. This, in turn, limits the range of frequencies in EIS measurements of practical EDLCs [14, 274–276].

7.3.4 Method of Solution And Data Processing

Equations (7.4) were solved using the commercial finite element solver COMSOL 3.5a, along with the boundary and initial conditions given by Equations (7.5). The capacitance under equilibrium conditions and the capacitance determined using EIS simulations were computed as follows.

7.3.4.1 Integral Capacitance Under Equilibrium Conditions

The double layer integral capacitance under equilibrium conditions corresponds to the time-independent surface potential, i.e., $\psi_s(t) = \psi_{dc}$. Then, the Stern and diffuse layer integral capacitances C_s^{St} and C_s^D are defined by dividing the surface charge density [9, 35, 90, 201, 202] $q_s(x) = \epsilon_0\epsilon_r E(x)$ by their respective potential difference [9, 90, 228]. Here, $E(x) = |-d\psi/dx|$ is the norm of the local electric field. The integral capacitances C_s^{St} and C_s^D of planar electrodes assuming constant electrolyte properties and accounting for the finite ion size are given by [4, 9, 90, 95, 228],

$$C_s^{St} = \frac{q_s(0)}{\psi_s - \psi_D} = \frac{\epsilon_0\epsilon_r}{H} \tag{7.6a}$$

$$C_s^D = \frac{q_s(H)}{\psi_D} = \frac{2zeN_Ac_\infty\lambda_D}{\psi_D}\sqrt{\frac{2}{\nu_p}\log\left[1 + 2\nu_p\sinh^2\left(\frac{ze\psi_D}{2k_BT}\right)\right]} \tag{7.6b}$$

where $\psi_D = \psi(H)$ is the electric potential computed at the Stern layer/diffuse layer interface $x = H$ by solving the steady-state equilibrium modified Poisson-Boltzmann model at surface potential ψ_{dc} and electrolyte concentration c_∞ [4, 95, 146, 228]. Then, the total integral capacitance C_s was calculated using the series

formula as [9, 90, 228],

$$\frac{1}{C_s} = \frac{1}{C_s^{St}} + \frac{1}{C_s^D} \tag{7.7}$$

Note that $\psi_D = \psi_{dc}$ when computing the capacitance C_s^D [Equation (8.15b)] without the Stern layer.

7.3.5 Differential Capacitance Under Equilibrium Conditions

Unlike the integral capacitance, the differential capacitance C_{diff} is defined as $dq_s/d\psi_s$ as discussed in Section 2.1. Under equilibrium conditions, the double layer differential capacitance is given by [4, 102],

$$\frac{1}{C_{diff}} = \frac{1}{C_{diff}^{St}} + \frac{1}{C_{diff}^D} \quad \text{with} \quad C_{diff}^{St} = \frac{\epsilon_0 \epsilon_r}{H} \tag{7.8a}$$

where C_{diff}^{St} and C_{diff}^D denote the Stern layer and diffuse layer differential capacitances, respectively. Here, ϵ_0 and ϵ_r are the free space permittivity and relative permittivity of the electrolyte, respectively. The diffuse layer differential capacitance accounting for finite ion size is expressed as [4, 102],

$$C_{diff}^D = \frac{\dfrac{\epsilon_0 \epsilon_r}{\lambda_D} \sinh\left(\dfrac{ze\psi_D}{k_B T}\right)}{\left[1 + 2\nu_p \sinh^2\left(\dfrac{ze\psi_D}{2k_B T}\right)\right] \sqrt{\dfrac{2}{\nu_p} \log\left[1 + 2\nu_p \sinh^2\left(\dfrac{ze\psi_D}{2k_B T}\right)\right]}} \tag{7.8b}$$

where the valency of the symmetric electrolyte is denoted by z, while T is the temperature, c_∞ is the bulk molar concentration of electrolyte, e is the elementary charge, N_A and k_B are the Avogadro constant and Boltzmann constant, respectively. The packing parameter is defined as $\nu_p = 2a^3 N_A c_\infty$ where a is the effective ion diameter. The electric potential at the Stern/diffuse layer interface is denoted by ψ_D. Note that $\psi_D = \psi_s$ for simulations without Stern layer. It is also important to note that in the presence of the Stern layer, the value of ψ_D in Equations (7.6b) and (7.8b) is unknown. In fact, ψ_D varies significantly with varying ψ_s. Its value must be determined numerically by solving the equilibrium modified Poisson-Boltzmann model with the Stern layer [4, 146, 149, 228].

7.3.5.1 Simulating EIS Measurements

EIS measurements were simulated by numerically imposing the harmonic surface electric potential given by Equation (7.1). The corresponding transient surface capacitive current density was estimated as [201, 202, 291, 311, 312, 323–326],

$$j_C(t) = \frac{dq_s}{dt} = \epsilon_0 \epsilon_r \frac{dE_s}{dt} \tag{7.9}$$

where $E_s(t) = -\left(\partial\psi/\partial x\right)(x = 0, t)$ is the electric field at the electrode surface $x = 0$ at time t. Simulations of EIS measurements were run for at least 50 periods (i.e., $t \geq 50/f$) to ensure the current density and impedance had reached their stationary and periodic states. Then, the electrochemical impedance Z as well as the associated differential capacitance C_s^{EIS} were computed using Equations (7.2) and (7.3), respectively. The convergence criterion was defined such that the maximum relative difference in the predicted C_s^{EIS} was less than 2% when (1) multiplying the total number of finite elements by two, (2) dividing the time step by two, and (3) running the EIS simulations for 50 more periods. The time step was imposed to be $\Delta t \lesssim 1/400f$. The mesh size was smallest at the electrode surface due to large potential gradient and then gradually increased. The maximum mesh size was specified to be 0.01 nm at the electrode surface and 1 nm in the rest of the domain. The total number of finite elements was less than 300 for all cases simulated in the present study.

7.3.5.2 Validation

The numerical tool was validated based on three cases reported in the literature. First, the predicted equilibrium electric potential profile in the diffuse layer was validated against the exact solution for planar electrodes [8, 35, 90] with $\epsilon_r = 78.5$, $c_\infty = 0.01$ and 0.001 mol/L, $\nu_p = 0$, and $\psi_D = 0.1$ V. Second, the computed integral capacitances for the Stern and diffuse layers under equilibrium conditions were validated against Equations (7.6a) and (7.6b) for (i) $\psi_s = 0.1$ V, $c_\infty = 0.01$

mol/L, and $a = 0.66$ nm as well as (ii) $\psi_s = 0.5$ V, $c_\infty = 1$ mol/L, and $a = 0.66$ nm. Third, the predicted transient ion concentration and electric potential profiles were compared with the numerical solutions for planar electrodes using PNP and MPNP models reported in Ref. [146]. Comparison was made for a wide range of packing parameter ν_p and dimensionless potential ($ze\psi_D/k_BT$). Good agreement was obtained between our results and reported values of $c_i(x,t)$ and $\psi(x,t)$ [146] for all cases considered.

7.4 Results and Discussions

7.4.1 EIS in Dilute Electrolyte Solutions

7.4.1.1 Predictions By PNP Model Without Stern Layer

Figure 7.2(a) shows the predicted diffuse layer differential capacitance C_s^{EIS} from EIS simulations using Equation (7.3) as a function of frequency ranging from 10 to 10^7 Hz. Results were obtained by numerically solving the classical PNP model without the Stern layer, i.e., $\nu_p = 0$ and $H = 0$ nm. The electrolyte concentration was either $c_\infty = 0.001$ or 0.01 mol/L while $\psi_{dc} = 0.1$ V. The effect of diffusion coefficient was assessed by performing simulations for $D = 2\times10^{-8}$, 2×10^{-9}, and 2×10^{-10} m^2/s. Figure 7.2(a) demonstrates that, for $D = 2\times10^{-8}$ m^2/s, the diffuse layer differential capacitance C_s^{EIS} was independent of frequency for $f \leq 10^5$ Hz for both electrolyte concentrations considered. Then, it decreased with increasing frequency beyond 10^5 Hz. Similarly, for smaller diffusion coefficients $D = 2\times10^{-9}$ and 2×10^{-10} m^2/s, C_s^{EIS} was independent of frequency for $f \leq 10^4$ and 10^3 Hz, respectively. Below these frequencies, C_s^{EIS} was independent of diffusion coefficient and was identical to the theoretical diffuse layer differential capacitance given by Equation (7.8b) with $\nu_p = 0$. This suggests that ion transport by diffusion becomes a limiting factor in charge storage for frequencies larger than a critical frequency which depends on the ion diffusion coefficient D.

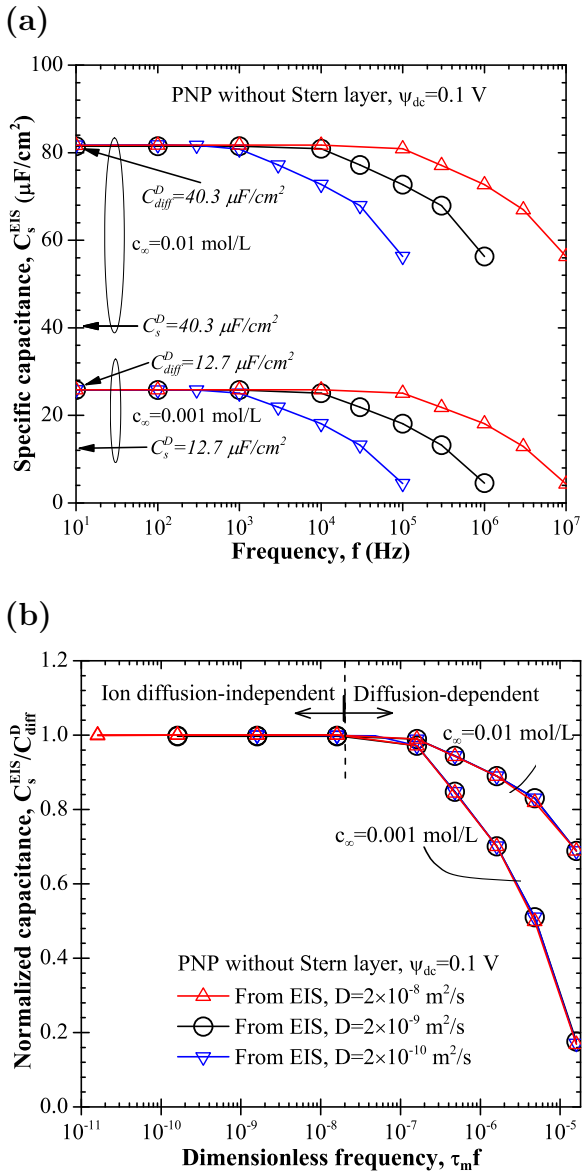

Figure 7.2: (a) Differential capacitance determined from EIS simulations as a function of frequency f and (b) normalized differential capacitance C_s^{EIS}/C_{diff}^D as a function of dimensionless frequency $\tau_m f$ for different values of ion diffusion coefficient. Results were obtained by numerically solving the classical PNP model without Stern layer ($H = 0$ nm) for $c_\infty = 0.001$ or 0.01 mol/L and $\psi_{dc} = 0.1$ V. The theoretical diffuse layer integral and differential capacitances, denoted by C_s^D and C_{diff}^D [Equations (7.6b) and (7.8b)], are also shown.

Figure 7.2(a) also shows the the theoretical equilibrium diffuse layer integral capacitance C_s^D given by Equation (7.6b) with $\nu_p = 0$ for $c_\infty = 0.001$ and 0.01 mol/L and equals to 12.7 μF/cm^2 and 40.3 μF/cm^2, respectively. It is evident that the equilibrium diffuse layer differential capacitance C_{diff}^D was larger than the integral capacitance C_s^D [Equation (7.6b)] by about 100%.

As opposed to a dielectric capacitor, the electric double layer capacitance of porous electrodes is known to depend on frequency. The origin of this so-called "capacitance dispersion" of electrode materials [11, 302, 303, 327–330] has been attributed to various phenomena such as surface inhomogeneity (e.g., defect) [330], surface roughness [11, 327–329], pore size distribution in porous electrodes [302, 303], as well as specific ion adsorption [11, 329], to name a few. However, Figure 7.2(a) demonstrates that electric double layers feature capacitance dispersion at high frequencies even for perfectly planar electrodes when only electrostatic phenomena were accounted for. Similar trend was observed in Refs. [287–290] based on the exact solution of the linearized PNP model without Stern layer and assuming zero DC potential. Then, Figure 7.2(a) establishes that, besides the above-mentioned mechanisms, the capacitance dispersion can be also attributed to the fact that, at high frequencies, ion transport cannot follow the rapid variations in the electric potential.

Moreover, Figure 7.2(b) plots the normalized differential capacitance C_s^{EIS}/C_{diff}^D as a function of dimensionless frequency $\tau_m f$ where τ_m is the characteristic diffusion time scale defined as

$$\tau_m = \lambda_m^2/D \quad \text{with} \quad \lambda_m = (\epsilon_0 \epsilon_r k_B T/2e^2 z^2 N_A c_m)^{1/2} \tag{7.10}$$

Here, λ_m is analogous to the Debye length λ_D defined based on the maximum concentration c_m instead of the bulk electrolyte concentration c_∞. The data of C_s^{EIS} and C_{diff}^D were the same as those shown in Figure 7.2. Note that the traditional diffusion characteristic time is typically defined as $\tau_L = L^2/D$ [128] where the

characteristic length is the computational domain length L. Here, τ_L was not the proper characteristic time since the predicted C_s^{EIS} at low frequency was found to be independent of L as previously discussed. In addition, Figure 7.2(b) shows that the critical frequency below which C_s^{EIS} is constant was independent of electrolyte concentration c_∞. Then, time scales involving c_∞ are also inadequate including the characteristic time for charge relaxation defined as $\tau_D = \lambda_D^2/D$ [128]. Figure 7.2(b) demonstrates that the predicted C_s^{EIS}/C_{diff}^D versus $\tau_m f$ curves for three different diffusion coefficients overlapped for each value of electrolyte concentration considered. Moreover, two region can be identified in Figure 7.2(b). First, for $\tau_m f < 2 \times 10^{-8}$, ion transport is fast enough to follow the variation in the electric potential $\psi_s(t)$ and thus the differential capacitance C_s^{EIS} is independent of frequency. In these cases, C_s^{EIS}/C_{diff}^D was equal to 1.0 regardless of the electrolyte concentration c_∞. Second, for $\tau_m f > 2 \times 10^{-8}$, ion transport was the limiting phenomenon for charge storage and C_s^{EIS} decreased with increasing frequency.

To better understand these results, Figures 7.3(a) and 7.3(b) show the imposed surface potential $\psi_s(t)$ and the resulting instantaneous surface charge density $q_s(t) = \epsilon_0 \epsilon_r E_s(t)$ as a function of dimensionless time $t \times f$ ranging from 0 to 10 at two different frequencies, i.e., $f = 10$ and 10^5 Hz. The electrolyte concentration was $c_\infty = 0.01$ mol/L and the diffusion coefficient was taken as $D = 2 \times 10^{-8}$, 2×10^{-9}, or 2×10^{-10} m^2/s. The model and other parameters were identical to those used to generate Figure 7.2. Note that the origin of time t was shifted to the time when $q_s(t)$ reached its stationary periodic oscillations. Figure 7.3(a) shows that the instantaneous surface charge density $q_s(t)$ was nearly in phase with the imposed surface potential $\psi_s(t)$ at $f = 10$ Hz. At this frequency, the diffusion coefficient had no effect on the predicted $q_s(t)$ and the plots overlap for $D = 2 \times 10^{-8}$ to 2×10^{-10} m^2/s. In addition, Figure 7.3(b) shows $q_s(t)$ and $\psi_s(t)$ at high frequency $f = 10^5$ Hz. It is evident that $q_s(t)$ and $\psi_s(t)$ were nearly in phase with each other for $D = 2 \times 10^{-8}$ m^2/s. However, they were not in phase for

small values of D. The phase depended on the diffusion coefficient. In addition, the amplitude of $q_s(t)$ increased with increasing diffusion coefficient and decreased with increasing frequency.

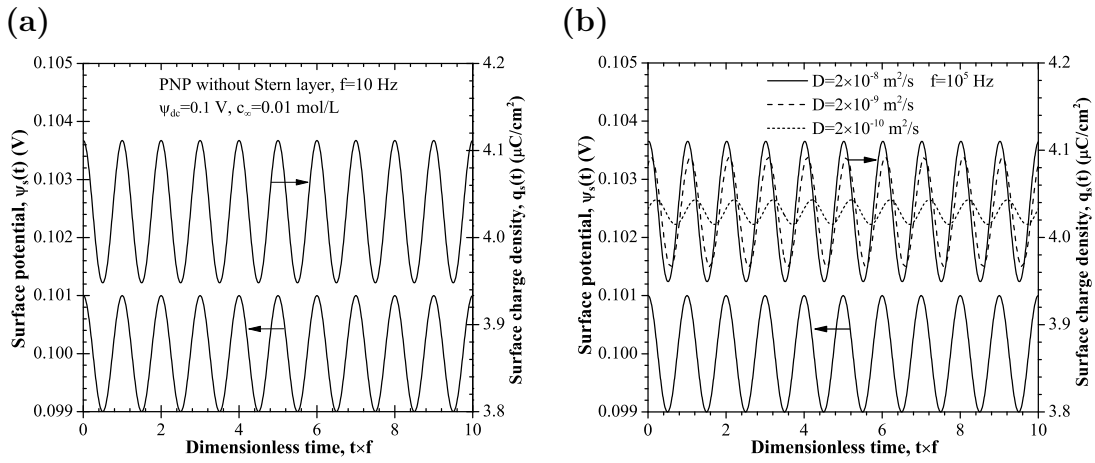

Figure 7.3: Imposed surface potential $\psi_s(t)$ and predicted instantaneous surface charge density $q_s(t)$ as a function of dimensionless time $t \times f$ for (a) $f = 10$ Hz and (b) $f = 10^5$ Hz obtained by numerically solving the classical PNP model without Stern layer. The electrolyte concentration was $c_\infty = 0.01$ mol/L while $\psi_{dc} = 0.1$ V and $D = 2 \times 10^{-8}$, 2×10^{-9}, and 2×10^{-10} m^2/s.

Furthermore, Figure 7.4(a) shows the predicted phase angle φ between the instantaneous charge density $q_s(t)$ and the imposed surface potential $\psi_s(t)$ for the same frequency range and parameters as those used to generate Figure 7.2. Figure 7.4(a) shows that the phase angle φ was nearly zero at low frequency and increased rapidly beyond a critical frequency. In addition, for a given frequency f, the phase angle decreased with increasing diffusion coefficient D thanks to faster ion transport. It also decreased with increasing electrolyte concentration due to decreasing electrolyte resistance to ionic current [311, 322].

Finally, Figure 7.4(b) plots the phase angle shown in Figure 7.4(a) as a function of the dimensionless frequency $\tau_m f$. Here also, the plots of phase angle φ versus $\tau_m f$ for different values of diffusion coefficient D collapsed on one line for each

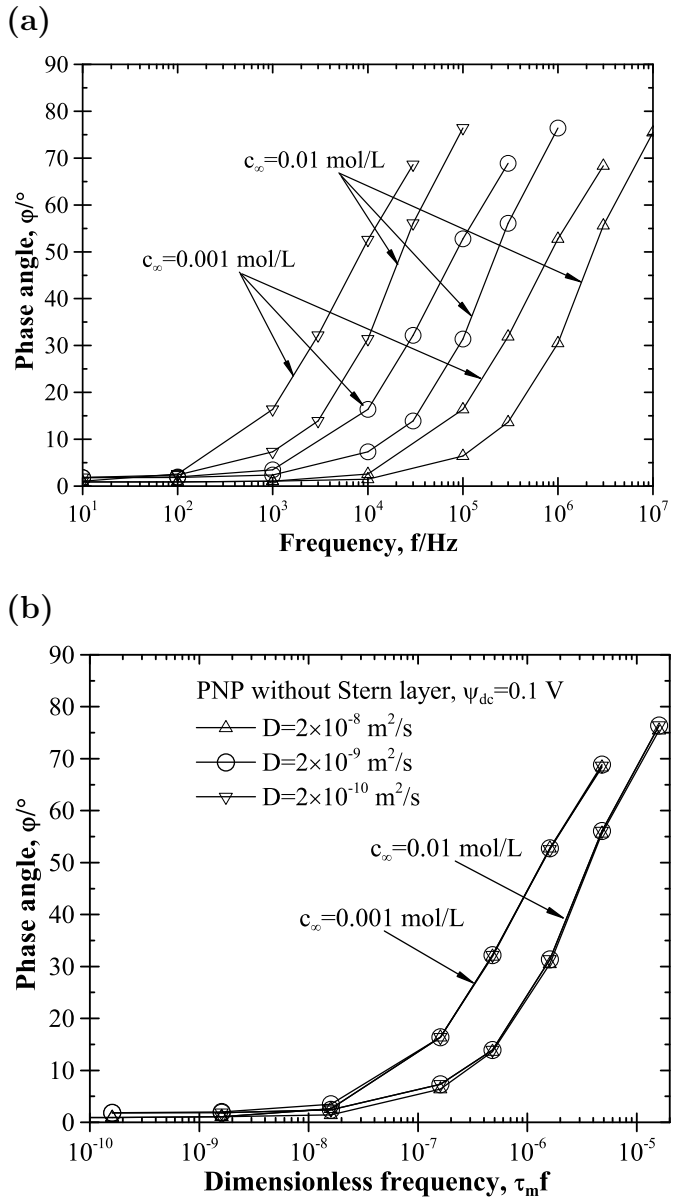

Figure 7.4: Predicted phase angle φ between the instantaneous surface charge density $q_s(t)$ and the imposed surface potential $\psi_s(t)$ as a function of (a) frequency f and (b) dimensionless frequency $\tau_m f$. Results were obtained by numerically solving the classical PNP model without Stern layer with $c_\infty = 0.001$ or 0.01 mol/L, $\psi_{dc} = 0.1$ V for $D = 2 \times 10^{-8}$, 2×10^{-9}, and 2×10^{-10} m^2/s.

concentration considered. This confirms that τ_m is the characteristic time for ion diffusion in electric double layer during EIS measurements. Note also that

the phase angle of the impedance $\phi(f)$ in Equation (7.2) was related to $\varphi(f)$ by $\phi(f) = \varphi(f) - 90^\circ$ (not shown).

7.4.1.2 Predictions By PNP Model With Stern Layer

Figure 7.5 shows the differential capacitance C_s^{EIS} retrieved from EIS [Equation (7.3)] as a function of dimensionless frequency $\tau_m f$ ranging from 10^{-10} to 2×10^{-4} as well as the theoretical equilibrium differential C_{diff} and integral C_s capacitances [Equations (7.7) and (7.8)]. Results were obtained by solving the PNP model accounting for a Stern layer of thickness $H = a/2 = 0.33$ nm. The electrolyte concentration was set to be $c_\infty = 0.01$ and 0.001 mol/L, $\psi_{dc} = 0.1$ V while $D = 2 \times 10^{-8}$, 2×10^{-9}, and 2×10^{-10} m^2/s.

The trend of the differential capacitance C_s^{EIS} as a function of $\tau_m f$ was similar to the predictions of PNP model without Stern layer shown in Figure 7.2(b). However, the critical dimensionless frequency $\tau_m f$ was larger and equal to 10^{-7} when accounting for the Stern layer. Note also that the equilibrium double layer differential capacitance C_{diff} was larger than the corresponding integral capacitance C_s by $60\% - 80\%$ for different values of c_∞ instead of 100% when the Stern layer was not accounted for [Figure 7.2].

7.4.2 EIS in Concentrated Electrolyte Solutions

Figure 7.6 shows the numerically predicted differential capacitance C_s^{EIS} retrieved from EIS [Equation (7.3)] as a function of dimensionless frequency $\tau_m f$ ranging from 10^{-9} to 2×10^{-2}. The results were obtained by solving the MPNP model with a Stern layer [Equations (7.4) and (7.5)] for $H = a/2 = 0.33$ nm, $c_\infty = 1$ mol/L, $\psi_{dc} = 0.3$ V, and three values of $D = 2 \times 10^{-8}$, 2×10^{-9}, and 2×10^{-10} m^2/s. Figure 7.6 also shows the corresponding theoretical equilibrium differential C_{diff} and integral C_s capacitances [Equations (7.7) and (7.8)]. Here, the Stern layer and diffuse

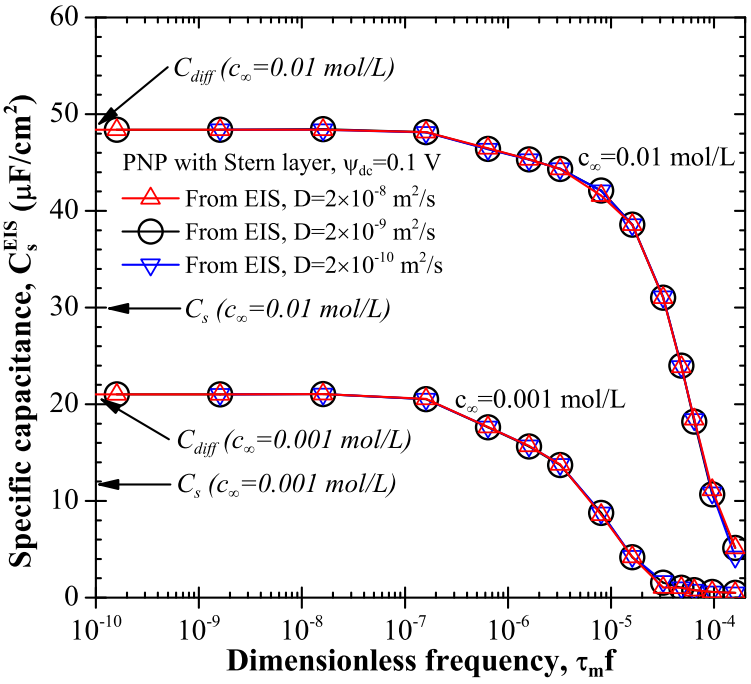

Figure 7.5: Predicted differential capacitance C_s^{EIS} determined from EIS [Equation (7.3)] as a function of dimensionless frequency $\tau_m f$. Results were obtained by numerically solving the classical PNP model with Stern layer along with the theoretical differential C_{diff} and integral C_s capacitances [Equations (7.7) and (7.8)] with $c_\infty = 0.01$ and 0.001 mol/L, $H = a/2 = 0.33$ nm, $\psi_{dc} = 0.1$ V, and $D = 2 \times 10^{-8}$, 2×10^{-9}, and 2×10^{-10} m^2/s.

layer integral capacitances predicted by Equation (7.6) were $C_s^{St} = 210.6$ μF/cm^2 and $C_s^{D} = 186.1$ μF/cm^2, respectively, resulting in $C_s = 98.8$ μF/cm^2. Figure 7.6 indicates that the differential capacitance C_s^{EIS} for $c_\infty = 1$ mol/L was constant and was identical to the theoretical value [Equation (7.8)] for dimensionless frequency $\tau_m f$ less than 36.4×10^{-4} corresponding to $f = 4 \times 10^7$ Hz. This value should be compared with $\tau_m f = 10^{-7}$ for electrolyte concentrations $c_\infty = 0.01$ and 0.001 mol/L (Figure 7.5). The difference can be attributed to the fact that the electrolyte resistance to ionic current decreases significantly as the electrolyte concentration increases and ion transport to and away from the electrode becomes

limiting only at very large frequencies. Thus, at high concentrations, ions can respond nearly instantaneously to the rapid variation in electric potential $\psi_s(t)$. Figure 7.6 also demonstrates that the differential capacitance decreased sharply for dimensionless frequency $\tau_m f$ larger than 6.4×10^{-4}. It is expected to decrease at much smaller frequencies when simulating the electrode and accounting for its electrical resistance. This was observed in the capacitance versus scan rate curves retrieved in the simulations of cyclic voltammetry in EDLCs [149]. Overall, the characteristic time τ_m given by Equation (7.10) is the proper characteristic time scale for low and high concentrations using PNP or MPNP model with or without Stern layer. Finally, Figure 7.6 indicates that equilibrium differential double layer capacitance was smaller than the corresponding integral capacitance by about 20% for $c_\infty = 1$ mol/L and $\psi_{dc} = 0.3$ V.

7.4.3 Relative Difference Between Differential and Integral Capacitances

The previous sections established that the double layer differential capacitance was larger than its integral capacitance under low electrolyte concentration (Figures 7.2 and 7.5) while it was smaller than the integral capacitance under large electrolyte concentration and electric potential (Figure 7.6).

In order to quantify the relative difference between the double layer differential and integral capacitances, the relative error was defined as $\delta = \left|(C_s^{EIS} - C_s)/C_s\right|$ where C_s is the total double layer integral capacitance [Equation (7.7)] and C_s^{EIS} is the differential capacitance retrieved by EIS using Equation (7.3) at low frequency in the diffusion-independent regime.

Figure 7.7 shows the computed relative error δ as a function of DC potential ψ_{dc} ranging from 0.01 to 0.5 V. Predictions of C_s^{EIS} for $\psi_{dc} \leq 0.1$ V and $c_\infty = 0.01$ mol/L were obtained by numerically solving the PNP model with or without a

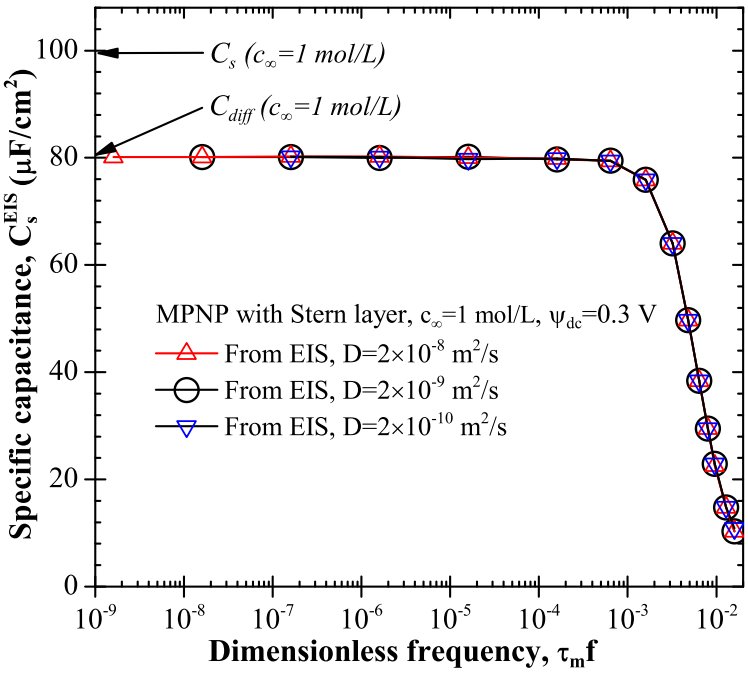

Figure 7.6: Predicted differential capacitance C_s^{EIS} determined from EIS [Equation (7.3)] as a function of dimensionless frequency $\tau_m f$. Results were obtained by numerically solving the MPNP model with Stern layer along with the theoretical equilibrium differential C_{diff} and integral C_s capacitance [Equations (7.7) and (7.8)] with $H = a/2 = 0.33$ nm, $c_\infty = 1$ mol/L, $\psi_{dc} = 0.3$ V, and $D = 2 \times 10^{-8}$, 2×10^{-9}, and 2×10^{-10} m^2/s.

Stern layer for frequency $f = 10$ Hz. Predictions of C_s^{EIS} for $\psi_{dc} > 0.1$ V and $c_\infty = 1$ mol/L were obtained by solving the MPNP model with a Stern layer for frequency $f = 10^3$ Hz. It is evident that the relative error increased with increasing DC potential for any model considered. For cases with low DC potential and low concentration based on the PNP model, the relative error was smaller when accounting for the Stern layer. However, it grows rapidly from less than 5% for $\psi_{dc} = 0.01$ V to more than 60% for $\psi_{dc} = 0.1$ V. For concentration $c_\infty = 1$ mol/L and $\psi_{dc} > 0.1$ V, which are typical of EDLCs, the double layer differential capacitance was smaller than the integral capacitance. In fact, the relative error increased from 0.2% to 45% as the DC potential increased from 0.05 to 0.5 V.

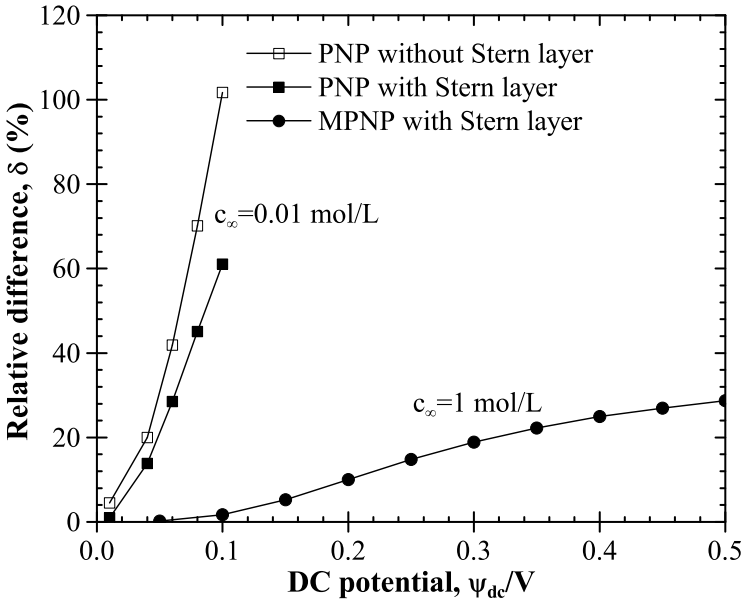

Figure 7.7: Relative error between equilibrium double layer differential capacitance C_s^{EIS} and integral capacitance C_s as a function of DC potential obtained by solving (i) the classical PNP model with or without a Stern layer for $c_\infty = 0.01$ mol/L and (ii) the MPNP model with the Stern layer for $c_\infty = 1$ mol/L with $H = a/2 = 0.33$ nm and $D = 2 \times 10^{-9}$ m^2/s.

Overall, Figure 7.7 indicates that the double layer differential capacitance differed from the integral capacitance unless at very low DC potential. Note that the electric potential window is typically larger than 1 V for actual EDLCs. Therefore, the differential and integral capacitances should be discriminated when comparing the EDLC capacitances measured using EIS, CV, and galvanostatic techniques. We expect that the confusion between C_{diff} and C_{int} could explain some of the reported discrepancies between EIS and CV or galvanostatic charge/discharge measurements of the capacitances of supercapacitors [43, 78, 79, 285, 286, 293, 294].

7.5 Conclusions

This chapter presented numerical simulations of electrochemical impedance spectroscopy measurements for determining the electric double layer capacitance near a planar electrode in aqueous electrolyte solutions. The double layer dynamics was simulated using (i) the PNP model with or without Stern layer for low electrolyte concentrations and electric potential, and (ii) the MPNP model with a Stern layer for large electrolyte concentration and electric potential.

For a given value of electrolyte concentration c_∞, the predicted C_s^{EIS} and impedance phase shift φ plotted versus $\tau_m f$ for various values of ion diffusion coefficient overlapped on a single line for all models considered. Here, the ion diffusion characteristic time was defined as $\tau_m = \lambda_m^2/D$ using the Debye length $\lambda_m = (\epsilon_0 \epsilon_r k_B T/2e^2 z^2 N_A c_m)^{1/2}$ based on the maximum ion concentration c_m. The electric double layer capacitance was found to be constant for dimensionless frequency $\tau_m f$ less than a critical value depending on the electrolyte concentration. However, electric double layers featured an intrinsic "capacitance dispersion" at high frequencies. This was attributed to the fact that ion transport could not follow the fast variation in electric potential.

The double layer differential capacitance differed significantly from its integral capacitance for DC potential larger than 0.5 V, typical of potential window in practical EDLCs. Therefore, the differential and integral capacitances should always be explicitly discriminated when reporting the capacitances of EDLCs measured using different techniques.

CHAPTER 8

Physical Interpretation of Cyclic Voltammetry for EDLCs

The previous chapter reported physical modeling and simulations of electrochemical impedance spectroscopy for measuring the differential capacitance of EDLCs. Cyclic voltammetry is another experimental technique widely used to characterize the performance of supercapacitors. The chapter presents physical modeling and interpretation of cyclic voltammetry for measuring the integral capacitance of EDLCs.

8.1 Introduction

Cyclic voltammetry (CV) is a powerful tool in the field of electrochemistry [9, 331]. It has been used extensively to characterize the performance of various electrical energy storage devices such as electrochemical capacitors (also known as supercapacitors) [10, 31, 40], batteries [332, 333], and fuel cells [334, 335]. In these applications, the charged electrodes are typically immersed in the electrolyte solution. Electric double layers form at the electrode/electrolyte interfaces which are accessible to ions present in the electrolyte. Figure 8.1 shows a schematic of the electric double layer structure consisting of the Stern and diffuse layers forming near the surface of a positively charged electrode. Figure 8.1b shows the electric circuit representation of an electric double layer capacitance including the electrode resistance, the Stern layer and diffuse layer capacitances in series [8–10, 36].

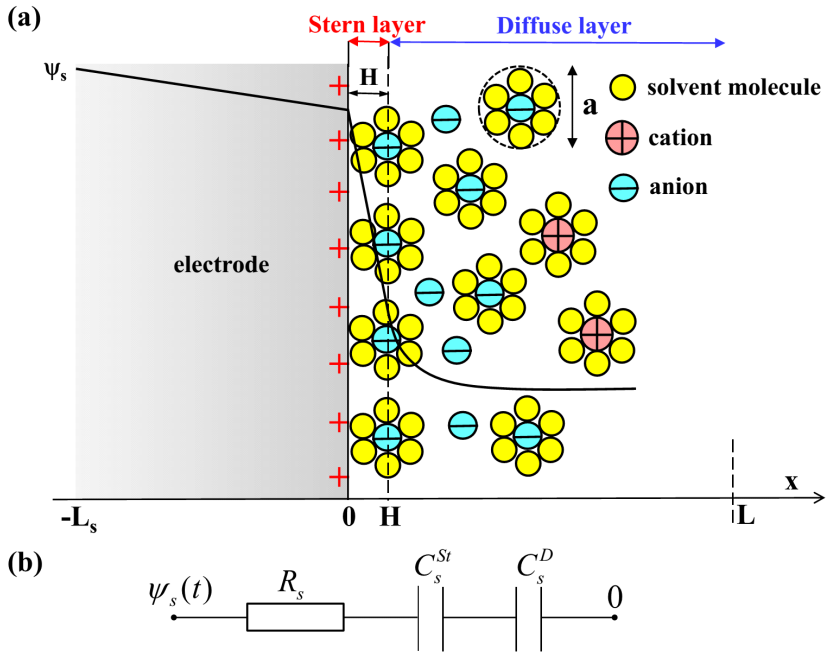

Figure 8.1: Schematic of (a) the electric double layer structure showing the arrangement of solvated anions and cations near an electrode/electrolyte interface and the simulated computational domain consisting of a Stern layer and the diffuse layer and (b) the electrode resistance along with the Stern and diffuse layer capacitances in series [8–10].

CV measurements consist of imposing an electric potential at the electrodes which varies periodically and linearly with time [9, 331]. The resulting electric current is recorded. The total charge accumulated at the electrode surface can be found by integrating the electric current with respect to time [10, 75, 120, 266, 336]. Then, the capacitance can be estimated as the total charge divided by the "potential window" [10, 75, 266, 336, 337]. Capacitance is typically measured at different scan rates to characterize the performance of energy storage devices such as electric double layer capacitors (EDLCs). The capacitance measured at low scan rates is maximum and close to the capacitance under equilibrium conditions.

Moreover, the shape of CV curves has been used extensively to deduce the electrochemical processes involved in the charging and discharging of EDLCs

[39, 209, 338–340]. For example, the current initially increases when charging EDLCs from zero potential. Then, it decreases upon further increase in the electric potential. Thus, a "hump" is typically observed in the CV curves. Different interpretations have been proposed in the literature to explain this observation. For example, Pell *et al.* [341] investigated the effect of the electrolyte concentration on the charging/discharging of EDLCs. The electrode was carbon foil formed using carbon powders while the electrolyte was tetraethylammonium tetrafluoroborate (TEATFB) in propylene carbonate with concentration ranging from 0.08 to 1 mol/L. The authors observed a hump in CV curves at low electrolyte concentration of 0.08 mol/L which was absent at larger ones. Consequently, the authors attributed its reason to the "*electrolyte starvation*" due to limited amount of ions at low concentrations. The same interpretation was suggested for EDLCs with both aqueous (H_2SO_4) and organic ($TEABF_4$) electrolytes with 1 mol/L concentration [342]. Moreover, the hump was also attributed to redox reactions at the electrode surface [40, 295, 343–351] as well as the "*difference of diffusion capability between solvated anions and cations in the electrolyte*" [349]. Recently, Mysyk *et al.* [352, 353] experimentally investigated this effect for EDLCs with electrodes made of pitch-derived and viscose-based carbons in both aqueous and organic electrolytes. The authors systematically measured the CV curves for these carbon electrodes featuring different specific surface area and pore size. They observed the hump for carbon electrodes with small pore size in electrolytes with large ion size. Thus, they speculated that the "*available active surface becomes fully saturated with ions*" before reaching the maximum potential. Then, the current began to decrease even as the potential further increased. However, there is still no clear and definitive explanations to this observed phenomenon. In addition, to the best of our knowledge, no studies have attempted to elucidate this question using physics-based numerical simulations.

This chapter aims to develop a model for simulating electric double layer ca-

pacitors by accounting for transport phenomena in both the electrode and the electrolyte under large potential and with concentrated electrolyte solutions. It also aims to provide physical interpretations of CV measurements used to determine electric double layer capacitance.

8.2 Background

8.2.1 Cyclic Voltammetry

In CV measurements, the surface potential ψ_s is imposed to vary periodically and linearly with time t as,

$$\psi_s(t) = \begin{cases} \psi_{max} - v[t - 2(m-1)\tau_{CV}] & \text{for} \quad 2(m-1)\tau_{CV} \leq t < (2m-1)\tau_{CV} \quad (8.1a) \\ \psi_{min} + v[t - (2m-1)\tau_{CV}] & \text{for} \quad (2m-1)\tau_{CV} \leq t < 2m\tau_{CV} \quad (8.1b) \end{cases}$$

where v is the scan rate in V/s, $m(= 1,\ 2,\ 3, ...)$ is the cycle number, and $\tau_{CV} = (\psi_{max} - \psi_{min})/v$ is half the cycle period. The latter represents the time for varying the surface potential from its maximum ψ_{max} to its minimum ψ_{min} values or versa vice. Here, $\psi_{max} - \psi_{min}$ is referred to as the "potential window". Note that the measurements are referred to as "linear sweep voltammetry" when $\psi_s(t) = \psi_{min} + vt$ or $\psi_s(t) = \psi_{max} - vt$.

The results of CV measurements are typically plotted in terms of current or current density versus surface potential, referred to as "CV curves". The surface charge density q_s accumulated at the electrode surface during one cycle can be estimated by computing the area enclosed by the CV curves [10, 75, 149, 266, 336, 337]. Then, the areal integral capacitance C_s (in F/m^2) can be computed from CV measurements as [10, 75, 149, 266, 336, 337],

$$C_s = \frac{q_s}{\psi_{max} - \psi_{min}} = \frac{1}{\psi_{max} - \psi_{min}} \oint \frac{j_s}{2v} d\psi_s \quad (8.2)$$

where j_s is the surface current density (in A/m^2).

8.2.2 Numerical Simulations of Cyclic Voltammetry

Numerous studies have simulated CV measurements of electric double layers. These simulations were based on either equivalent RC circuit models [120, 121, 123, 126] or the classical Poisson-Nernst-Planck (PNP) model assuming point-charges [331, 354–356]. However, these models suffer from severe limitations and thus invalid for practical EDLCs as discussed in Chapter 2. Moreover, the effects of electrodes were typically neglected in simulating CV measurements using the PNP model [331, 354, 355]. However, studies have demonstrated that the electrode electrical conductivity significantly affected the charging performance of EDLCs [32, 34, 357–359].

Efforts have been made in recent literature to account for the effect of finite ion size in modeling ion transport in concentrated electrolyte solutions under large electric potential [95, 130, 146]. For example, Kilic *et al.* [146] derived a modified Poisson-Nernst-Planck (MPNP) model valid for binary and symmetric electrolytes under large electrolyte concentration and electric potential as discussed in Chapter 2. However, to the best of our knowledge, no studies have simulated CV measurements for electric double layers under large electrolyte concentrations and electric potential other than by using RC circuit models [120, 121, 123, 126, 331, 354, 355]. Given the limitations of the latter, it is important to develop a model that can simulate CV measurements under practical conditions and account for the presence of the electrode in simulating the charging/discharging of EDLCs. This model will be useful to identify the important parameters affecting the performance of EDLCs and to elucidate the electrochemical processes involved.

This chapter aims to develop a model for simulating the electric double layer dynamics in CV measurements while simultaneously accounting for transport phenomena in both the electrode and the electrolyte. It also aims (i) to identify the dimensionless parameters that govern the CV measurements, (ii) to provide a

physical interpretation of the shape of CV curves, and (iii) to investigate the effect of the electrode electrical conductivity on the predicted double layer capacitance. The dynamics of the electric double layer forming near a planar electrode in aqueous electrolyte solutions during CV measurements was simulated as a function of scan rate. A MPNP model with a Stern layer [95,130,146] was used while simultaneously accounting for the electrode. The results were compared with analytical expressions for the capacitances under equilibrium conditions.

8.3 Analysis

8.3.1 Schematics and Assumptions

Figure 8.1 shows the schematic of the computational domain used to simulate a planar electrode of thickness L_s immersed in an electrolyte solution. The region of electrolyte solution consists of two layers corresponding to (1) a Stern layer of thickness H near the electrode surface and (2) a diffuse layer beyond. A time-dependent electric potential $\psi_s(t)$ was prescribed at the electrode surface ($x = -L_s$) and was zero far away from the electrode surface ($x = L$). The electrode thickness L_s and the length of the electrolyte domain were specified to be $L_s = 0$ or 100 nm and $L = 80$ nm, respectively. Here, the length L corresponded to half of the distance between the anode and the cathode. For binary and symmetric electrolytes, both the electric potential and the electrolyte concentration remained unchanged at the middle plane ($x = L$) when L was much larger than the double layer thickness [128, 291, 316, 360]. Thus, it sufficed to simulate only half of the domain by imposing zero electric potential and bulk electrolyte concentration c_∞ at $x = L$. In addition, the electric double layer thickness decreases with increasing electrolyte concentration [8,9,35,36,95,146]. Increasing the value of L by a factor of two was found to have no effect (i) on the predicted specific capacitance under equilibrium conditions and (ii) on the capacitance C_s and j_C versus ψ_s curves

retrieved from CV simulations at low scan rates defined by Equations (8.2) and (8.17), respectively. However, the values of C_s predicted at large scan rates were found to decrease with increasing L. In addition, the j_C versus ψ_s curves predicted at large scan rates became more asymmetric as L increased as discussed in Section 8.4.4. These can be attributed to the fact that the charge storage took longer as it could not follow the fast variation in the electric potential under large scan rates when the electrolyte domain length L increased [128, 149, 360].

To make the problem mathematically tractable, the following assumptions were made: (1) anions and cations had the same effective diameter and diffusion coefficient which were assumed to be constant and independent of electrolyte concentration [95, 146, 200], (2) the electrolyte dielectric permittivity was constant and equals to that of water, (3) isothermal conditions prevailed throughout the electrode and electrolyte, (4) advection of the electrolyte was assumed to be negligible, (5) the ions could only accumulate at the electrode surface and could not diffuse into the electrode, i.e., there was no ion insertion, and (6) the specific ion adsorption due to non-electrostatic forces were assumed to be negligible.

8.3.2 Mathematical Formulation

The local electric potential $\psi(x,t)$ in the electrode was governed by the Poisson equation expressed as [361–365],

$$\frac{\partial}{\partial x}\left(\sigma_s \frac{\partial \psi}{\partial x}\right) = 0 \quad \text{for} \quad -L_s \leq x < 0 \tag{8.3}$$

where σ_s is the electrical conductivity of the electrode material expressed in S/m. Moreover, the local electric potential $\psi(x,t)$ and ion concentrations $c_i(x,t)$ at time t and location x in the electrolyte solution were computed by solving the MPNP model with a Stern layer for large electrolyte concentration [95, 130, 146, 149]. For binary and symmetric electrolytes, the valency is such that $z_1 = -z_2 = z$ and the bulk ion concentration is given by $c_{1\infty} = c_{2\infty} = c_\infty$. Then, assuming identical

diffusion coefficient $D_1 = D_2 = D$, the MPNP model with Stern layer can be written as [95, 130, 146, 149],

$$\frac{\partial}{\partial x}\left(\epsilon_0\epsilon_r\frac{\partial \psi}{\partial x}\right) = \begin{cases} 0 & \text{for } 0 \le x < H \quad (8.4a) \\ -eN_A z(c_1 - c_2) & \text{for } H \le x \le L \quad (8.4b) \end{cases}$$

$$\frac{\partial c_i}{\partial t} = \frac{\partial}{\partial x}\left(D\frac{\partial c_i}{\partial x} + \frac{z_i D}{R_u T}Fc_i\frac{\partial \psi}{\partial x} + \frac{\nu_p D c_i}{2c_\infty - \nu_p(c_1+c_2)}\frac{\partial (c_1+c_2)}{\partial x}\right) \quad \text{for } H \le x \le L \quad (8.4c)$$

where $c_i(x,t)$ is the local molar concentration of ion species "i" ($i = 1,\ 2$) while ϵ_0 and ϵ_r are the free space permittivity ($\epsilon_0 = 8.854 \times 10^{-12}$ F/m) and the relative permittivity of the electrolyte solution, respectively. The absolute temperature is denoted by T, e is the elementary charge ($e = 1.602 \times 10^{-19}$ C), N_A is the Avogadro's number ($N_A = 6.022 \times 10^{23}$ mol^{-1}) while F and R_u are the Faraday constant ($F = eN_A$ sA/mol) and the universal gas constant ($R_u = 8.314$ JK^{-1}mol^{-1}), respectively. The packing parameter is defined as $\nu_p = 2a^3 N_A c_\infty$ where a is the effective ion diameter. It represents the ratio of the total bulk ion concentration to the maximum ion concentration $c_{max} = 1/N_A a^3$ assuming a simple cubic ion packing [4, 95, 130]. Therefore, ν_p should not be larger than unity for the model to be physically acceptable [4, 95, 130]. Equations (8.4b) and (8.4c) reduce to the classical Poisson-Nernst-Planck model when $\nu_p = 0$ [95, 130, 146]. Note that in Refs. [95, 130, 146], the Stern layer was accounted for via a boundary condition relating the potential drop across the Stern layer and the potential gradient at the Stern/diffuse layer interface. Here, the electric potential in the Stern layer was solved explicitly. In fact, these two approaches are equivalent for planar electrodes [130, 146, 149, 228].

Moreover, the surface electric potential $\psi_s(t)$ expressed by Equation (8.1) was imposed, i.e.,

$$\psi = \psi_s(t), \text{ at } x = -L_s \quad (8.5a)$$

The electric potential and current density were continuous across the electrode/electrolyte interface located at $x = 0$ nm so that [366],

$$\psi\big|_{x=0^-} = \psi\big|_{x=0^+} \quad \text{and} \quad -\sigma_s \frac{\partial \psi}{\partial x}\bigg|_{x=0^-} = -\epsilon_0 \epsilon_r \frac{\partial^2 \psi}{\partial x \partial t}\bigg|_{x=0^+} \tag{8.5b}$$

Similarly, the electric potential and displacement were continuous across the Stern/diffuse layer interface located at $x = H$ [8, 90, 149],

$$\psi\big|_{x=H^-} = \psi\big|_{x=H^+} \quad \text{and} \quad \epsilon_0 \epsilon_r \frac{d\psi}{dx}\bigg|_{x=H^-} = \epsilon_0 \epsilon_r \frac{d\psi}{dx}\bigg|_{x=H^+} \tag{8.5c}$$

In addition, the mass flux vanishes for both ion species at the electrode surface since there is no ion insertion [assumption (6)] so that [95, 130, 146, 149],

$$D\frac{\partial c_i}{\partial x} + \frac{z_i D}{R_u T} F c_i \frac{\partial \psi}{\partial x} + \frac{\nu_p D c_i}{2c_\infty - \nu_p (c_1 + c_2)} \frac{\partial (c_1 + c_2)}{\partial x} = 0, \text{ at } x = H \tag{8.5d}$$

Far away from the electrode surface, the electric potential and ion concentration are such that,

$$\psi(x = L, t) = 0 \quad \text{and} \quad c_i(x = L, t) = c_\infty \tag{8.5e}$$

Finally, the initial condition are given by,

$$\psi(-L_s \leq x \leq L, t = 0) = 0 \quad \text{and} \quad c_i(0 \leq x \leq L, t = 0) = c_\infty \tag{8.5f}$$

Note that, when $L_s = 0$ nm, Equations (8.3) to (8.5) correspond to simulations without accounting for the presence of the electrode.

8.3.3 Dimensional Analysis

The following scaling parameters were introduced to make the formulation dimensionless,

$$x^* = \frac{x}{\lambda_D}, \quad t^* = \frac{tD}{\lambda_D^2}, \quad \psi^* = \frac{\psi}{R_u T / zF}, \quad \text{and} \quad c_i^* = \frac{c_i}{c_\infty} \tag{8.6}$$

Then, the governing Equations (8.3) to (8.5) were transformed into dimensionless form as,

$$\frac{\partial^2 \psi^*}{\partial x^{*2}} = 0 \quad \text{for } -L_s/\lambda_D \leq x^* < 0 \tag{8.7a}$$

$$\frac{\partial^2 \psi^*}{\partial x^{*2}} = \begin{cases} 0 & \text{for } \ 0 \leq x^* < H/\lambda_D = a/2\lambda_D \quad (8.7b) \\ -\frac{1}{2}(c_1^* - c_2^*) & \text{for } \ a/2\lambda_D = H/\lambda_D \leq x^* \leq L/\lambda_D \quad (8.7c) \end{cases}$$

$$\frac{\partial c_i^*}{\partial t^*} = \frac{\partial}{\partial x^*}\left(\frac{\partial c_i^*}{\partial x^*} + \mathrm{sgn}(z_i) c_i \frac{\partial \psi^*}{\partial x^*} + \frac{\nu_p c_i^*}{2 - \nu_p(c_1^* + c_2^*)} \frac{\partial (c_1^* + c_2^*)}{\partial x^*}\right) \quad \text{for } a/2\lambda_D = H/\lambda_D \leq x^* \leq L/\lambda_D \quad (8.7d)$$

where the packing parameter is defined as $\nu_p = 2c_\infty/(1/a^3 N_A)$. It represents the ratio of the total bulk ion concentration to the maximum ion concentration $1/a^3 N_A$ assuming a simple cubic packing of ions of diameter a.

The dimensionless potential $\psi_s^*(t^*)$ imposed at the electrode surface in CV measurements is given by,

$$\psi_s^*(t^*) =$$

$$\begin{cases} \psi_{max}^* - v^*[t^* - 2(m-1)\tau_{CV}^*] & \text{for } \ 2(m-1)\tau_{CV}^* \leq t^* \leq (2m-1)\tau_{CV}^* \quad (8.8a) \\ \psi_{min}^* + v^*[t^* - (2m-1)\tau_{CV}^*] & \text{for } \ (2m-1)\tau_{CV}^* \leq t^* \leq 2m\tau_{CV}^* \quad (8.8b) \end{cases}$$

where $\tau_{CV}^* = (\psi_{max}^* - \psi_{min}^*)/v^*$ represents the dimensionless half cycle period and $v^* = (\lambda_D^2/D)/[(R_u T/zF)/v]$ is the dimensionless scan rate. It can be interpreted as the ratio of the ion diffusion time scale (λ_D^2/D_1) and the characteristic time for reaching the thermal potential $R_u T/zF$ at scan rate v. Moreover, $\psi_{max}^* = \psi_{max}/(R_u T/zF)$ and $\psi_{min}^* = \psi_{min}/(R_u T/zF)$ are the maximum and minimum surface potentials, respectively, scaled by the thermal potential. They can be also interpreted as the ratio of characteristic times to reach ψ_{max} or ψ_{min} and the characteristic time for reaching the thermal potential at scan rate v.

The boundary conditions at the electrode/electrolyte interface located at $L^* = L/\lambda_D$ can be written in dimensionless form as,

$$\psi^*\big|_{x^*=0^-} = \psi^*\big|_{x^*=0^+} \quad \text{and} \quad \frac{\sigma_s^*}{\psi_{max}^* - \psi_{min}^*} \frac{L_s^*}{L^*} \frac{\partial \psi^*}{\partial x^*}\bigg|_{x^*=0^-} = \frac{\partial^2 \psi^*}{\partial x^* \partial t^*}\bigg|_{x^*=0^+} \quad (8.9)$$

where $L_s^* = L_s/\lambda_D$ and $L^* = L/\lambda_D$ are the electrode thickness and inter-electrode distance, respectively, scaled by the Debye length representing an estimate of the double layer thickness.

Similarly, the boundary conditions at the Stern/diffuse layer interface located at $x^* = a^*/2$ became in dimensionless form as,

$$\psi^*\big|_{x^*=(a^*/2)^-} = \psi^*\big|_{x^*=(a^*/2)^+}, \quad \left.\frac{d\psi^*}{dx^*}\right|_{x^*=(a^*/2)^-} = \left.\frac{d\psi^*}{dx^*}\right|_{x^*=(a^*/2)^+}, \quad \text{and} \tag{8.10}$$

$$\frac{\partial c_i^*}{\partial x^*} + \mathrm{sgn}(z_i) c_i \frac{\partial \psi^*}{\partial x^*} + \frac{\nu_p c_i^*}{2 - \nu_p (c_1^* + c_2^*)} \frac{\partial (c_1^* + c_2^*)}{\partial x^*} = 0, \quad \text{at } x^* = a^*/2 \tag{8.11}$$

where $a^* = a/\lambda_D$ is the effective ion diameter scaled by the Debye length.

Finally, the dimensionless boundary conditions at $x^* = L^* = L/\lambda_D$ and the initial conditions for ψ^* and c_i^* became,

$$\psi^*(x^* = L^*, t^*) = 0 \quad \text{and} \quad c_i^*(x^* = L^*, t^*) = 1, \tag{8.12}$$

$$\psi^*(-L_s^* \le x^* \le L^*, t^* = 0) = 0 \quad \text{and} \quad c_i^*(0 \le x^* \le L^*, t^* = 0) = 1 \tag{8.13}$$

Considering the dimensionless governing equations and associated boundary and initial conditions, eight key dimensionless similarity parameters can be identified for binary and symmetric electrolytes. They are expressed as,

$$v^* = \frac{\lambda_D^2/D}{(R_u T/zF)/v}, \quad \psi_{max}^* = \frac{\psi_{max}}{R_u T/zF}, \quad \psi_{min}^* = \frac{\psi_{min}}{R_u T/zF}, \quad L^* = \frac{L}{\lambda_D},$$
$$a^* = \frac{a}{\lambda_D}, \quad \nu_p = 2a^3 N_A c_\infty, \quad \sigma_s^* = \frac{\sigma_s(\psi_{max} - \psi_{min})/L_s}{Fzc_\infty D/L}, \quad \text{and} \quad L_s^* = \frac{L_s}{\lambda_D} \tag{8.14}$$

8.3.4 Constitutive Relations

In order to solve Equations (8.4) and (8.5), the electrode conductivity σ_s and electrolyte properties ϵ_r, z, c_∞, a and D along with the temperature T and the surface potential $\psi_s(t)$ are needed. The electrical conductivity of activated carbons is on the order of 10^{-6} to 10^2 S/m [357,358]. Here, the electrode electrical conductivity was taken as $\sigma_s = 10$ or 0.01 S/m. The present study focuses on aqueous electrolyte solution at room temperature so that $T = 298$ K with $\epsilon_r = 78.5$ [253]. The effective ion diameter and diffusion coefficient were taken as $a = 0.66$ nm [200] and $D = 2 \times 10^{-9}$ m^2/s [253], respectively, while the valency was $z = 1$. These values

correspond to solvated ions such as K^+ and Cl^- in aqueous solutions [200, 253]. The electrolyte concentration was chosen as $c_\infty = 1.0$ mol/L corresponding to typical values in actual EDLCs. In addition, the Stern layer thickness H was approximated as the radius of solvated ions, i.e., $H = a/2 = 0.33$ nm [9, 35, 36]. Moreover, in the surface electric potential $\psi_s(t)$ [Equation (8.1)], ψ_{max} was varied from 0.3 to 0.5 V while $\psi_{min} = 0.0$ V. The case of $\psi_{max} = 0.5$ V corresponds to a typical potential difference of 1.0 V between the anode and the cathode typical of aqueous EDLCs.

8.3.5 Method of Solution and Data Processing

The models were solved using the commercial finite element solver COMSOL 4.1. The capacitance under equilibrium conditions and the capacitance retrieved from CV simulations were computed as follows.

8.3.5.1 Capacitance Under Equilibrium Conditions

The capacitance under equilibrium conditions corresponds to the time-independent surface potential, i.e., $\psi_s(t) = \psi_{max}$. Then, the areal Stern and diffuse layer specific capacitances C_s^{St} and C_s^D are defined by dividing the surface charge density [35, 202] $q_s(x) = \epsilon_0\epsilon_r E(x)$ by their respective potential difference [9, 90, 228]. Here, $E(x) = |-d\psi/dx|$ is the norm of the local electric field. The areal capacitances C_s^{St} and C_s^D of planar electrodes assuming constant electrolyte properties and accounting for the finite ion size are given by [4, 9, 90, 95, 228],

$$C_s^{St} = \frac{\epsilon_0\epsilon_r}{H} = \frac{2\epsilon_0\epsilon_r}{a} \tag{8.15a}$$

$$C_s^D = \frac{2zeN_Ac_\infty\lambda_D}{\psi_D}\sqrt{\frac{2}{\nu_p}\log\left[1 + 2\nu_p\sinh^2\left(\frac{ze\psi_D}{2k_BT}\right)\right]} \tag{8.15b}$$

where $\psi_D = \psi(H)$ is the electric potential computed at the Stern layer/diffuse layer interface $x = H$. Here, it was obtained by solving the steady-state equilib-

rium modified Poisson-Boltzmann (MPB) model at surface potential ψ_{dc} and electrolyte concentration c_∞ [4, 95, 146, 228]. Then, the total specific capacitance C_s under equilibrium conditions was calculated using the series formula as [9,90,228],

$$\frac{1}{C_s} = \frac{1}{C_s^{St}} + \frac{1}{C_s^{D}} \tag{8.16}$$

Numerical convergence study was performed as discussed in Refs. [199, 228]. The maximum mesh size was specified to be 0.01 nm at the electrode surface and 1 nm in the rest of the domain.

8.3.5.2 Simulating CV Measurements

CV measurements were simulated by numerically imposing the periodic surface electric potential given by Equation (8.1). The dimensionless governing equations (8.4) were solved along with the boundary and initial conditions given by Equations (8.5). The corresponding transient surface capacitive current density was estimated as [201, 202, 291, 311, 312, 323–326],

$$j_C(t) = -\sigma_s \left.\frac{\partial \psi}{\partial x}\right|_{x=0^-} = -\epsilon_0 \epsilon_r \left.\frac{\partial^2 \psi}{\partial x \partial t}\right|_{x=0^+} \quad \text{and} \tag{8.17}$$

$$j_C^*(t^*) = -\frac{\sigma_s^*}{\psi_{max}^* - \psi_{min}^*} \frac{L_s^*}{L^*} \left.\frac{\partial \psi^*}{\partial x^*}\right|_{x^*=0^-} = -\left.\frac{\partial^2 \psi^*}{\partial x^* \partial t^*}\right|_{x^*=0^+} \tag{8.18}$$

Simulations of CV measurements were run for at least 5 periods (i.e., $t \geq 10\tau_{CV}$) to ensure the current density had reached its stationary and periodic states. Then, the areal capacitance C_s was computed using Equation (8.2). The numerical convergence criterion was defined such that the maximum relative difference in the retrieved value of C_s was less than 1% when (1) reducing the mesh size by a factor five, (2) dividing the time step by five, and (3) running the CV simulations for 5 more periods. The time step was imposed to be $\Delta t \approx \tau_{CV}/1000 = (\psi_{max} - \psi_{min})/1000v$. Note that this time step decreased with increasing scan rate v and was several orders of magnitude smaller than the characteristic time for diffusion L^2/D. In addition, further reduction in the time step below the Debye relaxation

time λ_D^2/D was also found to have no effect on the predicted values of j_C and C_s. The mesh size was the smallest at the electrode surface due to large potential gradient and then gradually increased. The maximum mesh size was specified to be 0.001 nm at the electrode surface and 1 nm in the rest of the domain. The total number of finite elements was less than 400 for all cases simulated in the present study.

8.3.6 Validation

The numerical tool was validated based on three equilibrium and transient cases reported in the literature. First, the equilibrium electric potential profile in the diffuse layer predicted by solving the MPB model was validated against the exact solution for planar electrodes [8, 35, 90] with $\epsilon_r = 78.5$, $c_\infty = 0.01$ and 0.001 mol/L, $\nu_p = 0$, and $\psi_D = 0.1$ V. Second, the computed specific capacitances for the Stern and diffuse layers obtained from the MPB model were validated against Equations (8.15a) and (8.15b) for (i) $\psi_s = 0.1$ V, $c_\infty = 0.01$ mol/L, and $a = 0.66$ nm as well as (ii) $\psi_s = 0.5$ V, $c_\infty = 1$ mol/L, and $a = 0.66$ nm. Third, the transient ion concentration and electric potential profiles predicted by solving the PNP and MPNP models with constant surface potential were compared with the numerical solutions for planar electrodes reported in Ref. [146]. Comparison was made against the reported values of $c_i(x,t)$ and $\psi(x,t)$ for a wide range of packing parameter ν_p and dimensionless potential $(zF\psi_D/R_uT)$ [146]. Good agreement was obtained between our results and reported values for all cases considered.

8.4 Results and Discussions

8.4.1 Dimensional Analysis

Figure 8.2 shows the predicted current density j_C versus surface potential ψ_s (CV curves) obtained from CV simulations for three cases featuring different values of

T, L, a, c_∞, D, v, ψ_{max}, and ψ_{min} as summarized in Table 8.1. However, the dimensionless numbers for all cases were identical, namely, $\psi^*_{max} = 19.47$, $\psi^*_{min} = 0$, $L^* = 263.2$, $a^* = 2.17$, $\nu_p = 0.346$, $L^*_s = 0$, and $\sigma^*_s \to \infty$. Results were obtained by numerically solving the MPNP model with a Stern layer [Equations (8.7) to (8.13)] without electrode, i.e., $L_s = 0$ nm. Figure 8.2 shows that the predicted $j_C - \psi_s$ curves were significantly different for these three cases. However, Figure 8.2 demonstrates that the dimensionless $j^*_C - \psi^*_s$ curves overlapped after using the scaling parameters defined by Equation (8.6). Overall, these results demonstrate that (i) the scaling parameters defined by Equations (8.6) and the dimensional analysis for CV simulations were valid and (ii) the double layer charging dynamics near planar electrodes in CV measurements was governed by eight dimensionless numbers, i.e., v^*, ψ^*_{max}, ψ^*_{min}, L^*, a^*, ν_p, L^*_s, and σ^*_s given by Equation (8.14).

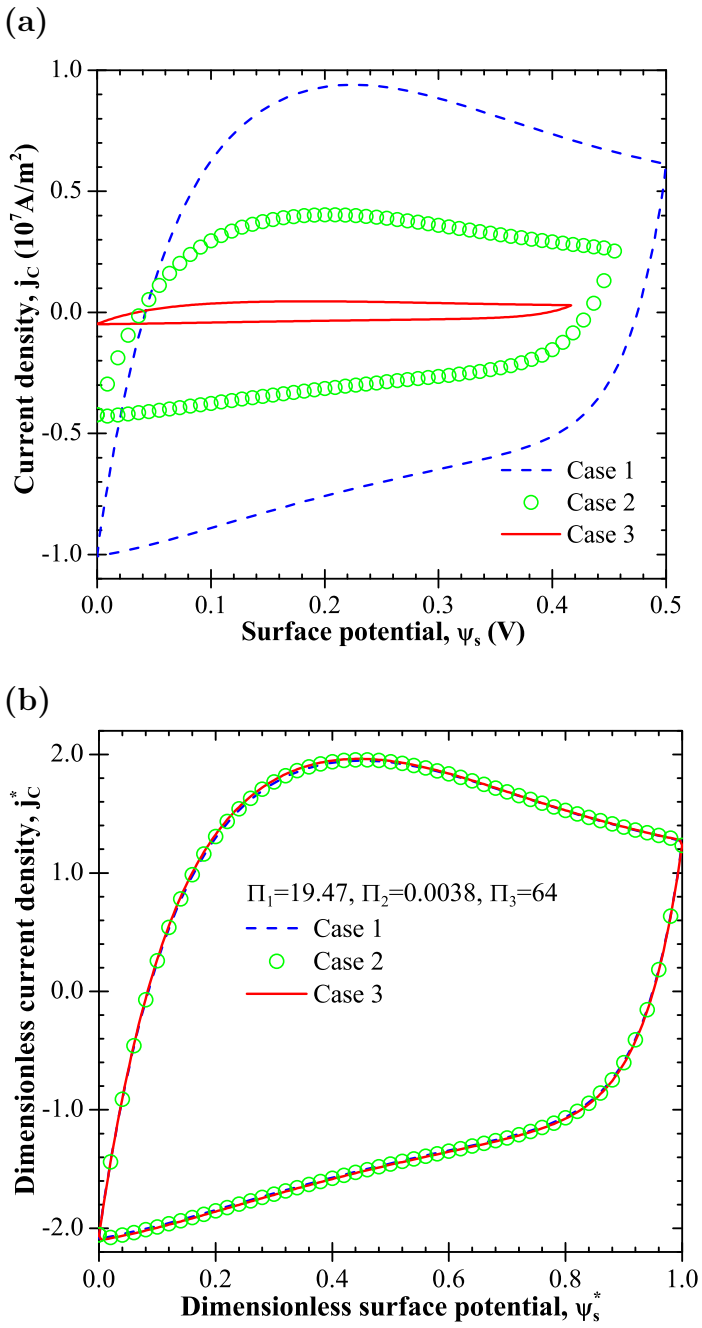

Figure 8.2: Predicted (a) j_C versus ψ_s curves and (b) j_C^* versus ψ_s^* curves from CV simulations for three cases with parameters given in Table 8.1. Results were obtained by numerically solving the MPNP model with a Stern layer [Equations (8.7) to (8.13)] without accounting for the electrode ($L_s = 0$ nm) with $\psi_{max}^* = 19.47$, $\psi_{min}^* = 0$, $L^* = 263.2$, $a^* = 2.17$, $\nu_p = 0.346$, $L_s^* = 0$, and $\sigma_s^* \to \infty$.

Table 8.1: Parameters in simulations without accounting for the electrode ($L_s = 0$ nm or $\sigma_s \to \infty$) and such that $\psi^*_{max} = 19.47$, $\psi^*_{min} = 0$, $L^* = 263.2$, $a^* = 2.17$, $\nu_p = 0.346$, $L^*_s = 0$, and $\sigma^*_s \to \infty$.

	T **(K)**	L **(nm)**	a **(nm)**	c_∞ **(mol/L)**	D **(m^2/s)**	v **(V/s)**	ψ_{max} **(V)**	ψ_{min} **(V)**
Case 1	298	80	0.66	1.0	2×10^{-9}	10^7	0.5	0
Case 2	270.9	88	0.726	0.751	1.25×10^{-9}	4.70×10^6	0.455	0
Case 3	248.3	96	0.792	0.579	2×10^{-10}	5.79×10^5	0.417	0

8.4.2 Effect of Scan Rate

Figures 8.3a and 8.3b show the numerically predicted j_C^* versus ψ_s^* curves from CV simulations for dimensionless scan rate v^* ranging from 1.8×10^{-4} to 18. The results were obtained by solving the MPNP model with a Stern layer [Equations (8.7) to (8.13)] without the electrode ($L_s = 0$ nm). The dimensionless numbers were $\psi_{max}^* = 19.47$, $\psi_{min}^* = 0$, $L^* = 263.2$, $a^* = 2.17$, $\nu_p = 0.346$, $L_s^* = 0$, and $\sigma_s^* \to \infty$. Figures 8.3a and 8.3b demonstrate that the magnitude of the current density j_C^* increased significantly with increasing dimensionless scan rate v^*. This can be attributed to the fact that a fast change in the surface potential resulted in a large local electric field and thus a large current density according to Equation (8.17). In addition, a "hump" was observed in the j_C^* versus ψ_s^* curve for $v^* = 1.8 \times 10^{-2}$ shown in Figure 8.3a. The hump disappeared when further increasing v^* and the j_C^* versus ψ_s^* curve became "leaf-like" for $v^* = 1.8 \times 10^{-1}$ as shown in Figure 8.3b. This is typical of EDLCs at large scan rates corresponding to large resistance to ionic current [31, 40, 347, 351, 367]. These trends are similar to those experimentally observed for EDLCs made of porous carbons [31, 40, 347, 351, 367]. Moreover, the predicted j_C^* became nearly linearly proportional to the imposed surface potential v^* for $v^* > 1.8$. In these cases, the electric double layer behaved as a pure resistor [40].

Figure 8.4 shows the slope of the j_C versus ψ_s curves as a function of dimensionless scan rate v^* ranging from 0.18 to 18. The model and other parameters were identical to those used to produce Figure 8.4.2. It is evident that the slope of j_C versus ψ_s curves increased with increasing v^* and gradually reached a constant plateau for $v^* \geq 1.8$. It is interesting to note that this plateau corresponds to the conductance of an electrolyte solution with ionic conductivity σ (in S/m) and thickness L given by [132, 311, 322, 324],

$$S = \frac{\sigma}{L} = \frac{1}{L} \frac{F^2}{R_u T} \sum_{i=1}^{2} z_i^2 D_i c_{i\infty} \tag{8.19}$$

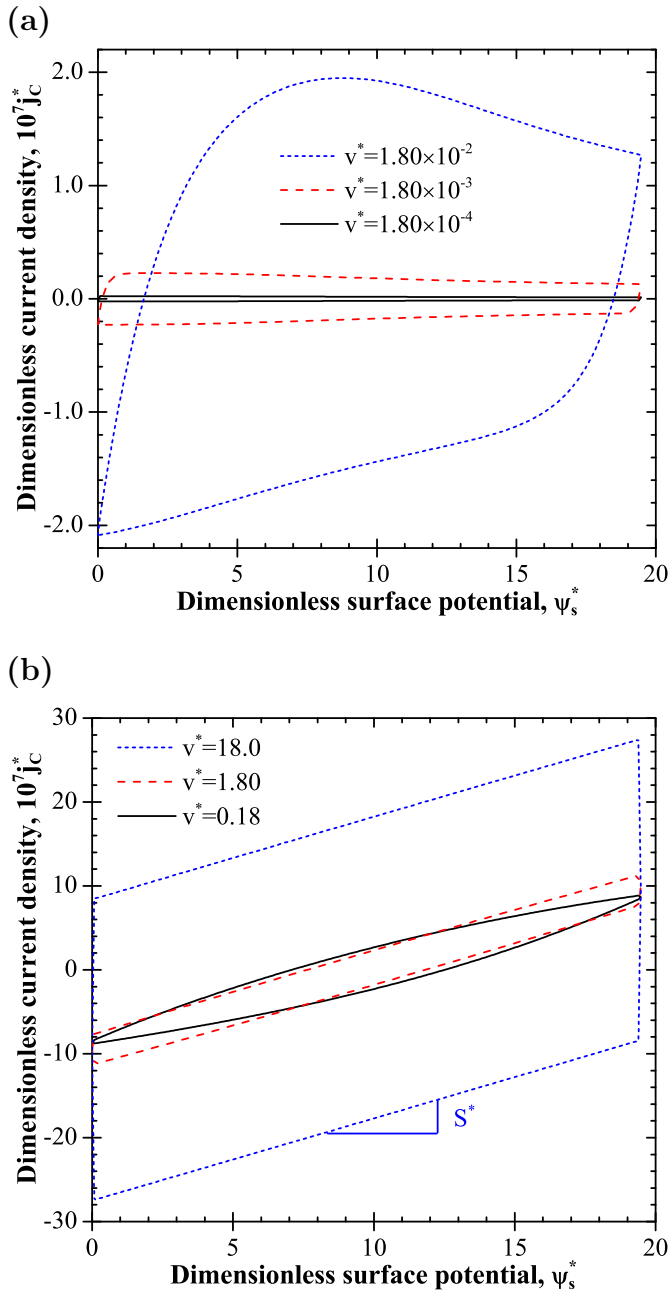

Figure 8.3: Predicted j_C^* versus ψ_s^* curves from CV simulations for dimensionless scan rate ranging from (a) $v^* = 1.8 \times 10^{-4} - 1.8 \times 10^{-2}$ and (b) $v^* = 0.18 - 18$. Results were obtained by numerically solving the MPNP model with a Stern layer [Equations (8.7) to (8.13)] without accounting for the electrode ($L_s = 0$ nm) with $\psi_{max}^* = 19.47$, $\psi_{min}^* = 0$, $L^* = 263.2$, $a^* = 2.17$, $\nu_p = 0.346$, $L_s^* = 0$, and $\sigma_s^* \to \infty$.

This result confirms that the predicted electrolyte ionic conductivity was indeed equal to the theoretical value when ignoring the electrode contribution to the resistance.

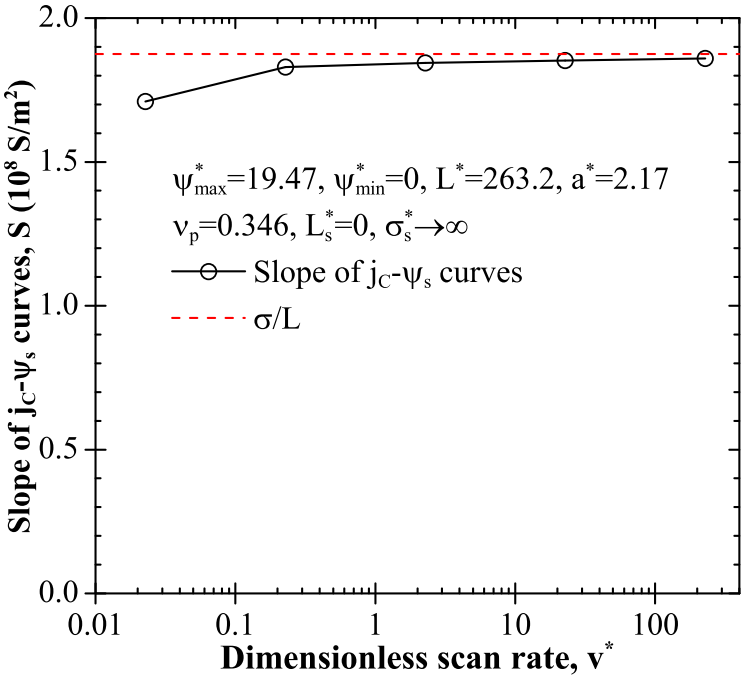

Figure 8.4: Slope of the predicted j_C versus ψ_s curves from CV simulations as a function of dimensionless scan rate v^*. Results were obtained by numerically solving the MPNP model with a Stern layer [Equations (8.7) to (8.13)] without accounting for the electrode ($L_s = 0$ nm) with $\psi^*_{max} = 19.47$, $\psi^*_{min} = 0$, $L^* = 263.2$, $a^* = 2.17$, $\nu_p = 0.346$, $L^*_s = 0$, and $\sigma^*_s \to \infty$. The theoretical value of σ/L given by Equation (8.19) was also shown for comparison purposes.

8.4.3 Effect of Diffusion Coefficient

Figure 8.5(a) shows the specific capacitance C_s retrieved from CV simulations using Equation (2.3) as a function of scan rate v ranging from 10^2 to 10^9 V/s. Three values of ion diffusion coefficient were used, i.e., $D = 2 \times 10^{-10}$, 2×10^{-9}, or 2×10^{-8} m^2/s. The model and other parameters were identical to those used

in Case 1 and summarized in Table 8.1. Figure 8.5(a) demonstrates that C_s was constant and independent of diffusion coefficient D for scan rate v smaller than a critical value and decreased rapidly beyond. This critical scan rate increased with increasing ion diffusion coefficient. For scan rates larger than a critical value, ion diffusion becomes a limiting factor in charge storage. Note that the scan rate v in CV measurements on mesoporous EDLCs typically ranged from 10^{-3} to 200 V/s [31, 347, 351, 367]. The scan rate for planar electrodes considered here was larger due to the small electrical resistance compared with that of mesoporous electrodes.

Figure 8.5(b) shows the specific capacitance C_s shown in Figure 8.5(a) but plotted as a function of dimensionless scan rate v^*. It is evident that all the curves now collapsed on a single line for the three different values of diffusion coefficient. Moreover, two regimes can be identified in Figure 8.5(b). First, for $v^* < 2 \times 10^{-4}$, ion transport is fast enough to follow the variation in the electric potential $\psi_s(t)$ and the retrieved specific capacitance C_s is independent of scan rate and ion diffusion. In these cases, C_s was equal to $C_s = 87.5$ μF/cm^2. This value was identical to the specific capacitance under equilibrium conditions predicted by Equations (8.15) and (8.16). Second, for $v^* > 2 \times 10^{-4}$, ion diffusion was the limiting phenomenon for charge storage and C_s decreased with increasing scan rate. Note that similar behavior was also observed in simulating double layer charging dynamics for electrochemical impedance spectroscopy (EIS) in our previous study [148]. However, unlike CV simulations, the capacitance retrieved from EIS predictions did not match the capacitance under equilibrium conditions even at small frequencies [148]. This suggests that CV measurements should be preferred to EIS when measuring the capacitance of EDLCs.

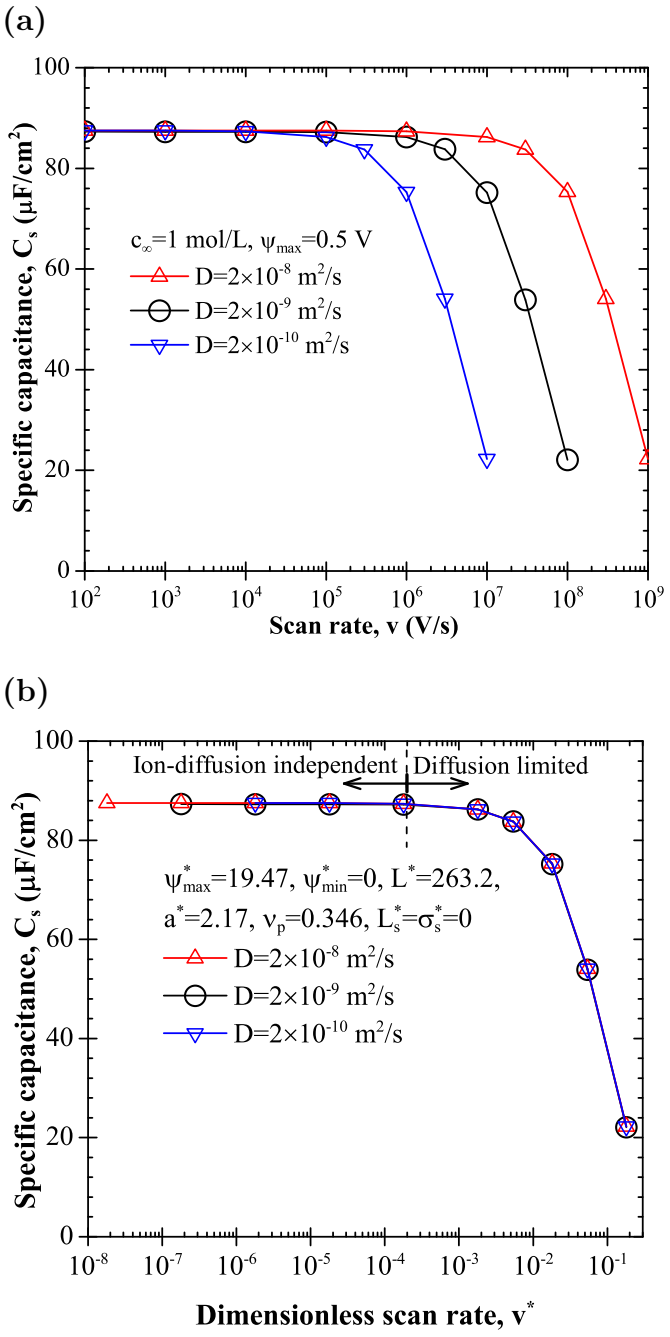

Figure 8.5: Predicted specific capacitance C_s from CV simulations as a function of (a) scan rate v and (b) dimensionless scan rate Π_3. Results were obtained by numerically solving the MPNP model with a Stern layer [Equations (8.7) to (8.13)] without accounting for the electrode ($L_s = 0$ nm). The diffusion coefficient D was chosen as $D = 2 \times 10^{-10}$ to 2×10^{-8} m^2/s while $\psi^*_{max} = 19.47$, $\psi^*_{min} = 0$, $L^* = 263.2$, $a^* = 2.17$, $\nu_p = 0.346$, $L^*_s = 0$, and $\sigma^*_s \to \infty$.

8.4.4 Interpretation of The Hump in CV Curves

Figure 8.6a shows the predicted j_C versus ψ_s curves from CV simulations for three values of potential window, i.e., $\Delta\psi = 0.3$, 0.4, and 0.5 V. Results were obtained by solving the MPNP model with a Stern layer [Equations (8.7) to (8.13)] without the electrode ($L_s = 0$ nm). Other parameters were identical to those used to reproduce the results shown in Figure 8.3. It is evident that j_C reached the maximum value at about $\psi_s = 0.2$ V for all three curves and then decreased for larger surface potential. Thus, a hump was observed around $\psi_s = 0.2$ V typical of experimental cyclic voltammetry measurements [40, 345–348, 352].

Here, the hump was not due to "*electrolyte starvation*" as suggested in Ref. [341] since the electrolyte concentration was large, i.e. $c_\infty = 1$ mol/L. Moreover, redox reactions were not responsible for the observed hump, as suggested in Refs. [295, 343–351], since only electrostatic phenomenon was accounted for in the present study. Finally, we simulated symmetric electrolytes with identical ion diameter and diffusion coefficient for both cations and anions. Thus, the hump was not due to "*difference of diffusion capability between solvated anions and cations in the electrolyte*" as proposed in Ref. [349].

To physically interpret the observed hump in j_C versus ψ_s curves, Figure 8.6b shows the corresponding anion concentration c_2 at the electrode surface $x = 0$ nm as a function of surface potential for the same cases considered in Figure 8.6a. The maximum ion concentration $c_{max} = 1/N_A a^3$ due to finite ion size (Section 9.3.3) was also plotted in Figure 8.6b. It is evident that the surface anion concentration c_2 increased rapidly with increasing potential up to $\psi_s = 0.2$ V. This regime corresponded to the increase of current density j_C shown in Figure 8.6a where it reached a maximum at $\psi_s = 0.2$ V corresponding to the crest of the hump. For $\psi_s > 0.2$ V, the anion concentration asymptotically approached its maximum value c_{max}. Then, the ion accumulation near the electrode surface

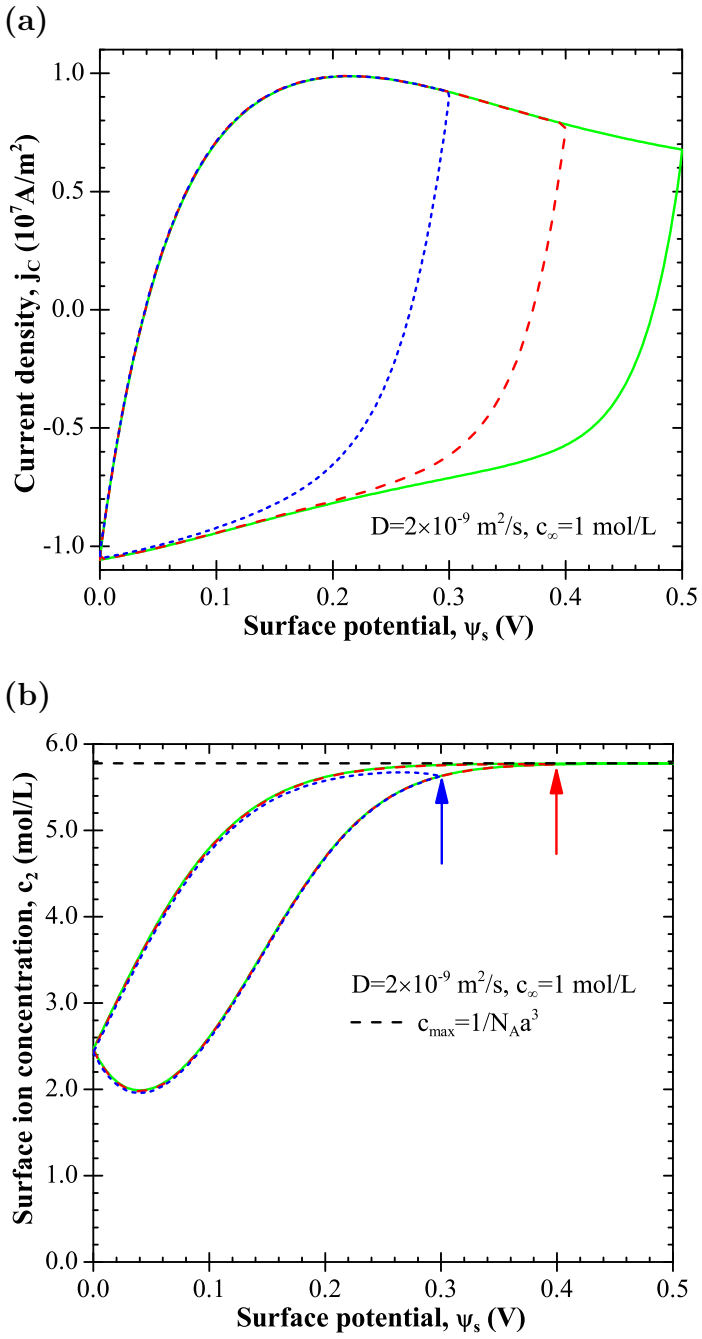

Figure 8.6: Predict (a) j_C versus ψ_s and (b) $c_2(x = 0)$ versus ψ_s curves determined from CV simulations for three values of potential window, i.e., $\psi_{max} - \psi_{min} = 0.3$, 0.4, and 0.5 V. Results were obtained by numerically solving the MPNP model with a Stern layer [Equations (8.4) and (8.5)] without accounting for the electrode ($L_s = 0$ nm) for $v = 10^7$ V/s, $D = 2 \times 10^{-9}$ m^2/s, and $c_\infty = 1$ mol/L.

became slower as the electric potential increased. This, in turn, resulted in the decrease in the current density j_C (Figure 8.6a). Overall, these results demonstrate that the hump observed experimentally in CV curves for EDLCs can be attributed to the saturation of ion concentration at the electrode surface. These results and interpretation appear to support those proposed in Refs. [352, 353] based on experimental results for large electrolyte concentrations. In addition, a hump was also observed in the predicted j_C versus ψ_s curves for small electrolyte concentration $c_\infty = 0.05$ or 0.1 mol/L (not shown) but at much smaller scan rates than those for larger concentrations. Then, for mesoporous electrodes, the hump observed under small electrolyte concentrations could be also attributed to the saturation of ion concentration in addition to "*electrolyte starvation*". However, the morphology of mesoporous electrodes can significantly affect the charging and discharging of EDLCs [31, 39, 209, 338–340]. Therefore, more detailed and systematic simulations accounting for three-dimensional electrode morphology with nanosize pores are essential to further understand the charging performance of mesoporous EDLCs.

Finally, Figure 8.7(a) shows the j_C versus ψ_s curves predicted for three different values of ion diffusion coefficient, i.e., $D = 2 \times 10^{-9}$, 2×10^{-8}, or 2×10^{-7} m^2/s. The potential window was $\Delta\psi = 0.5$ V. The model and other parameters were identical to those used to generate Figures 8.4.4 and 8.4.4. Figure 8.7(a) shows that the hump was observed in the j_C versus ψ_s curve for small diffusion coefficient $D = 2 \times 10^{-9}$ m^2/s. However, the hump disappeared when increasing the ion diffusion coefficient to $D = 2 \times 10^{-8}$ and 2×10^{-7} m^2/s. In addition, the j_C versus ψ_s curves became nearly symmetric along the line of zero current density $j_C = 0$ A/m^2. It is interesting to note that Lin *et al.* [209, 340] observed a similar trend for EDLCs made of TiC-derived carbons with pore diameter ranging from 0.68 to 1.0 nm in organic electrolytes. The authors attributed the symmetry of CV curves to the reduction in "steric hindering" of ions in large pores, i.e., smaller

electrolyte ionic resistance [209,340]. Here, the symmetry in the CV curves can be attributed to the fact that the ion transport can respond nearly instantaneously to the variation in electric potential for large ion diffusion coefficient. This, in turn, leads to smaller ionic resistance according to Equation (8.19).

To justify this interpretation, Figure 8.7(b) shows the the corresponding transient surface charge density $q_s(t) = \epsilon_0 \epsilon_r E_s(t)$ as a function of dimensionless time $t/2t_0$. It also shows the imposed surface potential $\psi_s(t)$. It is evident that the surface charge density $q_s(t)$ responded nearly instantaneously to the surface potential $\psi_s(t)$ for large diffusion coefficient $D = 2\times10^{-8}$ and 2×10^{-7} m^2/s. However, there was a lag between $q_s(t)$ and $\psi_s(t)$ for small ion diffusion coefficient $D = 2 \times 10^{-9}$ m^2/s. This confirms that the ion transport was unable to follow the fast variation of surface potential for small diffusion coefficients. In practice, EDLC electrodes are made of mesoporous materials. Then, a large effective ion diffusion coefficient would be beneficial for improving the charging performance and power density of EDLCs. Note that decreasing the electrolyte thickness L was found to have the same effect on the predicted j_C versus ψ_s curves (Figure 8.7(a)) and on q_s versus $t/2t_0$ curves (Figure 8.7(b)) as proportionally increasing the ion diffusion coefficient (not shown).

8.4.5 Effect of The Electrode

The above simulations did not account for the electrode. These simulations corresponded to electrode with zero thickness $L_s = 0$ nm or infinite electrical conductivity $\sigma_s \to \infty$. If taking $\sigma_s = 10$ S/m and $L_s = 100$ nm, the magnitude of the predicted j_C^* was found to decrease by a factor 2 (not shown) compared with results obtained without electrode (Figure 8.3). This was due to the increase in the overall electrical resistance of the system.

Figure 8.8 shows the slope of the j_C versus ψ_s curves from CV simulations as

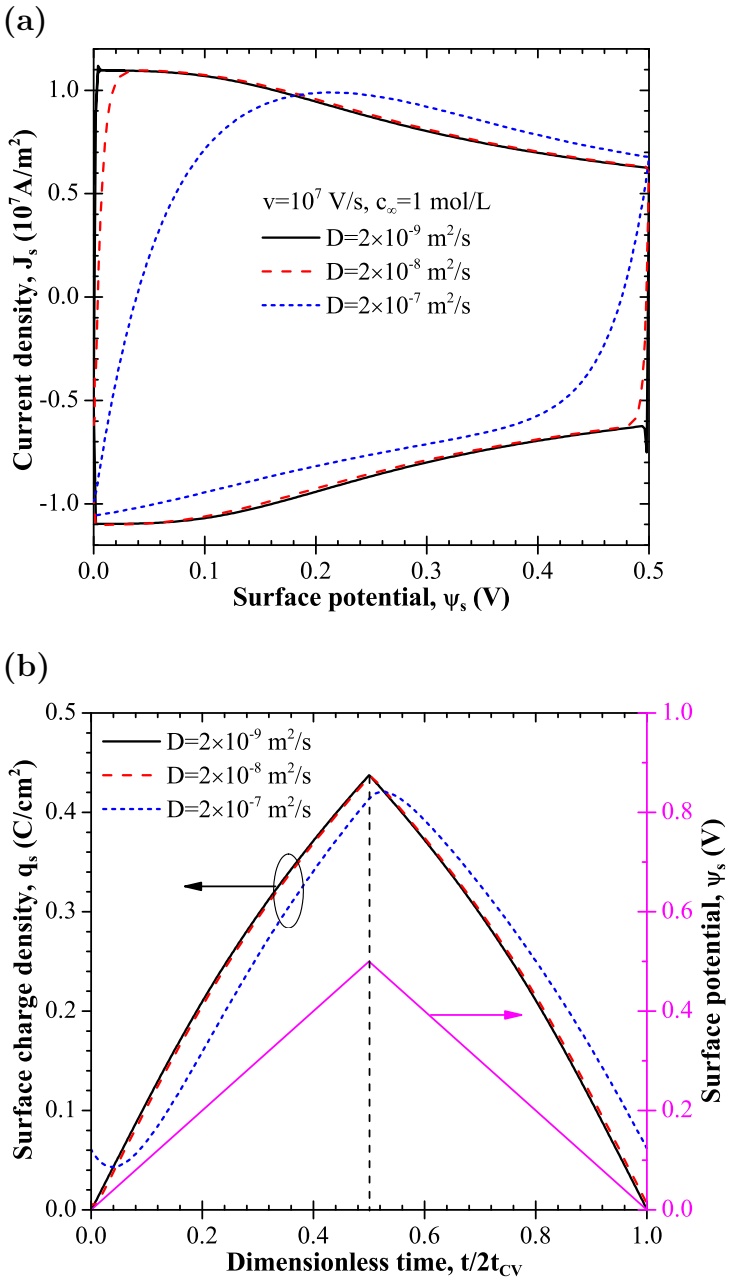

Figure 8.7: Plots of (a) j_C versus ψ_s and (b) q_s versus dimensionless time $t/2t_0$ predicted from CV simulations for three values of ion diffusion coefficient, i.e. $D = 2 \times 10^{-9}$, 2×10^{-8}, and 2×10^{-7} m^2/s. Results were obtained by numerically solving the MPNP model with a Stern layer [Equations (8.4) and (8.5)] without accounting for the electrode ($L_s = 0$ nm) for $v = 10^7$ V/s and $c_\infty = 1$ mol/L.

a function of dimensionless scan rate v^* for three cases with or without electrode, namely, (i) $\sigma_s \to \infty$ S/m (or $L_s = 0$ nm), (ii) $\sigma_s = 10$ S/m and $L_s = 100$ nm, and (iii) $\sigma_s = 0.01$ S/m and $L_s = 100$ nm. Other parameters were identical to those used to generate Figure 8.3. Results for the limiting case of $\sigma_s \to \infty$ were taken from Figure 8.4. Figure 8.8 demonstrates that the slope of j_C versus ψ_s curve was dominated by the electrode when its conductivity was small (e.g., $\sigma_s = 0.01$ S/m). For a relatively large electrode conductivity (e.g., $\sigma_s = 10$ S/m), the slope corresponded to the effective conductance of the electrode and electrolyte in series expressed as $(L/\sigma)_{eff} = L/\sigma + L_s/\sigma_s$.

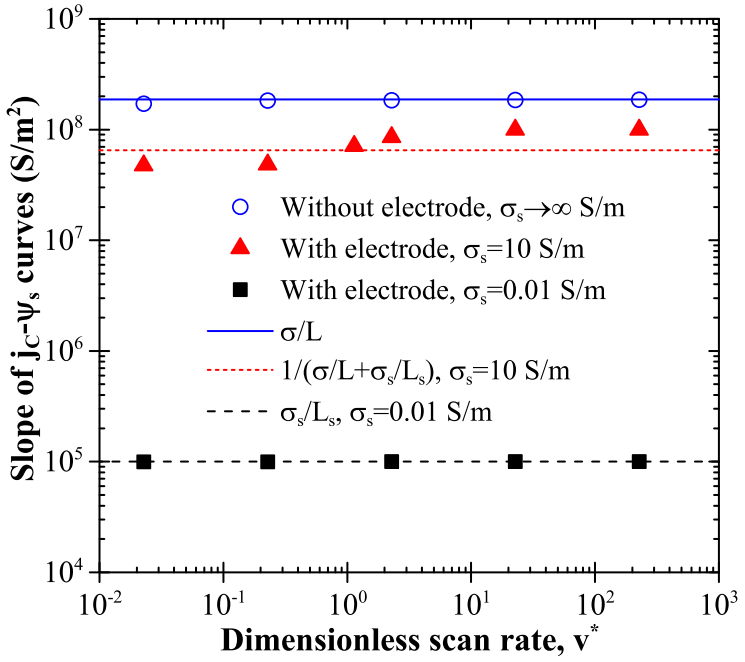

Figure 8.8: Slope of the j_C versus ψ_s curves predicted from CV simulations as a function of dimensionless scan rate v^* for $\sigma_s \to \infty$, $\sigma_s = 10$, and 0.01 S/m, respectively. Results were obtained by numerically solving the MPNP model with a Stern layer [Equations (8.7) to (8.13)] accounting for the electrode with $L = 80$ nm and $L_s = 100$ nm.

Finally, Figure 8.9 shows the predicted specific capacitance C_s from CV simulations as a function of dimensionless scan rate v^* for the three cases considered

in Figure 8.8. Here again, the value of C_s retrieved from CV curves was constant and equal to $C_s = 87.5$ μF/cm^2 for v^* smaller than a critical value which depended on σ_s. Then, it was identical to the specific capacitance under equilibrium conditions predicted by Equations (8.15) and (8.16) and was independent of the electrode electrical conductivity σ_s. Beyond the critical dimensionless scan rate v^*_{cr}, predicted values of C_s decreased rapidly with increasing v^*. In addition, v^*_{cr} increased significantly with increasing electrode electrical conductivity σ_s. Figure 8.9 established that the electrode electrical conductivity does not affect the double layer capacitance retrieved from CV measurements at low scan rates. However, it significantly affects the measured capacitance at large scan rates which reflects the charging rate performance of EDLCs.

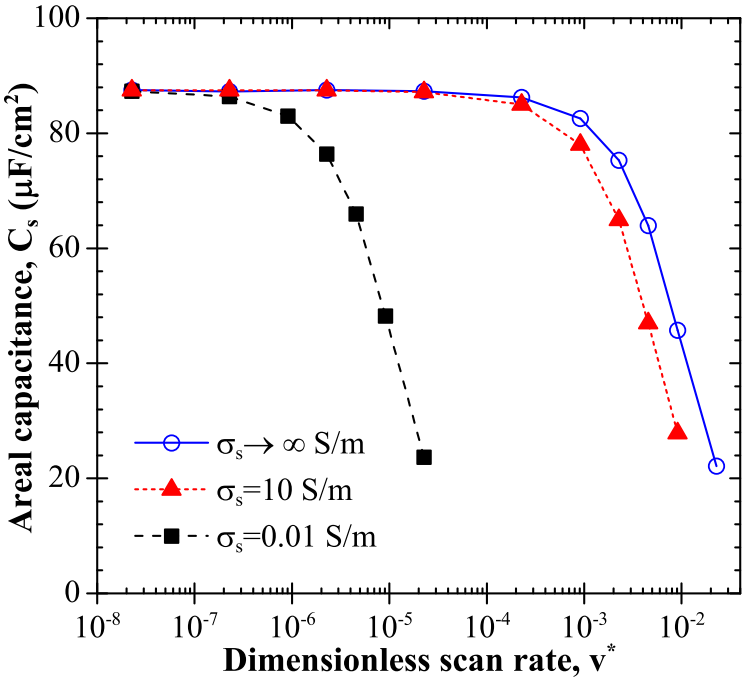

Figure 8.9: Predicted specific capacitance from CV simulations as a function of dimensionless scan rate v^* for three cases corresponding to $\sigma_s \to \infty$, $\sigma_s = 10$, and 0.01 S/m. Results were obtained by numerically solving the MPNP model with a Stern layer [Equations (8.7) to (8.13)] accounting for the electrode with $L_s = 100$ nm.

8.5 Conclusions

This chapter presented numerical simulations of cyclic voltammetry measurements for determining the electric double layer capacitance near a planar electrode in aqueous electrolyte solutions. For the first time, a modified Poisson-Nernst-Planck model accounting for the Stern layer was used to simulate the transient double layer dynamics under large electrolyte concentration and electric potential while simultaneously accounting for the electrode electrical conductivity. A dimensional analysis was performed and dimensionless numbers governing the CV measurements were also identified. The following conclusions can be drawn:

1. Eight dimensionless numbers given by Equation (8.14) were identified to govern the electron and ion transport in the charging dynamics of electric double layers in binary symmetric electrolytes with planar electrode during CV measurements.

2. For electrodes with large radius of curvature, the hump observed in CV curves was due to the saturation of ion concentration at the electrode surface as the electric potential increased.

3. The predicted EDL capacitance from CV simulations was constant and equal to the capacitance under equilibrium conditions for small dimensionless scan rate, i.e., $v^* \ll 1$.

4. The electrode had no effect on the EDL capacitance measured at scan rates smaller than a critical value. This critical scan rate decreased with increasing electrode electrical conductivity.

The model developed here can be readily extended to simulate the charging/discharging of mesoporous EDLCs by accounting for the three-dimensional electrode architecture [199, 244]. In fact, the above governing equations and boundary conditions remain valid for mesoporous electrodes as long as continuum theory is valid. The

latter has been examined in the literature [215–218] and is typically accepted when the pore diameter is larger than $3-5$ nm [215–218]. Then, the model can be used to identify the optimum electrode architecture to achieve maximum capacitance and charging performance.

CHAPTER 9

Physical Modeling of EDLCs With Asymmetric Electrolytes

The previous chapter reported simulations of EDLCs with binary and symmetric electrolytes. However, practical electrolytes are typically asymmetric. This chapter derives a new model from first principles valid for asymmetric electrolytes and/or in the presence of multiple ion species. It also presents physical modeling of cyclic voltammetry for EDLCs with binary asymmetric electrolytes and identifies the self-similar behavior of double layer integral capacitance.

9.1 Introduction

Cyclic voltammetry (CV) is a powerful technique in the field of electrochemistry [9,331,368]. It has been the subject of intense studies in electrochemical sensing [9, 331,368] and in electrical energy storage and conversion [31,149,177,333,369,370]. In these applications [31, 149, 177, 333, 369, 370], the electric potential is typically above 1 V while the electrolyte concentration is at least 1 mol/L. Numerous studies [4,7,95,102,130,146,148–152,199,228,244,371] have demonstrated that the finite ion size must be accounted for when simulating electric double layers at such large electric potential and/or large electrolyte concentrations. However, these studies have been mostly limited to binary and symmetric electrolytes [4,7,95,102, 130,146,148–152,199,228,244,371]. Practical electrolytes are typically asymmetric in nature due to the difference in (i) their ion diffusion coefficients [253], (ii) their ion sizes such as in ionic liquids [372], and/or (iii) their ion valencies such

as aqueous H_2SO_4 and Na_2SO_4. Moreover, the use of electrolyte mixtures with more than two ion species have been investigated in many practical applications such as supercapacitors [373–375], water desalination [376, 377], electrokinetics in colloidal systems [108, 113–119, 378, 379], electrochemical measurements involving supporting electrolytes [380–382], and various biological processes including gating and permeation in ion channels [156–162].

Figure 9.1(a) shows a schematic of the electric double layer structure consisting of Stern and diffuse layers forming near a planar electrode [8, 9, 149]. Several studies have considered ion species with different effective diameters resulting in multiple Stern layers with different thicknesses near the electrode surface [108, 118, 119, 378, 379]. There were no free charges within the Stern layer immediately adjacent to the electrode surface while all ion species co-existed in the diffuse layer [108, 118, 119, 378, 379]. By contrast, only ion species of intermediate sizes existed in the intermediate Stern layer(s). Such electric double layer structure was typically used along with PB or MPB models [108, 118, 119, 378, 379]. However, the associated ion concentrations do not satisfy the overall electroneutrality condition across the electrolyte domain expressed as $\sum_{i=1}^{N} \int_{-L}^{L} z_i c_i(x,t) = 0$, even for uniform concentrations typically used as initial conditions [95, 130, 146, 148–152]. This was caused by the small ions present in the intermediate Stern layer(s). For example, for binary and asymmetric electrolytes with valencies $(z_i)_{1\leq i\leq 2}$ and initial bulk ion concentrations $(c_{i\infty})_{1\leq i\leq 2}$, the above integral initially reduces to $\sum_{i=1}^{2} \int_{-L}^{L} z_i c_{i\infty} dx = 2z_2 c_{2\infty}(H_1 - H_2) \neq 0$ where $H_i = a_i/2$ (i=1 and 2) is the Stern layer boundaries defined according to the diameters of the larger (a_1) and smaller (a_2) ions, respectively. Note that $c_1(x,t)$ and $c_2(x,t)$ were non-zero for $-L + H_1 \leq x \leq L - H_1$ and $-L + H_2 \leq x \leq L - H_2$, respectively. This issue becomes particularly severe when simulating electric double layers in a finite electrolyte domain.

This chapter aims to develop a model, from first principles, for simulating elec-

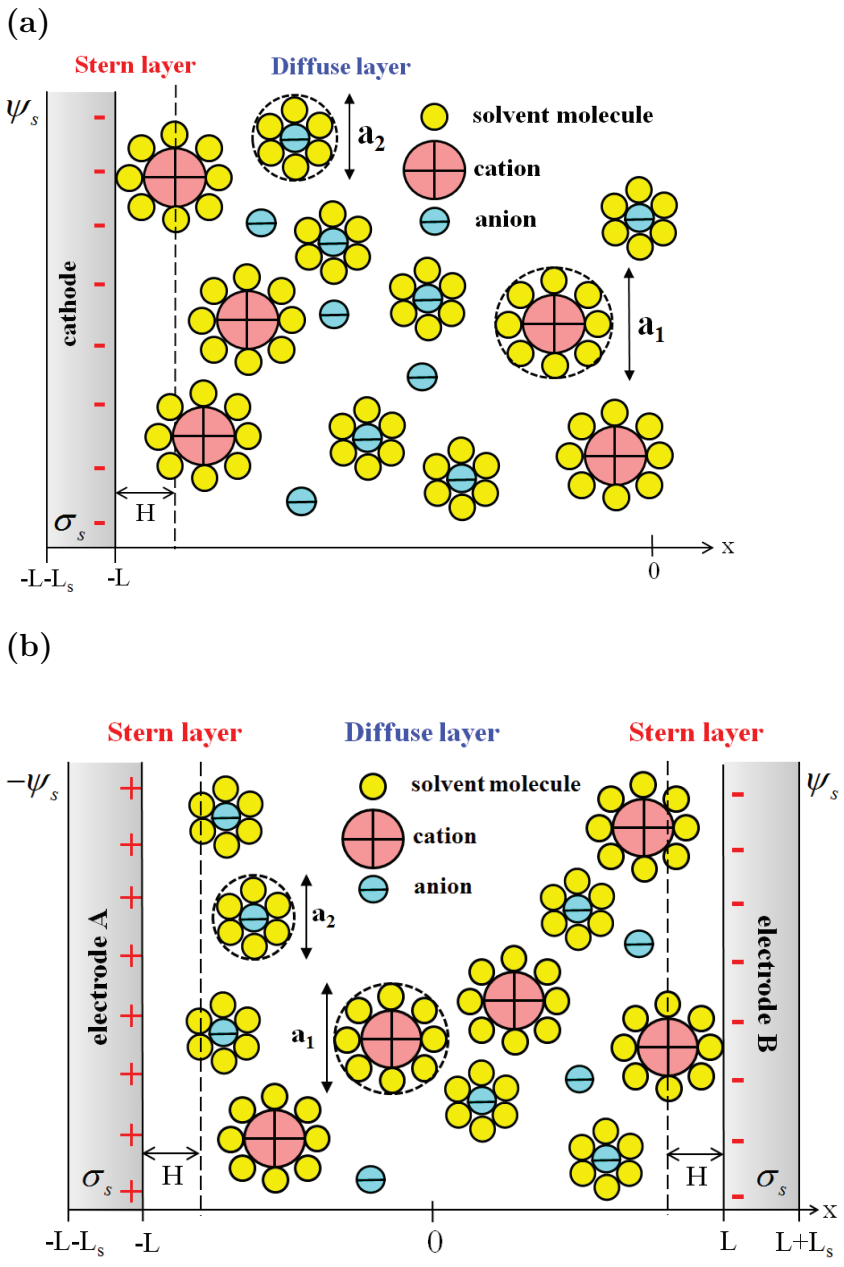

Figure 9.1: Schematic and the computational domain of the electric double layer structure consisting of Stern and diffuse layers (a) near a planar electrode (i.e., with the half domain) and (b) between two planar electrodes (i.e., with the full domain). Here, the ion diameters of large and small ion species were denoted by a_1 and a_2, respectively.

tric double layer dynamics valid for asymmetric electrolytes and/or for multiple ion species accounting for different ion diameters, as well as different valencies and diffusion coefficients. The model was used to simulate CV measurements for binary asymmetric electrolytes.

9.2 Background

Existing simulations [95–99,103–119,378,379] of asymmetric electrolytes based on continuum theory and accounting for finite ion size are mainly limited to equilibrium conditions as discussed in Chapter 2. Recent efforts have been made to account for the effect of finite ion size in modeling ion transport in concentrated electrolyte solutions and/or under large electric potential [95, 130, 146, 150–162]. For example, Kilic *et al.* [146] derived a modified Poisson-Nernst-Planck (MPNP) model valid for binary and symmetric electrolytes under large electrolyte concentration and electric potential. The authors added an excess term accounting for the entropic contribution due to finite-size ions in the expression of the Helmholtz free energy. This resulted in an excess term in the expressions of the chemical potentials and mass fluxes [95,130,146,151]. However, this MPNP model does not apply to asymmetric electrolytes or to multiple ion species [95, 130, 146, 148–152].

Alternatively, several authors [153–155] incorporated the finite ion size in ion mass fluxes using the activity coefficient to account for the deviation from ideal electrolyte solutions. However, these studies [153–155] were also limited to binary and symmetric electrolytes. Note that the MPNP model developed by Kilic *et al.* [146] can be also formulated in a form equivalent to that based on the activity coefficient [95, 119, 130]. Based on this MPNP model [146], Wang and Pilon [149] performed numerical simulations reproducing CV measurements for electric double layer capacitors with binary and symmetric electrolytes for large concentration and potential window. The model simultaneously accounted for the finite ion size, Stern and diffuse layers, and the electrode electrical conductivity. A scaling anal-

ysis was performed and dimensionless numbers governing CV measurements were identified [149].

Davidson and Goulbourne [156] extended the MPNP model to multiple ion species but with symmetric ion diameter and valency. Eisenberg and co-workers [157–159] developed a MPNP model for binary asymmetric electrolytes based on the variation principle. Horng *et al.* [160] later extended this model [157–159] for asymmetric electrolytes with multiple ion species. However, these MPNP models [157–160] were expressed as integral-differential equations, thus making the numerical solution procedure highly involved particularly for three-dimensional geometries.

Lu and Zhou [161,162] extended the expression of chemical potential developed in Refs. [97, 98] and proposed a "size-modified" Poisson-Nernst-Planck (SMPNP) model for asymmetric electrolytes and multiple ion species. In their model [161, 162], they introduced a parameter "$k_i = a_i/a_0$" representing the ratio of ion diameter a_i and the diameter of solvent molecules a_0. The authors considered different cases for $k_i > 1$ and justified that the model successfully constrained the ion concentrations below their maximum values. However, this SMPNP model breaks down when neglecting the size of solvent molecules and $k_i \to \infty$ since the excess term accounting for finite ion sizes approaches infinity.

To the best of our knowledge, no study has simulated CV curves for electric double layer capacitors with asymmetric electrolytes and/or with multiple ion species while accounting for the finite ion size. This chapter aims to develop, from first principles, a model for simulating electric double layer dynamics valid for asymmetric electrolytes and/or for multiple ion species. It simultaneously accounts for (1) asymmetric electrolytes with (2) multiple ion species of (3) finite ion size, and for (4) Stern and diffuse layers. The model will be useful for simulating electric double layers in various electrochemical, colloidal, and biological systems.

9.3 Analysis

9.3.1 Generalized Modified Poisson-Nernst-Planck Model

Previous studies [95, 130, 153–155, 312, 383] established that the effect of finite ion size on the electric double layer dynamics can be generally accounted for by employing the activity coefficient γ_i in the expression of the chemical potential of each ion species "i". The ion mass flux is proportional to the gradient of chemical potential. Then, a generalized modified Poisson-Nernst-Planck (GMPNP) model consisting of the Gauss law coupled with the mass conservation equations for each one of the N ion species can be formulated as,

$$\begin{cases} \nabla \cdot (\epsilon_0 \epsilon_r \nabla \psi) = -F \sum_{i=1}^{N} z_i c_i & \text{(9.1a)} \\ \dfrac{\partial c_i}{\partial t} = \nabla \cdot \left[D_i c_i \left(\dfrac{F z_i}{R_u T} \nabla \psi + \nabla \ln(\gamma_i c_i) \right) \right] \quad \text{for} \quad i = 1, 2, ..., N & \text{(9.1b)} \end{cases}$$

where ψ is the local electric potential while c_i and D_i are the molar concentration and diffusion coefficient of ion species "i" in the electrolyte solution, respectively. Here, ϵ_0 and ϵ_r are the free space permittivity ($\epsilon_0 = 8.854 \times 10^{-12}$ F/m) and the relative permittivity of the electrolyte solution, respectively. The temperature is denoted by T (in K), while F and R_u are the Faraday constant ($F = 96485.3$ sA/mol) and the universal gas constant ($R_u = 8.314$ JK^{-1}mol^{-1}), respectively.

Among various forms of activity coefficient existing in the literature, the "Langmuir type" activity coefficient [113–119, 153, 384–387] directly relates γ_i to the ion diameter a_i to account for the exclusion volume caused by the finite size of ion species. It is expressed as [384, 385],

$$\gamma_i = \frac{1}{1 - \sum_{i=1}^{N} \dfrac{c_i}{c_{i,max}}} \tag{9.2}$$

where $c_{i,max}$ is the maximum ion concentration of ion species "i" and is given by $c_{i,max} = 1/N_A a_i^3$ when assuming simple cubic ion packing. Here, N_A is the

Avogadro's number ($N_A = 6.022 \times 10^{23}$ mol^{-1}). Note that as the ion diameter vanishes, i.e., $a_i = 0$, $c_{i,max}$ tends to infinity and γ_i approaches 1. It is also interesting to note that Equation (9.2) is a simplified expression of the activity coefficient based on the Boublik-Mansoori-Carnahan-Starling-Leland equation-of-state [95, 99, 106, 107].

By employing the "Langmuir type" activity coefficient given by Equation (9.2), the GMPNP model can be written as,

$$\begin{cases} \nabla \cdot (\epsilon_0 \epsilon_r \nabla \psi) = -F \sum_{i=1}^{N} z_i c_i & \text{(9.3a)} \\ \dfrac{\partial c_i}{\partial t} = \nabla \cdot \left(\underbrace{D_i \nabla c_i}_{\text{Diffusion}} + \underbrace{\dfrac{D_i F z_i c_i}{R_u T} \nabla \psi}_{\text{Migration}} + \underbrace{\dfrac{D_i N_A c_i \sum_{i=1}^{N} a_i^3 \nabla c_i}{1 - N_A \sum_{i=1}^{N} a_i^3 c_i}}_{\text{Correction due to asymmetric ion sizes}} \right) & \text{(9.3b)} \end{cases}$$

Note that for vanishing ion diameter ($a_i = 0$), Equations (9.1) and (9.3) reduce to the classical PNP model [149]. In addition, for binary and symmetric electrolytes, $N = 2$, $z_1 = -z_2$, $D_1 = D_2$, and $a_1 = a_2$, and Equations (9.1) and (9.3) reduce to the MPNP model developed in Refs. [95, 146]. Note also that the GMPNP model can be also derived by considering the excess chemical potential μ_i^{ex} for each ion species "i" and by noting its direct relation to the activity coefficient γ_i given by $\mu_i^{ex} = k_B T \ln(\gamma_i)$ [95, 312, 384].

Compared with previous MPNP models [95,130,146,148–162], the present generalized MPNP (GMPNP) model, given by Equations (9.1) to (9.3), has several attractive features. First, it applies to asymmetric electrolytes and/or multiple ion species. Second, it does not present any additional challenges in the numerical solution procedure compared with the MPNP model for binary symmetric electrolytes [95,130,146,148,149,151,152]. Moreover, it can be conveniently applied to three-dimensional geometries unlike those expressed as integral-differential equations [157–160]. Third, it is consistent with the classical or existing models when

considering ions as point charges or having identical diameters. Fourth, it can be readily extended by employing other forms of activity coefficient based on available expressions of excess chemical potential μ_i^{ex} such as the Boublik-Mansoori-Carnahan-Starling-Leland equation-of-state [95, 99].

9.3.2 Schematics and Assumptions

In the present study, the double layer structure with multiple Stern layers proposed in Refs. [108, 118, 119, 378, 379] was not adopted because this does not satisfy the overall electroneutrality condition, as discussed previously. Instead, the electric double layer was assumed to consist of (i) a single Stern layer adjacent to the electrode surface and (ii) a diffuse layer beyond. Wang *et al.* [7, 149] previously showed that the electrode curvature has negligible effect on the areal integral capacitance for electrode or pore radii larger than 40 nm. Therefore, analysis of planar electrodes is representative of macroporous and mesoporous electrodes with large enough radii of curvature.

Figure 9.1(a) shows the half domain used in previous simulations for binary and symmetric electrolytes [149]. By contrast, Figure 9.1(b) shows the schematic of the computational domain used to simulate the electrolyte solution consisting of binary asymmetric electrolytes between two identical planar electrodes A and B. In the present study, simulations with the former and the latter domains were referred to as "half-domain simulations" and "full-domain simulations", respectively. Here, the effective ion diameters of the larger and smaller ion species were denoted by a_1 and a_2, respectively. The region of electrolyte solution consisted of three layers including (1) the Stern layer of thickness H near each electrode surface located at $x = \pm L$ and (2) the diffuse layer between the Stern layers, i.e., $-L + H \leq x \leq L - H$. Here, the thickness H was approximated as the effective radius of the largest ion referred to as ion species 1, i.e., $H = a_1/2$.

To make the problem mathematically tractable, the following assumptions were made: (1) the effective ion diameter was assumed to be independent of electrolyte concentration [95, 146, 200], (2) the electrolyte dielectric permittivity was constant and equal to that of water. Note that the dielectric permittivity may depend on electric field and temperature [7, 189, 190, 199]. However, it is typically assumed to be constant in scaling analysis, as performed in Refs. [4, 95, 128, 130, 146, 151, 152, 371] and in the present study. (3) isothermal conditions prevailed throughout the electrode and electrolyte, (4) advection of the electrolyte was assumed to be negligible, (5) the ions could only accumulate at the electrode surface and could not diffuse into the electrode, i.e., there was no ion insertion, and (6) the specific ion adsorption due to non-electrostatic forces was assumed to be negligible.

9.3.3 One-dimensional Formulation

The local electric potential $\psi(x,t)$ in the identical solid electrodes A and B of electrical conductivity σ_s and thickness L_s was governed by the Poisson equation expressed as [149, 388, 389],

$$\frac{\partial}{\partial x}\left(\sigma_s \frac{\partial \psi}{\partial x}\right) = 0 \quad \text{for} \quad -L_s - L \leq x < -L \quad \text{and} \quad L < x \leq L + L_s \tag{9.4}$$

Moreover, the local electric potential $\psi(x,t)$ and molar ion concentrations $c_i(x,t)$ at time t and location x in the binary asymmetric electrolyte solution were computed by solving the generalized MPNP model with a Stern layer. For planar electrodes, the generalized MPNP model [Equations (9.3)] in the diffuse layer ($-L + H \leq x \leq L - H$) can be expressed in its one-dimensional form as,

$$\begin{cases} \dfrac{\partial}{\partial x}\left(\epsilon_0 \epsilon_r \dfrac{\partial \psi}{\partial x}\right) = -F \displaystyle\sum_{i=1}^{2} z_i c_i & \text{(9.5a)} \\ \dfrac{\partial c_i}{\partial t} = -\dfrac{\partial N_i}{\partial x} & \text{(9.5b)} \end{cases}$$

Here, N_i denotes the mass flux of ion species "i" expressed as,

$$N_i(x,t) = -\frac{D_i F z_i c_i}{R_u T}\frac{\partial \psi}{\partial x} - D_i \frac{\partial c_i}{\partial x} - \frac{D_i N_A c_i}{1 - N_A \sum_{i=1}^{2} a_i^3 c_i}\frac{\partial}{\partial x}\left(\sum_{i=1}^{2} a_i^3 c_i\right) \tag{9.6}$$

Moreover, the Stern layers can be accounted for via the boundary conditions relating the potential drop across the Stern layer and the potential gradient at the Stern/diffuse layer interface located at $x = (L-H)$ and $x = -(L-H)$ [7,95,146]. Then, it suffices to simulate only the diffuse layer in the computational domain defined by $-L + H \leq x \leq L - H$ [7,95,146]. For planar electrodes, the boundary conditions accounting for the Stern layers are given by [7,95,146],

$$\frac{\partial \psi}{\partial x}(x = L - H, t) = \frac{1}{H}\left[\psi(x = L, t) - \psi(x = L - H, t)\right] \quad \text{and} \tag{9.7a}$$

$$-\frac{\partial \psi}{\partial x}(x = -L + H, t) = \frac{1}{H}\left[-\psi(x = -L, t) - \psi(x = -L + H, t)\right] \tag{9.7b}$$

The electric potential and current density were continuous across the electrode/electrolyte interface located at $x = \pm L$ so that [149,366],

$$\psi(x = -L^-) = \psi(x = -L^+) \text{ and } -\sigma_s \frac{\partial \psi}{\partial x}(x = -L^-) = -\epsilon_0 \epsilon_r \frac{\partial^2 \psi}{\partial x \partial t}(x = -L^+) \tag{9.8a}$$

$$\psi(x = L^-) = \psi(x = L^+) \text{ and } -\sigma_s \frac{\partial \psi}{\partial x}(x = L^+) = -\epsilon_0 \epsilon_r \frac{\partial^2 \psi}{\partial x \partial t}(x = L^-) \tag{9.8b}$$

Moreover, at the Stern/diffuse layer interface located at $x = \pm(L - H)$, the mass fluxes of ion species vanish since there is no ion insertion in the electrode material [Assumption (5)] such that,

$$N_i(-L + H, t) = 0 \quad \text{and} \quad N_i(L - H, t) = 0 \tag{9.9}$$

The initial conditions in the diffuse layer satisfy the electroneutrality condition and are given by,

$$\psi(x, t = 0) = 0, \quad c_1(x, t = 0) = c_{1,\infty}, \quad \text{and} \quad c_2(x, t = 0) = -c_{1,\infty} z_1 / z_2 \tag{9.10}$$

where $c_{i,\infty}$ represents the bulk ion concentration of ion species "i".

Note that the Ohmic IR drop due to the electrolyte solution is typically the major source of resistance. It is often accounted for via a resistance in an equivalent RC circuit while ignoring the electric double layer structure [9, 390]. By contrast, the present study accounted for the detailed electric double layer structure. Thus, the electric potential drop in the electrolyte solution was rigorously obtained by numerically solving the GMPNP model along with the boundary conditions [Equations (9.5) to (9.10)].

9.3.4 Dimensional Analysis

Equations (9.4) to (9.10) constitute the one-dimensional generalized MPNP model with a Stern layer for binary asymmetric electrolytes accounting for the electrodes. Based on our previous studies [149], the following scaling parameters were introduced,

$$x^* = \frac{x}{\lambda_D},\ t^* = \frac{tD_1}{\lambda_D^2},\ \psi^* = \frac{\psi}{R_uT/z_1F},\ \text{and}\ c_i^* = \frac{c_i}{c_{1,\infty}} \tag{9.11}$$

where $\lambda_D = \sqrt{\epsilon_0\epsilon_r R_uT/F^2 \sum_{i=1}^{2} z_i^2 c_{i,\infty}}$ is the Debye length for binary asymmetric electrolytes [35]. Then, the governing Equation (9.4) in the electrode can be expressed, in dimensionless form, as

$$\frac{\partial}{\partial x^*}\left(\frac{\partial \psi^*}{\partial x^*}\right) = 0 \qquad \begin{array}{l}\text{for } -(L_s+L)/\lambda_D \le x < -L/\lambda_D \\ \text{and} \quad L/\lambda_D < x \le (L+L_s)/\lambda_D\end{array} \tag{9.12}$$

Similarly, the governing Equations (9.5) in the electrolyte were transformed into the dimensionless form as,

$$\begin{cases} \dfrac{\partial^2 \psi^*}{\partial x^{*2}} = -\dfrac{c_1^* + z_2^* c_2^*}{1 - z_2^*} & \text{(9.13a)} \\ \qquad\qquad \text{for} \quad (-L + a_1/2)/\lambda_D \le x^* \le (L - a_1/2)/\lambda_D & \\ \dfrac{\partial c_i^*}{\partial t^*} = -\dfrac{\partial N_i^*}{\partial x^*} & \text{(9.13b)} \end{cases}$$

with the dimensionless ion flux N_i^* given by,

$$N_i^*(x^*,t^*) = -\frac{D_i}{D_1}\frac{\partial c_i^*}{\partial x^*} - \frac{D_i}{D_1}\frac{z_i}{z_1}c_i^*\frac{\partial \psi^*}{\partial x^*} - \frac{D_i}{D_1}\frac{c_i^*}{2-\sum_{i=1}^{2}\nu_{pi}c_i^*}\frac{\partial}{\partial x^*}\sum_{i=1}^{2}\nu_{pi}c_i^* \quad (9.14)$$

where $z_2^* = z_2/z_1$ is the ratio of valencies between smaller and larger ion species, i.e., $z_2^* = -1$ for symmetric electrolytes. Here, the packing parameter for ion species "i" is defined as $\nu_{pi} = 2c_{1\infty}/(1/a_i^3 N_A)$. It represents the ratio of the total bulk ion concentration to the maximum ion concentration $1/a_i^3 N_A$ assuming a simple cubic packing of ions of diameter a_i.

The dimensionless potential $\psi_s^*(t^*)$ imposed at the electrode surface in CV measurements is given by,

$$\psi_s^*(t^*) =$$

$$\begin{cases} \psi_{max}^* - v^*[t^* - 2(m-1)\tau_{CV}^*] & \text{for } 2(m-1)\tau_{CV}^* \le t^* \le (2m-1)\tau_{CV}^* \quad (9.15a) \\ \psi_{min}^* + v^*[t^* - (2m-1)\tau_{CV}^*] & \text{for } (2m-1)\tau_{CV}^* \le t^* \le 2m\tau_{CV}^* \quad (9.15b) \end{cases}$$

where $\tau_{CV}^* = (\psi_{max}^* - \psi_{min}^*)/v^*$ represents the dimensionless half cycle period and $v^* = (\lambda_D^2/D_1)/[(R_uT/z_1F)/v]$ is the dimensionless scan rate. It can be interpreted as the ratio of the ion diffusion time scale (λ_D^2/D_1) and the characteristic time for reaching the thermal potential R_uT/z_1F at scan rate v. Moreover, $\psi_{max}^* = \psi_{max}/(R_uT/z_1F)$ and $\psi_{min}^* = \psi_{min}/(R_uT/z_1F)$ are the maximum and minimum surface potentials, respectively, scaled by the thermal potential. They can be also interpreted as the ratio of characteristic times to reach ψ_{max} or ψ_{min} and the characteristic time for reaching the thermal potential at scan rate v.

Moreover, the boundary conditions [Equations (9.7) and (9.9)] at the Stern/diffuse layer interface located at $x^* = \pm(L - a_1/2)/\lambda_D$ can be written in dimensionless form as,

$$\frac{2}{a_1^*}\frac{\partial \psi^*}{\partial x^*}(x^* = L^* - a_1^*/2, t^*) = \psi_s^*(t^*) - \psi^*(x^* = L^* - a_1^*/2, t^*) \quad (9.16a)$$

$$-\frac{2}{a_1^*}\frac{\partial \psi^*}{\partial x^*}(x^* = -L^* + a_1^*/2, t^*) = -\psi_s^*(t^*) - \psi^*(x^* = -L^* + a_1^*/2, t^*) \quad (9.16b)$$

$$N_i^*(L^* - a_1^*/2, t^*) = N_i^*(-L^* + a_1^*/2, t^*) = 0 \quad (9.16c)$$

where $L^* = L/\lambda_D$ and $a_1^* = a_1/\lambda_D$ are respectively the half inter-electrode distance and the effective ion diameter scaled by the Debye length representing the thickness of the electric double layer. Similarly, the boundary conditions [Equations (9.8)] at the electrode/electrolyte interface located at $x^* = \pm L/\lambda_D$ became, in dimensionless form,

$$\psi^*(x = \pm L^{\pm}/\lambda_D) = \psi^*(x = \pm L^{\mp}/\lambda_D) \quad \text{and} \quad (9.17a)$$

$$\frac{\sigma_s^*}{\psi_{max}^* - \psi_{min}^*} \frac{L_s^*}{L^*} \frac{\partial \psi^*}{\partial x^*}(x^* = \pm L^{\pm}/\lambda_D) = \frac{\partial^2 \psi^*}{\partial x^* \partial t^*}(x^* = \pm L^{\mp}/\lambda_D) \quad (9.17b)$$

where $L_s^* = L_s/\lambda_D$ is the electrode thickness scaled by the Debye length. Note that $\sigma_s^* = [\sigma_s(\psi_{max} - \psi_{min})/L_s]/(F z_1 c_{1\infty} D_1/L)$ represents the ratio of the characteristic current density in the electrode to that in the electrolyte. It can be also interpreted as the ratio of time scales for charge transport in the electrolyte and in the electrode.

Similarly, the dimensionless initial conditions for ψ^* and c_i^* in the diffuse layer, for $-L^* + a_1^*/2 \leq x^* \leq L^* - a_1^*/2$, simplify as,

$$\psi^*(x^*, t^* = 0) = 0, \quad c_1^*(x^*, t^* = 0) = 1, \quad \text{and} \quad c_2^*(x^*, t^* = 0) = -1/z_2^* \quad (9.18)$$

Considering the dimensionless governing equations and associated boundary and initial conditions, eleven key dimensionless similarity parameters can be identified as

$$\begin{aligned} &v^* = \frac{\lambda_D^2/D_1}{(R_u T/z_1 F)/v}, \quad \psi_{max}^* = \frac{\psi_{max}}{R_u T/z_1 F}, \quad \psi_{min}^* = \frac{\psi_{min}}{R_u T/z_1 F}, \quad L^* = \frac{L}{\lambda_D}, \\ &a_1^* = \frac{a_1}{\lambda_D}, \quad \nu_{p1} = 2a_1^3 N_A c_{1\infty}, \quad \nu_{p2} = 2a_2^3 N_A c_{1\infty}, \quad D_2^* = \frac{D_2}{D_1}, \quad z_2^* = \frac{z_2}{z_1}, \\ &\sigma_s^* = \frac{\sigma_s(\psi_{max} - \psi_{min})/L_s}{F z_1 c_{1\infty} D_1/L}, \quad \text{and} \quad L_s^* = \frac{L_s}{\lambda_D} \end{aligned} \quad (9.19)$$

where ν_{p1} represents the packing parameter due to finite ion size of ion species "1". Note that v^*, ψ_{max}^*, ψ_{min}^*, L^*, a_1^*, and ν_{p1} were identical to or direct functions of those identified in Ref. [149] for the CV simulations of electric double layer capacitors with binary symmetric electrolytes. When considering binary asymmetric

electrolytes, three additional dimensionless numbers appear, namely, ν_{p2}, D_2^*, and z_2^*. The dimensionless numbers σ_s^* and L_s^* account for the charge transport in the electrode.

9.3.5 Constitutive Relations

In order to solve Equations (9.5) to (9.10) or Equations (9.13) to (9.18), the electrolyte properties ϵ_r, a_i, z_i, D_i, $c_{1\infty}$ along with the temperature T, and the surface potential $\psi_s(t)$ are needed. The present study focuses on binary electrolytes at room temperature $T = 298$ K with different ion diameter, diffusion coefficient, and/or valency. The electrolyte relative permittivity was taken as that of water $\epsilon_r = 78.5$ [253] while the effective ion diameter a_i ranged from 0.60 nm to 1.0 nm typical of solvated ion diameters [200]. The valencies ($z_1 : z_2$) corresponded also to realistic conditions including $1 : -1$, $1 : -2$, $2 : -2$, or $1 : -3$. The ion diffusion coefficients D_i varied from 1.957×10^{-9} m^2/s to 5.273×10^{-9} m^2/s representative of aqueous and organic electrolytes [253]. The initial and bulk ion concentrations was $c_{1,\infty} = 1.0$ mol/L and $c_{2,\infty} = -c_{1,\infty} z_1/z_2$ satisfying the overall electroneutrality condition. Moreover, the maximum and minimum surface electric potentials were $\psi_{max} = 0.5$ V and $\psi_{min} = -0.5$ V, respectively. The scan rate in actual CV measurements for electrical energy storage devices ranges typically from 10^{-3} to 200 V/s [31, 177, 333, 369, 370]. Here, the scan rate v varied over a wider range from 10^{-2} to 10^8 V/s. This was due to two main reasons. First, small electrode thickness ($0 - 100$ nm) was considered along with realistic values (> 1 μm) to validate the scaling analysis. The capacitance starts to decrease at very large scan rate for such small electrode thickness [149]. Second, asymptotic behaviors of electric double layers were explored at very large scan rates. Our previous study [149] established that electric double layers behave as a resistor under such conditions. Finally, the electrode electrical conductivity was chosen to be 10^{-5} to 10^2 S/m typical of carbon materials [357, 358].

9.3.6 Method of Solution

The governing Equations (9.5) and (9.6) were solved along with the boundary and initial conditions given by Equations (9.7) to (9.10) using the commercial finite element solver COMSOL 4.2. CV measurements were simulated by numerically imposing the periodic surface electric potential given by Equation (8.1).

Simulations of CV measurements were performed for at least three cycles. The numerical convergence criterion was defined such that the maximum relative difference in the predicted capacitive current density j_C was less than 1% when (i) reducing the mesh size by a factor of two and (ii) dividing the time step by two. The mesh size was the smallest at the electrode surfaces due to the large potential gradient and then gradually increased. Converged solutions were achieved by imposing a time step of $\Delta t \approx \tau_{CV}/800 = (\psi_{max} - \psi_{min})/800v$ with the mesh size $\Delta x/L = 5 \times 10^{-14}$ at the Stern/diffuse layer interface with a growth rate of 1.3 up to $\Delta x/L = 1/250$ in the rest of the domain. Based on these convergence criteria, the total number of finite elements was less than 1910 for all cases simulated in the present study.

9.3.7 Data Processing

The capacitive current density j_C from CV simulations was computed based on its definition as [149, 291, 323, 324, 391],

$$j_C(t) = -\epsilon_0 \epsilon_r \left. \frac{\partial^2 \psi}{\partial x \partial t} \right|_{x_L \text{ or } -x_L} \quad \text{at} \quad x_L = L - H \quad \text{or} \quad -x_L = -(L - H) \tag{9.20}$$

The corresponding dimensionless capacitive current density j_C^* at $x_L^* = L^* - a_1^*/2$ and $-x_L^* = -L^* + a_1^*/2$ is expressed as,

$$j_C^*(t^*) = \frac{j_C(t)}{F z_1 D_1 c_{1,\infty}/\lambda_D} = -\sum_{i=1}^{2} z_i^{*2} c_{i,\infty}^* \left. \frac{\partial^2 \psi^*}{\partial x^* \partial t^*} \right|_{x_L^* \text{ or } -x_L^*} \tag{9.21}$$

In order to reproduce typical CV measurements, the current densities $j_C(t)$ and $j_C^*(t^*)$ were plotted as functions of $\psi_s(t)$ and $\psi_s^*(t^*)$, respectively.

9.3.8 Validation

The numerical tool was validated based on existing solutions reported in the literature. The transient ion concentration and electric potential profiles were predicted by solving the PNP and MPNP models for binary and symmetric electrolytes ($N = 2$, $z_1 = -z_2 = z$, and $a_1 = a_2$) with constant surface electric potential. The results were successfully compared with the reported numerical solutions for $c_i(x,t)$ and $\psi(x,t)$ for a wide range of packing parameter ν_p and dimensionless surface potential ψ_s^* [146].

9.4 Results and Discussions

Results in the Appendix (Figures A.2 and A.3) demonstrate that half-domain CV simulations should only be used for symmetric electrolytes while the full domain must be simulated for asymmetric electrolytes. Consequently, all the following CV simulations were performed for the entire domain consisting of electrolyte solution between two identical planar electrodes.

9.4.1 Asymmetric Versus Symmetric Electrolytes

9.4.1.1 Effect of Asymmetric Ion Diameter

Figure 9.2 shows CV curves predicted for three cases with different ion diameters, namely (i) $a_1 = a_2 = 0.60$ nm, (ii) $a_1 = 0.66$ nm and $a_2 = 0.60$ nm, and (iii) $a_1 = a_2 = 0.66$ nm. The ion valencies and diffusion coefficients were $z_1 = -z_2 = 1$ and $D_1 = D_2 = 1.957 \times 10^{-9}$ m^2/s, respectively. Other parameters were $c_{1,\infty} = 1$ mol/L, $v = 10^4$ V/s, $L = 200$ μm, $\psi_{max} = \psi_{min} = 0.5$ V, $T = 298$ K, and $\epsilon_r = 78.5$. Results were obtained by solving the GMPNP model with a Stern layer [Equations (9.5) to (9.10)] without accounting for the potential drop across the electrodes corresponding to $\sigma_s \to \infty$ S/m or $L_s = 0$ m. Figure 9.2 demonstrates that the

current density j_C for asymmetric electrolyte with $a_1 = 0.66$ nm and $a_2 = 0.60$ nm lay between those obtained for symmetric electrolytes with ion diameter a equals to 0.66 nm and 0.60 nm. The relative difference in j_C between asymmetric and symmetric electrolytes was about 9%. Figure 9.2 also indicates that the predicted current density j_C increased with decreasing ion diameter. This can be attributed to the fact that smaller ions have larger maximum ion concentrations $c_{i,max}$ and thus feature a larger gradient in electric potential near the electrode surface [95]. This, in turn, led to a larger capacitive current density according to Equation (9.20). Overall, these results demonstrate that the unequal ion size needs to be accounted for in order to accurately predict the current density for asymmetric electrolytes.

9.4.1.2 Effect of Asymmetric Valency

Figure 9.3 shows the CV curves predicted for electrolytes with different valencies, namely (i) $z_1 = -z_2 = 1$, (ii) $z_1 = 1$ and $z_2 = -2$, and (iii) $z_1 = -z_2 = 2$. Here, the ion diameters and diffusion coefficients were identical such that $a_1 = a_2 = 0.60$ nm, $D_1 = D_2 = 1.957 \times 10^{-9}$ m^2/s, and $L_s = 0$ m. It is evident that the predicted current density j_C for asymmetric valency $z_1 = 1$ and $z_2 = -2$ lay between those obtained for symmetric valency with $z_1 = -z_2 = 1$ and $z_1 = -z_2 = 2$. The relative difference in current density j_C between asymmetric and symmetric electrolytes was about 9%. Moreover, j_C increased with increasing valency $|z_i|$. This can be attributed to the fact that increasing the valency $|z_i|$ led to increasing the amount of charges accumulated near the electrode surface. This, in turn, led to a larger local electric field near the electrode surface and thus larger current density.

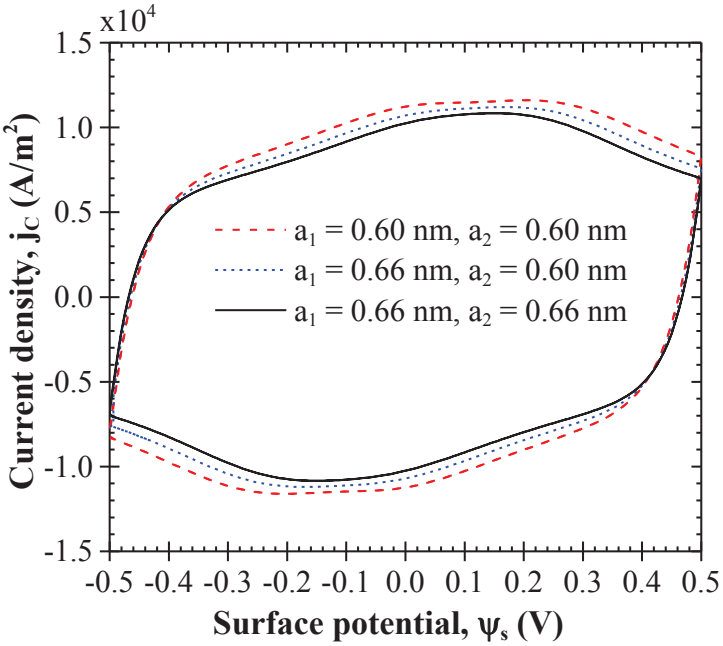

Figure 9.2: Predicted j_C versus ψ_s curves from CV simulations for three cases with different ion diameters, namely, (i) $a_1 = a_2 = 0.60$ nm, (ii) $a_1 = 0.66$ and $a_2 = 0.60$ nm, and (iii) $a_1 = a_2 = 0.66$ nm. Results were obtained by solving the GMPNP model with a Stern layer [Equations (9.5) to (9.10)] without accounting for the potential drop across the electrodes corresponding to $\sigma_s \to \infty$ S/m or $L_s = 0$ m. Other parameters were $c_{1,\infty} = 1$ mol/L, $v = 10^4$ V/s, $L = 200$ μm, $\psi_{max} = \psi_{min} = 0.5$ V, $T = 298$ K, and $\epsilon_r = 78.5$.

9.4.1.3 Effect of Asymmetric Diffusion Coefficient

Figures 9.4 show j_C versus ψ_s predicted at (a) low scan rate $v = 10^2$ V/s and (b) high scan rate $v = 10^5$ V/s for three cases with different ion diffusion coefficients, namely (i) $D_1 = D_2 = 2.69D_0$, (ii) $D_1 = D_0$ and $D_2 = 2.69D_0$, and (iii) $D_1 = D_2 = D_0$ with $D_0 = 1.957 \times 10^{-9}$ m^2/s. The ion diameter and valency were identical namely, $a_1 = a_2 = 0.60$ nm and $z_1 = -z_2 = 1$ while the electrode thickness was zero, i.e., $L_s = 0$ m. Figure 9.4a demonstrates that, at low scan rate $v = 10^2$ V/s, the predicted CV curves overlapped for all three cases despite

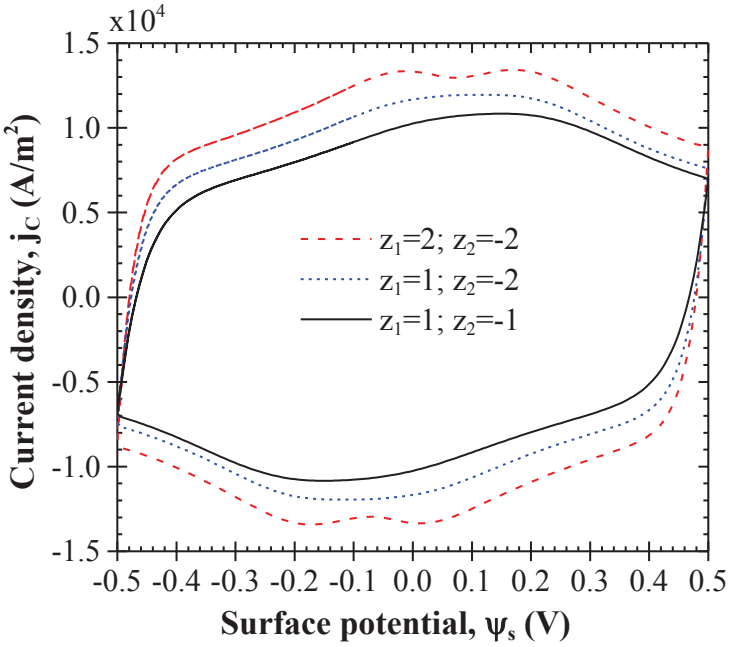

Figure 9.3: Predicted j_C versus ψ_s curves from CV simulations for three cases with different valencies, namely, (i) $z_1 = -z_2 = 2$, (ii) $z_1 = 1$ and $z_2 = -2$, and (iii) $z_1 = -z_2 = 1$. The model and other parameters were identical to those used to generate the results shown in Figure 9.2.

differences in diffusion coefficients. Moreover, the CV curves were symmetric about the $j_C = 0$ axis. Note that similar phenomena were also observed in CV simulations for binary and symmetric electrolytes [149]. This can be attributed to the fact that ion transport is diffusion-independent at low scan rates [149] and is controlled by the electric field. On the other hand, Figure 9.4b demonstrates that the predicted CV curves became distorted at large scan rate $v = 10^5$ V/s. Here, the predicted current density j_C and thus the capacitance increased with increasing ion diffusion coefficient D_1 or D_2. Indeed, larger diffusion coefficients enable ions to better follow the rapid variations in electric potential [149]. These results demonstrate that asymmetric ion diffusion coefficients must be accounted for in CV simulations at large scan rates but have no effect on CV curves at low scan rates.

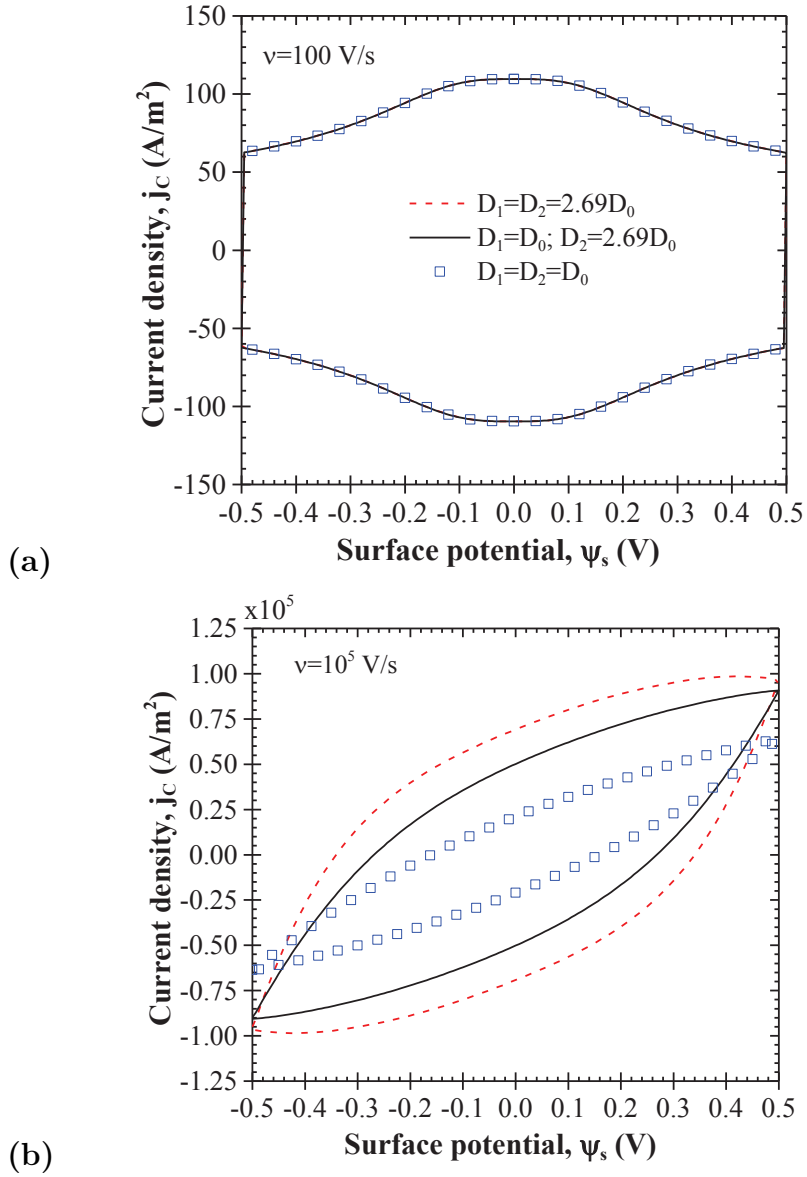

Figure 9.4: Predicted j_C versus ψ_s curves from CV simulations for (a) $v = 10^2$ V/s and (b) $v = 10^5$ V/s. Three cases with different ion diffusion coefficients were considered, namely, (i) $D_1 = D_2 = 2.69D_0$, (ii) $D_1 = D_0$ and $D_2 = 2.69D_0$, and (iii) $D_1 = D_2 = D_0$ along with $D_0 = 1.957 \times 10^{-9}$ m^2/s. The model and other parameters were identical to those used to generate the results shown in Figure 9.2.

9.4.2 Dimensional Analysis

Table 9.1 summarizes the different values of v, L, T, ψ_{max}, ψ_{min}, a_i, D_i, z_i, and $c_{i\infty}$ for four different cases of binary asymmetric electrolytes considered. Parameters used in Case 1 corresponded to aqueous asymmetric electrolyte KOH [149, 200, 253]. Note that the dimensionless numbers for all four cases were identical, namely, $v^* = 1.8 \times 10^{-5}$, $\psi^*_{max} = -\psi^*_{min} = 19.5$, $L^* = 3.29 \times 10^5$, $a^*_1 = 2.17$, $\nu_{p1} = 0.346$, $\nu_{p2} = 0.26$, $D^*_2 = 2.5$, $z^*_2 = -1$, $\sigma^*_s \to \infty$, and $L^*_s = 0$. Figures 9.5a shows the predicted j_C versus ψ_s curves obtained for these four cases. Results were obtained by numerically solving the generalized MPNP model with a Stern layer [Equations (9.5) to (9.10)]. Figure 9.5a indicates that the CV curves were significantly different in these four cases. However, Figure 9.5b shows that the same data plotted in terms of dimensionless current density j^*_C versus dimensionless surface potential ψ^*_s collapsed on a single CV curve. Note that such self-similar behaviors were also observed for cases with $z^*_2 = -2$ and $z^*_2 = -3$. Overall, these results illustrated that the governing equations and the boundary and initial conditions were properly scaled by parameters defined in Equations (9.11). More importantly, they show that the electric double layer dynamics for binary asymmetric electrolytes near planar electrodes in CV measurements were governed by eleven dimensionless similarity parameters, namely, v^*, ψ^*_{max}, ψ^*_{min}, L^*, a^*_1, ν_{p1}, ν_{p2}, D^*_2, z^*_2, σ^*_s, and L^*_s given by Equation (9.19).

Moreover, a dimensionless areal integral capacitance can be defined as

$$C^*_s = \frac{C_s}{z_1 e N_A D_1 c_{1,\infty}/\lambda_D v} = \frac{1}{\psi^*_{max} - \psi^*_{min}} \oint \frac{j^*_C}{2v^*} d\psi^*_s \tag{9.22}$$

where C_s is defined in Equation (8.2). Graphically, C^*_s corresponds to the area enclosed by the j^*_C versus ψ^*_s curve. Figure 9.5b demonstrates that C^*_s depends only on the eleven dimensionless numbers so that $C^*_s = f(v^*, \psi^*_{max}, \psi^*_{min}, L^*, a^*_1, \nu_{p1}, \nu_{p2}, D^*_2, z^*_2, \sigma^*_s, L^*_s)$. This relation can be used to formulate design rules for EDLCs with asymmetric electrolytes. However, finding this multidimensional function falls be-

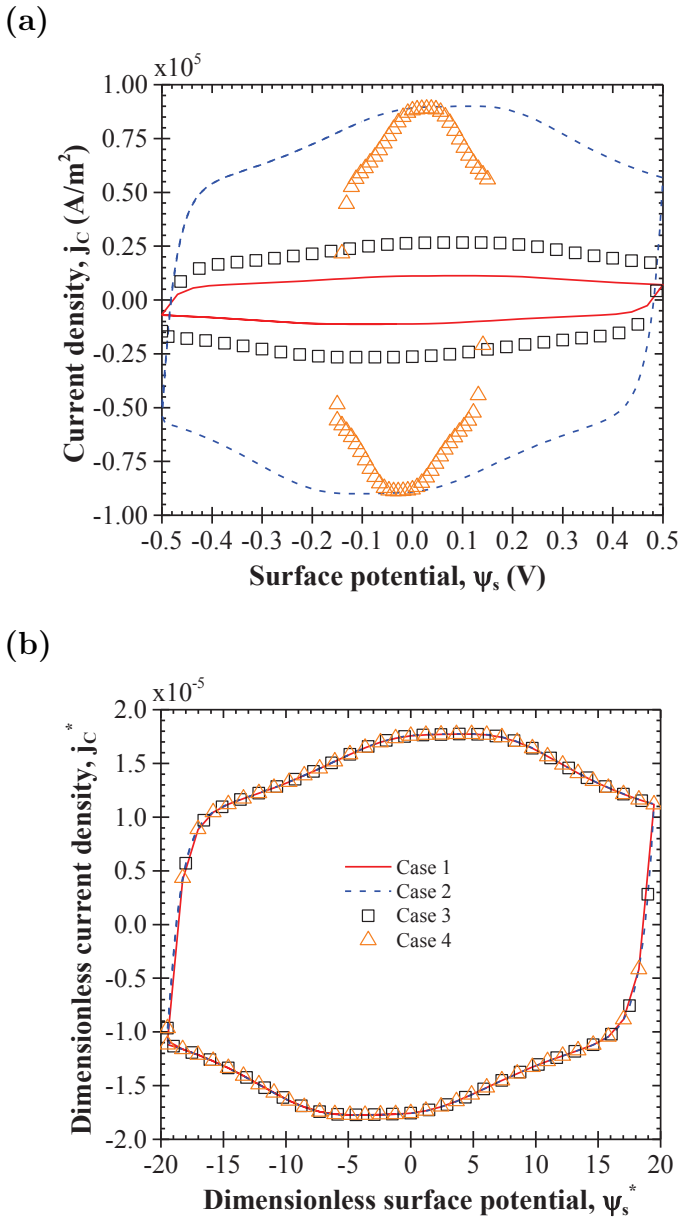

Figure 9.5: Predicted (a) j_C versus ψ_s curves and (b) j_C^* versus ψ_s^* curves from CV simulations for four cases with parameters given in Table 9.1. Results were obtained by numerically solving the generalized MPNP model with a Stern layer [Equations (9.5) to (9.10)] for $v^* = 1.8 \times 10^{-5}$, $\psi_{max}^* = -\psi_{min}^* = 19.5$, $L^* = 3.29 \times 10^5$, $a_1^* = 2.17$, $\nu_{p1} = 0.346$, $\nu_{p2} = 0.26$, $D_2^* = 2.5$, $z_2^* = -1$, $\sigma_s^* \to \infty$, and $L_s^* = 0$.

yond the scope of this study.

Table 9.1: Parameters used in CV simulations reported in Figure 9.5. In these four cases, the dimensionless numbers were identical and equal to $v^* = 1.8 \times 10^{-5}$, $\psi^*_{max} = -\psi^*_{min} = 19.5$, $L^* = 3.29 \times 10^5$, $a^*_1 = 2.17$, $\nu_{p1} = 0.346$, $\nu_{p2} = 0.26$, $D^*_2 = 2.5$, $z^*_2 = -1$, $\sigma^*_s \to \infty$, and $L^*_s = 0$.

	v	L	T	$\psi_{max} = -\psi_{min}$	ϵ_r	a_1	a_2	D_1	D_2	z_1	z_2	$c_{1\infty}$
	(V/s)	**(μm)**	**(K)**	**(V)**	$--$	**(nm)**	**(nm)**	**(m^2/s)**	**(m^2/s)**	$--$	$--$	**(mol/L)**
Case 1	10^4	100	298	0.5	78.5	0.66	0.60	2×10^{-9}	5×10^{-9}	1	-1	1
Case 2	2×10^4	50	298	0.5	157	0.33	0.30	1×10^{-9}	2.5×10^{-9}	1	-1	8
Case 3	1.33×10^4	75	298	0.5	104.7	0.495	0.45	1.5×10^{-9}	3.75×10^{-9}	1	-1	2.37
Case 4	1.33×10^4	75	89.4	0.15	348.9	0.495	0.45	5×10^{-8}	1.25×10^{-9}	1	-1	2.37

Finally, Figure 9.6 shows the predicted j_C^* versus ψ_s^* curves for three cases with $z_2^* = -1, -2$, and -3, respectively. The model and the other ten dimensionless numbers were identical to those used to generate the results shown in Figure 9.5. It is evident that j_C^* and therefore C_s^* increased as z_2^* decreased (i.e., increasing $|z_2^*|$) due to the increase in the amount of charges accumulated at the electrode surface which induced a larger electric current.

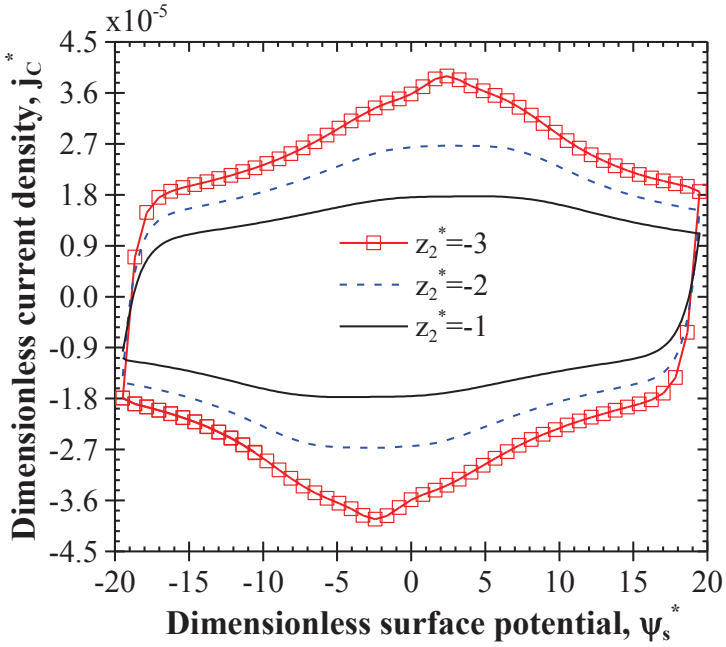

Figure 9.6: Predicted j_C^* versus ψ_s^* curves from CV simulations for three different values of z_2^*, namely, $z_2^* = -1,\ -2$, and -3. The model and other dimensionless numbers were identical to those used to generate the results shown in Figure 9.5.

9.4.3 Capacitance Versus Scan Rate

Figure 9.7a shows the double layer areal integral capacitance C_s predicted from CV simulations and estimated using Equation (8.2) as a function of scan rate v ranging from 10^{-2} to 10^7 V/s for 17 cases of binary asymmetric electrolytes without accounting for the potential drop across the electrodes. This corresponds to cases with infinitely large electrode electrical conductivity ($\sigma_s \to \infty$ S/m)

or zero electrode thickness ($L_s \rightarrow 0$ m). Table 9.2 summarizes the values of the ten dimensionless parameters L^*, z_2^*, $\psi_{max}^* = -\psi_{min}^*$, D_2^*, a_1^*, ν_{p1}, ν_{p2}, σ_s^*, and L_s^* along with the maximum capacitances $C_{s,0}$ corresponding to the plateau observed in C_s versus v at low scan rates. Note that $C_{s,0}$ depends on a variety of parameters including ψ_s, a_1, a_2, z_1, z_2, and $c_{1\infty}$. However, it falls beyond the scope of this manuscript to find an analytical expression relating these parameters for asymmetric electrolytes. A remarkably broad range of values were considered for each dimensionless number. It is evident that these C_s versus v curves as well as $C_{s,0}$ were significantly different from one another. Figure 9.7b shows the same data as those shown in Figure 9.7a but plotted in terms of $C_s/C_{s,0}$ as a function of $2v^*L^*/[(1+D_2^*)(\psi_{max}^* - \psi_{min}^*)]$. It is interesting to note that all the curves collapsed on a single line, irrespective of the different values of L^*, z_2^*, $\psi_{max}^* = -\psi_{min}^*$, D_2^*, a_1^*, ν_{p1}, and ν_{p2}. The Appendix presents the effects of each parameter separately. To the best of our knowledge, the present study is the first to identify this self-similar behavior of electric double layer integral capacitance in CV measurements. Fitting the dimensionless data shown in Fig. 9.7b yields the following correlation with a coefficient of determination equal to 0.999,

$$\frac{C_s}{C_{s,0}} = \frac{1}{1 + \left[\dfrac{2v^*L^*/(1+D_2^*)(\psi_{max}^* - \psi_{min}^*)}{1.22}\right]^{1.44}} \tag{9.23}$$

The dimensionless x-axis in Figure 9.7b can be interpreted as the ratio of two time scales,

$$\frac{2v^*L^*}{(1+D_2^*)(\psi_{max}^* - \psi_{min}^*)} = \frac{2\lambda_D L/(D_1+D_2)}{(\psi_{max} - \psi_{min})/v} = \frac{\tau_{RC}}{\tau_{CV}} \tag{9.24}$$

where τ_{RC} is the "RC time scale" for binary asymmetric electrolytes corresponding to the characteristic time of ions' electrodiffusion [128] and τ_{CV} is the half cycle period of CV measurements. They are expressed as,

$$\tau_{RC} = \sqrt{\tau_L \tau_D} = \frac{\lambda_D L}{(D_1+D_2)/2} \quad \text{and} \quad \tau_{CV} = \frac{\psi_{max} - \psi_{min}}{v} \tag{9.25}$$

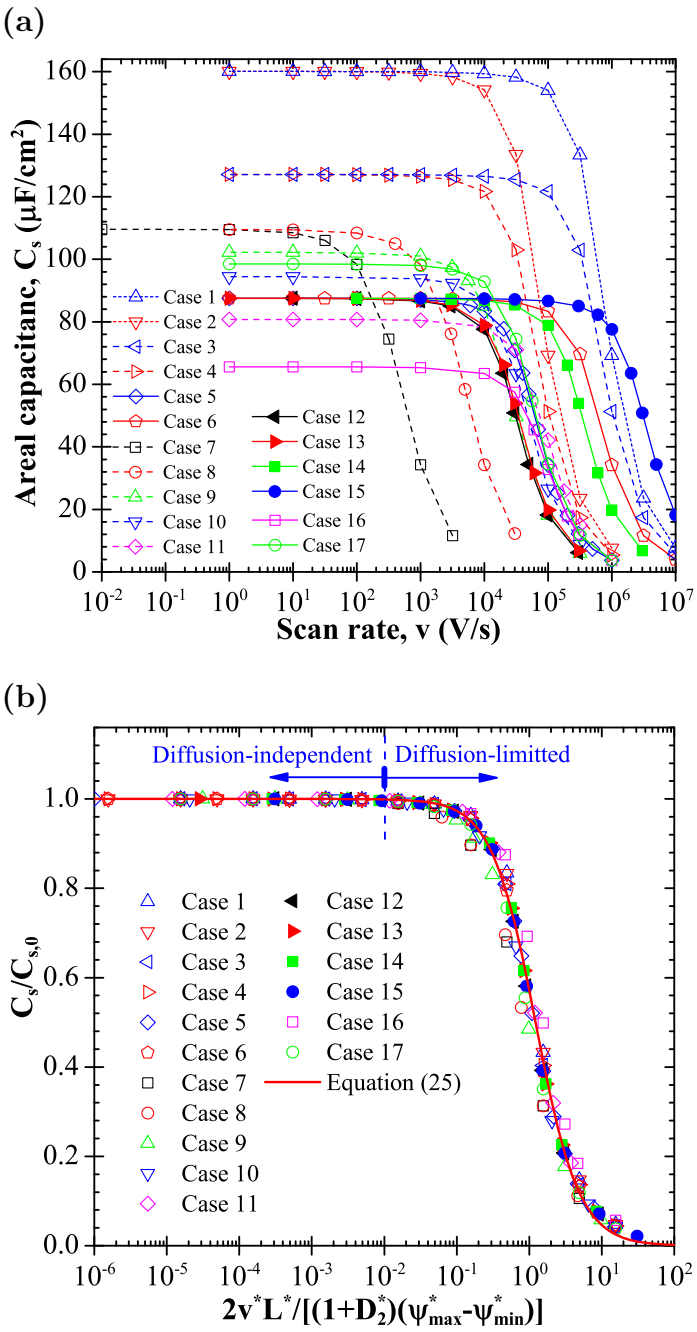

Figure 9.7: Predicted (a) capacitance C_s as a function of scan rate v and (b) ratio $C_s/C_{s,0}$ as a function of $2v^*L^*/[(1+D_2^*)(\psi^*_{max}-\psi^*_{min})]$ obtained from CV simulations for cases 1 to 17 without accounting for the potential drop across the electrodes (i.e., $\sigma_s^* \to \infty$ or $L_s^* = 0$) with dimensionless parameters L^*, z_2^*, $\psi^*_{max} = -\psi^*_{min}$, D_2^*, a_1^*, ν_{p1}, and ν_{p2} summarized in Table 9.2.

Here, $\tau_L = 2L^2/(D_1 + D_2)$ is the time scale for ion diffusion in binary asymmetric electrolytes and $\tau_D = 2\lambda_D^2/(D_1 + D_2)$ has been termed as the "charge relaxation time scale" [128]. Note that τ_{RC} reduces to the corresponding "RC time scale" of binary symmetric electrolytes when $D_2^* = 1$ as considered in Refs. [128, 130, 152]. Figure 9.7b indicates that two regimes can be clearly identified: (i) $2v^*L^*/[(1 + D_2^*)(\psi_{max}^* - \psi_{min}^*)] \ll 1$ or $\tau_{RC} \ll \tau_{CV}$, corresponds to the quasi-equilibrium or ion diffusion-independent regime and (ii) $2v^*L^*/[(1 + D_2^*)(\psi_{max}^* - \psi_{min}^*)] \gg 1$ or $\tau_{RC} \gg \tau_{CV}$, corresponds to ion diffusion-limited regime.

Table 9.2: Dimensionless parameters for 29 cases of CV simulations reported in Figures 9.7 and 9.8 along with the respective values of maximum capacitance $C_{s,0}$.

	L^*	z_2^*	$\psi_{max}^* = -\psi_{min}^*$	D_2^*	a_1^*	ν_{p1}	ν_{p2}	σ_s^*	L_s^*	$C_{s,0}$ $(\mu F/\mathbf{cm}^2)$
Case 1	32900	-3	19.5	1	2.17	0.346	0.346	∞	0	160.1
Case 2	329000	-3	19.5	1	2.17	0.346	0.346	∞	0	160.1
Case 3	32900	-2	19.5	1	2.17	0.346	0.346	∞	0	127.1
Case 4	329000	-2	19.5	1	2.17	0.346	0.346	∞	0	127.1
Case 5	32900	-1	19.5	1	2.17	0.346	0.346	∞	0	87.5
Case 6	329000	-1	19.5	1	2.17	0.346	0.346	∞	0	87.5
Case 7	329000	-1	0.195	1	2.17	0.346	0.346	∞	0	109.6
Case 8	329000	-1	1.95	1	2.17	0.346	0.346	∞	0	109.5
Case 9	329000	-1	9.75	1	2.17	0.346	0.346	∞	0	102.2
Case 10	329000	-1	14.625	1	2.17	0.346	0.346	∞	0	94.44
Case 11	329000	-1	25.35	1	2.17	0.346	0.346	∞	0	87.77
Case 12	329000	-1	19.5	0.01	2.17	0.346	0.346	∞	0	87.5
Case 13	329000	-1	19.5	0.1	2.17	0.346	0.346	∞	0	87.5
Case 14	329000	-1	19.5	10	2.17	0.346	0.346	∞	0	87.5
Case 15	329000	-1	19.5	100	2.17	0.346	0.346	∞	0	87.5
Case 16	329000	-1	19.5	1	3.06	0.97	0.26	∞	0	65.6
Case 17	329000	-1	19.5	1	1.97	0.26	0.26	∞	0	98.5

Continued on next page

Table 9.2 – *Continued from previous page*

	L^*	z_2^*	$\psi_{max}^* = -\psi_{min}^*$	D_2^*	a_1^*	ν_{p1}	ν_{p2}	σ_s^*	L_s^*	$C_{s,0}$ $(\mu F/\mathbf{cm}^2)$
Case 18	263.1	-1	19.5	1	2.17	0.346	0.346	1.61×10^{-7}	329	87.5
Case 19	263.1	-1	19.5	1	2.17	0.346	0.346	1.61×10^{-4}	329	87.5
Case 20	263.1	-1	19.5	1	2.17	0.346	0.346	1.61×10^{-1}	329	87.5
Case 21	263.1	-1	19.5	1	2.17	0.346	0.346	∞	329	87.5
Case 22	32900	-1	19.5	1	2.17	0.346	0.346	1.61×10^{-4}	0	87.5
Case 23	32900	-1	19.5	1	2.17	0.346	0.346	1.61×10^{-4}	329	87.5
Case 24	32900	-1	19.5	1	2.17	0.346	0.346	1.61×10^{-4}	3290	87.5
Case 25	32900	-1	19.5	1	2.17	0.346	0.346	1.61×10^{-4}	98400	87.5
Case 26	16400	-3	19.5	100	2.17	0.346	0.346	1.61×10^{-4}	233000	101.4
Case 27	32900	-2	19.5	10	2.17	0.346	0.346	1.61×10^{-4}	98400	97.0
Case 28	403000	-2	19.5	1	2.17	0.346	0.346	0.0566	121000	97.0
Case 29	403000	-2	19.5	10	2.17	0.346	0.346	0.0566	121000	97.0

9.4.4 Effect of The Electrode

The above simulations ignored the potential drop across the electrodes. Figure 9.8a shows the double layer areal integral capacitance C_s predicted from CV simulations as a function of scan rate v ranging from 10^{-2} to 10^{8} V/s for 12 cases accounting for charge transport in the electrodes. Table 9.2 summarizes the values of the eleven dimensionless parameters L^*, z_2^*, $\psi_{max}^* = -\psi_{min}^*$, D_2^*, a_1^*, ν_{p1}, ν_{p2}, σ_s^*, and L_s^* along with the maximum capacitances $C_{s,0}$ for cases 18 to 29. It is evident that the curves C_s versus v were significantly different from one another due to the broad range of parameters considered. Figure 9.8b shows the same data as those shown in Figure 9.8a but plotted in terms of $C_s/C_{s,0}$ as a function of $\tau_{RC}/\tau_{CV}(1 + 80/\sigma_s^*)$. The fitted curve given by Equation (9.23) for cases ignoring the potential drop across the electrodes ($\sigma_s^* \to \infty$ or $L_s^* \to 0$) was also shown in Figure 9.8b for comparison purposes. It is interesting to note that all the curves collapsed on a single line, irrespective of the different values of L^*, z_2^*, $\psi_{max}^* = -\psi_{min}^*$, D_2^*, a_1^*, ν_{p1}, ν_{p2}, σ_s^*, and L_s^*.

The dimensionless x-axis in Figure 9.8b can be interpreted as,

$$\frac{\tau_{RC}}{\tau_{CV}}\left(1 + \frac{80}{\sigma_s^*}\right) = \frac{\tau_{RC}}{\tau_{CV}}\left(1 + 80\frac{\tau_s}{\tau_d}\right) \tag{9.26}$$

where $\sigma_s^* = \tau_d/\tau_s$ represents the ratio of characteristic charge transport time scale in the electrolyte τ_d to that in the electrode τ_s as discussed previously. Note that when σ_s^* is very large (e.g., $\sigma_s^* \gg 80$), the charge transport in the electrode is much faster than that in the electrolyte. Then, it suffices to simulate the electrolyte in CV simulations.

9.5 Conclusions

This chapter developed a generalized modified Poisson-Nernst-Planck model for simulating electric double layer dynamics. This model was derived from first principles based on excess chemical potential and Langmuir activity coefficient

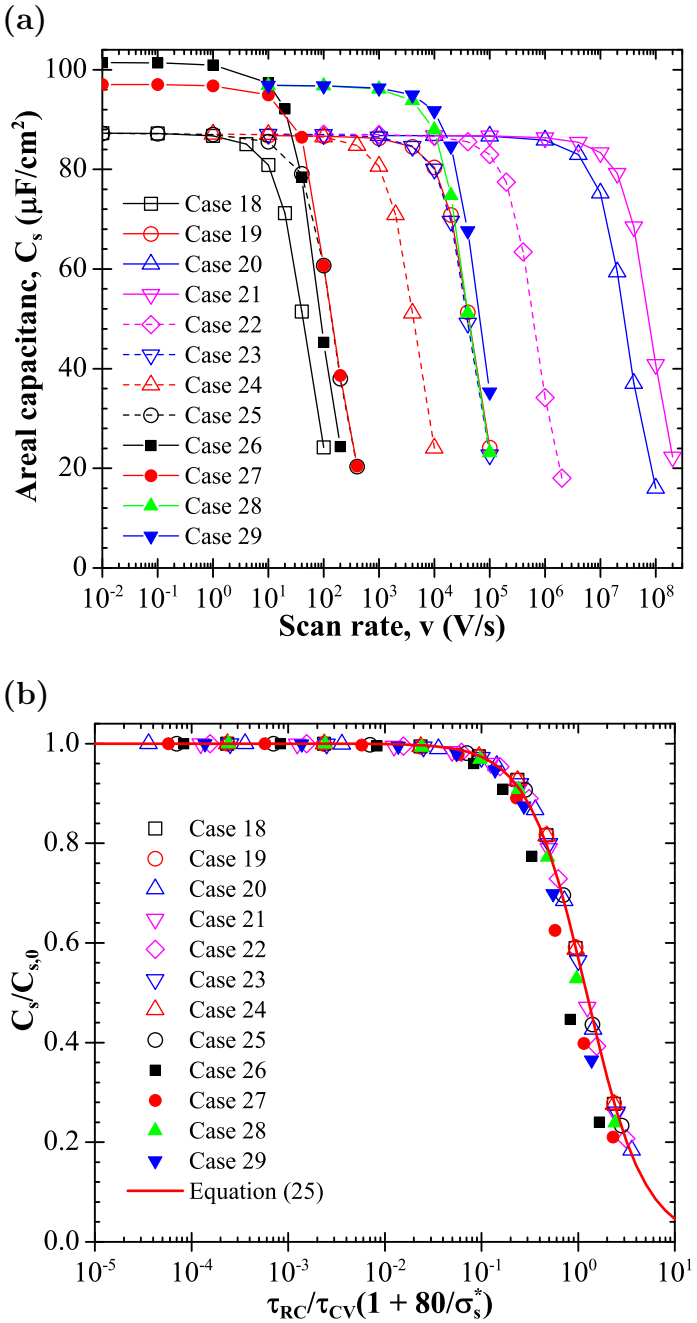

Figure 9.8: Predicted (a) capacitance C_s as a function of scan rate v and (b) ratio $C_s/C_{s,0}$ as a function of $\tau_{RC}/\tau_{CV}(1 + 80/\sigma_s^*)$ obtained from CV simulations for cases 18 to 29 with dimensionless parameters L^*, z_2^*, $\psi_{max}^* = -\psi_{min}^*$, D_2^*, a_1^*, ν_{p1}, ν_{p2}, σ_s^*, and L_s^* summarized in Table 9.2.

accounting simultaneously for (1) asymmetric electrolytes with (2) multiple ion species of (3) finite ion size, and (4) Stern and diffuse layers. This study established that asymmetric ion diameters and valencies must be accounted for in CV simulations with asymmetric electrolytes for all scan rates. By contrast, asymmetric ion diffusion coefficient affected the CV curves only at large scan rates.

Dimensional analysis of the governing equations was also performed for CV measurements with planar electrodes. Eleven dimensionless numbers given by Equation (9.19) were identified to govern the CV measurements of electric double layer in binary asymmetric electrolytes between two identical planar electrodes of finite thickness. For the first time, a self-similar behavior was identified for the electric double layer integral capacitance estimated from CV measurements with binary asymmetric electrolytes and planar electrodes. Physical interpretation was also provided. This model provides a theoretical framework to investigate more complex situations with asymmetric electrolytes and/or multiple ion species such as redox reactions in pseudocapacitors and the interplay of Faradaic and capacitive currents encountered in fast-scan cyclic voltammetry.

CHAPTER 10

Analysis of Cyclic Voltammetry for Pseudocapacitive Materials

10.1 Introduction

As previously discussed, pseudocapacitors hold great promises for meeting the energy and power demands in current and emerging applications [1, 25, 27–30, 45–59, 392]. In-depth understanding of transport phenomena in pseudocapacitors can enable their optimization in a rational and efficient way.

An semi-empirical approach based on cyclic voltammetry measurements has been developed and used extensively to discriminate the contributions of electric double layers and redox reactions to the total current and capacitance [29, 30, 177, 369, 370, 393–406]. Specifically, the measured total current j_t at a given surface potential ψ_s is assumed to relate to the scan rate v according to the semi-empirical relationship [29, 30, 177, 369, 370, 393–406],

$$j_t(\psi_s) = k_1(\psi_s)v + k_2(\psi_s)v^{1/2} \tag{10.1}$$

This approach was initially supported by two facts. First, the capacitive current j_C is known to vary linearly with the scan rate v in the absence of redox reactions, i.e., $j_C = k_1 v$ and $j_F = 0$ [9, 10]. Second, the Faradaic current j_F due to surface redox reactions in a semi-infinite electrolyte domain without ion intercalation in the electrode is proportional to $v^{1/2}$ when ignoring the presence of electric double layers, i.e., $j_F = k_2 v^{1/2}$ and $j_C = 0$ [9, 407–410]. The coefficients k_1 and k_2 are

semi-empirical coefficients determined experimentally and depend on the potential ψ_s imposed at the current collector. In practice, Equation (10.1) can be written as,

$$\frac{j_t}{v^{1/2}} = k_1 v^{1/2} + k_2 \tag{10.2}$$

Thus, k_1 and k_2 for a given electric potential ψ_s can be determined as the the slope and intercept of the $j_t/v^{1/2}$ versus $v^{1/2}$ plot, respectively [29,30,177,369,370,393–406]. To the best of our knowledge, despite its extensive usage, this semi-empirical analysis has not been rigorously demonstrated particularly when electric double layers, redox reactions, and ion insertion in the electrode occur simultaneously.

This study aims to develop a physicochemical model for simulating pseudocapacitors and asymmetric (hybrid) supercapacitors by accurately and simultaneously accounting for the electric double layer coupled with redox reaction at the electrode/electrolyte interface. It also aims to rigorously demonstrate Equation (10.1) used widely in analyzing pseudocapacitors.

10.2 Background

Equivalent RC circuit/transmission line models [44, 123, 278, 411–415] have been used to study the charging/discharging dynamics of pseudocapacitors. However, the equivalent RC circuit/transmission line models suffer from drawbacks as stated in Ref. [304]: *"First, it is possible for two different models to produce the same impedance response [...]. Second, the overall impedance expressions corresponding to most models give little or no direct information about the physical meaning of the elements for such models."* In fact, these models have to be fitted with experimental data to retrieve the resistances and capacitances. Moreover, the classical RC circuit models, consisting of constant resistances and capacitances, neglect ion diffusion and non-uniform ion concentration in the electrolyte [128–130]. Therefore, these models are invalid for electric double layers at large ion

concentrations and electric potential, typical of energy storage devices [128–130].

Alternatively, homogeneous models were also developed for pseudocapacitors [134,136,138–142,144,416–420]. These models treat the heterogeneous microstructure of the mesoporous electrodes as homogeneous with some effective macroscopic properties determined from effective medium approximation and depending on porosity and specific area [134, 136, 138–142, 144, 416–420]. Moreover, these models typically imposed the double layer areal capacitance (in F/m^2) or volumetric capacitance (in F/m^3) instead of predicting them [134,136,138–142,144,416–420]. In addition, the double layer capacitances imposed in these models were typically assumed to be constant and independent of electric potential [134, 136, 138–142, 144, 416–420]. However, the double layer capacitance is known to vary nonlinearly with electric potential at large electric potentials and electrolyte concentrations [4, 95, 97, 102]. In addition, these simulations have been focused mainly on supercapacitors consisting of porous hydrous RuO_2 electrodes and electrolytes such as H_2SO_4 [134, 136, 138–141, 416–419] with redox reactions, for the positive electrode, given by [134, 136, 138–141, 416–419],

$$H_{0.8}RuO_2{\cdot}xH_2O \underset{\text{discharge}}{\overset{\text{charge}}{\rightleftharpoons}} H_{0.8-\delta}RuO_2{\cdot}xH_2O + \delta H^+ + \delta e^- \tag{10.3}$$

and for the negative electrode, given by [134, 136, 138–141, 416–419],

$$H_{0.8}RuO_2{\cdot}xH_2O + \delta H^+ + \delta e^- \underset{\text{discharge}}{\overset{\text{charge}}{\rightleftharpoons}} H_{0.8+\delta}RuO_2{\cdot}xH_2O \tag{10.4}$$

The literature, however, lacks studies for other pseudocapacitive materials.

Finally, first-principle molecular dynamic (MD) simulations have been performed in recent years to explore the fundamental electrochemical behaviors of pseudocapacitive materials including RuO_2 [421–423], TiO_2 [424], MnO_2 [425], and MoO_3 [426]. However, MD simulations are limited to extremely small time- and length-scales both far smaller than those encountered in actual supercapacitor experiments. Therefore, they are inadequate for performing extensive and

systematic study of actual devices due to their computational cost and time requirement.

This chapter aims to develop a continuum model to accurately simulate the coupled transport and electrochemical phenomena in pseudocapacitors and asymmetric supercapacitors. It is unique in that it simultaneously accounts for (i) the charge transport in both electrode and electrolyte, (ii) the electric double layer dynamics coupled with redox reaction, as well as (iii) finite ion sizes and the associated Stern layer. It also aims to rigorously examine the semi-empirical approach based on cyclic voltammetry measurements and the validity of Equations (10.1) and (10.2) used for analyzing pseudocapacitors.

10.3 Analysis

10.3.1 Schematics and Assumptions

Figure 10.1 shows the schematic of the computational domain and of the associated coordinate system used to simulate the electrolyte solution consisting of $LiClO_4$ in propylene carbonate (PC) of concentration c_∞ between two planar electrodes. The region of electrolyte solution consists of three layers corresponding to a Stern layer of thickness H near each electrode surface and a diffuse layer beyond. The present study considers an asymmetric supercapacitor consisting of a cathode made of transition metal oxide M_pO_q and an anode made of carbon. The following redox reaction was assumed to take place at the Stern/diffuse layer interface located at $x = -L + H$ near the cathode,

$$n\mathrm{Li}^+ + \mathrm{M}_p\mathrm{O}_q + n\mathrm{e}^- \rightleftharpoons \mathrm{Li}_n\mathrm{M}_p\mathrm{O}_q \tag{10.5}$$

To make the problem mathematically tractable, the following assumptions were made: (1) electrodiffusion of Li^+ and ClO_4^- ions in the electrolyte and intercalation of Li atoms in the electrode were one-dimensional as often assumed in

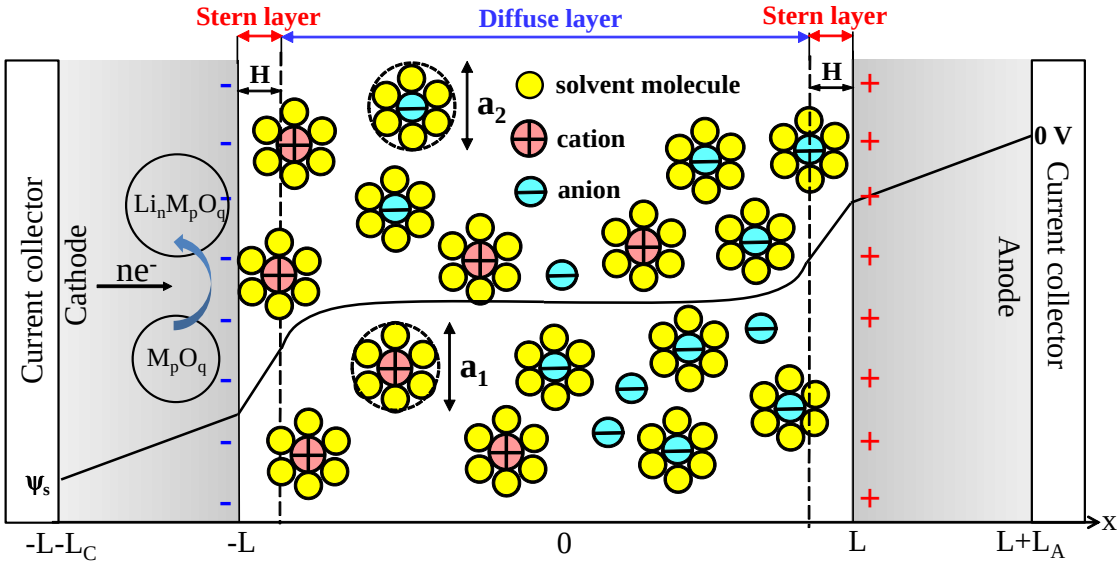

Figure 10.1: Schematic of the computational domain and coordinate system used in simulating asymmetric supercapacitors with planar electrodes.

simulations of supercapacitors [134, 136, 138–142, 144, 148, 149, 260, 416–420]. (2) The Stern layer thickness H was approximated as the radius of the largest solvated ions [260] so as to satisfy the electroneutrality condition. The approach defining multiple Stern layers at a given electrode surface was not retained for reasons discussed in Ref. [260]. (3) The electrode and electrolyte transport properties were constant. (4) Isothermal conditions prevailed throughout the electrode and electrolyte. Assumptions (3) and (4) were satisfied for small temperature variation in the device. (5) Advection of the electrolyte was assumed to be negligible due to the absence of electrolyte flow conditions. (6) The redox reaction was assumed to take place at the Stern/diffuse layer interface near the cathode at $x = -L + H$ [9, 132, 250, 360, 427, 428]. Note that redox reactions in batteries and supercapacitors are typically considered as "heterogeneous" such that they take place only at the electrode/electrolyte interface [9, 132, 250, 360, 427, 428]. (7) Li atoms were able to diffuse or intercalate into the electrode after the reduction reaction [429–431]. This condition was realistic for pseudocapacitors or asymmetric

supercapacitors with electrodes made of Nb_2O_5 or MnO_2 [30, 142, 144, 415, 420], and (8) the specific ion adsorption due to non-electrostatic forces was assumed to be negligible. This assumption was considered reasonable based on the fact that previous simulations of EDLCs [7,199] ignoring specific ion adsorption agreed well with experimental data.

10.3.2 Governing Equations

The local electric potential $\psi(x,t)$ in the cathode of thickness L_C and in the anode of thickness L_A is governed by the one-dimensional Poisson equation expressed as [149, 260, 388, 389],

$$\frac{\partial}{\partial x}\left(\sigma_C \frac{\partial \psi}{\partial x}\right) = 0 \quad \text{for} \quad -L_C - L \leq x \leq -L \tag{10.6}$$

$$\frac{\partial}{\partial x}\left(\sigma_A \frac{\partial \psi}{\partial x}\right) = 0 \quad \text{for} \quad L \leq x \leq L + L_A \tag{10.7}$$

where σ_C and σ_A are the electrical conductivities of the cathode and anode, respectively. The transient local molar concentration of intercalated Li atoms in the cathode, denoted by $c_{1,C}(x,t)$, is governed by the mass diffusion equation given by [388, 389, 429–431],

$$\frac{\partial c_{1,C}}{\partial t} = \frac{\partial}{\partial x}\left(D_{1,C} \frac{\partial c_{1,C}}{\partial x}\right) \quad \text{for} \quad -L_C - L \leq x \leq -L \tag{10.8}$$

where $D_{1,C}$ is the diffusion coefficient of intercalated lithium atoms in the cathode.

Moreover, the ion transport in the diffuse layer $-L + H \leq x \leq L - H$ of the electrolyte solution is governed by the generalized modified Poisson-Nernst-Planck (GMPNP) model [260] derived in Chapter 9. The GMPNP model is valid for asymmetric electrolytes. For binary asymmetric electrolytes, it is expressed as [260],

$$\begin{cases} \dfrac{\partial}{\partial x}\left(\epsilon_0 \epsilon_r \dfrac{\partial \psi}{\partial x}\right) = -F \displaystyle\sum_{i=1}^{2} z_i c_i & \text{(10.9a)} \\ \dfrac{\partial c_i}{\partial t} = -\dfrac{\partial N_i}{\partial x} & \text{(10.9b)} \end{cases}$$

where $\psi(x,t)$ is the local electric potential and $c_i(x,t)$ is the molar concentration of ion species "i" ($i = 1$ or 2) in the electrolyte solution. Here, species 1 and 2 refer to Li^+ and ClO_4^- ions in the electrolyte, respectively. Moreover, F is the Faraday constant ($F = 96485.3$ sA/mol), ϵ_0 and ϵ_r are the free space permittivity ($\epsilon_0 = 8.854 \times 10^{-12}$ F/m) and the relative permittivity of the electrolyte solution, respectively. The mass flux of ion species "i", denoted by $N_i(x,t)$, is defined as [260],

$$N_i(x,t) = -D_i \frac{\partial c_i}{\partial x} - \frac{D_i F z_i c_i}{R_u T} \frac{\partial \psi}{\partial x} - \frac{D_i N_A c_i}{1 - N_A \sum_{i=1}^{2} a_i^3 c_i} \frac{\partial}{\partial x} \left(\sum_{i=1}^{2} a_i^3 c_i \right) \quad (10.10)$$

where D_i and a_i are the diffusion coefficient and the effective ion diameter of ion species "i" in the electrolyte solution, respectively. The temperature is denoted by T (in K), while N_A and R_u are the Avogadro's number ($N_A = 6.022 \times 10^{23}$ mol^{-1}) and the universal gas constant ($R_u = 8.314$ $JK^{-1}mol^{-1}$), respectively. The first and second terms of Equation (10.10) represent the ions' diffusion and electrostatic migration, respectively, while the last term represents the correction due to the finite ion sizes [260].

10.3.3 Boundary and Initial Conditions

The one-dimensional model given by Equations (10.6) to (10.9) consist of six second order in space and first order in time partial differential equations. Therefore, they require twelve boundary conditions and six initial conditions. First, the electric potential was imposed as 0 V at the anode surface ($x = L + L_A$) while it was imposed as $\psi_s(t)$ at the cathode surface ($x = -L_C - L$). During cyclic voltammetry measurements, $\psi_s(t)$ is imposed as [260],

$$\psi_s(t) = \begin{cases} \psi_{max} - v[t - 2(m-1)\tau_{CV}] & \text{for } 2(m-1)\tau_{CV} \leq t < (2m-1)\tau_{CV} \quad (10.11a) \\ \psi_{min} + v[t - (2m-1)\tau_{CV}] & \text{for } (2m-1)\tau_{CV} \leq t < 2m\tau_{CV} \quad (10.11b) \end{cases}$$

where m is the number of cycles of period τ_{CV} while ψ_{max} and ψ_{min} are the maximum and minimum electric potentials, respectively.

The Stern layers was accounted for via the following boundary conditions at the Stern/diffuse layer interfaces near the anode ($x = L - H$) and cathode ($x = -L + H$) [7, 95, 146, 260],

$$\frac{\partial \psi}{\partial x}(L - H, t) = \frac{1}{H}\left[\psi(L, t) - \psi(L - H, t)\right] \tag{10.12a}$$

$$-\frac{\partial \psi}{\partial x}(-L + H, t) = \frac{1}{H}\left[\psi(-L, t) - \psi(-L + H, t)\right] \tag{10.12b}$$

The current density was continuous across the electrode/electrolyte interfaces located at $x = \pm L$ and across the Stern/diffuse interfaces located at $x = \pm(L - H)$ [149, 260, 366, 389, 432]. These boundary conditions representing the continuity of current density can be expressed as,

$$-\sigma_C \frac{\partial \psi}{\partial x}(-L, t) = j_C(-L + H, t) + j_F(-L + H, t) \tag{10.13a}$$

$$-\sigma_A \frac{\partial \psi}{\partial x}(L, t) = j_C(L - H, t) \tag{10.13b}$$

Here, $j_C(x, t)$ is the capacitive current density (in A/m^2) due to the electric double layer forming at the anode and cathode defined as [291, 323, 324],

$$j_C(x, t) = -\epsilon_0 \epsilon_r \frac{\partial^2 \psi}{\partial x \partial t}(x, t) \tag{10.14}$$

Moreover, $j_F(x, t)$ is the Faradaic current density (in A/m^2) due to redox reactions and Li insertion into the electrode. It is typically described by the generalized Frumkin-Butler-Volmer model expressed as [9, 132, 250, 360, 427, 433],

$$j_F(-L + H, t) = j_{F,0}(-L + H, t)\Big[e^{(1-\alpha)(z_1 F/R_u T)(\Delta\psi_H - \Delta\psi_{Eq})} - e^{-\alpha(z_1 F/R_u T)(\Delta\psi_H - \Delta\psi_{Eq})}\Big] \tag{10.15}$$

where $\Delta\psi_H$ is the electrical potential drop across the Stern layer at the cathode, i.e., $\Delta\psi_H = \psi(-L, t) - \psi(-L + H, t)$. Here, $\Delta\psi_{eq}$ is the equilibrium potential difference [9, 132, 388, 429, 432, 434–436]. For electrodes made of transition metal oxides, $\Delta\psi_{eq}$ is typically expressed as a function of the "state-of-charge" $c_{1,C}/c_{1,C,max}$ by fitting experimental data for the "open-circuit potential" [388, 429, 432, 434–436]. The so-called exchange current density, denoted by

$j_{F,0}(x,t)$, is expressed as [388, 429, 432, 434, 435],

$$j_{F,0}(-L+H,t) = Fz_1k_0c_1^{1-\alpha}(c_{1,C,max}-c_{1,C})^{\alpha}(c_{1,C})^{\alpha} \tag{10.16}$$

where $c_{1,C,max}$ is the maximum concentration of intercalated lithium atoms in the cathode while k_0 is the reaction rate constant expressed in $\mathrm{m}^{2+\alpha}\mathrm{mol}^{1-\alpha}\mathrm{s}^{-1}$. Note that in Equation (10.16), $c_{1,C}$ and c_1 were evaluated at the cathode/electrolyte interface located at $x = -L$ and at the Stern/diffuse layer interface near the cathode located at $x = -L + H$, respectively, i.e., $c_{1,C} = c_{1,C}(-L,t)$ and $c_1 = c_1(-L+H,t)$. Here, the transfer coefficient α was assumed to be 0.5 corresponding to identical energy barriers for forward and backward reactions [9, 132, 250, 360, 427].

Moreover, the mass flux of intercalated lithium atoms in the electrode was zero at the cathode/current collector interface ($x = -L - L_C$) while it was continuous across the cathode/electrolyte interface ($x = -L$). These boundary conditions for the concentrations of Li atoms in the electrode and Li^+ ions in the electrolyte are expressed as,

$$-D_{1,C}\frac{\partial c_{1,C}}{\partial x}(-L-L_C,t) = 0 \tag{10.17a}$$

$$-D_{1,C}\frac{\partial c_{1,C}}{\partial x}(-L,t) = \frac{j_F(-L+H,t)}{F} \tag{10.17b}$$

Furthermore, the mass flux of Li^+ ions was continuous across the Stern/diffuse layer interface ($x = -L+H$) near the redox-active cathode while it vanished near the carbon anode such that,

$$N_1(-L+H,t) = \frac{j_F(-L+H,t)}{F} \quad \text{and} \quad N_1(L-H,t) = 0 \tag{10.18}$$

The mass fluxes of ClO_4^- ions vanished at both the anode and cathode, for lack of redox reactions and ion insertion, so that

$$N_2(-L+H,t) = N_2(L-H,t) = 0 \tag{10.19}$$

Finally, the initial electric potential was assumed to be uniform across the device and given by,

$$\psi(-L - L_C \leq x \leq L + L_A, 0) = 0 \tag{10.20}$$

Similarly, the initial ion concentrations were uniform in the electrode and electrolyte and satisfied electroneutrality according to,

$$\begin{aligned} &c_{1,C}(-L - L_C \leq x \leq -L, 0) = 0, \quad c_1(-L + H \leq x \leq L - H, 0) = c_{1,\infty}, \\ &\text{and} \quad c_2(-L + H \leq x \leq L - H, 0) = -z_1 c_{1,\infty}/z_2 \end{aligned} \tag{10.21}$$

Equations (10.6) to (10.21) reduce to simulating electric double layer capacitors with a binary and asymmetric electrolyte when $j_F = 0$, as performed in Refs. [149, 260]. Note also that the model given by Equations (10.6) to (10.21) can be extended to pseudocapacitors with redox-active cathode and anode by adding the corresponding Faradaic current j_F and the associated ion intercalation in the anode.

10.3.4 Constitutive Relations

A total of 21 input parameters were needed to solve Equations (10.6) to (10.21) including (i) the electrolyte properties ϵ_r, $(a_i)_{i=1,2}$, $(z_i)_{i=1,2}$, $(D_i)_{i=1,2}$, and $c_{1,\infty}$, (ii) the electrode properties σ_C, $D_{1,C}$, σ_A, k_0, and $\Delta\psi_{eq}$, (iii) the dimensions L, L_C, and L_A, and (iv) the operating conditions T, ψ_{max}, ψ_{min}, and v.

The present study focused on propylene carbonate (PC) organic electrolyte solution at room temperature so that $T = 298$ K with $\epsilon_r = 64.4$ [219]. The solvated ion diameters of Li^+ and ClO_4^- in PC were taken as $a_1 = 0.67$ nm and $a_2 = 1.0$ nm [253, 437], respectively. The Stern layer thickness H was defined based on the largest solvated ions [260], i.e., $H = a_2/2$. The Li^+ and ClO_4^- ion diffusion coefficients in PC were reported to be $D_1 = 2.6 \times 10^{-10}$ m^2/s [437,438] and $D_2 = 3.3 \times 10^{-10}$ m^2/s [437, 438], respectively. The initial bulk ion concentrations

were imposed as $c_{1,\infty} = c_{2,\infty} = 1$ mol/L since $z_1 = -z_2 = 1$.

The cathode was assumed to be made of Nb_2O_5 while the anode was made of activated carbon. Their respective electrical conductivities were $\sigma_C = 6.9 \times 10^{-2}$ S/m and $\sigma_A = 5$ S/m [357,358]. The reaction rate constant k_0 for transition metal oxides has been reported between 10^{-11} and 10^{-8} $m^{2.5}mol^{-0.5}s^{-1}$ [362,388,432,439]. Here, its baseline value was taken as $k_0 = 10^{-9}$ $m^{2.5}mol^{-0.5}s^{-1}$. The maximum intercalated lithium concentration in the cathode was estimated as $c_{1,C,max} = n\rho/M$ where ρ and M are the density and molar weight of the fully intercalated metal oxide $Li_nM_pO_q$ [141, 416], respectively. For fully intercalated Nb_2O_5, $M = 279.7$ g/mol, $\rho \approx 4.6$ g/cm^3, and $n = 2$ [30, 440] yielding $c_{1,C,max} \approx 32.9$ mol/L. The diffusion coefficient of intercalated lithium atoms in transition metal oxides is typically in the range from 10^{-16} to 10^{-10} m^2/s [362, 441]. Here, its baseline value was taken as $D_{1,C} = 10^{-14}$ m^2/s.

Moreover, the electrolyte thickness was takes as $2L = 20$ μm while the electrode thickness $L_C = L_A$ ranges from to 20 nm to 10 μm. For practical purposes, electrodes with $L_C = L_A = 10$ μm corresponded to semi-infinite electrodes. The temperature was constant and equal to 298 K. The maximum and minimum values of the surface electric potential $\psi_s(t)$ were imposed as $\psi_{max} = 0.8$ V and $\psi_{min} = 0.2$ V, respectively. In addition, the equilibrium potential difference $\Delta\psi_{eq}$ was assumed to be zero for the sake of simplicity [391, 442–444]. Finally, the scan rate v was arbitrarily varied from 10^{-3} to 10 V/s. This range covers the scan rates typically encountered in actual CV measurements of pseudocapacitors and asymmetric supercapacitors [29, 30, 177, 369, 370, 393–406].

10.3.5 Dimensional Analysis

Based on our previous studies [149, 260], the following scaling parameters were used to scale the governing equations for ψ, c_i, and $c_{1,C}$ as well as the associated

boundary and initial conditions,

$$x^* = \frac{x}{\lambda_D},\ t^* = \frac{tD_1}{\lambda_D^2},\ \psi^* = \frac{\psi}{R_uT/z_1F},\ c_i^* = \frac{c_i}{c_{1,\infty}},\ \text{and}\ c_{1,C}^* = \frac{c_{1,C}}{c_{1,C,max}} \quad (10.22)$$

where $\lambda_D = \sqrt{\epsilon_0\epsilon_r R_uT/F^2 \sum_{i=1}^{2} z_i^2 c_{i,\infty}}$ is the Debye length for binary asymmetric electrolytes representing an estimate of the diffuse layer thickness [35].

The governing equations for the electric potential in the electrodes [Equations (10.6) to (10.8)] assuming constant electrode electrical conductivities can be expressed in dimensionless form as

$$\frac{\partial}{\partial x^*}\left(\sigma_C^* \frac{\partial \psi^*}{\partial x^*}\right) = 0 \quad \text{for} \quad -(L^* + L_C^*) \leq x^* < -L^* \quad (10.23)$$

$$\frac{\partial}{\partial x^*}\left(\sigma_A^* \frac{\partial \psi^*}{\partial x^*}\right) = 0 \quad \text{for} \quad L^* < x^* \leq L^* + L_A^* \quad (10.24)$$

where $\sigma_j^* = [\sigma_j(\psi_{max} - \psi_{min})/L_C]/(Fz_1c_{1,\infty}D_1/L)$, with j being C or A, represent the ratios of the characteristic current densities in the cathode and anode, respectively, to that in the electrolyte. They can also be interpreted as the ratio of time scale for charge transport in the electrolyte to that in the cathode or anode [260].

Similarly, the mass conservation Equation (10.8) in the electrode was non-dimensionalized as,

$$\frac{\partial c_{1,C}^*}{\partial t^*} = \frac{\partial}{\partial x^*}\left(D_{1,C}^* \frac{\partial c_{1,C}^*}{\partial x^*}\right) \quad \text{for} \quad -(L^* + L_C^*) \leq x^* \leq -L^* \quad (10.25)$$

where $D_{1,C}^* = D_{1,C}/D_1$ is the ratio of lithium atom diffusion coefficient in the cathode to that of Li^+ ions in the electrolyte. Here, $L^* = L/\lambda_D$ is the dimensionless half electrolyte thickness while $L_C^* = L_C/\lambda_D$ and $L_A^* = L_A/\lambda_D$ are the dimensionless cathode and anode thicknesses, respectively.

Moreover, the GMPNP model [Equations (10.9)] in the diffuse layer of the electrolyte, defined by $-L^*+H^* \leq x^* \leq L^*-H^*$, was transformed in dimensionless form as,

$$\begin{cases} \dfrac{\partial^2 \psi^*}{\partial x^{*2}} = -\dfrac{c_1^* + z_2^* c_2^*}{1 - z_2^*} & (10.26a) \\ \dfrac{\partial c_i^*}{\partial t^*} = -\dfrac{\partial N_i^*}{\partial x^*} & (10.26b) \end{cases}$$

Here, $H^* = a_2^*/2$ where $a_2^* = a_2/\lambda_D$ is the dimensionless effective anion diameter scaled by the Debye length. The dimensionless mass flux N_i^* was given by,

$$N_i^*(x^*, t^*) = -D_i^* \frac{\partial c_i^*}{\partial x^*} - D_i^* z_i^* c_i^* \frac{\partial \psi^*}{\partial x^*} - \frac{D_i^* c_i^*}{2 - \sum_{i=1}^{2} \nu_{pi} c_i^*} \frac{\partial}{\partial x^*} \sum_{i=1}^{2} \nu_{pi} c_i^* \tag{10.27}$$

where $z_2^* = z_2/z_1$ and $D_2^* = D_2/D_1$ are the ratios of the valencies and diffusion coefficients between anions and cations, respectively. Note that $z_2^* = -1$ and $D_2^* = 1$ for symmetric electrolytes. Here, the packing parameter for ion species "i" is defined as $\nu_{pi} = 2c_{1,\infty}/(1/a_i^3 N_A)$. It represents the ratio of the total bulk ion concentration to the maximum ion concentration $1/a_i^3 N_A$ assuming a simple cubic packing of ions of diameter a_i [102, 130].

The dimensionless electric potentials imposed at the current collector/electrode interfaces are given by [260, 445],

$$\psi^*(L^* + L_A^*, t^*) = 0 \quad \text{and} \quad \psi^*(-L^* - L_C^*, t^*) = \psi_s^* \tag{10.28}$$

where $\psi_s^*(t^*)$ is the dimensionless surface potential. Under cyclic voltammetry testing, it is given by [260],

$$\psi_s^*(t^*) = \begin{cases} \psi_{max}^* - v^*[t^* - 2(m-1)\tau_{CV}^*] & \text{for } 2(m-1)\tau_{CV}^* \le t^* \le (2m-1)\tau_{CV}^* \quad \text{(10.29a)} \\ \psi_{min}^* + v^*[t^* - (2m-1)\tau_{CV}^*] & \text{for } (2m-1)\tau_{CV}^* \le t^* \le 2m\tau_{CV}^* \quad \text{(10.29b)} \end{cases}$$

where $\tau_{CV}^* = (\psi_{max}^* - \psi_{min}^*)/v^*$ represents the dimensionless half cycle period and $v^* = (\lambda_D^2/D_1)/[(R_u T/z_1 F)/v]$ is the dimensionless scan rate. It can be interpreted as the ratio of the ion diffusion time scale $\tau_d = \lambda_D^2/D_1$ and the characteristic time $\tau_{th} = R_u T/z_1 F$ necessary to reach the thermal potential at scan rate v, i.e., $v^* = \tau_d/\tau_{th}$ [260]. Moreover, $\psi_{max}^* = \psi_{max}/(R_u T/z_1 F)$ and $\psi_{min}^* = \psi_{min}/(R_u T/z_1 F)$ are the maximum and minimum surface potentials, respectively, scaled by the thermal potential. The latter represents the electric potential of ions such that their potential energy equals their thermal energy given by $k_B T$. Note that ψ_{max}^* and ψ_{min}^* can be also interpreted as the ratio of characteristic times to reach ψ_{max}

or ψ_{min} to the characteristic time for reaching the thermal potential at scan rate v [260].

Moreover, the boundary conditions [Equations (10.12)] accounting for the Stern layer at both electrodes can be written in dimensionless form as,

$$\frac{\partial \psi^*}{\partial x^*}(L^* - a_2^*/2, t^*) = \frac{2}{a_2^*}\left[\psi^*(L^*, t^*) - \psi^*(L^* - a_2^*/2, t^*)\right] \quad (10.30a)$$

$$-\frac{\partial \psi^*}{\partial x^*}(-L^* + a_2^*/2, t^*) = \frac{2}{a_2^*}\left[\psi^*(-L^*, t^*) - \psi^*(-L^* + a_2^*/2, t^*)\right] \quad (10.30b)$$

Similarly, the boundary conditions [Equations (10.13)] representing the continuity of current density became in dimensionless form at the cathode surface,

$$-\frac{\sigma_C^*}{\psi_{max}^* - \psi_{min}^*}\frac{L_C^*}{L^*}\frac{\partial \psi^*}{\partial x^*}(-L^*, t^*) = j_C^*(-L^* + a_2^*/2, t^*) + j_F^*(-L^* + a_2^*/2, t^*) \quad (10.31a)$$

while at the anode surface, it was expressed as

$$-\frac{\sigma_A^*}{\psi_{max}^* - \psi_{min}^*}\frac{L_A^*}{L^*}\frac{\partial \psi^*}{\partial x^*}(L^*, t^*) = j_C^*(L^* - a_2^*/2, t^*) \quad (10.31b)$$

Here, the dimensionless capacitive and Faradaic current densities, scaled by the ionic current density $Fz_1D_1c_{1,\infty}/\lambda_D$ representing the characteristic current density due to ion diffusion, are given by,

$$j_C^*(L^* - a_2^*/2, t^*) = -(1 - z_2^*)\frac{\partial^2 \psi^*}{\partial x^* \partial t^*}(L^* - a_2^*/2, t^*) \quad (10.32a)$$

$$j_C^*(-L^* + a_2^*/2, t^*) = -(1 - z_2^*)\frac{\partial^2 \psi^*}{\partial x^* \partial t^*}(-L^* + a_2^*/2, t^*) \quad (10.32b)$$

$$j_F^*(-L^* + a_2^*/2, t^*) = j_{F,0}^*(-L^* + a_2^*/2, t^*)\Big[e^{(1-\alpha)(\Delta\psi_H^* - \Delta\psi_{eq}^*)} - e^{-\alpha(\Delta\psi_H^* - \Delta\psi_{eq}^*)}\Big] \quad (10.32c)$$

Here, $j_{F,0}^*$ is the dimensionless exchange current density expressed as,

$$j_{F,0}^*(-L^* + a_2^*/2, t^*) = k_0^* c_{1,C,max}^* c_1^{*1-\alpha}(1 - c_{1,C}^*)^\alpha (c_{1,C}^*)^\alpha \quad (10.33)$$

where $c_{1,C,max}^* = c_{1,C,max}/c_{1,\infty}$ is the ratio of maximum lithium atom concentration in the cathode to the bulk lithium ion concentration in the electrolyte. Moreover,

$c^*_{1,C} = c_{1,C}/c_{1,C,max}$ is the ratio of lithium atom concentration at the cathode surface to its maximum value $c_{1,C,max}$, i.e., $c^*_{1,C}$ ranges from 0 to 1. The dimensionless reaction rate constant is expressed as $k^*_0 = k_0 c^{\alpha}_{1,\infty}\lambda_D/D_1$. It can be interpreted as the ratio of the time scale of ion diffuse in the electrolyte given by λ^2_D/D_1 to the redox reaction time scale given by $\lambda_D/k_0 c^{\alpha}_{1,\infty}$.

In addition, the dimensionless mass flux boundary conditions for N^*_1 and N^*_2 were given, at the cathode Stern/diffuse layer interface, by

$$N^*_1(-L^* + a^*_2/2, t^*) = j^*_F(-L^* + a^*_2/2, t^*) \quad \text{and} \quad N^*_2(-L^* + a^*_2/2, t^*) = 0 \tag{10.34}$$

and at the anode Stern/diffuse layer interface, by

$$N^*_1(L^* - a^*_2/2, t^*) = N^*_2(L^* - a^*_2/2, t^*) = 0 \tag{10.35}$$

Finally, the initial dimensionless electric potential was given by,

$$\psi^*(-L^* - L^*_C \le x^* \le L^* + L^*_A, 0) = 0 \tag{10.36}$$

Similarly, the initial uniform concentrations in the electrode and electrolyte were in the following dimensionless form,

$$\begin{aligned} &c^*_1(-L^* - L^*_C \le x^* \le -L^*, 0) = 0, \quad c^*_1(-L^* + a^*_2/2 \le x^* \le L^* - a^*_2/2, 0) = 1, \\ &\text{and} \quad c^*_2(-L^* + a^*_2/2 \le x^* \le L^* - a^*_2/2, 0) = -1/z^*_2 \end{aligned} \tag{10.37}$$

Overall, the scaling analysis demonstrates that the dimensionless governing equations and associated boundary and initial conditions are governed by only

seventeen dimensionless similarity parameters. They can be identified as

$$v^* = \frac{\lambda_D^2/D_1}{(R_uT/z_1F)/v}, \quad \psi_{max}^* = \frac{\psi_{max}}{R_uT/z_1F}, \quad \psi_{min}^* = \frac{\psi_{min}}{R_uT/z_1F}, \quad L^* = \frac{L}{\lambda_D},$$
$$a_2^* = \frac{a_2}{\lambda_D}, \quad \nu_{p1} = 2a_1^3 N_A c_{1,\infty}, \quad \nu_{p2} = 2a_2^3 N_A c_{1,\infty}, \quad D_2^* = \frac{D_2}{D_1}, \quad z_2^* = \frac{z_2}{z_1},$$
$$\sigma_C^* = \frac{\sigma_C(\psi_{max} - \psi_{min})/L_C}{Fz_1c_{1,\infty}D_1/L}, \quad \sigma_A^* = \frac{\sigma_A(\psi_{max} - \psi_{min})/L_A}{Fz_1c_{1,\infty}D_1/L},$$
$$L_C^* = \frac{L_C}{\lambda_D}, \quad L_A^* = \frac{L_A}{\lambda_D}, \quad D_{1,C}^* = \frac{D_{1,C}}{D_1}, \quad c_{1,C,max}^* = \frac{c_{1,C,max}}{c_{1,\infty}},$$
$$k_0^* = \frac{k_0 c_{1,\infty}^{1/2}\lambda_D}{D_1}, \quad \text{and} \quad \Delta\psi_{eq}^* = \frac{\psi_{eq}}{R_uT/z_1F} \tag{10.38}$$

Note that v^*, ψ_{max}^*, ψ_{min}^*, L^*, a_2^*, ν_{p1}, ν_{p2}, D_2^*, z_2^*, σ_C^*, σ_A^*, L_C^*, and L_A^* were identical to those identified in Ref. [260] for CV simulations of electric double layer capacitors with binary asymmetric electrolytes. For asymmetric supercapacitors with redox reactions and ion insertion taking place at the cathode, four additional dimensionless numbers appeared, namely, $D_{1,C}^*$, $c_{1,C,max}^*$, k_0^*, and $\Delta\psi_{eq}^*$.

10.3.6 Method of Solution and Data Processing

The governing Equations (10.6) and (10.10) were solved in dimensional form along with the boundary and initial conditions given by Equations (10.12) to (10.21) using the commercial finite element solver COMSOL 4.3b. CV measurements were simulated by numerically imposing the periodic surface electric potential given by Equation (10.11).

The numerical convergence criterion was defined such that the maximum relative difference in the predicted current densities j_C and j_F at the cathode Stern/diffuse layer interface ($x = -L + H$) was less than 1% when dividing both the mesh size and the time step by a factor of two. This corresponded to imposing a time step of $\Delta t \approx t_{CV}/1000 = (\psi_{max} - \psi_{min})/1000v$. The mesh size was the smallest at the Stern/diffuse layer interface due to the large potential gradient and then gradually increased. The mesh size was specified to be less than 0.025 nm

at the Stern/diffuse layer interface while it was $L_C/25$ and $L_A/25$ in the electrode domains and $L/50$ in the diffuse layer. The total number of finite elements was about 350 for all cases simulated in the present study.

The instantaneous capacitive density $j_C(t)$ and Faradaic current density $j_F(t)$ were computed according to Equations (10.14) and (10.15), respectively. The instantaneous total current density j_t was computed as the sum of the capacitive and Faradaic current densities, i.e., $j_t(t) = j_C(t) + j_F(t)$. CV curves at a specific scan rate were obtained by plotting $j_t(t)$, $j_C(t)$, and $j_F(t)$ versus $\psi_s(t)$.

10.3.7 Validation

The numerical tool was validated based on three cases reported in the literature. First, the transient ion concentration and electric potential profiles were predicted by solving the PNP and MPNP models without redox reactions for binary and symmetric electrolytes ($N = 2$, $z_1 = -z_2 = z$, $D_1 = D_2$, and $a_1 = a_2$) with constant surface electric potential. The results were successfully compared with the reported numerical solutions of $c_i(x,t)$ and $\psi(x,t)$ for planar electrodes for a wide range of packing parameter ν_p and dimensionless surface potential ψ_s^* [146].

Second, the transient Faradaic current was predicted from the linear sweep voltammetry simulations with surface redox reactions near planar electrodes and with ion diffusion in semi-infinite electrolyte domain. The numerical results with vanishing ion size ($a_i = 0$ nm) agreed well with the classical "Randles-Sevčik" solution [9, 407–410] for a wide range of scan rate.

Third, the CV curves were predicted by solving the generalized MPNP model for the surface redox reaction with four ion species near a hemispherical electrode of radius 0.71 mm assuming zero surface electric field. Figure 10.2 compares the predicted Faradaic current j_F versus ψ_s curve with the numerical solution reported in Ref. [15] for one-electron redox reaction with four ion species. The ion valencies

were $z_1 = +3$, $z_2 = +2$, $z_3 = +1$, and $z_4 = -1$ while other parameters were $a_i = 0.66$ nm, $v = 0.05$ V/s, $c_{1\infty} = 0.005$ mol/L, $c_{sup} = 0.15$ mol/L, $\psi_{min} = -0.5$ V, $\psi_{max} = 0.2$ V, $k_0 = 0.01$ m/s, and $\psi_0 = -0.175$ V. The bulk ion concentrations were $c_{1,\infty} = 0.005$ mol/L, $c_{2,\infty} = 0$ mol/L, $c_{3,\infty} = 0.15$ mol/L, $c_{4,\infty} = 0.165$ mol/L. The ion diffusion coefficients were $D_1 = 0.9 \times 10^{-9}$ m^2/s, $D_2 = 10^{-9}$ m^2/s, $D_3 = 1.8 \times 10^{-9}$ m^2/s, and $D_4 = 1.95 \times 10^{-9}$ m^2/s while their valencies were $z_1 = 3$, $z_2 = 2$, $z_3 = 1$, and $z_4 = -1$. Good agreement was observed between our simulation results and those reported in Ref. [15].

10.4 Results and Discussions

10.4.1 Numerical Cyclic Voltammetry

10.4.1.1 Predicted CV Curves

Figures 10.3 shows the numerically predicted capacitive j_C, Faradaic j_F, and total j_t current densities versus surface potential ψ_s curves from CV simulations for four cases with different L_C and $D_{1,C}$, i.e., (i) $L_C = 20$ nm and $D_{1,C} = 10^{-10}$ m^2/s, (ii) $L_C = 500$ nm and $D_{1,C} = 10^{-10}$ m^2/s, (iii) $L_C = 20$ nm and $D_{1,C} = 10^{-14}$ m^2/s, and (iv) $L_C = 500$ nm and $D_{1,C} = 10^{-14}$ m^2/s. The other parameters were identical to those used in Case 1 of Table 10.1. Results were obtained by numerically solving the GMPNP model with the Stern layer accounting for the potential drop and Li diffusion in the cathode. Figures 10.3(a) to 10.3(c) demonstrate that the predicted total current density j_t was dominated by the Faradaic current density j_F. Moreover, the predicted j_t or j_F remained nearly the same among Cases (i) to (iii). Furthermore, Figure 10.3(b) demonstrates that, unlike other cases, Case (iv) featured a smaller Faradaic current density j_F by about a factor of two due to the large electrode thickness L_C and the small Li atom diffusion coefficient $D_{1,C}$. This can be attributed to the fact that the electrode cannot be fully charged, i.e., cannot reach $c_{1,C}(-L_C \leq x \leq -L) = c_{1,C,max}$, when its thickness is large and

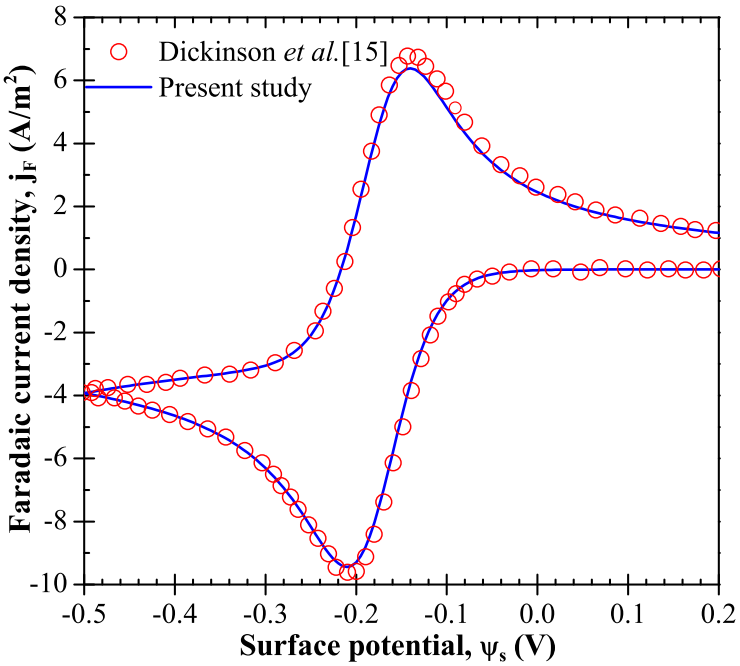

Figure 10.2: Comparison of predicted Faradaic current j_F versus ψ_s curve from CV simulations for a hemispherical electrode of radius 0.71 mm with the numerical solution reported in Ref. [15]. Results were obtained by numerically solving the generalized MPNP model assuming zero surface electric field with $a_i = 0$ nm (i=1, 2, 3, and 4), $v = 0.05$ V/s, $\psi_{max} = 0.2$, $\psi_{min} = -0.5$, $k_0 = 0.01$ m/s, and $\psi_0 = -0.175$ V. The bulk ion concentrations were $c_{1,\infty} = 0.005$ mol/L, $c_{2,\infty} = 0$ mol/L, $c_{3,\infty} = 0.15$ mol/L, $c_{4,\infty} = 0.165$ mol/L. The ion diffusion coefficients were $D_1 = 0.9\times10^{-9}$ m^2/s, $D_2 = 10^{-9}$ m^2/s, $D_3 = 1.8\times10^{-9}$ m^2/s, and $D_4 = 1.95\times10^{-9}$ m^2/s while their valencies were $z_1 = 3$, $z_2 = 2$, $z_3 = 1$, and $z_4 = -1$.

when the diffusion process of Li atoms in the electrode is slow. This, in turn, led to smaller values of j_F than when the electrode was thin and the Li atom diffusion coefficient was relatively large. For practical pseudocapacitor applications, such cases should be avoided.

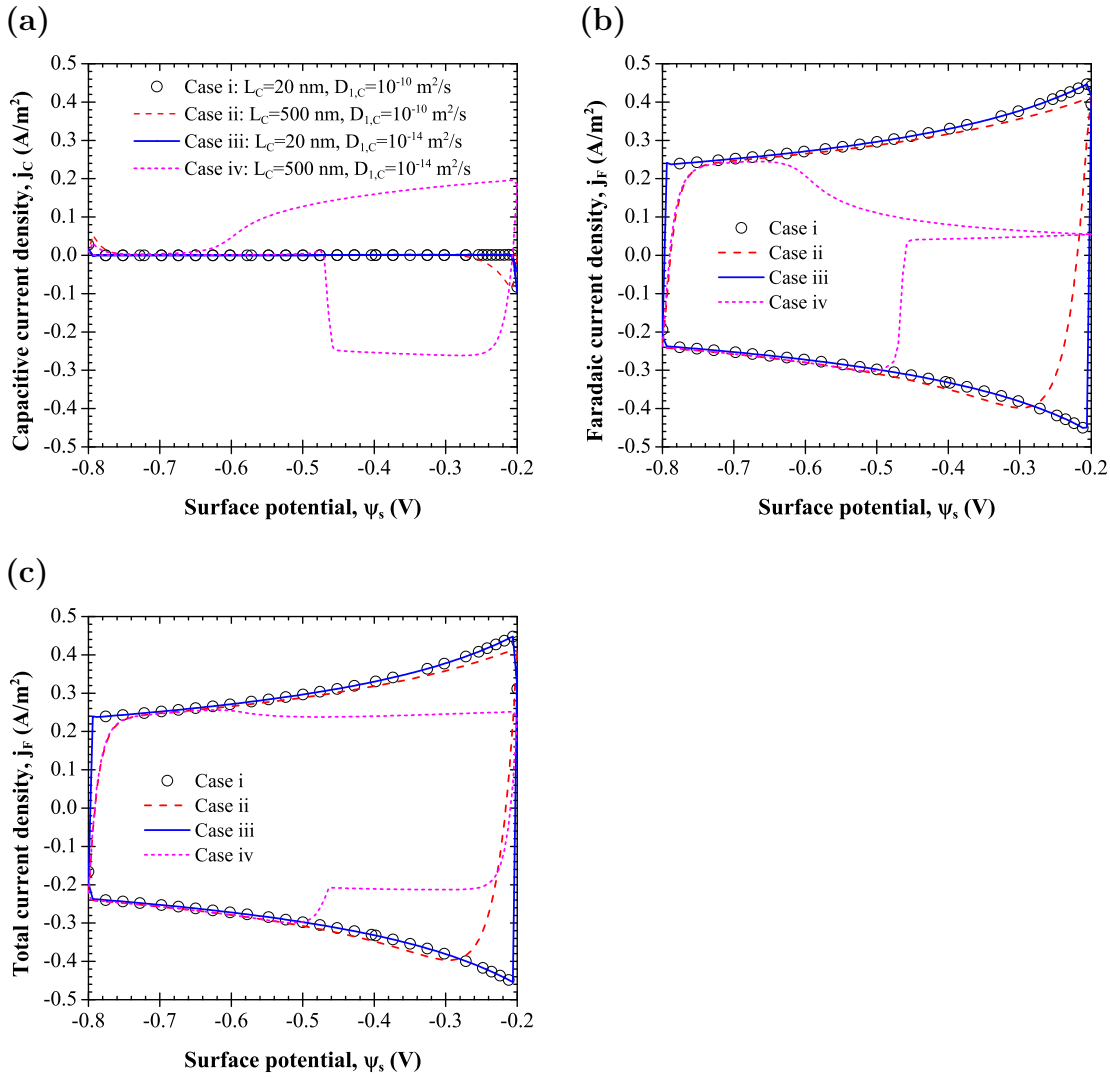

Figure 10.3: Numerically predicted capacitive j_C, Faradaic j_F, and total j_t current densities versus surface potential ψ_s curves from CV simulations for four cases with different L_C and $D_{1,C}$.

10.4.1.2 Proof of the Relationship $j_t = k_1 v + k_2 v^{1/2}$

Figure 10.4 shows the predicted j_t/v as a function of $1/v^{1/2}$ at surface potential $\psi_s = -0.6$ V and -0.4 V obtained from CV simulations for asymmetric supercapacitors. Results were obtained by numerically solving Equations (10.6) to (10.21) with parameters identical to those reported in Case 1 of Table 10.1.

Figure 10.4 demonstrates that j_t/v increased linearly with increasing $1/v^{1/2}$, i.e., $j_t/v = k_1 + k_2 1/v^{1/2}$. It is evident that the parameters k_1 and k_2 depend on the potential ψ_s. This, in turn, proved that Equation (10.1) is valid for CV simulations in the presence of both electric double layers and redox reactions as well as Li atom intercalation in the electrode.

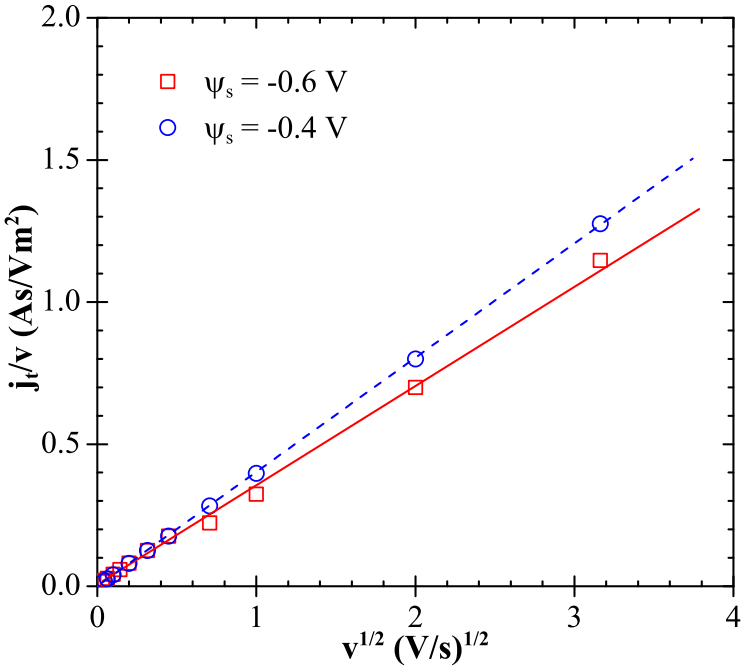

Figure 10.4: Predicted j_t/v as a function of $1/v^{1/2}$ for asymmetric supercapacitors at surface potential $\psi_s = -0.6$ V and -0.4 V. Results were obtained by numerically solving Equations (10.6) to (10.21) for CV simulations with parameters identical to those reported in Case 1 of Table 10.1.

10.4.2 Dimensionless CV curves

10.4.2.1 Dimensionless Analysis

Table 10.1 summarizes the different values of v, ψ_{min}, ψ_{max}, T, z_1, z_2, a_1, a_2, D_1, D_2, $c_{1\infty}$, ϵ_r, L, σ_C, σ_A, $L_C = L_A$, $D_{1,C}$, $c_{1,C,max}$, k_0, and $\Delta\psi_{eq}$ for four different cases considered. For all of them, the dimensionless numbers were identical,

Table 10.1: Parameters used in CV simulations reported in Figure 10.5 with $\Delta\psi_{eq} = 0$ V and $z_1 = -z_2 = 1$ for all cases considered. In these four cases, the dimensionless numbers were identical and equal to $v^* = 1.13 \times 10^{-8}$, $\psi^*_{max} = 31.2$, $\psi^*_{min} = 7.79$, $L^* = 3641.5$, $a^*_2 = 3.65$, $\nu_{p,1} = 1.21$, $\nu_{p,2} = 0.36$, $D^*_2 = 1.27$, $z^*_2 = -1$, $\sigma^*_C = 0.16$, $\sigma^*_A = 12$, $L^*_C = L^*_A = 36415$, $D^*_{1,C} = 3.8 \times 10^{-5}$, $k^*_0 = 3.34 \times 10^{-8}$, and $\Delta\psi^*_{eq} = 0$.

Parameters	**Case 1**	**Case 2**	**Case 3**	**Case 4**
v **(V/s)**	1	0.1	0.215	0.0091
ψ_{max} **(V)**	0.8	0.8	0.8	0.6
ψ_{min} **(V)**	0.2	0.2	0.2	0.15
T (K)	298	298	298	223.5
a_1 **(nm)**	0.67	0.67	1.44	1.92
a_2 **(nm)**	1.0	1.0	2.16	2.88
D_1 **(m^2/s)**	2.6×10^{-10}	2.6×10^{-11}	2.6×10^{-10}	2.6×10^{-11}
D_2 **(m^2/s)**	3.3×10^{-10}	3.3×10^{-11}	3.3×10^{-10}	3.3×10^{-11}
$c_{1,\infty}$ **(mol/L)**	1.0	1.0	0.1	0.042
ϵ_r	78.5	78.5	36.4	36.4
L **(μm)**	1.0	1.0	2.15	2.87
σ_C **(S/m)**	0.069	0.0069	0.0069	3.88×10^{-4}
σ_A **(S/m)**	5	5	5	5
$L_C = L_A$ **(μm)**	10	10	21.5	28.7
$D_{1,C}$ **(m^2/s)**	10^{-14}	10^{-15}	10^{-14}	10^{-15}
$c_{1,C,max}$ **(mol/L)**	32.9	32.9	3.29	1.39
k_0 **($m^{2.5}mol^{-0.5}s^{-1}$)**	10^{-9}	10^{-10}	1.47×10^{-9}	1.69×10^{-10}

namely, $v^* = 1.13 \times 10^{-8}$, $\psi^*_{max} = 31.2$, $\psi^*_{min} = 7.79$, $L^* = 3641.5$, $a^*_2 = 3.65$, $\nu_{p,1} = 1.21$, $\nu_{p,2} = 0.36$, $D^*_2 = 1.27$, $z^*_2 = -1$, $\sigma^*_C = 0.165$, $\sigma^*_A = 0.165$, $L^*_C = L^*_A = 36415$, $D^*_{1,C} = 3.8 \times 10^{-5}$, $c^*_{1,C,max} = 32.9$, $k^*_0 = 3.34 \times 10^{-8}$, and $\Delta\psi^*_{eq} = 0$. Figures 10.5a and 10.5b show the predicted capacitive and Faradaic current densities j_C and j_F versus surface potential ψ_s from CV simulations for these four cases. Results were obtained by numerically solving the GMPNP model

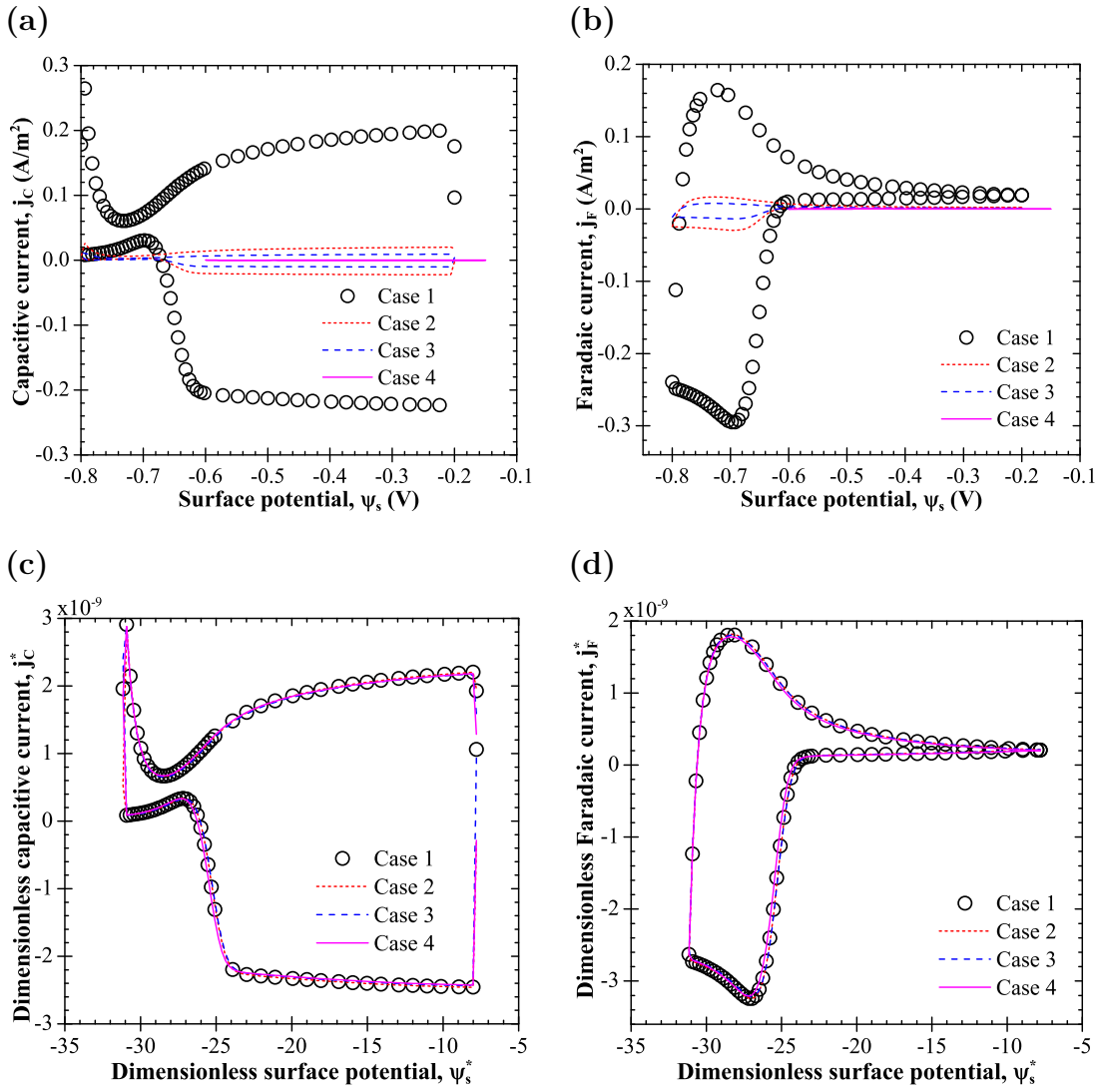

Figure 10.5: Predicted dimensional (a) j_C versus ψ_s curves, (b) j_F versus ψ_s curves, and corresponding dimensionless (c) j_C^* versus ψ_s^* curves, and (d) j_F^* versus ψ_s^* curves from CV simulations for cases 1 to 4 with parameters given in Table 10.1. Results were obtained by numerically solving the GMPNP model with the Stern layer accounting for the potential drop and Li diffusion in the cathode.

with the Stern layer accounting for the potential drop and Li diffusion in the cathode. Figures 10.5a and 10.5b indicate that capacitive and Faradaic current densities j_C and j_F were significantly different in these four cases. However, Figures 10.5c and 10.5d plot the dimensionless current densities j_C^* and j_F^* versus ψ_s^*

curves and demonstrate that they overlapped for all four cases considered. These results established that the governing equations and boundary and initial conditions were properly scaled and that the dimensionless CV curves are uniquely determined by the dimensionless numbers given by Equations (10.38).

10.4.2.2 Different Forms of CV Curves

Figure 10.6 shows the predicted dimensionless current densities j_C^*, j_F^*, and j_t^* versus ψ_s^* curves from CV simulations for four different values of dimensionless reaction rate constant k_0^*, i.e., (a) $k_0^* = 3.34 \times 10^{-7}$, (b) $k_0^* = 3.34 \times 10^{-8}$, (c) $k_0^* = 3.34 \times 10^{-9}$, and (d) $k_0^* = 3.34 \times 10^{-10}$. The dimensionless diffusion coefficient $D_{1,C}^*$ was small and equal to $D_{1,C}^* = 3.8 \times 10^{-5}$ for these four cases. The other dimensionless numbers were identical to those reported in Table 10.1. Figures 10.6(a) and 10.6(b) demonstrate that, for a small value of $D_{1,C}^* = 3.8 \times 10^{-5}$, the dimensionless current densities j_C^*, j_F^*, and j_t^* versus ψ_s^* curves had the similar shape and magnitude for $k_0^* > 3.34 \times 10^{-7}$. Further increasing k_0^* had no effect on the predicted j_C^*, j_F^*, and j_t^* versus ψ_s^* curves. Thus, the Faradaic current density was limited by the diffusion of Li atoms in the electrode. On the other hand, Figures 10.6(c) and 10.6(d) demonstrate that the predicted Faradaic current density j_F^* decreased with decreasing values of k_0^*. In this regime, the dimensionless Faradaic current density j_F^* was limited by redox reaction rate and thus j_t^* was dominated by the dimensionless capacitive current density j_C^*.

Similarly, Figure 10.7 shows the predicted current densities j_C^*, j_F^*, and j_t^* versus ψ_s^* curves for four cases with different values of k_0^*, i.e., (a) $k_0^* = 3.34 \times 10^{-4}$, (b) $k_0^* = 3.34 \times 10^{-6}$, (c) $k_0^* = 3.34 \times 10^{-8}$, and (d) $k_0^* = 3.34 \times 10^{-9}$. For these four cases, the Li atom diffusion coefficient $D_{1,C}^*$ was significantly larger than that in previous simulations shown in Figure 10.6 and equal to $D_{1,C}^* = 38$. The other dimensionless numbers remained the same as those of Table 10.1. Figures 10.7(a) to 10.7(c) demonstrate that, for large values of $D_{1,C}^*$ and $k_0^* > 3.34 \times 10^{-8}$, the

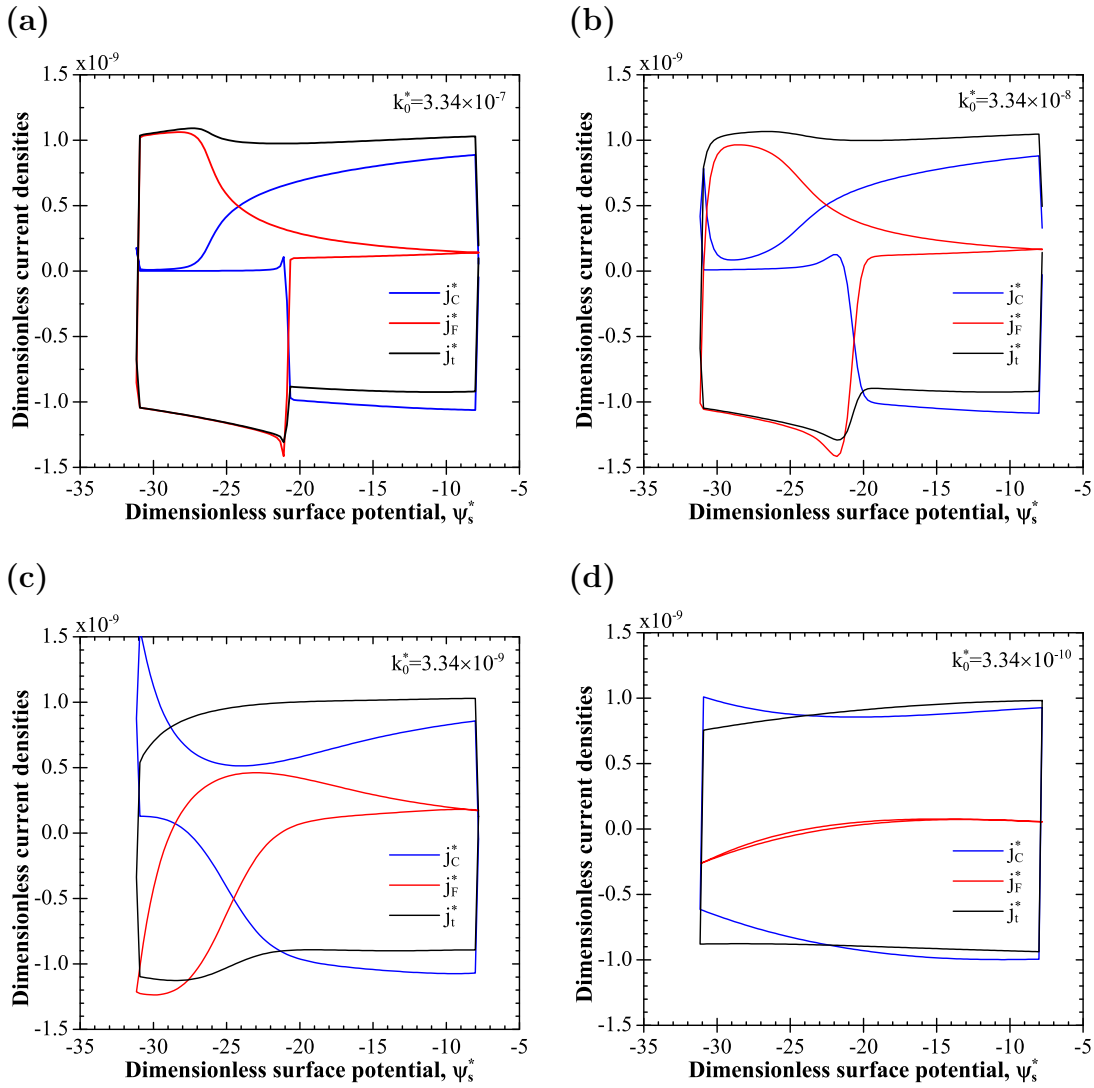

Figure 10.6: Predicted dimensionless CV curves for four different values of dimensionless reaction rate constant k_0^*, namely, (a) $k_0^* = 3.34 \times 10^{-7}$, (b) $k_0^* = 3.34 \times 10^{-8}$, (c) $k_0^* = 3.34 \times 10^{-9}$, and (d) $k_0^* = 3.34 \times 10^{-10}$. Here, $D_{1,C}^*$ was small and equal to 3.8×10^{-5}. The other dimensionless parameters were identical to those reported in Table 10.1.

predicted CV curves were nearly symmetric and j_C^* was nearly zero. Moreover, the total dimensionless current density j_t^* was dominated by j_F^* unlike that observed in Figure 10.6 with small $D_{1,C}^*$. Indeed, CV curves shown in Figures 10.7(a) to 10.7(c) correspond to fast redox reactions and Li atom intercalation in the

electrodes. These CV curves were similar to those observed experimentally with MnO_2/gold or MnO_2/graphene composite electrodes in Refs. [446, 447]. Finally, Figure 10.7(d) demonstrates that j_F^* decreased significantly when decreasing k_0^* to $k_0^* < 3.34 \times 10^{-9}$. Then, the total current density j_t^* was dominated by j_C^*. In this regime, the Faradaic current was limited by redox reactions similar to that observed in Figure 10.6(d).

10.4.3 Current Versus Scan Rate Analysis

Figure 10.8 shows the dimensionless total j_t^*, capacitive j_C^*, and Faradaic j_F^* current densities predicted for Nb_2O_5/carbon asymmetric supercapacitors as a function of scan rate v ranging from 10^{-3} to 10 V/s. Results were obtained by solving the GMPNP model with the Stern layer accounting for the potential drop and Li diffusion in the cathode with parameters reported in Section 10.3.4. Figure 10.8 demonstrates that the j_C^* increased nearly linearly with v^* and j_F^* was proportional to $v^{*1/2}$ for the range of scan rates considered. Note that the capacitive j_C^* and Faradaic j_F^* current densities j_F^* dominate at large and small scan rates, respectively. It is evident that the total current density j_t^* was given by $j_t^* = k_1^* v^* + k_2^* v^{*1/2}$. These results establish that this widely used formula for analyzing pseudocapacitive materials is indeed valid in the presence of both electric double layers and redox reactions with ion intercalation.

10.5 Conclusion

This chapter developed a physicochemical model for simulating asymmetric supercapacitors and pseudocapacitors by simultaneously accounting for (1) asymmetric electrolytes with (2) finite ion size, (3) Stern and diffuse layers, and (4) redox reactions with associated ion insertion in the pseudocapacitive electrode. Dimensional analysis of the governing equations was also performed for CV measure-

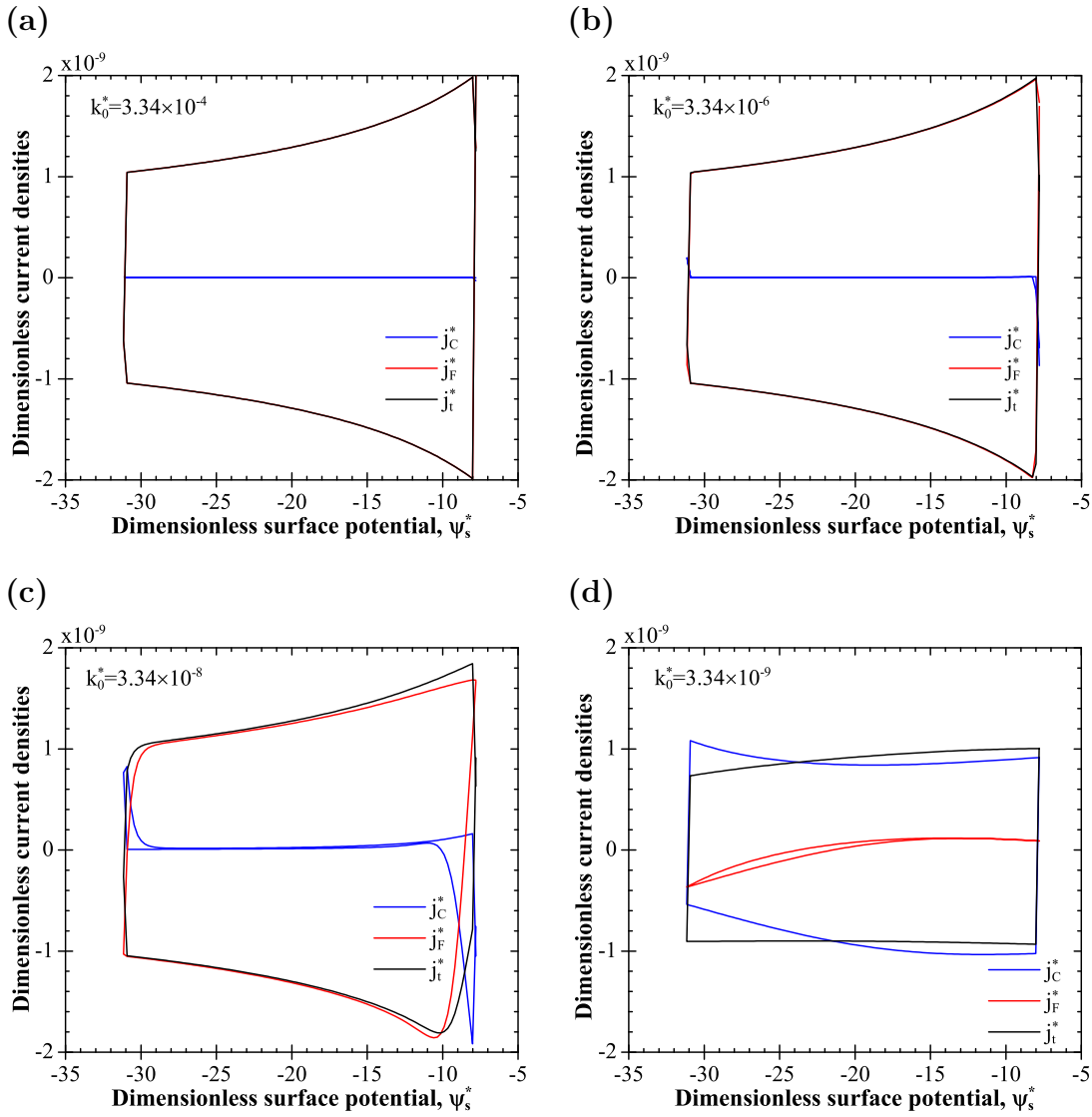

Figure 10.7: Predicted dimensionless CV curves for four different values of dimensionless reaction rate constant k_0^*, namely, (a) $k_0^* = 3.34 \times 10^{-7}$, (b) $k_0^* = 3.34 \times 10^{-8}$, (c) $k_0^* = 3.34 \times 10^{-9}$, and (d) $k_0^* = 3.34 \times 10^{-10}$. Here, $D_{1,C}^*$ was large and equal to 3.8×10^{-5}. The other dimensionless parameters were identical to those reported in Table 10.1.

ments of asymmetric supercapacitors with 21 dimensional parameters. Seventeen dimensionless numbers given by Equation (10.38) were identified to govern the CV measurements of asymmetric supercapacitors using binary asymmetric electrolytes

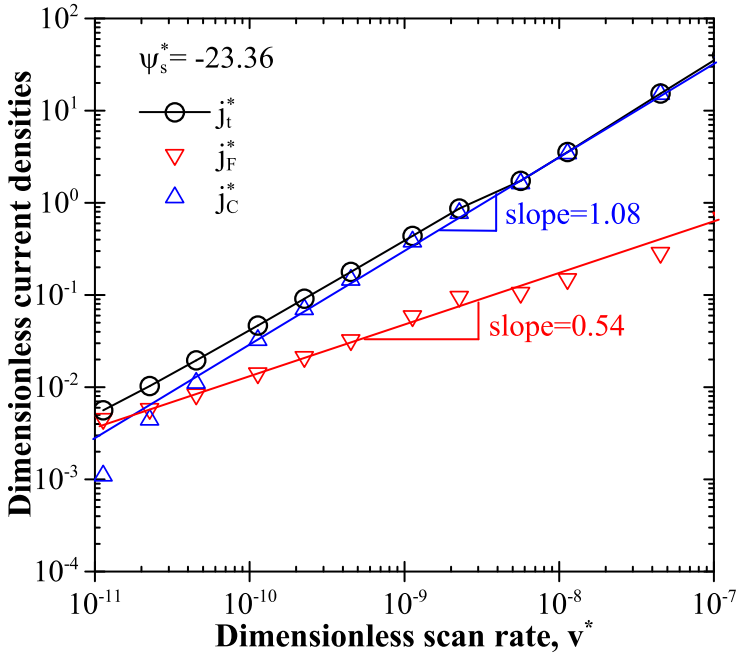

Figure 10.8: Predicted dimensionless total j_t^*, capacitive j_C^*, and Faradaic j_F^* current densities for Nb_2O_5/carbon asymmetric supercapacitors at surface potential $\psi_s^* = -23.36$ as a function of scan rate v^* ranging from 10^{-11} to 10^{-7}. The dimensionless numbers were $\psi_{max}^* = 31.2$, $\psi_{min}^* = 7.79$, $L^* = 3641.5$, $a_2^* = 3.65$, $\nu_{p,1} = 1.21$, $\nu_{p,2} = 0.36$, $D_2^* = 1.27$, $z_2^* = -1$, $\sigma_C^* = 0.16$, $\sigma_A^* = 12$, $L_C^* = L_A^* = 36415$, $D_{1,C}^* = 3.8 \times 10^{-5}$, $k_0^* = 3.34 \times 10^{-8}$, and $\Delta\psi_{eq}^* = 0$

between two planar electrodes. The Faradaic current was limited by diffusion of Li atoms in the electrode for small $D_{1,C}^*$ and it was limited by redox reactions for small k_0^*. This study rigorously established that, in CV measurements of pseudocapacitive materials, the total current was expressed as $j_t = k_1 v + k_2 v^{1/2}$ where the first and second terms on the right-hand-side of Equation (11.2) correspond to capacitive and Faradaic currents, respectively.

CHAPTER 11

Conclusions and Future Work

This chapter summarizes the main contributions of the present study and makes recommendations for future work beyond the results reported in this thesis.

11.1 Main Contributions

The present study not only presented physicochemical models of electrochemical capacitors but also provided rigorous interpretations to experimental observations and design rules for ECs. The main contributions of this thesis can be summarized as follows.

11.1.1 Development of Physicochemical Models

The present study identified the important phenomena that must be simultaneously accounted for in order to accurately simulate actual EDLCs characterized by large electrolyte concentrations and surface electric potentials. It established that (i) both Stern and diffuse layers, (ii) finite ion size, (iii) the dependency of electrolyte permittivity on the local electric field, (iv) the asymmetric nature of the electrolytes, and (v) the curvature of the electrode/electrolyte interface must be accounted for.

New boundary conditions have been derived to account for the presence of the Stern layer without resolving it in the computational domain. These boundary conditions have enabled the first simulations of three-dimensional electrode

structures of EDLCs. The results were validated against experimental data.

Moreover, a generalized modified Poisson-Nernst-Planck (GMPNP) model was developed from first principles to simulate electric double layer dynamics simultaneously accounting for (1) asymmetric electrolytes with (2) multiple ion species of (3) finite ion size, and (4) Stern and diffuse layers.

Finally, a dynamic physicochemical model was developed for pseudocapacitors and asymmetric supercapacitors by rigorously and simultaneously accounting for the electric double layer coupled with reversible redox reaction as well as ion insertion in the electrode.

Note that all the simulations performed did not rely on fitting parameters unlike those using traditional approaches [199, 244, 260]. In addition, simulations were systematically validated against experimental data reported in the literature.

11.1.2 Physical Understanding of Electrochemical Capacitors

The dynamic models developed here have enabled rigorous physical interpretation of experimental observations. For example, this study established that electric double layers feature an intrinsic "capacitance dispersion" at high frequencies in electrochemical impedance spectroscopy (EIS) measurements. This was attributed to the fact that ion transport could not follow the fast variation in electric potential. Moreover, this study also established that the "hump" observed in CV curves of EDLCs was due to the saturation of ion concentration at the electrode surface and not due to "electrolyte starvation" [341, 342], "redox reactions" [40, 295, 343–351], or "difference of diffusion capability between solvated anions and cations" [349] as proposed in the literature.

This study also revealed that the predicted EDL integral capacitance was constant and equal to the capacitance under quasi-equilibrium conditions for dimensionless scan rate $v^* \ll 1$ in CV measurements where v^* is given by Equation

(8.14). Then, the electrode had no effect on the EDL capacitance measured at scan rates smaller than a critical value. Similarly, the EDL differential capacitance was independent of frequency for dimensionless frequency $\tau_m f \ll 1$ in EIS measurements where τ_m is given by Equation (7.10).

Dimensional analysis was performed based on the GMPNP model and eleven dimensionless numbers given by Equation (9.19) were identified to govern the CV measurements of electric double layer in binary asymmetric electrolytes between two identical planar electrodes of finite thickness. For the first time, a self-similar behavior was identified for the electric double layer integral capacitance estimated from CV measurements. It was expressed as,

$$\frac{C_s}{C_{s,0}} = \frac{1}{1 + \left[\frac{\tau_{RC}}{1.22\tau_{CV}}\left(1 + \frac{80}{\sigma_s^*}\right)\right]^{1.44}} \tag{11.1}$$

where $C_{s,0}$ is the maximum capacitance observed in curves of C_s versus scan rate v at low scan rates while τ_{RC} and τ_{CV}, given by Equation (9.25), are the "RC time scale" for binary asymmetric electrolytes and the half cycle period of CV measurements, respectively. Finally, σ_s^* is the dimensionless electrode electrical conductivity given by Equation (9.19). This study also established that asymmetric ion diameters and valencies must be accounted for in CV simulations with asymmetric electrolytes for all scan rates. By contrast, asymmetric ion diffusion coefficient affected the CV curves only at large scan rates.

Finally, this study rigorously establishes that, in CV measurements of pseudocapacitive materials, the total current was expressed as

$$j_t = k_1 v + k_2 v^{1/2} \tag{11.2}$$

where the first and second terms on the right-hand-side of Equation (11.2) correspond to capacitive and Faradaic currents, respectively. This equation was formulated in a semi-empirical manner in the literature. The present study established its validity rigorously.

11.1.3 Design Rules

The models and results reported here are useful to rationalize the design of electrochemical capacitors and to provide rules for optimizing the porous electrode architecture of ECs and for selecting the electrolyte. For example, a scaling law was derived, for the first time, to predict the integral areal capacitance of carbon-based EDLCs with complex electrode morphology. It is expressed as the product of an analytical expression for planar electrodes [Equation (6.16)] and a semi-empirical function $f(R_0^* - a^*/2)$ accounting for the porous electrode morphology. The latter was obtained using experimentally-measured integral areal capacitance for EDLCs with various porous carbon electrodes and binary symmetric electrolytes. The scaling law indicates that the integral areal capacitance was most sensitive to the ions' effective diameter and valency and to the electrolyte dielectric constant. It was also sensitive to the pore radius R_0 only as R_0 approaches the ion radius $a/2$. Overall, to achieve large integral areal capacitance (i) the effective ion diameter a should be small, (ii) the electrolyte dielectric constant ϵ_r should be large, (iii) the pores should be monodisperse and their diameter $2R_0$ should be tailored to match the ion diameter, i.e., $2R_0 \approx a$, and (iv) the ion valency should be large.

Finally, these models will also be useful for simulating and designing various practical electrochemical, colloidal, and biological systems for a wide range of applications.

11.2 Future Work

This section presents several recommendations and suggestions for future modeling efforts to further optimize EDLCs and pseudocapacitors.

11.2.1 Future Modeling of Electric Double Layer Capacitors

Dynamic Modeling of EDLCs With 3D Electrode Structures

Chapters 7 to 9 presented dynamic modeling of planar EDLCs based on the MPNP or GMPNP model with Stern layer and accounting for charge transport in the electrode. These simulations can be extended to EDLCs with three-dimensional ordered electrode structures. This can be accomplished by combining the MPNP or GMPNP model with the new boundary conditions derived in Chapter 3 accounting for the presence of Stern layer. These simulations would help reveal the effects of the 3D electrode morphology on the charging/discharging performance and power density of EDLCs. Moreover, it will also be useful to simulate the charging/discharging of 3D EDLCs with the actual length scale and accounting for the potential drop and ion diffusion throughout the mesoporous electrode structure and across interfaces. Such simulations would offer a direct way to identify key design parameters for improving the energy and power densities of actual devices.

Modeling of EDLCs With Electrolyte Mixtures

Recently, electrolyte mixtures with multiple ion species have been considered as a way to extend the working conditions and improve the performances of EDLCs [373–375, 448]. For example, electrolyte mixtures could widen the operation temperature and improve the electrical conductivity of EDLCs [373–375, 448]. Such electrolyte mixtures include $NaClO_4$ and $NaPF_6$ in ethylene carbonate-dimethyl carbonate [448] and ionic liquid mixture with $[C_3mpy][Tf_2N]$ and $[C_4mpip][Tf_2N]$ [374], for example. The GMPNP model developed in Chapter 9 can be readily used to simulate such systems involving asymmetric electrolytes with multiple ion species. The corresponding results would provide guidelines on selecting the optimum electrolyte mixture.

Future Experiments for EDLCs

Experiments are needed to validate the scaling laws developed in Chapter 9 for EDLCs with asymmetric electrolytes. For example, CV measurements could be performed for different binary asymmetric electrolytes such as H_2SO_4, Na_2SO_4, and Li_2SO_4 using planar electrodes. Moreover, future 3D dynamic modeling of EDLCs should be validated against experimental data on charging/discharging of supercapacitors with 3D ordered electrode structures. The validation could be made by comparing the predicted and measured CV curves.

11.2.2 Future Modeling of Pseudocapacitors and Asymmetric Supercapacitors

Pseudocapacitive Electrodes With 3D Structures

Pseudocapacitors and asymmetric supercapacitors employ pseudocapacitive materials (e.g., RuO_2, TiO_2, MnO_2, V_2O_5, and Nb_2O_5) to increase the capacitance and the energy density of supercapacitors via fast redox reactions. The three-dimensional electrode structures significantly affect the performance of these supercapacitors. Indeed, 3D ordered pseudocapacitive electrodes provide many advantages including fast ion transport paths, good electronic conductivity, and improved electrochemical stability at high charging/discharging rates [370, 449–455].

First, the model developed in Chapter 10 along with the boundary conditions developed in Chapter 5 can be used for simulating the coupled transport and electrochemical phenomena in pseudocapacitive materials with three-dimensional ordered structures. In fact, ordered electrode structures also significantly simplify the simulations due to reduced geometric complexity and computational cost. Such simulations would help identify the optimum 3D electrode morphologies for increasing the energy and power densities of the devices.

Second, scaling analysis could be performed for pseudocapacitors by analogy with what has been described in Chapters (6) to (9) for EDLCs. This analysis would use the dimensionless similarity parameters identified in Chapters (6) to (9) and experimental data reported in the literature for mesoporous Nb_2O_5 [30, 398], MoO_3 [370], and CeO_2 [456], for example.

Asymmetric Supercapacitors With Optimum Electrode Combinations

Asymmetric supercapacitors provide opportunities to enhance both energy and power densities by combining the advantages of pseudocapacitors and EDLCs. The model developed in Chapter 10 can be readily used for extensive and systematic simulations of asymmetric supercapacitors with various combinations of the electrodes. Then, these simulations would help identify optimum combinations of redox active electrodes and carbon-based electrodes to improve the overall device' performance.

Supercapacitors With Composite Electrodes

Composite electrodes such as carbon-based mesoporous electrodes coated with redox-active materials (e.g., carbon nanotube/SnO_2 [46], carbon/MnO_2 [45, 447, 457, 458], graphene/RuO_2 [392], graphene/$Ni(OH)_2$ [392], carbon nanotube/V_2O_5 [458], and gold/MnO_2 [446]) have attracted significant attention in recent years [28, 45–47, 392, 446, 447, 457, 458]. These composite electrodes provide advantages including (i) they enhanced overall electrical conductivity of the electrodes and (ii) they increased the amount of redox-active sites for pseudocapacitive materials provided by the 3D carbon scaffold with tunable macro/mesopores [28, 45–47, 392, 446, 447, 457, 458]. Here, it is essential to understand the role of 3D electrode structures and the composites in affecting the ion transport and redox reactions for optimizing the electrode architecture. Modeling of such systems could be

achieved by combining the models developed in Chapters 5 and 10. Important design parameters to be investigated include the thickness of the coated redox-active materials and the electrode structure/pore size. These parameters need to be optimized to improve the charge storage capability and charging time [28, 45–47, 392, 446, 447, 457, 458].

11.2.3 Thermal Modeling of Supercapacitors

Thermal behaviors such as heat generation during charging/discharging are key issues affecting the performances, reliability, lifetime, and safety of electrical energy storage devices such as batteries and supercapacitors [445]. The transport and electrochemical phenomena involved determine the thermal behaviors of these devices. Physical modeling provides a good way to thoroughly understand the thermal behaviors of supercapacitors. For example, the thermal oscillation behavior of EDLCs has been recently studied and rigorously interpreted by members of our research group thanks to detailed physical modeling of transport phenomena involved [445]. However, such simulations have not been extended to pseudocapacitors involving exothermic or endothermic redox-reactions. This can be achieved by incorporating thermal transport in the model developed in Chapter 10 of this thesis. These simulations and results could provide guidelines for avoiding premature performance degradation and potential hazards.

APPENDIX A

Appendix: Supplemental Material to Chapter 9

A.1 Full domain simulations

Figure A.1 shows the predicted capacitive current density j_C versus surface potential ψ_s at the electrode A and $-\psi_s$ at electrode B. Results were obtained by solving the generalized MPNP model with a Stern layer [Equations (9.5) to (9.10)] for the full domain $-L + H \leq x \leq L - H$. The ion diameters were imposed as $a_1 = 0.66$ nm and $a_2 = 0.60$ nm while the valencies and diffusion coefficients were chosen to be symmetric as $z_1 = -z_2 = 1$ and $D_1 = D_2 = 1.957 \times 10^{-9}$ m^2/s. Other parameters were $c_{1,\infty} = 1$ mol/L, $T = 298$ K, $\epsilon_r = 78.5$, $v = 10^4$ V/s, and $L = 200$ μm. Figure A.1 shows that the transient capacitive current densities j_C at two electrodes were always exactly opposite satisfying the charge conservation principle [459]. Similar results were also observed for electrolytes with asymmetric valency and diffusion coefficient (not shown).

A.2 Revisiting half domain simulations

When simulating the half domain, e.g., $-L + H \leq x \leq 0$, the boundary conditions at the middle plane located at $x = 0$ were required [148, 149]. In previous simulations for symmetric electrolytes, the electric potential and ion concentrations were assumed to be constant satisfying the electroneutrality condition such that [148, 149],

$$\psi(x = 0, t) = 0, \quad c_1(x = 0, t) = c_{1\infty}, \quad \text{and} \quad c_2(x = 0, t) = -c_{1,\infty} z_1 / z_2 \quad \text{(A.1)}$$

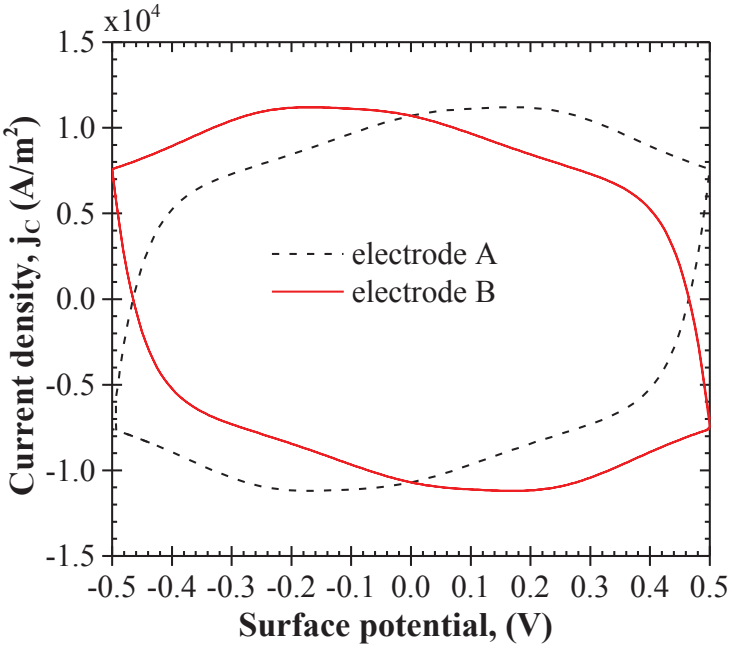

Figure A.1: Predicted CV curves at the electrodes A and B for the full domain. Results were obtained by numerically solving the generalized MPNP model with a Stern layer [Equations (9.5) to (9.10)] with $a_1 = 0.66$ nm, $a_2 = 0.60$ nm, $z_1 = 1$, $z_2 = -1$, $D_1 = D_2 = 1.957 \times 10^{-9}$ m^2/s while $c_{1\infty} = 1$ mol/L, $T = 298$ K, $\epsilon_r = 78.5$, $v = 10^4$ V/s, and $L = 200$ μm.

The corresponding dimensionless boundary conditions at the middle plane located at $x^* = 0$ were,

$$\psi^*(x^* = 0, t^*) = 0, \quad c_1^*(x^* = 0, t^*) = 1, \quad \text{and} \quad c_2^*(x^* = 0, t^*) = 1/z_2^* \qquad \text{(A.2)}$$

In order to assess the validity of half-domain simulations, as performed in Refs. [148, 149], Figure A.2a shows the predicted j_C versus ψ_s curves with symmetric electrolytes for (i) the full-domain simulations with $-L + H \leq x \leq L - H$ as well as for (ii) the half-domain simulations with $0 \leq x \leq L - H$. Results were obtained by solving the GMPNP model with a Stern layer [Equations (9.5) to (9.10) and (A.1)]. Note that zero potential and bulk ion concentrations [Equation (A.1)] were imposed at the midplane $x = 0$ for half-domain simulations as previously

discussed. The ion diameters were taken as $a_1 = a_2 = 0.66$ nm while the valencies and diffusion coefficients were $z_1 = -z_2 = 1$ and $D_1 = D_2 = 1.957 \times 10^{-9}$ m^2/s. Other parameters were $c_{1,\infty} = 1$ mol/L, $v = 10^4$ V/s, $L = 200$ μm, $\psi_{max} = \psi_{min} = 0.5$ V, $T = 298$ K, and $\epsilon_r = 78.5$. It is evident that, for symmetric electrolytes, the predicted CV curves obtained for the half-domain were identical to those obtained for the full-domain. This established that, for symmetric electrolytes, it suffices to perform CV simulations for only half of the electrolyte domain by virtue of antisymmetry in the electric potential. This has the advantage of reducing the number of meshes and the computational time. On the other hand, Figure A.2b shows the predicted current density j_C versus ψ_s obtained by simulating the full as well as the half domains for asymmetric electrolytes with $a_1 = 0.66$ nm and $a_2 = 0.60$ nm. The model and other parameters were identical to those used to generate the results shown in Figure A.2a. Figure A.2b demonstrates that the predicted current density j_C obtained by simulating the half-domain differed from that obtained by simulating the full-domain. In fact, the difference increased with increasing difference in ion diameters (not shown). Note that similar trend was also observed for electrolytes with asymmetric valency. This can be attributed to the fact that for asymmetric electrolytes, the potential $\psi(0,t)$ in the middle plane between the two electrodes was not equal to 0. In other words, the boundary condition $\psi(0,t)$=0 V, given by Equation (A.1), is not valid for asymmetric electrolytes.

Figure A.3 shows the predicted electric potential $\psi(t)$ at the middle plane ($x = 0$) as a function of time t from CV simulations with the entire domain for three cases. Here, three different combinations of ion diameters were considered, namely, (i) $a_1 = 1.0$ nm and $a_1 = 0.60$ nm, (ii) $a_1 = 0.66$ nm and $a_1 = 0.60$ nm, and (iii) $a_1 = a_2 = 0.66$ nm. It is evident that the electric potential at the middle plane remained zero and invariant with time for the case with equal ion diameters while it oscillated and deviated away from zero for cases with unequal

ion diameters. In addition, the deviation increased with increasing the difference in the unequal ion diameters. However, the ion concentrations remained $c_{i,\infty}$ at the middle plane (not shown). These results demonstrate that, for asymmetric electrolytes, the boundary conditions given by Equations (A.1) at the middle plane were invalid and thus full entire domain must be simulated.

A.3 Effect of finite ion size

In order to demonstrate the necessity of accounting for the finite ion size, Figure A.4a shows the predicted CV curves j_C versus ψ_s with finite ion size $a_1 = a_2 = a = 0.66$ nm as well as with vanishing ion size, i.e., $a_1 = a_2 = a = 0$ nm. For both cases, the Stern layer thickness was imposed to be $H = 0.33$ nm. The model and other parameters were identical to those used to generate the results shown in Figure 2. Note that the model with $a_1 = a_2 = 0$ nm and $H = 0.33$ nm corresponds to the PNP model with a Stern layer. Figure A.4a demonstrates that the model neglecting the finite ion size significantly overpredicted the current density j_C for almost the entire range of surface potential ψ_s. Moreover, Figure A.4b shows the corresponding surface cation concentration as a function of surface potential ψ_s for the same cases considered in Figure A.4a. It demonstrates that the surface cation concentration was bounded to its maximum value $c_{max} = 1/N_A a^3 = 5.77$ mol/L when accounting for the finite ion size. By contrast, the surface cation concentration reached an unrealistically large value of 116 mol/L when neglecting the finite ion size. Overall, these results demonstrated that the finite ion size must be accounted for in simulating electric double layer dynamics for surface potential larger than 0.5 V and ion concentration lager than 1 mol/L.

Note that in a recent study [460], the classical PNP model with a Stern layer was used for simulating the electric double layer dynamics with constant surface potential of 1 V. The results were shown to be qualitatively consistent to those predicted by molecular dynamics simulations [460]. However, the authors imposed

the surface charge density so that the "steric limit" due to finite ion size were not violated [460]. Unfortunately, unlike the surface potential or capacitive current density, the surface charge density cannot be imposed at the electrode surface in many practical applications such as in supercapacitors and batteries.

A.4 Capacitance versus scan rate

A.4.1 Scaling of valency and inter-electrode distance

Figure A.5a shows the double layer capacitance C_s predicted from CV simulations and estimated using Equation (8.2) as a function of scan rate v ranging from 1 to 10^7 V/s for $L = 10$ or 100 μm and $z_2 = -1$, -2, or -3. The other parameters were identical among all these cases, namely, $a_1 = a_2 = 0.66$ nm, $z_1 = 1$, $D_1 = 2 \times 10^{-9}$ m^2/s, $c_{1\infty} = 1$ mol/L, $T = 298$ K, and $\epsilon_r = 78.5$. It is evident that these C_s versus v curves were significantly different from one another. For all cases considered, the predicted capacitances C_s reached their respective maxima, denoted by $C_{s,0}$, at small scan rates where C_s was independent of v and L. Such conditions corresponded to the quasi-equilibrium or diffusion-independent regime [149]. In this regime, ion transport was fast enough to follow the variation in the electric potential and the predicted areal integral capacitance C_s was independent of the scan rate and ion diffusion [149]. On the other hand, for large scan rates, Figure A.5a shows that the predicted C_s decreased rapidly with increasing v due to the fact that charging and discharging became limited by ion diffusion. Note that similar phenomena were also observed in CV simulations for binary and symmetric electrolytes [149]. Moreover, the critical scan rate v at which the capacitance C_s started decreasing was smaller for larger inter-electrode distance $2L$. Indeed, it takes longer time for ion species to transport to the electrode surface for a larger inter-electrode distance. In addition, the predicted value of C_s increased with decreasing z_2 (i.e., increasing $|z_2|$), as previously discussed.

Figure A.5b shows the dame data as shown in Figure A.5a but plotted in terms of $C_s/C_{s,0}$ as a function of the product v^*L^*. It is interesting to note that all curves collapsed on a single line, irrespective of their different values of L and z_2. These results demonstrate that the valency and inter-electrode distance were successfully scaled when plotting $C_s/C_{s,0}$ as a function of v^*L^*.

A.4.2 Scaling of potential window

Figure A.6a shows the predicted C_s versus v curves for six cases with different values of potential window, namely, $\psi_{max} - \psi_{min} = 0.01$, 0.1, 0.5, 0.75, 1.0, and 1.3 V. The model and other parameters were identical to those used to generate the results shown in Figure A.1. It is evident that the C_s versus v curves were significantly different from one another. However, Figure A.6b shows that the same data collapsed on a single line when plotting in terms of $C_s/C_{s,0}$ as a function of $v^*L^*/(\psi^*_{max} - \psi^*_{min})$. This demonstrates that the potential window in CV measurements was successfully scaled using $v^*L^*/(\psi^*_{max} - \psi^*_{min})$.

A.4.3 Scaling of asymmetric diffusion coefficients

Figure A.7a shows the predicted C_s versus v curves for five cases with different values of diffusion coefficient, namely, $D_2 = 0.01D_1$, $0.1D_1$, $1.0D_1$, $10D_1$, and $100D_1$ while $D_1 = 1.957 \times 10^{-9}$ m^2/s. The model and other parameters were identical to those used to generate the results shown in Figure A.1. It is evident that the C_s versus v curves were significantly from one another. However, Figure A.7b shows that the same data collapsed on a single line when plotting in terms of $C_s/C_{s,0}$ as a function of $v^*L^*/(1+D^*_2)$. This demonstrates that the asymmetric diffusion coefficients in CV measurements was successfully scaled using $v^*L^*/(1+D^*_2)$.

A.4.4 Effect of ion diameter

Figure A.8a shows the predicted C_s versus v curves for three cases with different values of ion diameters, namely, $a_1 = a_2 = 0.60$ nm, $a_1 = a_2 = 0.66$ nm, and $a_1 = 1.0$ nm, $a_2 = 0.6$ nm. The model and other parameters were identical to those used to generate the results shown in Figure A.1. It is evident that the maximum capacitance increased with decreasing ion diameters. Moreover, the C_s versus v curves were significantly from one another. However, Figure A.7b shows that the same data collapsed on a single line when plotting in terms of $C_s/C_{s,0}$ as a function of $v^*L^*/[(1 + D_2^*)(\psi_{max}^* - \psi_{min}^*)]$, irrespective of the different ion diameters.

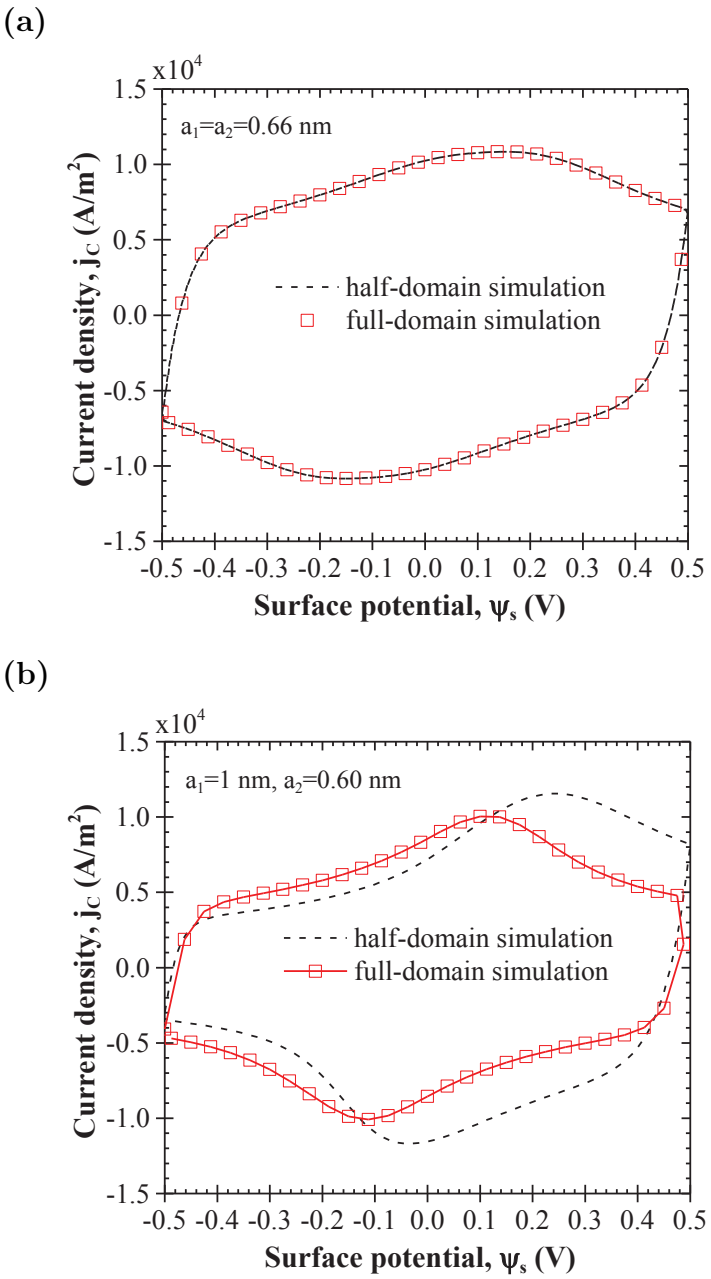

Figure A.2: Predicted j_C versus ψ_s curves for (a) symmetric electrolytes with $a_1 = a_2 = 0.66$ nm and (b) asymmetric electrolytes with $a_1 = 1.0$ nm and $a_2 = 0.60$ nm. Results were obtained by numerically solving the generalized MPNP model with a Stern layer [Equations (9.5) to (9.10)] with $z_1 = -z_2 = 1$, $D_1 = D_2 = 1.957 \times 10^{-9}$ m^2/s, $c_{1\infty} = 1$ mol/L, $v = 10^4$ V/s, $L = 100$ μm, $T = 298$ K, and $\epsilon_r = 78.5$.

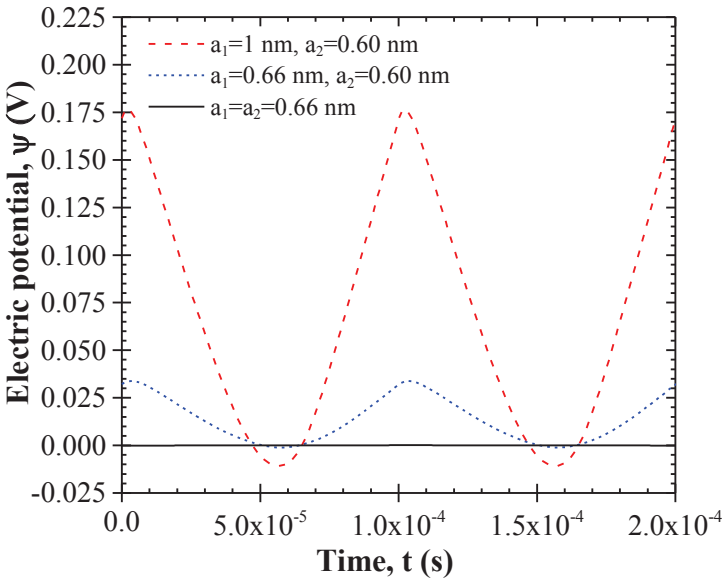

Figure A.3: Predicted electric potential ψ at the middle plane as function of time t from CV simulations for the entire domain. Three cases with different ion diameters were considered, namely, (i) $a_1 = 1.0$ nm and $a_1 = 0.60$ nm, (ii) $a_1 = 0.66$ nm and $a_1 = 0.60$ nm, and (iii) $a_1 = a_2 = 0.66$ nm. The model and other parameters were identical to those used to generate the results shown in Figure A.1.

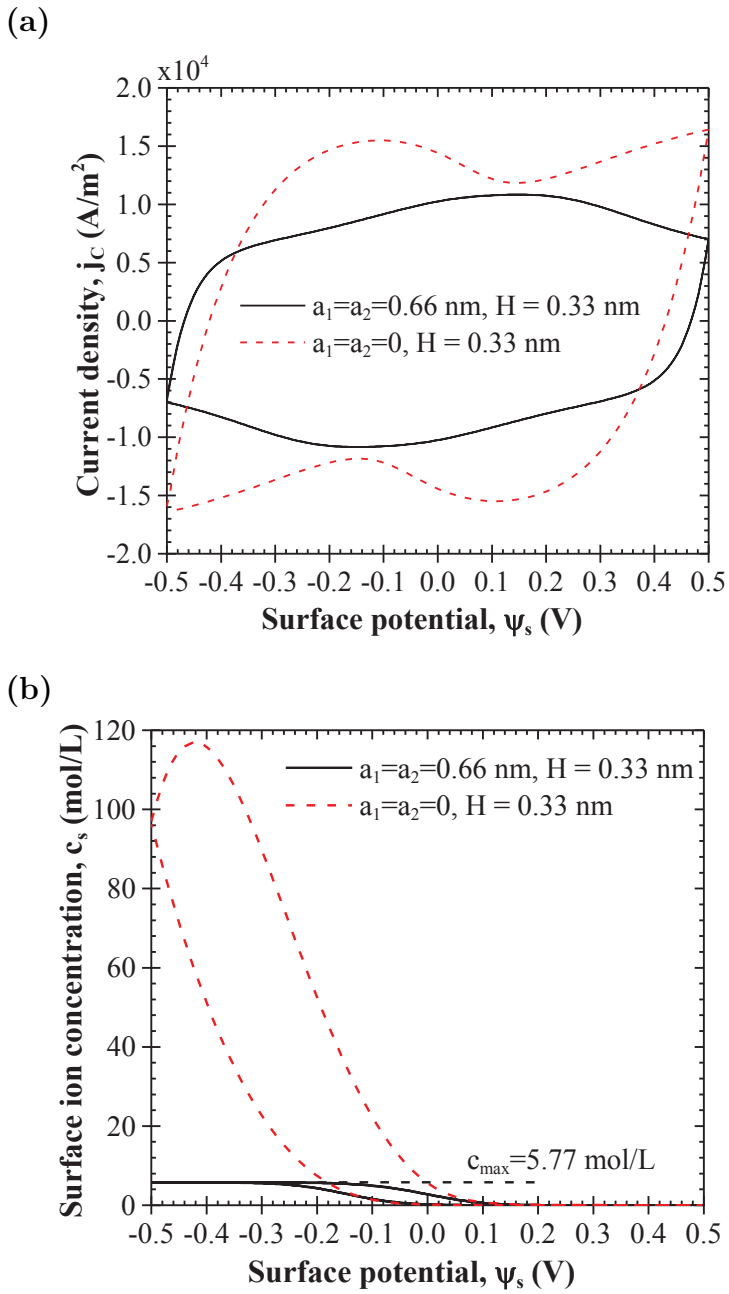

Figure A.4: Predicted (a) j_C versus ψ_s curves and (b) surface cation concentration c_s versus ψ_s curves from CV simulations for two cases with finite ion diameters $a_1 = a_2 = 0.60$ nm and with vanishing ion diameters $a_1 = a_2 = 0$ nm, respectively. The model and other parameters were identical to those used to generate the results shown in Figure A.1.

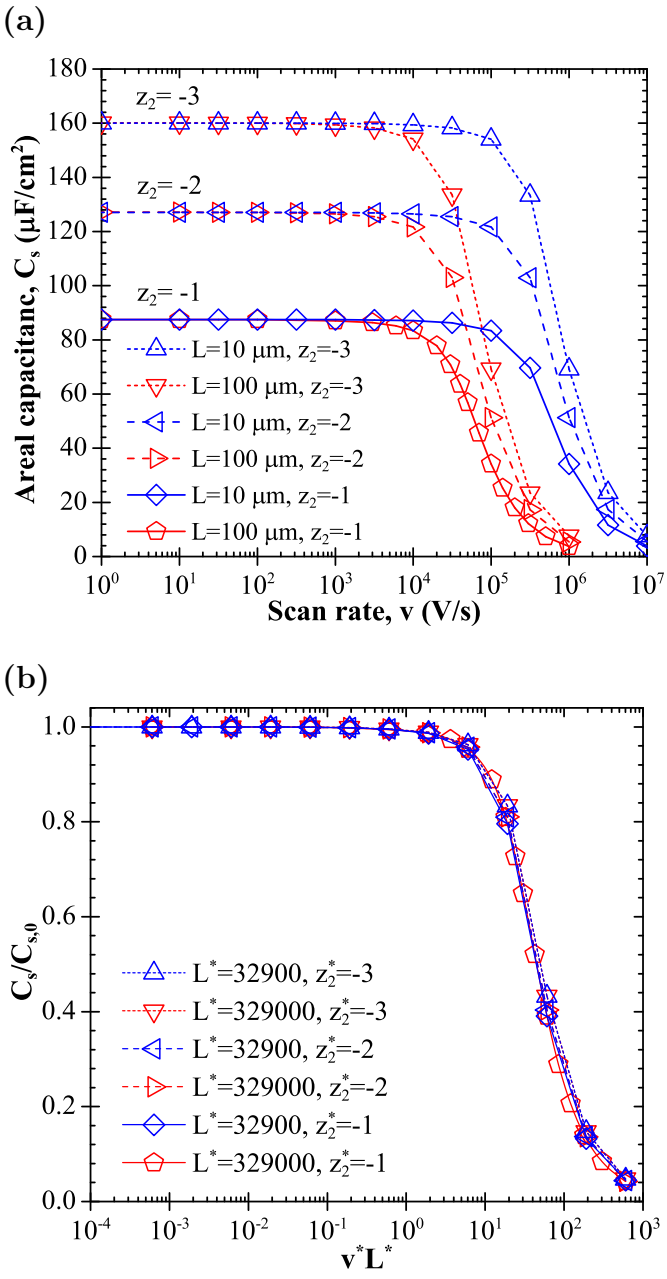

Figure A.5: Predicted (a) capacitance C_s as a function of scan rate v and (b) $C_s/C_{s,0}$ as a function of v^*L^* obtained from CV simulations for $L = 10$ or 100 μm and $z_2 = -1$, -2, or -3. The other parameters were identical among all cases, namely, $D_1 = 1.957 \times 10^{-9}$ m^2/s, $c_\infty = 1$ mol/L, $T = 298$ K, and $\epsilon_r = 78.5$.

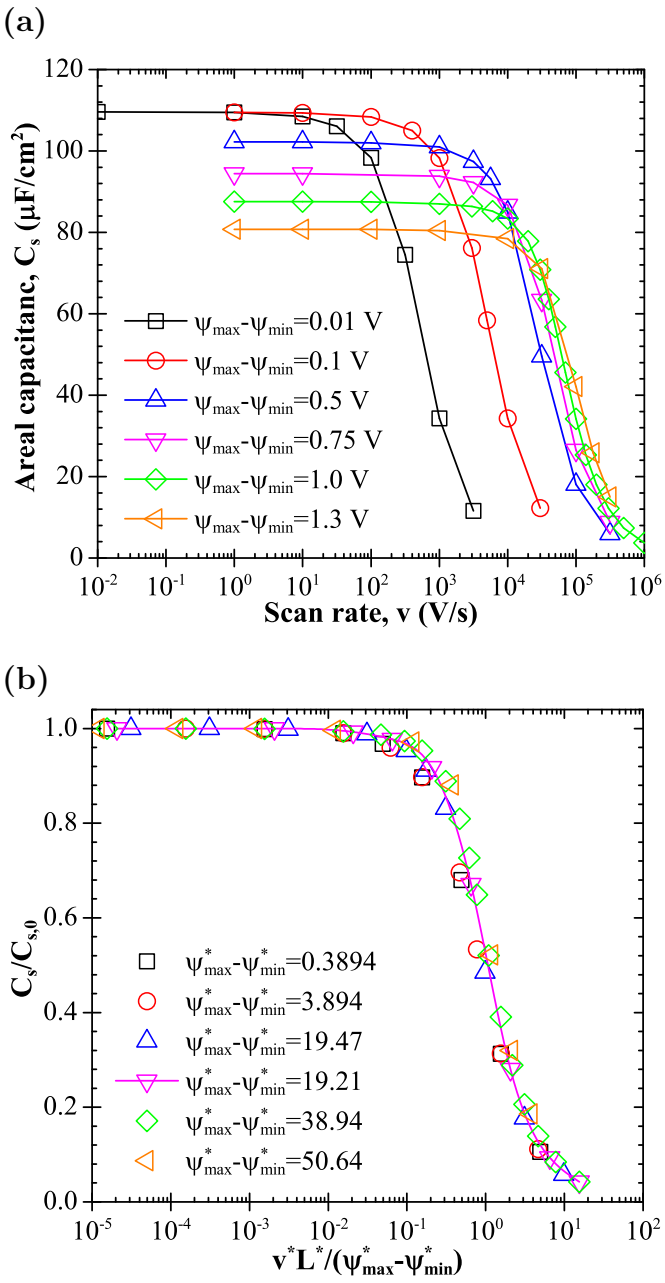

Figure A.6: Predicted (a) capacitance C_s versus scan rate v and (b) $C_s/C_{s,0}$ versus $v^*L^*/(\psi^*_{max} - \psi^*_{min})$ from CV simulations for six cases with different values of potential window, namely, $\psi_{max} - \psi_{min}$ = 0.01, 0.1, 0.5, 0.75, 1.0, and 1.3 V. The model and other parameters were identical to those used to generate the results shown in Figure A.1.

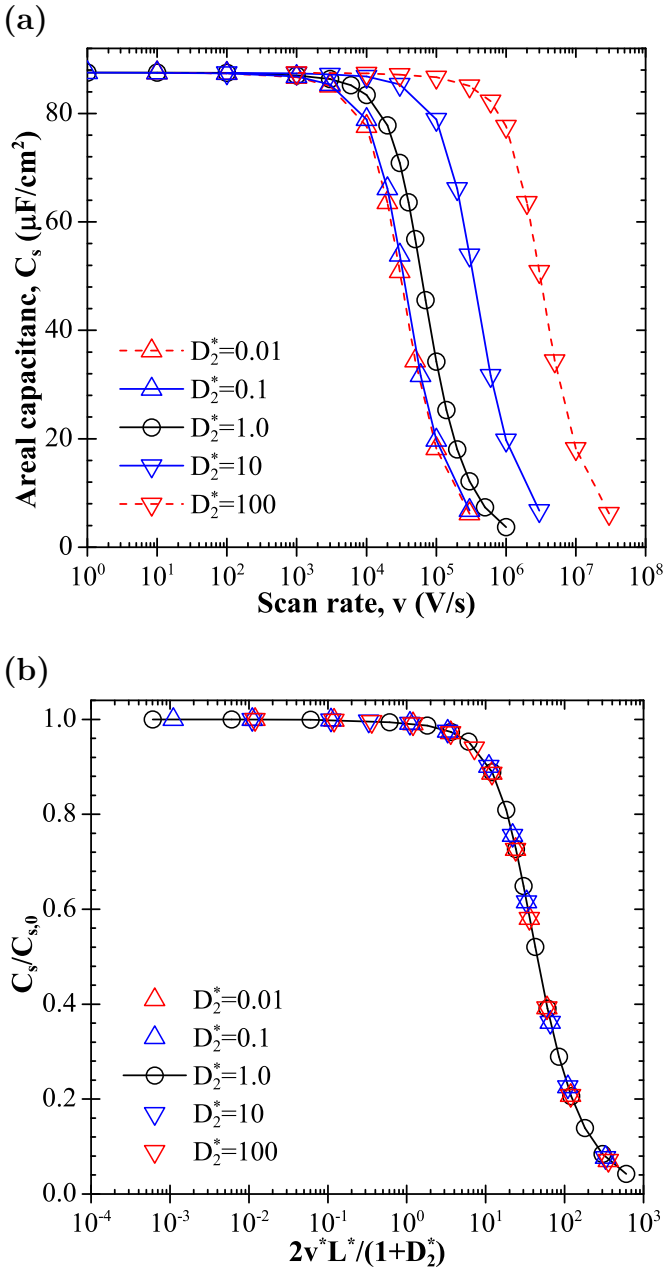

Figure A.7: Predicted (a) capacitance C_s versus scan rate v and (b) $C_s/C_{s,0}$ versus $v^*L^*/(1+D_2^*)$ from CV simulations for five cases with different ion diffusion coefficients, namely, $D_2 = 0.01D_1$, $0.1D_1$, $1.0D_1$, $10D_1$, and $100D_1$ with $D_1 = 1.957 \times 10^{-9}$ m^2/s. The model and other parameters were identical to those used to generate the results shown in Figure A.1.

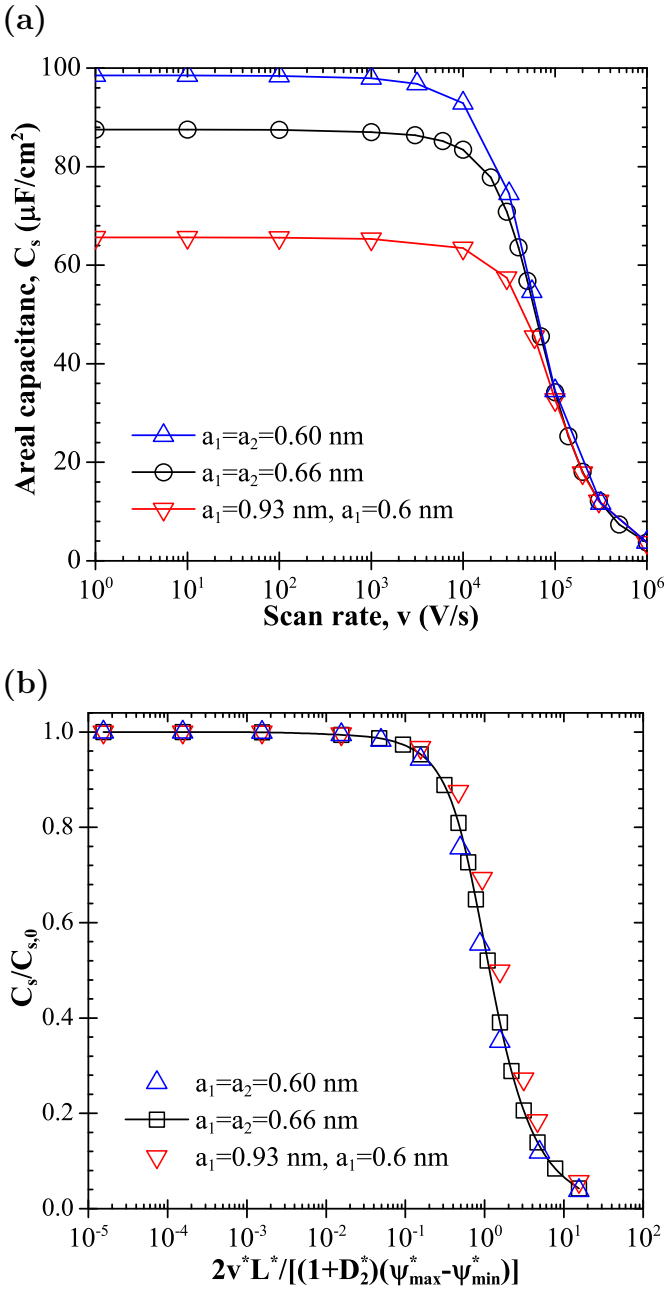

Figure A.8: Predicted (a) capacitance C_s versus scan rate v and (b) $C_s/C_{s,0}$ versus $2v^*L^*/[(1+D_2^*)(\psi_{max}^*-\psi_{min}^*)]$ from CV simulations for three sets of ion diameters, namely, $a_1 = a_2 = 0.60$ nm, $a_1 = a_2 = 0.66$ nm, and $a_1 = 0.93$ nm, $a_2 = 0.6$ nm. The model and other parameters were identical to those used to generate the results shown in Figure A.1.

References

[1] US Department of Energy, *Basic Research Needs for Electrical Energy Storage*. `http://www.osti.gov/accomplishments/documents/fullText/ACC0330.pdf`, 2007.

[2] J. R. Miller and P. Simon, "Electrochemical capacitors for energy management," *Science*, vol. 321, no. 5889, pp. 651–652, 2008.

[3] L. Yang, B. H. Fishbine, A. Migliori, and L. R. Pratt, "Dielectric saturation of liquid propylene carbonate in electrical energy storage applications," *Journal of Chemical Physics*, vol. 132, no. 4, pp. 1–4, No. 044701, 2010.

[4] M. S. Kilic, M. Z. Bazant, and A. Ajdari, "Steric effects in the dynamics of electrolytes at large applied voltages. I. Double-layer charging," *Physical Review E*, vol. 75, no. 2, No. 021502, 2007.

[5] H. J. Liu, W. J. Cui, L. H. Jin, C. X. Wang, and Y. Y. Xia, "Preparation of three-dimensional ordered mesoporous carbon sphere arrays by a two-step templating route and their application for supercapacitors," *Journal of Materials Chemistry*, vol. 19, no. 22, pp. 3661–3667, 2009.

[6] S. W. Woo, K. Dokko, H. Nakano, and K. Kanamura, "Preparation of three dimensionally ordered macroporous carbon with mesoporous walls for electric double-layer capacitors," *Journal of Materials Chemistry*, vol. 18, no. 14, pp. 1674–1680, 2008.

[7] H. Wang and L. Pilon, "Mesoscale modeling of electric double layer capacitors with three-dimensional ordered structures," *Journal of Power Sources*, vol. 221, pp. 252–260, 2013.

[8] R. J. Hunter, *Foundations of Colloid Science*. Oxford, UK: Oxford University Press, 2nd ed., 2001.

[9] A. J. Bard and L. R. Faulkner, *Electrochemical Methods: Fundamentals and Applications*. New York, NY: John Wiley & Sons, 2001.

[10] B. E. Conway, *Electrochemical Supercapacitors: Scientific Fundamentals and Technological Applications*. New York, NY: Kluwer Academic/Plenum Publishers, 1999.

[11] A. Lasia, "Electrochemical impedance spectroscopy and its applications," in *Modern Aspects of Electrochemistry, No. 32* (B. E. Conway, J. O. M. Bockris, and R. E. White, eds.), ch. 2, pp. 143–248, New York, NY: Kluwer Academic Publishers, 2002.

[12] M. E. Orazem and B. Tribollet, *Electrochemical Impedance Spectroscopy*. Hoboken, New Jersey: John Wiley & Sons, 2008.

[13] X. Z. Yuan, C. Song, H. Wang, and J. Zhang, *Electrochemical Impedance Spectroscopy in PEM Fuel Cells: Fundamentals and Applications*. London, UK: Springer-Verlag, 2010.

[14] P. L. Taberna, P. Simon, and J. F. Fauvarque, "Electrochemical characteristics and impedance spectroscopy studies of carbon-carbon supercapacitors," *Journal of The Electrochemical Society*, vol. 150, no. 3, pp. 292–300, 2003.

[15] E. J. F. Dickinson, J. G. Limon-Petersen, N. V. Rees, and R. G. Compton, "How much supporting electrolyte is required to make a cyclic voltammetry experiment quantitatively "diffusional"? A theoretical and experimental investigation," *Journal of Physical Chemistry C*, vol. 113, no. 25, pp. 11157–11171, 2009.

[16] H. Wang and L. Pilon, "Reply to comments on "Intrinsic limitations of impedance measurements in determining electric double layer capacitances"by H. Wang and L. Pilon [Electrochimica Acta 63 (2012) 55]," *Electrochimica Acta*, vol. 76, no. 0, pp. 529 – 531, 2012.

[17] R. M. Dell and D. A. J. Rand, "Energy storage - a key technology for global energy sustainability," *Journal of Power Sources*, vol. 100, no. 1-2, pp. 2–17, 2001.

[18] A. S. Arico, P. Bruce, B. Scrosati, J. M. Tarascon, and W. V. Schalkwijk, "Nanostructured materials for advanced energy conversion and storage devices," *Nature Materials*, vol. 4, no. 5, pp. 366–377, 2005.

[19] M. B. McElroy, X. Lu, C. P. Nielsen, and Y. Wang, "Potential for wind-generated electricity in China," *Science*, vol. 325, no. 5946, pp. 1378–1380, 2009.

[20] J. H. Wee, , and K. S. Choi, "CO_2 emission and avoidance in mobile applications," *Renewable and Sustainable Energy Reviews*, vol. 14, no. 2, pp. 814–820, 2010.

[21] U. D. of Energy, "The smart grid: An introduction." `http://www.oe.energy.gov/DocumentsandMedia/DOE_SG_Book_Single_Pages(1).pdf`, 2008.

[22] D. Lindley, "The energy storage problem," *Nature*, vol. 463, no. 7277, pp. 18–20, 2010.

[23] R. F. Service, "New 'supercapacitor' promises to pack more electrical punch," *Science*, vol. 313, no. 5789, p. 902, 2006.

[24] E. Karden, S. Ploumen, B. Fricke, T. Miller, and K. Snyder, "Energy storage devices for future hybrid electric vehicles," *Journal of Power Sources*, vol. 168, no. 1, pp. 2–11, 2007.

[25] R. Kotz and M. Carlen, "Principles and applications of electrochemical capacitors," *Electrochimica Acta*, vol. 45, no. 15, pp. 2483–2498, 2000.

[26] A. Burke, "Ultracapacitors: why, how, and where is the technology," *Journal of Power Sources*, vol. 91, no. 1, pp. 37–50, 2000.

[27] P. Simon and Y. Gogotsi, "Materials for electrochemical capacitors," *Nature Materials*, vol. 7, no. 11, pp. 845–854, 2008.

[28] Y. Zhang, H. Feng, X. Wu, L. Wang, A. Zhang, T. Xia, H. Dong, X. Li, and L. Zhang, "Progress of electrochemical capacitor electrode materials: A review," *International Journal of Hydrogen Energy*, vol. 34, no. 11, pp. 4889–4899, 2009.

[29] J. W. Kim, V. Augustyn, and B. Dunn, "The effect of crystallinity on the rapid pseudocapacitive response of Nb_2O_5," *Advanced Energy Materials*, vol. 2, no. 1, p. 141148, 2012.

[30] V. Augustyn, J. Come, M. A. Lowe, J. W. Kim, P.-L. Taberna, S. H. Tolbert, H. D. A. na, P. Simon, and B. Dunn, "High-rate electrochemical energy storage through Li^+ intercalation pseudocapacitance," *Nature Materials*, vol. 12, pp. 518–522, 2013.

[31] D. Pech, M. Brunet, H. Durou, P. Huang, V. Mochalin, Y. Gogotsi, P. L. Taberna, and P. Simon, "Ultrahigh-power micrometre-sized supercapacitors based on onion-like carbon," *Nature Nanotechnology*, vol. 5, no. 9, pp. 651–654, 2010.

[32] A. G. Pandolfo and A. F. Hollenkamp, "Carbon properties and their role in supercapacitors," *Journal of Power Sources*, vol. 157, no. 1, pp. 11–27, 2006.

[33] E. Frackowiak, "Carbon materials for supercapacitor application," *Physical Chemistry Chemical Physics*, vol. 9, no. 15, pp. 1774–1785, 2007.

[34] L. L. Zhang and X. S. Zhao, "Carbon-based materials as supercapacitor electrodes," *Chemical Society Reviews*, vol. 38, no. 9, pp. 2520–2531, 2009.

[35] J. H. Masliyah and S. Bhattacharjee, *Electrokinetic and Colloid Transport Phenomena*. Hoboken, NJ: John Wiley & Sons, 2006.

[36] H. J. Butt and M. Kappl, *Surface and Interfacial Forces*. Weinheim, Germany: Wiley-VCH Verlag GmbH & Co. KGaA, 2010.

[37] J. Chmiola, G. Yushin, Y. Gogotsi, C. Portet, P. Simon, and P. L. Taberna, "Anomalous increase in carbon capacitance at pore sizes less than 1 nanometer," *Science*, vol. 313, no. 5794, pp. 1760–1763, 2006.

[38] J. Chmiola, G. Yushin, R. Dash, and Y. Gogotsi, "Effect of pore size and surface area of carbide derived carbons on specific capacitance," *Journal of Power Sources*, vol. 158, no. 1, pp. 765–772, 2006.

[39] J. Chmiola, C. Largeot, P. L. Taberna, P. Simon, and Y. Gogotsi, "Desolvation of ions in subnanometer pores and its effect on capacitance and double-layer theory," *Angewandte Chemie International Edition*, vol. 47, no. 18, pp. 3392–3395, 2008.

[40] E. Frackowiak and F. Beguin, "Carbon materials for the electrochemical storage of energy in capacitors," *Carbon*, vol. 39, no. 6, pp. 937–950, 2001.

[41] G. Gryglewicz, J. Machnikowski, E. Lorenc-Grabowska, G. Lota, and E. Frackowiak, "Effect of pore size distribution of coal-based activated carbons on double layer capacitance," *Electrochimica Acta*, vol. 50, no. 5, pp. 1197–1206, 2005.

[42] C. Vix-Guterl, E. Frackowiak, K. Jurewicz, M. Friebe, J. Parmentier, and F. Beguin, "Electrochemical energy storage in ordered porous carbon materials," *Carbon*, vol. 43, no. 6, pp. 1293–1302, 2005.

[43] A. B. Fuertes, G. Lota, T. A. Centeno, and E. Frackowiak, "Templated mesoporous carbons for supercapacitor application," *Electrochimica Acta*, vol. 50, no. 14, pp. 2799–2805, 2005.

[44] B. E. Conway, V. Birss, and J. Wojtowicz, "The role and utilization of pseudocapacitance for energy storage by supercapacitors," *Journal of Power Sources*, vol. 66, no. 1, pp. 1–14, 1997.

[45] W. Wei, X. Cui, W. Chen, and D. G. Ivey, "Manganese oxide-based materials as electrochemical supercapacitor electrodes," *Chemical Society Reviews*, vol. 40, no. 3, pp. 1697–1721, 2011.

[46] X. Zhao, B. M. Sńchez, P. J. Dobson, and P. S. Grant, "The role of nanomaterials in redox -based supercapacitors for next generation energy storage devices," *Nanoscale*, vol. 3, pp. 839–855, 2011.

[47] G. Wang, L. Zhang, and J. Zhang, "A review of electrode materials for electrochemical supercapacitors," *Chemical Society Reviews*, vol. 41, no. 2, pp. 797–828, 2012.

[48] Q. T. Qu, Y. Shi, L. L. Li, W. L. Guo, Y. P. Wu, H. P. Zhang, S. Y. Guan, and R. Holze, "$V_2O_5 \cdot 0.6H_2O$ nanoribbons as cathode material for

asymmetric supercapacitor in k2so4 solution," *Electrochemistry Communications*, vol. 11, no. 6, p. 13251328, 2009.

[49] Q. Qu, P. Zhang, B. Wang, Y. Chen, S. Tian, Y. Wu, and R. Holze, "Electrochemical performance of MnO_2 nanorods in neutral aqueous electrolytes as a cathode for asymmetric supercapacitors," *Journal of Physical Chemistry C*, vol. 113, no. 31, p. 1402014027, 2009.

[50] J. W. Long, D. Bélanger, T. Brousse, W. Sugimoto, M. B. Sassin, and O. Crosnier, "Asymmetric electrochemical capacitors - stretching the limits of aqueous electrolytes," *MRS Bulletin*, vol. 36, no. 7, pp. 513–522, 2011.

[51] Z. Fan, J. Yan, T. Wei, L. Zhi, G. Ning, T. Li, and F. Wei, "Asymmetric supercapacitors based on graphene/MnO_2 and activated carbon nanofiber electrodes with high power and energy density," *Advanced Functional Materials*, vol. 21, no. 12, p. 23662375, 2011.

[52] Y.-P. Lin and N.-L. Wu, "Characterization of $MnFe_2O_4$/$LiMn_2O_4$ aqueous asymmetric supercapacitor," *Journal of Power Sources*, vol. 196, no. 2, pp. 851–854, 2011.

[53] F. Wang, S. Xiao, Y. Hou, C. Hu, L. Liu, and Y. Wu, "Electrode materials for aqueous asymmetric supercapacitors," *RSC Advances*, vol. 3, no. 32, pp. 13059–13084, 2013.

[54] L.-J. Xie, J.-F. Wu, C.-M. Chen, C.-M. Zhang, L. Wan, J.-L. Wang, Q.-Q. Kong, C.-X. Lv, K.-X. Li, and G.-H. Sun, "A novel asymmetric supercapacitor with an activated carbon cathode and a reduced graphene oxide-cobalt oxide nanocomposite anode," *Journal of Power Sources*, vol. 242, pp. 148–156, 2013.

[55] K. Naoi, W. Naoi, S. Aoyagi, J. ichi Miyamoto, and T. Kamino, "New generation "nanohybrid supercapacitor"," *Accounts of Chemical Research*, vol. 46, no. 5, p. 10751083, 2013.

[56] Y. G. Wang, Z. D. Wang, and Y. Y. Xia, "An asymmetric supercapacitor using RuO_2/TiO_2 nanotube composite and activated carbon electrodes," *Electrochimica Acta*, vol. 50, no. 28, pp. 5641–5646, 2005.

[57] V. Khomenko, E. Raymundo-Piñero, and F. Béguin, "Optimisation of an asymmetric manganese oxide/activated carbon capacitor working at 2V in aqueous medium," *Journal of Power Sources*, vol. 153, no. 1, pp. 183–190, 2006.

[58] L. Demarconnay, E. R.-P. nero, and F. Béguin, "Adjustment of electrodes potential window in an asymmetric carbon/MnO_2 supercapacitor," *Journal of Power Sources*, vol. 196, no. 1, pp. 580–586, 2011.

[59] T. Brousse, P.-L. Taberna, O. Crosnier, R. Dugas, P. Guillemet, Y. Scudeller, Y. Zhou, F. Favier, D. Bélanger, and P. Simon, "Long-term cycling behavior of asymmetric activated carbon/MnO_2 aqueous electrochemical supercapacitor," *Journal of Power Sources*, vol. 173, no. 1, pp. 633–641, 2007.

[60] M. Jayalakshmi and K. Balasubramanian, "Simple capacitors to supercapacitors - An overview," *International Journal of Electrochemcal Science*, vol. 3, no. 11, pp. 1196–1217, 2008.

[61] J. P. Zheng, P. J. Cygan, , and T. R. Jow, "Hydrous Ruthenium oxide as an electrode material for electrochemical capacitors," *Journal of The Electrochemical Society*, vol. 142, no. 8, pp. 2699–2703, 1995.

[62] J. P. Zheng and T. R. Jow, "High energy and high power density electrochemical capacitors," *Journal of Power Sources*, vol. 62, no. 2, pp. 155–159, 1996.

[63] A. Rudge, I. Raistrick, S. Gottesfeld, and J. P. Ferraris, "A study of the electrochemical properties of conducting polymers for application in electrochemical capacitors," *Electrochimica Acta*, vol. 39, no. 2, pp. 273–287, 1994.

[64] A. Rudge, J. Davey, I. Raistrick, S. Gottesfeld, and J. P. Ferraris, "Conducting polymers as active materials in electrochemical capacitors," *Journal of Power Sources*, vol. 47, no. 1-2, pp. 89–107, 1994.

[65] S. Ghosh and O. Inganas, "Conducting polymer hydrogels as 3D electrodes: Applications for supercapacitors," *Advanced Materials*, vol. 11, no. 14, pp. 1214–1218, 1999.

[66] G. A. Snook, P. Kao, and A. S. Best, "Conducting-polymer-based supercapacitor devices and electrodes," *Journal of Power Sources*, vol. 196, no. 1, pp. 1–12, 2011.

[67] Y. Lei, W. Cai, and G. Wilde, "Highly ordered nanostructures with tunable size, shape and properties: A new way to surface nano-patterning using ultra-thin alumina masks," *Progress in Materials Science*, vol. 52, no. 4, pp. 465–539, 2007.

[68] Y. S. Hu, P. Adelhelm, B. M. Smarsly, S. Hore, M. Antonietti, and J. Maier, "Synthesis of hierarchically porous carbon monoliths with highly ordered microstructure and their application in rechargeable Lithium batteries with high-rate capability," *Advanced Functional Materials*, vol. 17, no. 12, pp. 1873–1878, 2007.

[69] S. S. Mao and X. Chen, "Selected nanotechnologies for renewable energy applications," *International Journal of Energy Research*, vol. 31, no. 6-7, pp. 619–636, 2007.

[70] J. Liu, G. Cao, Z. Yang, D. Wang, D. Dubois, X. Zhou, G. L. Graff, L. R. Pederson, and J.-G. Zhang, "Oriented nanostructures for energy conversion and storage," *ChemSusChem*, vol. 1, no. 8-9, pp. 676–697, 2008.

[71] A. Stein, Z. Wang, and M. A. Fierke, "Functionalization of porous carbon materials with designed pore architecture," *Advanced Materials*, vol. 21, no. 3, pp. 265–293, 2009.

[72] M. S. Whittingham, "Materials challenges facing electrical energy storage," *MRS Bulletin*, vol. 33, no. 4, pp. 411–419, 2008.

[73] E. Barsoukov and J. R. Macdonald, *Impedance Spectroscopy: Theory, Experiment, and Applications*. Hoboken, New Jersey: John Wiley & Sons, 2nd ed., 2005.

[74] M. Arulepp, L. Permann, J. Leis, A. Perkson, K. Rumma, A. Janes, and E. Lust, "Influence of the solvent properties on the characteristics of a double layer capacitor," *Journal of Power Sources*, vol. 133, no. 2, pp. 320–328, 2004.

[75] H. Wang, H. S. Casalongue, Y. Liang, and H. Dai, "$Ni(OH)_2$ nanoplates grown on graphene as advanced electrochemical pseudocapacitor materials," *Journal of The American Chemical Society*, vol. 132, no. 21, pp. 7472–7477, 2010.

[76] L.-Q. Mai, F. Yang, Y.-L. Zhao, X. X, L. Xu, and Y.-Z. Luo, "Hierarchical $MnMoO_4/CoMoO_4$ heterostructured nanowires with enhanced supercapacitor performance," *Nature Communications*, vol. 2, no. 381, pp. 1–5, 2011.

[77] J. Feng, X. Sun, C. Wu, L. Peng, C. Lin, S. Hu, J. Yang, and Y. Xie, "Metallic few-layered VS_2 ultrathin nanosheets: High two-dimensional conductivity for in-plane supercapacitors," *Journal of The American Chemical Society*, vol. 133, no. 44, pp. 17832–17838, 2011.

[78] B. G. Choi, J. Hong, W. H. Hong, P. T. Hammond, and H. Park, "Facilitated ion transport in all-solid-state flexible supercapacitors," *ACS Nano*, vol. 5, no. 9, pp. 7205–7213, 2011.

[79] S. K. Meher and G. R. Rao, "Ultralayered Co_3O_4 for high-performance supercapacitor applications," *Journal of Physical Chemistry C*, vol. 115, no. 31, pp. 15646–15654, 2011.

[80] R. B. Rakhi, D. Cha, W. Chen, and H. N. Alshareef, "Electrochemical energy storage devices using electrodes incorporating carbon nanocoils and metal oxides nanoparticles," *Journal of Physical Chemistry C*, vol. 115, no. 29, pp. 14392–14399, 2011.

[81] H. L. F. von Helmholtz, "Studien üer electrische grenzschichten," *Annalen der Physik*, vol. 243, no. 7, pp. 337–382, 1879.

[82] V. S. Bagotsky, *Fundamentals of Electrochemistry*. Hoboken, NJ: John Wiley & Sons, 2nd ed., 2006.

[83] H. D. Young, R. A. Freedman, and L. Ford, *University Physics with Modern Physics*. San Francisco, CA: Pearson Education, 12th ed., 2007.

[84] D. Halliday, R. Resnick, and J. Walker, *Fundamentals of Physics*. Hoboken, NJ: John Wiley & Sons, 9th ed., 2010.

[85] J. Huang, B. G. Sumpter, and V. Meunier, "Theoretical model for nanoporous carbon supercapacitors," *Angewandte Chemie International Edition*, vol. 47, no. 3, pp. 520–524, 2008.

[86] J. Huang, B. G. Sumpter, and V. Meunier, "A universal model for nanoporous carbon supercapacitors applicable to diverse pore regimes, carbon materials, and electrolytes," *Chemistry - A European Journal*, vol. 14, no. 22, pp. 6614–6626, 2008.

[87] J. Huang, B. G. Sumpter, V. Meunier, G. Yushin, C. Portet, and Y. Gogotsi, "Curvature effects in carbon nanomaterials: Exohedral versus endohedral supercapacitors," *Journal of Materials Research*, vol. 25, no. 8, pp. 1525–1531, 2010.

[88] G. Gouy, "Constitution of the electric charge at the surace of an electrolyte,"

[89] D. L. Chapman, "A contribution to the theory of electrocapillarity," *Philosophical Magazine, Series 6*, vol. 25, no. 148, pp. 475–481, 1913.

[90] J. Lyklema, *Fundamentals of Interface and Colloid Science, Volume II: Solid-Liquid Interfaces*. San Diego, CA: Academic Press, 2001.

[91] H. Ohshima, *Theory of Colloid and Interfacial Electric Phenomena*. San Diego, CA: Academic Press, 2006.

[92] O. Stern, "The theory of the electrolytic double layer," *Zeitschrift für Elektrochemie und angewandte physikalische Chemie*, vol. 30, pp. 508–516, 1924.

[93] G. M. Torrie and J. P. Valleau, "The electrical double layer. III. modified Gouy-Chapman theory with unequal ion sizes," *Journal of Chemical Physics*, vol. 76, no. 9, pp. 4623–4630, 1982.

[94] J. Huang, R. Qiao, B. G. Sumpter, and V. Meunier, "Effect of diffuse layer and pore shapes in mesoporous carbon supercapacitors," *Journal of Materials Research*, vol. 25, no. 8, pp. 1469–1475, 2010.

[95] M. Z. Bazant, M. S. Kilic, B. D. Storey, and A. Ajdari, "Towards an understanding of induced-charge electrokinetics at large applied voltages in concentrated solutions," *Advances in Colloid and Interface Science*, vol. 152, no. 1-2, pp. 48–88, 2009.

[96] J. J. Bikerman, "Structure and capacity of electrical double layer," *Philosophical Magazine*, vol. 33, no. 220, pp. 384–397, 1942.

[97] I. Borukhov, D. Andelman, and H. Orland, "Steric effects in electrolytes: A modified Poisson-Boltzmann equation," *Physical Review Letters*, vol. 79, no. 3, pp. 435–438, 1997.

[98] I. Borukhov, D. Andelman, and H. Orland, "Adsorption of large ions from an electrolyte solution: a modified Poisson-Boltzmann equation," *Electrochimica Acta*, vol. 46, no. 2-3, pp. 221–229, 2000.

[99] P. M. Biesheuvel and M. van Soestbergen, "Counterion volume effects in mixed electrical double layers," *Journal of Colloid and Interface Science*, vol. 316, no. 2, pp. 490–499, 2007.

[100] C. W. Outhwaite and L. B. Bhuiyan, "An improved modified Poisson-Boltzmann equation in electric-double-layer theory," *Journal of the Chemical Society. Faraday Transactions II*, vol. 79, pp. 707–718, 1983.

[101] V. Vlachy, "Ionic effects beyond Poisson-Boltzmann theory," *Annual Review of Physical Chemistry*, vol. 50, pp. 145–165, 1999.

[102] A. A. Kornyshev, "Double-layer in ionic liquids: Paradigm change?," *Journal of Physical Chemistry B*, vol. 111, no. 20, pp. 5545–5557, 2007.

[103] A. R. J. Silalahi, A. H. Boschitsch, R. C. Harris, and M. O. Fenley, "Comparing the predictions of the nonlinear Poisson-Boltzmann equation and the ion size-modified Poisson-Boltzmann equation for a low-dielectric charged spherical cavity in an aqueous salt solution," *Journal of Chemical Theory and Computation*, vol. 6, no. 12, pp. 3631–3639, 2010.

[104] V. B. Chu, Y. Bai, J. Lipfert, D. Herschlag, and S. Doniach, "Evaluation of ion binding to DNA duplexes using a size-modified Poisson-Boltzmann theory," *Biophysical Journal*, vol. 93, no. 9, pp. 3202–3209, 2007.

[105] P. Grochowski and J. Trylska, "Continuum molecular electrostatics, salt effects, and counterion binding - A review of the Poisson-Boltzmann theory and its modifications," *Biopolymers*, vol. 89, no. 2, pp. 93–113, 2008.

[106] P. M. Biesheuvel and J. Lyklema, "Sedimentation-diffusion equilibrium of binary mixtures of charged colloids including volume effects," *Journal of Physics: Condensed Matter*, vol. 17, no. 41, pp. 6337–6352, 2005.

[107] P. M. Biesheuvel, F. A. M. Leermakers, and M. A. C. Stuart, "Self-consistent field theory of protein adsorption in a non-Gaussian polyelectrolyte brush," *Physical Review E*, vol. 73, no. 1, No. 011802, 2006.

[108] P. H. R. Alijó, F. W. Tavares, and E. C. B. Jr., "Double layer interaction between charged parallel plates using a modified Poisson-Boltzmann equation to include size effects and ion specificity," *Colloids and Surfaces A*, vol. 412, pp. 29–35, 2012.

[109] G. Tresset, "Generalized Poisson-Fermi formalism for investigating size correlation effects with multiple ions," *Physical Review E*, vol. 78, no. 6, No. 061506, 2008.

[110] B. Li, "Continuum electrostatics for ionic solutions with non-uniform ionic sizes," *Nonlinearity*, vol. 22, no. 4, pp. 811–833, 2009.

[111] S. Zhou, Z. Wang, and B. Li, "Mean-field description of ionic size effects with nonuniform ionic sizes: A numerical approach," *Physical Review E*, vol. 84, no. 2, No. 021901, 2011.

[112] J. Wen, S. Zhou, Z. Xu, and B. Li, "Competitive adsorption and ordered packing of counterions near highly charged surfaces: From mean-field theory to Monte Carlo simulations," *Physical Review E*, vol. 85, no. 4, No. 041406, 2012.

[113] J. J. Lopez-García, M. J. Aranda-Rascón, and J. Horno, "Excluded volume effect on the electrophoretic mobility of colloidal particles," *Journal of Colloid and Interface Science*, vol. 323, no. 1, pp. 146–152, 2008.

[114] M. J. Aranda-Rascon, C. Grosse, J. J. Lopez-Garcia, and J. Horno, "Electrokinetics of suspended charged particles taking into account the excluded volume effect," *Journal of Colloid and Interface Science*, vol. 335, no. 2, pp. 250–256, 2009.

[115] J. J. Lopez-García, J. Horno, and C. Grosse, "Equilibrium properties of charged spherical colloidal particles suspended in aqueous electrolytes: Finite ion size and effective ion permittivity effects," *Journal of Colloid and Interface Science*, vol. 380, no. 1, pp. 213–221, 2012.

[116] J. J. Lopez-García, M. J. Aranda-Rascón, and J. Horno, "Electrical double layer around a spherical colloid particle: The excluded volume effect," *Journal of Colloid and Interface Science*, vol. 316, no. 1, pp. 196–201, 2007.

[117] J. J. Lopez-García and J. Horno, "Poisson-Boltzmann description of the electrical double layer including ion size effects," *Langmuir*, vol. 27, no. 23, pp. 13970–13974, 2011.

[118] J. J. Lopez-García, M. J. Aranda-Rascón, C. Grosse, and J. Horno, "Equilibrium electric double layer of charged spherical colloidal particles: Effect of different distances of minimum ion approach to the particle surface," *Journal of Physical Chemistry B*, vol. 114, no. 22, pp. 7548–7556, 2010.

[119] J. J. Lopez-García, M. J. Aranda-Rascón, C. Grosse, and J. Horno, "Electrokinetics of charged spherical colloidal particles taking into account the effect of ion size constraints," *Journal of Colloid and Interface Science*, vol. 356, no. 1, pp. 325–330, 2011.

[120] W. G. Pell and B. E. Conway, "Voltammetry at a de Levie brush electrode as a model for electrochemical supercapacitor behaviour," *Journal of Electroanalytical Chemistry*, vol. 500, no. 1-2, pp. 121–133, 2001.

[121] W. G. Pell and B. E. Conway, "Analysis of power limitations at porous supercapacitor electrodes under cyclic voltammetry modulation and dc charge," *Journal of Power Sources*, vol. 96, no. 1, pp. 57–67, 2001.

[122] B. E. Conway and W. G. Pell, "Power limitations of supercapacitor operation associated with resistance and capacitance distribution in porous electrode devices," *Journal of Power Sources*, vol. 105, no. 2, pp. 169–181, 2002.

[123] F. Fabregat-Santiago, I. Mora-Sero, G. Garcia-Belmonte, and J. Bisquert, "Cyclic voltammetry studies of nanoporous semiconductors. capacitive and reactive properties of nanocrystalline TiO_2 electrodes in aqueous electrolyte," *Journal of Physical Chemistry B*, vol. 107, no. 3, pp. 758–768, 2003.

[124] S. Yoon, J. H. Jang, B. H. Ka, and S. M. Oh, "Complex capacitance analysis on rate capability of electric-double layer capacitor (EDLC) electrodes of different thickness," *Electrochimica Acta*, vol. 50, no. 11, pp. 2255–2262, 2005.

[125] S. Yoon, C. W. Lee, and S. M. Oh, "Characterization of equivalent series resistance of electric double-layer capacitor electrodes using transient analysis," *Journal of Power Sources*, vol. 195, no. 13, pp. 4391–4399, 2010.

[126] W. Lajnef, J. M. Vinassa, O. Briat, S. Azzopardi, and E. Woirgard, "Characterization methods and modelling of ultracapacitors for use as peak power sources," *Journal of Power Sources*, vol. 168, no. 2, pp. 553–560, 2007.

[127] M. Kaus, J. Kowa, and D. U. Sauer, "Modelling the effects of charge redistribution during self-discharge of supercapacitors," *Electrochimica Acta*, vol. 55, no. 25, pp. 7516–7523, 2010.

[128] M. Z. Bazant, K. Thornton, and A. Ajdari, "Diffuse-charge dynamics in electrochemical systems," *Physical Review E*, vol. 70, no. 2, No. 021506, 2004.

[129] K. T. Chu and M. Z. Bazant, "Nonlinear electrochemical relaxation around conductors," *Physical Review E*, vol. 74, no. 1, No. 011501, 2006.

[130] L. H. Olesen, M. Z. Bazant, and H. Bruus, "Strongly nonlinear dynamics of electrolytes in large ac voltages," *Physical Review E*, vol. 82, no. 1, No. 011501, 2010.

[131] E. J. F. Dickinson and R. G. Compton, "How well does simple RC circuit analysis describe diffuse double layer capacitance at smooth micro- and nanoelectrodes?," *Journal of Electroanalytical Chemistry*, vol. 655, no. 1, pp. 23–31, 2011.

[132] J. S. Newman and K. E. Thomas-Alyea, *Electrochemical Systems*. Hoboken, N.J.: John Wiley & Sons, 3rd ed., 2004.

[133] A. M. Johnson and J. Newman, "Desalting by means of porous carbon electrodes," *Journal of The Electrochemical Society*, vol. 118, no. 3, pp. 510–517, 1971.

[134] B. Pillay, *Design of Electrochemical Capacitors for Energy Storage*. Ph.D. Thesis, Deptartment of Chemical Engineering, University of California, Berkeley, CA, 1996.

[135] B. Pillay and J. Newman, "The influence of side reactions on the performance of electrochemical double-layer capacitors," *Journal of The Electrochemical Society*, vol. 143, no. 6, pp. 1806–1814, 1996.

[136] I. J. Ong and J. Newman, "Double-layer capacitance in a dual lithium ion insertion cell," *Journal of The Electrochemical Society*, vol. 146, no. 12, pp. 4360–4365, 1999.

[137] V. Srinivasan and J. W. Weidner, "Mathematical modeling of electrochemical capacitors," *Journal of The Electrochemical Society*, vol. 146, no. 5, pp. 1650–1658, 1999.

[138] C. Lin, J. A. Ritter, B. N. Popov, and R. E. White, "A mathematical model of an electrochemical capacitor with double-layer and Faradaic processes," *Journal of The Electrochemical Society*, vol. 146, no. 9, pp. 3168–3175, 1999.

[139] C. Lin, B. N. Popov, and H. J. Ploehn, "Modeling the effects of electrode composition and pore structure on the performance of electrochemical capacitors," *Journal of The Electrochemical Society*, vol. 149, no. 2, pp. 167–175, 2002.

[140] D. Dunn and J. Newman, "Predictions of specific energies and specific powers of double-layer capacitors using a simplified model," *Journal of The Electrochemical Society*, vol. 147, no. 3, pp. 820–830, 2000.

[141] H. Kim and B. N. Popov, "A mathematical model of oxide, carbon composite electrode for supercapacitors," *Journal of the Electrochemical Society*, vol. 150, no. 9, pp. 1153–1160, 2003.

[142] G. Sikha, R. E. White, and B. N. Popov, "A mathematical model for a lithium-ion battery/electrochemical capacitor hybrid system," *Journal of The Electrochemical Society*, vol. 152, no. 8, pp. 1682–1693, 2005.

[143] M. W. Verbrugge and P. Liu, "Microstructural analysis and mathematical modeling of electric double-layer supercapacitors," *Journal of The Electrochemical Society*, vol. 152, no. 5, pp. 79–87, 2005.

[144] S. Kazaryan, S. Razumov, S. Litvinenko, G. Kharisov, and V. Kogan, "Mathematical model of heterogeneous electrochemical capacitors and calculation of their parameters," *Journal of The Electrochemical Society*, vol. 153, no. 9, pp. 1655–1671, 2006.

[145] S. K. Griffiths and R. H. Nilson, "Optimum interparticle porosity for charge storage in a packed bed of nanoporous particles," *Journal of The Electrochemical Society*, vol. 157, no. 4, pp. 469–479, 2010.

[146] M. S. Kilic, M. Z. Bazant, and A. Ajdari, "Steric effects in the dynamics of electrolytes at large applied voltages. II. Modified Poisson-Nernst-Planck equations," *Physical Review E*, vol. 75, no. 2, No. 021503, 2007.

[147] S. Ghosal, "Electrokinetic flow and dispersion in capillary electrophoresis," *Annual Review of Fluid Mechanics*, vol. 38, pp. 309–338, 2006.

[148] H. Wang and L. Pilon, "Intrinsic limitations of impedance measurements in determining electric double layer capacitances," *Electrochimica Acta*, vol. 63, pp. 55–63, 2012.

[149] H. Wang and L. Pilon, "Physical interpretation of cyclic voltammetry for measuring electric double layer capacitances," *Electrochimica Acta*, vol. 64, pp. 130–139, 2012.

[150] J. Baker-Jarvis, B. Riddle, and A. M. Young, "Ion dynamics near charged electrodes with excluded volume effect," *IEEE Transactions on Dielectrics and Electrical Insulation*, vol. 6, no. 2, pp. 226–235, 1999.

[151] K. T. Chu and M. Z. Bazant, "Surface conservation laws at microscopically diffuse interfaces," *Journal of Colloid and Interface Science*, vol. 315, no. 1, pp. 319–329, 2007.

[152] H. Zhao, "Diffuse-charge dynamics of ionic liquids in electrochemical systems," *Physical Review E*, vol. 84, no. 5, No. 051504, 2011.

[153] M. J. Aranda-Rascon, C. Grosse, J. J. Lopez-Garcia, and J. Horno, "Influence of the finite ion size on the predictions of the standard electrokinetic model: Frequency response," *Journal of Colloid and Interface Science*, vol. 336, no. 2, pp. 857–864, 2009.

[154] J. Cervera, V. García-Morales, and J. Pellicer, "Ion size effects on the electrokinetic flow in nanoporous membranes caused by concentration gradients," *Journal of Physical Chemistry B*, vol. 107, no. 33, pp. 8300–8309, 2003.

[155] J. Cervera, P. Ramírez, J. A. Manzanares, and S. Mafé, "Incorporating ionic size in the transport equations for charged nanopores," *Microfluidics and Nanofluidics*, vol. 9, no. 1, pp. 41–53, 2010.

[156] J. D. Davidson and N. C. Goulbourne, "Nonlinear capacitance and electrochemical response of ionic liquid-ionic polymers," *Journal of Applied Physics*, vol. 109, no. 8, pp. 1–14, 2011.

[157] B. Eisenberg, Y. Hyon, and C. Liu, "Energy variational analysis of ions in water and channels: Field theory for primitive models of complex ionic fluids," *Journal of Chemical Physics*, vol. 133, no. 10, pp. 1–23, No. 104104, 2010.

[158] B. Eisenberg, "Multiple scales in the simulation of ion channels and proteins," *Journal of Physical Chemistry C*, vol. 114, no. 48, pp. 20719–20733, 2010.

[159] B. Eisenberg, "Crowded charges in ion channels," in *Advances in Chemical Physics* (S. A. Rice and A. R. Dinner, eds.), vol. 148, pp. 77–223, Hoboken, NJ: John Wiley & Sons, 2012.

[160] T.-L. Horng, T.-C. Lin, C. Liu, and B. Eisenberg, "PNP equations with steric effects: A model of ion flow through channels," *Journal of Physical Chemistry B*, vol. 116, no. 37, pp. 11422–11441, 2012.

[161] B. Lu and Y. C. Zhou, "Poisson-Nernst-Planck equations for simulating biomolecular diffusion-reaction processes II: Size effects on ionic distributions and diffusion-reaction rates," *Biophysical Journal*, vol. 100, no. 10, pp. 2475–2485, 2012.

[162] Y. C. Zhou, "Electrodiffusion of lipids on membrane surfaces," *Journal of Chemical Physics*, vol. 136, no. 20, No. 205103, 2012.

[163] R. M. Wightman, "Voltammetry with microscopic electrodes in new domains," *Science*, vol. 240, no. 4851, pp. 415–420, 1988.

[164] R. M. Penner, M. J. Heben, T. L. Longin, and N. S. Lewis, "Fabrication and use of nanometer-sized electrodes in electrochemistry," *Science*, vol. 250, no. 4984, pp. 1118–1121, 1990.

[165] J. Heinze, "Ultramicroelectrodes in electrochemistry," *Angewandte Chemie International Edition*, vol. 32, no. 9, pp. 1268–1288, 1993.

[166] K. Aoki, "Theory of ultramicroelectrodes," *Electroanalysis*, vol. 5, no. 8, pp. 627–639, 1993.

[167] K. Stulik, C. Amatore, K. Holub, V. Marecek, and W. Kutner, "Microelectrodes. definitions, characterization, and applications (technical report)," *Pure and Applied Chemistry*, vol. 72, no. 8, pp. 1483–1492, 2000.

[168] D. W. Arrigan, "Nanoelectrodes, nanoelectrode arrays and their applications," *Analyst*, vol. 129, no. 12, pp. 1157–1165, 2004.

[169] Y. Shao, M. V. Mirkin, G. Fish, S. Kokotov, D. Palanker, and A. Lewis, "Nanometer-sized electrochemical sensors," *Analytical Chemistry*, vol. 69, no. 8, pp. 1627–1634, 1997.

[170] R. W. Murray, "Nanoelectrochemistry: Metal nanoparticles, nanoelectrodes, and nanopores," *Chemical Reviews*, vol. 108, no. 7, pp. 2688–2720, 2008.

[171] S. R. Belding, F. W. Campbell, E. J. F. Dickinson, and R. G. Compton, "Nanoparticle-modified electrodes," *Physical Chemistry Chemical Physics*, vol. 12, no. 37, pp. 11208–11221, 2010.

[172] Y. G. Guo, J. S. Hu, and L. J. Wan, "Nanostructured materials for electrochemical energy conversion and storage devices," *Advanced Materials*, vol. 20, no. 15, pp. 2878–2887, 2008.

[173] P. Balaya, "Size effects and nanostructured materials for energy applications," *Energy & Environmental Science*, vol. 1, no. 6, pp. 645–654, 2008.

[174] A. Manthiram, A. Murugan, A. Sarkar, and T. Muraliganth, "Nanostructured electrode materials for electrochemical energy storage and conversion," *Energy & Environmental Science*, vol. 1, no. 6, pp. 621–638, 2008.

[175] D. S. Su and R. Schlogl, "Nanostructured carbon and carbon nanocomposites for electrochemical energy storage applications," *ChemSusChem*, vol. 3, no. 2, pp. 136–168, 2010.

[176] C. Liu, F. Li, L. P. Ma, and H. M. Cheng, "Advanced materials for energy storage," *Advanced Materials*, vol. 22, no. 8, pp. 28–62, 2010.

[177] J. Wang, J. Polleux, J. Lim, and B. Dunn, "Pseudocapacitive contributions to electrochemical energy storage in TiO_2 (anatase) nanoparticles," *Journal of Physical Chemistry C*, vol. 111, no. 40, pp. 14925–14931, 2007.

[178] G. G. Wallace, J. Chen, A. J. Mozer, M. Forsyth, D. R. MacFarlane, and C. Wang, "Nanoelectrodes: energy conversion and storage," *Materials Today*, vol. 12, no. 6, pp. 20–27, 2009.

[179] D. R. Rolison, J. W. Long, J. C. Lytle, A. E. Fischer, C. P. Rhodes, T. M. McEvoy, M. E. Bourg, and A. M. Lubers, "Multifunctional 3D nanoarchitectures for energy storage and conversion," *Chemical Society Reviews*, vol. 38, no. 1, pp. 226–252, 2009.

[180] S. V. Kalinin and N. Balke, "Local electrochemical functionality in energy storage materials and devices by scanning probe microscopies: Status and perspectives," *Advanced Materials*, vol. 22, no. 35, pp. 193–209, 2010.

[181] S. E. Pust, M. Salomo, E. Oesterschulze, and G. Wittstock, "Influence of electrode size and geometry on electrochemical experiments with combined SECM-AFM probes," *Nanotechnology*, vol. 21, no. 10, pp. 1–12, No. 105709, 2010.

[182] C. Li and K. J. Kjoller, *Scanning Electrochemical Potential Microscopy.* New York, NY: US Patent No. US 7.156.965 B1, Veeco Instrument Inc., 2007.

[183] C. Hurth, C. Li, and A. J. Bard, "Direct probing of electrical double layers by scanning electrochemical potential microscopy," *Journal of Physical Chemistry C*, vol. 111, no. 12, pp. 4620–4627, 2007.

[184] C. Baier and U. Stimmin, "Imaging single enzyme molecules under in situ conditions," *Angewandte Chemie International Edition*, vol. 48, no. 30, pp. 5542–5544, 2009.

[185] R. F. Hamou, P. U. Biedermann, A. Erbe, and M. Rohwerder, "Numerical simulation of probing the electric double layer by scanning electrochemical potential microscopy," *Electrochimica Acta*, vol. 55, no. 18, pp. 5210–5222, 2010.

[186] R. F. Hamou, P. U. Biedermann, A. Erbe, and M. Rohwerder, "Numerical analysis of debye screening effect in electrode surface potential mapping by scanning electrochemical potential microscopy," *Electrochemistry Communications*, vol. 12, no. 10, pp. 1391–1394, 2010.

[187] E. J. F. Dickinson and R. G. Compton, "Diffuse double layer at nanoelectrodes," *Journal of Physical Chemistry C*, vol. 113, no. 41, pp. 17585–17589, 2009.

[188] M. C. Henstridge, E. J. F. Dickinson, and R. G. Compton, "On the estimation of the diffuse double layer of carbon nanotubes using classical theory: Curvature effects on the Gouy-Chapman limit," *Chemical Physics Letters*, vol. 485, no. 1-3, pp. 167–170, 2010.

[189] F. Booth, "The dielectric constant of water and the saturation effect," *Journal of Chemical Physics*, vol. 19, no. 4, pp. 391–394, 1951.

[190] F. Booth, "Dielectric constant of polar liquids at high field strengths," *Journal of Chemical Physics*, vol. 23, no. 3, pp. 453–457, 1955.

[191] A. J. Appleby, "Electron transfer reactions with and without ion transfer," in *Modern Aspects of Electrochemistry, No. 38* (B. Conway, C. Vayenas, R. White, and M. Gamboa-Adelco, eds.), pp. 175–301, New York, NY: Kluwer Academic/Plenum Publishers, 2005.

[192] A. D. Buckingham, "Theory of the dielectric constant at high field strengths," *Journal of Chemical Physics*, vol. 25, no. 3, pp. 1–7, No. 428, 1956.

[193] I. C. Yeh and M. L. Berkowitz, "Dielectric constant of water at high electric fields: Molecular dynamics study," *Journal of Chemical Physics*, vol. 110, no. 16, pp. 1–8, No. 7935, 1999.

[194] R. L. Fulton, "The nonlinear dielectric behavior of water: Comparisons of various approaches to the nonlinear dielectric increment," *Journal of Chemical Physics*, vol. 130, no. 20, pp. 1–10, No. 204503, 2009.

[195] P. Zarzycki and K. M. Rosso, "Molecular dynamics simulation of the AgCl/electrolyte interfacial capacity," *Journal of Physical Chemistry C*, vol. 114, no. 21, pp. 10019–10026, 2010.

[196] Y. Gur, I. Ravina, and A. J. Babchin, "On the electrical double layer theory. II. the Poisson-Boltzmann equation including hydration forces," *Journal of Colloid and Interface Science*, vol. 64, no. 2, pp. 333–341, 1978.

[197] S. Basu and M. M. Sharma, "Effect of dielectric saturation on disjoining pressure in thin films of aqueous electrolytes," *Journal of Colloid and Interface Science*, vol. 165, no. 2, pp. 355–366, 1994.

[198] V. N. Paunov, R. I. Dimova, P. A. Kralchevsky, G. Broze, and A. Mehreteab, "The hydration repulsion between charged surfaces as an interplay of volume exclusion and dielectric saturation effects," *Journal of Colloid and Interface Science*, vol. 182, no. 1, pp. 239–248, 1996.

[199] H. Wang, J. Varghese, and L. Pilon, "Simulation of electric double layer capacitors with mesoporous electrodes: Effects of morphology and electrolyte permittivity," *Electrochimica Acta*, vol. 56, no. 17, pp. 6189–6197, 2011.

[200] J. N. Israelachvili, *Intermolecular and Surface Forces*. San Diego, CA: Academic Press, 3rd ed., 2010.

[201] D. J. Griffiths, *Introduction to Electrodynamics*. Upper Saddle River, NJ: Prentice Hall, 3rd ed., 1999.

[202] R. P. Feynman, R. B. Leighton, and M. Sands, *The Feynman Lectures on Physics*, vol. 2. New York, NY: Addison Wesley, 2nd ed., 2005.

[203] M. Endo, T. Maeda, T. Takeda, Y. J. Kim, K. Koshiba, H. Hara, and M. S. Dresselhaus, "Capacitance and pore-size distribution in aqueous and nonaqueous electrolytes using various activated carbon electrodes," *Journal of The Electrochemical Society*, vol. 148, no. 8, pp. 910–914, 2001.

[204] W. Xing, S. Z. Qiao, R. G. Ding, F. Lid, G. Q. Lu, Z. F. Yan, and H. M. Cheng, "Superior electric double layer capacitors using ordered mesoporous carbons," *Carbon*, vol. 44, no. 2, pp. 216–224, 2006.

[205] E. Raymundo-Piñero, K. Kierzek, J. Machnikowski, and F. Béguin, "Relationship between the nanoporous texture of activated carbons and their capacitance properties in different electrolytes," *Carbon*, vol. 44, no. 12, pp. 2498–2507, 2006.

[206] M. Sevilla, S. Alvarez, T. A. Centeno, A. B. Fuertes, and F. Stoeckli, "Performance of templated mesoporous carbons in supercapacitors," *Electrochimica Acta*, vol. 52, no. 9, pp. 3207–3215, 2007.

[207] C. Portet, G. Yushin, and Y. Gogotsi, "Effect of carbon particle size on electrochemical performance of EDLC," *Journal of The Electrochemical Society*, vol. 155, no. 7, pp. 531–536, 2008.

[208] C. Largeot, C. Portet, J. Chmiola, P. L. Taberna, Y. Gogotsi, and P. Simon, "Relation between the ion size and pore size for an electric double-layer capacitor," *Journal of The American Chemical Society*, vol. 130, no. 9, pp. 2730–2731, 2008.

[209] R. Lin, P. L. Taberna, J. Chmiola, D. Guay, Y. Gogotsi, and P. Simon, "Microelectrode study of pore size, ion size, and solvent effects on the charge/discharge behavior of microporous carbons for electrical double-layer capacitors," *Journal of The Electrochemical Society*, vol. 156, no. 1, pp. 7–12, 2009.

[210] J. A. Fernandez, S. Tennison, O. Kozynchenko, F. Rubiera, F. Stoeckli, and T. A. Centeno, "Effect of mesoporosity on specific capacitance of carbons," *Carbon*, vol. 47, no. 6, pp. 1598–1604, 2009.

[211] D. Banham, F. Feng, J. Burt, E. Alsrayheen, and V. Birss, "Bimodal, templated mesoporous carbons for capacitor applications," *Carbon*, vol. 48, no. 4, pp. 1056–1063, 2010.

[212] F. Li, N. van der Laak, S. W. Ting, and K. Y. Chan, "Varying carbon structures templated from KIT-6 for optimum electrochemical capacitance," *Electrochimica Acta*, vol. 55, no. 8, pp. 2817–2823, 2010.

[213] L. Yang, B. H. Fishbine, A. Migliori, and L. R. Pratt, "Molecular simulation of electric double-layer capacitors based on carbon nanotube forests," *Journal of The American Chemical Society*, vol. 131, no. 34, pp. 12373–12376, 2009.

[214] K. Tonurist, A. Janes, T. Thomberg, H. Kurig, and E. Lust, "Influence of mesoporous separator properties on the parameters of electrical double-layer capacitor single cells," *Journal of The Electrochemical Society*, vol. 156, no. 4, pp. 334–342, 2009.

[215] R. Qiao and N. R. Aluru, "Ion concentrations and velocity profiles in nanochannel electroosmotic flows," *Journal of Chemical Physics*, vol. 118, no. 10, pp. 4692–4701, 2003.

[216] H. Daiguji, "Ion transport in nanofluidic channels," *Chemical Society Reviews*, vol. 39, no. 3, pp. 901–911, 2010.

[217] J. C. T. Eijkel and A. van den Berg, "Nanofluidics and the chemical potential applied to solvent and solute transport," *Chemical Society Reviews*, vol. 39, no. 3, pp. 957–973, 2010.

[218] W. Sparreboom, A. van den Berg, and J. C. T. Eijkel, "Transport in nanofluidic systems: a review of theory and applications," *New Journal of Physics*, vol. 12, no. 1, pp. 1–23, No. 015004, 2010.

[219] G. J. Janz and R. P. T. Tomkins, *Nonaqueous Electrolytes Handbook*, vol. I. New York, NY: Academic Press, 1972.

[220] G. Moumouzias and G. Ritzoulis, "Relative permittivities and refractive indices of propylene carbonate + toluene mixtures from 283.15 K to 313.15 K," *Journal of Chemical & Engineering Data*, vol. 42, no. 4, pp. 710–713, 1997.

[221] M. Ue, "Mobility and ionic association of lithium and quaternary ammonium salts in propylene carbonate and γ-butyrolactone," *Journal of The Electrochemical Society*, vol. 141, no. 12, pp. 3336–3342, 1994.

[222] J. N. Israelachvili, *Intermolecular and Surface Forces*. San Diego, CA: Academic Press, 2nd ed., 1992.

[223] B. E. Conway, "Electrolyte solutions: Solvation and structural aspects," *Annual Review of Physical Chemistry*, vol. 17, pp. 481–528, 1966.

[224] Y. Marcus, "Ionic radii in aqueous solutions," *Chemical Reviews*, vol. 88, no. 8, pp. 1475–1498, 1988.

[225] V. N. Afanasev and A. N. Ustinov, "Adiabatic compressibility of hydrated complexes of electrolytes," *Electrochimica Acta*, vol. 54, no. 26, pp. 6455–6463, 2009.

[226] M. Noked, E. Avraham, A. Soffer, and D. Aurbach, "Assessing the concentration effect on hydration radii in aqueous solutions by electroadsorption on a carbon molecular sieve electrode," *Journal of Physical Chemistry C*, vol. 114, no. 31, pp. 13354–13361, 2010.

[227] N. Nanbu, T. Ebina, H. Uno, S. Ishizawa, and Y. Sasaki, "Physical and electrochemical properties of quaternary ammonium bis(oxalato)borates and their application to electric double-layer capacitors," *Electrochimica Acta*, vol. 52, no. 4, pp. 1763–1770, 2006.

[228] H. Wang and L. Pilon, "Accurate simulation of electric double layer capacitance for ultramicroelectrodes," *Journal of Physical Chemistry C*, vol. 115, no. 33, pp. 16711–16719, 2011.

[229] J. Lee, S. Yoon, T. Hyeon, S. M. Oh, and K. B. Kim, "Synthesis of a new mesoporous carbon and its application to electrochemical double-layer capacitors," *Chemical Communications*, vol. 21, pp. 2177–2178, 1999.

[230] H. Zhou, S. Zhu, M. Hibino, and I. Honma, "Electrochemical capacitance of self-ordered mesoporous carbon," *Journal of Power Sources*, vol. 122, no. 2, pp. 219–223, 2003.

[231] D. W. Wang, F. Li, H. T. Fang, M. Liu, G. Q. Lu, and H. M. Cheng, "Effect of pore packing defects in 2-D ordered mesoporous carbons on ionic transport," *Journal of Physical Chemistry B*, vol. 110, no. 17, pp. 8570–8575, 2006.

[232] H. Yamada, H. Nakamur, F. Nakahara, I. Moriguchi, and T. Kudo, "Electrochemical study of high electrochemical double layer capacitance of ordered porous carbons with both meso/macropores and micropores," *Journal of Physical Chemistry C*, vol. 111, no. 1, pp. 227–233, 2007.

[233] H. J. Liu, X. M. Wang, W. J. Cui, Y. Q. Dou, D. Y. Zhao, and Y. Y. Xia, "Highly ordered mesoporous carbon nanofiber arrays from a crab shell biological template and its application in supercapacitors and fuel cells," *Journal of Materials Chemistry*, vol. 20, no. 20, pp. 4223–4230, 2010.

[234] G. Sun, J. Wang, X. Liu, D. Long, W. Qiao, and L. Ling, "Ion transport behavior in triblock copolymer-templated ordered mesoporous carbons with different pore symmetries," *Journal of Physical Chemistry C*, vol. 114, no. 43, pp. 18745–18751, 2010.

[235] Y. Korenblit, M. Rose, E. Kockrick, L. Borchardt, A. Kvit, S. Kaskel, and G. Yushin, "High-rate electrochemical capacitors based on ordered mesoporous silicon carbide-derived carbon," *ACS Nano*, vol. 4, no. 3, pp. 1337–1344, 2010.

[236] D. Feng, Y. Lv, Z. Wu, Y. Dou, L. Han, Z. Sun, Y. Xia, G. Zheng, and D. Zhao, "Free-standing mesoporous carbon thin films with highly ordered pore architectures for nanodevices," *Journal of The American Chemical Society*, vol. 133, no. 38, pp. 15148–15156, 2011.

[237] N. Liu, H. Song, and X. Chen, "Morphology control of ordered mesoporous carbons by changing HCl concentration," *Journal of Materials Chemistry*, vol. 21, no. 14, pp. 5345–5351, 2011.

[238] J. Wang, C. Xue, Y. Lv, F. Zhang, B. Tu, and D. Zhao, "Kilogram-scale synthesis of ordered mesoporous carbons and their electrochemical performance," *Carbon*, vol. 49, no. 13, pp. 4580–4588, 2011.

[239] J.-W. Lang, X.-B. Yan, X.-Y. Yuan, J. Yang, and Q.-J. Xue, "Study on the electrochemical properties of cubic ordered mesoporous carbon for supercapacitors," *Journal of Power Sources*, vol. 196, no. 23, pp. 10472–10478, 2011.

[240] H. Q. Li, R. L. Liu, D. Y. Zhao, and Y. Y. Xia, "Electrochemical properties of an ordered mesoporous carbon prepared by direct tri-constituent co-assembly," *Carbon*, vol. 45, no. 13, pp. 2628–2635, 2007.

[241] H. Q. Li, J. Y. Luo, X. F. Zhou, C. Z. Yu, and Y. Y. Xia, "An ordered mesoporous carbon with short pore length and its electrochemical performances in supercapacitor applications," *Journal of The Electrochemical Society*, vol. 154, no. 8, pp. 731–736, 2007.

[242] C. Liang, Z. Li, and S. Dai, "Mesoporous carbon materials: Synthesis and modification," *Angewandte Chemie International Edition*, vol. 47, no. 20, pp. 3696–3717, 2008.

[243] Y. Deng, Y. Cai, Z. Sun, D. Gu, J. Wei, W. Li, X. Guo, J. Yang, and D. Zhao, "Controlled synthesis and functionalization of ordered large-pore mesoporous carbons," *Advanced Functional Materials*, vol. 20, no. 21, pp. 3658–3665, 2010.

[244] J. Varghese, H. Wang, and L. Pilon, "Simulating electric double layer capacitance of mesoporous electrodes with cylindrical pores," *Journal of The Electrochemical Society*, vol. 158, no. 10, pp. 1106–1114, 2011.

[245] E. M. Itskovich, A. A. Kornyshev, and M. A. Vorotyntsev, "Electric current across the metal-solid electrolyte interface I. Direct current, current-voltage characteristic," *Physica Status Solidi A*, vol. 39, no. 1, pp. 229–238, 1977.

[246] A. A. Kornyshev and M. A. Vorotyntsev, "Conductivity and space charge phenomena in solid electrolytes with one mobile charge carrier species, a review with original material," *Electrochimica Acta*, vol. 26, no. 3, pp. 303–323, 1981.

[247] A. Ajdari, "Pumping liquids using asymmetric electrode arrays," *Physical Review E*, vol. 61, no. 1, pp. 45–48, 2000.

[248] A. Bonnefont, F. Argoul, and M. Z. Bazant, "Analysis of diffuse-layer effects on time-dependent interfacial kinetics," *Journal of Electroanalytical Chemistry*, vol. 500, no. 1-2, pp. 52–61, 2001.

[249] L. H. Olesen, H. Bruus, and A. Ajdari, "ac electrokinetic micropumps: The effect of geometrical confinement, Faradaic current injection, and nonlinear surface capacitance," *Physical Review E*, vol. 73, no. 5, No. 056313, 2006.

[250] P. M. Biesheuvel, M. van Soestbergen, and M. Z. Bazant, "Imposed currents in galvanic cells," *Electrochimica Acta*, vol. 54, no. 21, pp. 4857–4871, 2009.

[251] P. M. Biesheuvel, A. A. Franco, and M. Z. Bazant, "Diffuse charge effects in fuel cell membranes," *Journal of The Electrochemical Society*, vol. 156, no. 2, pp. 225–233, 2009.

[252] P. M. Biesheuvel, Y. Fu, and M. Z. Bazant, "Diffuse charge and Faradaic reactions in porous electrodes," *Physical Review E*, vol. 83, no. 6, No. 061507, 2011.

[253] D. R. Lide, ed., *CRC Handbook of Chemistry and Physics*. Boca Raton, FL: CRC Press/Taylor & Francis, 90th ed., 2010.

[254] S. Senapati and A. Chandra, "Dielectric constant of water confined in a nanocavity," *Journal of Physical Chemistry B*, vol. 105, no. 22, pp. 5106–5109, 2001.

[255] J. Dzubiella and J. P. Hansen, "Electric-field-controlled water and ion permeation of a hydrophobic nanopore," *Journal of Chemical Physics*, vol. 122, no. 23, pp. 1–14, No. 234706, 2005.

[256] Y.-J. Kim, Y. Masutzawa, S. Ozaki, M. Endo, and M. S. Dresselhaus, "PVDC-based carbon material by chemical activation and its application to nonaqueous EDLC," *Journal of The Electrochemical Society*, vol. 151, no. 6, pp. 199–205, 2004.

[257] C. M. Yang, Y. J. Kim, M. Endo, H. Kanoh, M. Yudasaka, S. Iijima, and K. Kaneko, "Nanowindow-regulated specific capacitance of supercapacitor electrodes of single-wall carbon nanohorns," *Journal of The American Chemical Society*, vol. 129, no. 1, pp. 20–21, 2007.

[258] C. O. Ania, J. Pernak, F. Stefaniak, E. Raymundo-Piñero, and F. Béguin, "Polarization-induced distortion of ions in the pores of carbon electrodes for electrochemical capacitors," *Carbon*, vol. 47, no. 14, pp. 3158–3166, 2009.

[259] C. Merlet, B. Rotenberg, P. A. Madden, P.-L. Taberna, P. Simon, Y. Gogotsi, and M. Salanne, "On the molecular origin of supercapacitance in nanoporous carbon electrodes," *Nature Materials*, vol. 11, no. 4, pp. 306–310, 2012.

[260] H. Wang, A. Thiele, and L. Pilon, "Simulations of cyclic voltammetry for electric double layers in asymmetric electrolytes: A generalized modified Poisson-Nernst-Planck model," *Journal of Physical Chemistry C*, vol. 117, no. 36, p. 1828618297, 2013.

[261] B. J. Kirby, *Micro- and Nanoscale Fluid Mechanics: Transport in Microfluidic Devices*. Cambridge, UK: Cambridge University Press, 2010.

[262] H. Lu, W. Dai, M. Zheng, N. Li, G. Ji, and J. Cao, "Electrochemical capacitive behaviors of ordered mesoporous carbons with controllable pore sizes," *Journal of Power Sources*, vol. 209, pp. 243–250, 2012.

[263] K. Jurewicz, C. Vix-Guterl, E. Frackowiak, S. Saadallah, M. Reda, J. Parmentier, J. Patarin, and F. Beguin, "Capacitance properties of ordered porous carbon materials prepared by a templating procedure," *Journal of Physics and Chemistry of Solids*, vol. 65, no. 2-3, pp. 287–293, 2004.

[264] H. Nishihara, H. Itoi, T. Kogure, P. X. Hou, H. Touhara, F. Okino, and T. Kyotani, "Investigation of the ion storage/transfer behavior in an electrical double-layer capacitor by using ordered microporous carbons as model materials," *Chemistry - A European Journal*, vol. 15, no. 21, pp. 5355–5363, 2009.

[265] D. S. Yuan, J. Zeng, J. Chen, and Y. Liu, "Highly ordered mesoporous carbon synthesized via in situ template for supercapacitors," *International Journal of Electrochemical Science*, vol. 4, no. 4, pp. 562–570, 2009.

[266] J. Yan, T. Wei, B. Shao, F. Ma, Z. Fan, M. Zhang, C. Zheng, Y. Shang, W. Qian, and F. Wei, "Electrochemical properties of graphene nanosheet/carbon black composites as electrodes for supercapacitors," *Carbon*, vol. 48, no. 6, pp. 1731–1737, 2010.

[267] Y. Lv, L. Gan, M. Liu, W. Xiong, Z. Xu, D. Zhu, and D. S. Wright, "A self-template synthesis of hierarchical porous carbon foams based on banana peel for supercapacitor electrodes," *Journal of Power Sources*, vol. 209, pp. 152–157, 2012.

[268] L. Jiang, J. Yan, L. Hao, R. Xue, G. Sun, and B. Yi, "High rate performance activated carbons prepared from ginkgo shells for electrochemical supercapacitors," *Carbon*, vol. 56, pp. 146–154, 2013.

[269] F. Li, M. Morris, and K.-Y. Chan, "Electrochemical capacitance and ionic transport in the mesoporous shell of a hierarchical porous coreshell carbon structure," *Journal of Materials Chemistry*, vol. 21, no. 24, pp. 8880–8886, 2011.

[270] J. Zhou, J. He, C. Zhang, T. Wang, D. Sun, Z. Di, and D. Wang, "Mesoporous carbon spheres with uniformly penetrating channels and their use as a supercapacitor electrode material," *Materials Characterization*, vol. 61, no. 1, pp. 31–38, 2010.

[271] F. B. Sillars, S. I. Fletcher, M. Mirzaeian, and P. J. Hall, "Effect of activated carbon xerogel pore size on the capacitance performance of ionic liquid electrolytes," *Energy & Environmental Science*, vol. 4, no. 3, pp. 695–706, 2011.

[272] Y. Lv, F. Zhang, Y. Dou, Y. Zhai, J. Wang, H. Liu, Y. Xia, B. Tu, and D. Zhao, "A comprehensive study on KOH activation of ordered mesoporous carbons and their supercapacitor application," *Journal of Materials Chemistry*, vol. 22, no. 1, pp. 93–99, 2012.

[273] B.-Y. Chang and S.-M. Park, "Electrochemical impedance spectroscopy," *Annual Review of Analytical Chemistry*, vol. 3, pp. 207–229, 2010.

[274] J. Segalini, B. Daffos, P. L. Taberna, Y. Gogotsi, and P. Simon, "Qualitative electrochemical impedance spectroscopy study of ion transport into sub-nanometer carbon pores in electrochemical double layer capacitor electrodes," *Electrochimica Acta*, vol. 55, no. 25, pp. 7489–7494, 2010.

[275] J. R. Miller, R. A. Outlaw, and B. C. Holloway, "Graphene double-layer capacitor with ac line-filtering performance," *Science*, vol. 329, no. 5999, pp. 1637–1639, 2010.

[276] Y. Zhu, S. Murali, M. D. Stoller, K. J. Ganesh, W. Cai, P. J. Ferreira, A. Pirkle, R. M. Wallace, K. A. Cychosz, M. Thommes, D. Su, E. A. Stach, and R. S. Ruoff, "Carbon-based supercapacitors produced by activation of graphene," *Science*, vol. 332, no. 6037, pp. 1537–1541, 2011.

[277] H. Itoi, H. Nishihara, T. Kogure, and T. Kyotani, "Three-dimensionally arrayed and mutually connected 1.2-nm nanopores for high-performance electric double layer capacitor," *Journal of the American Chemical Society*, vol. 133, no. 5, pp. 1165–1167, 2011.

[278] R. H. Nilson, M. T. Brumbach, and B. C. Bunker, "Modeling the electrochemical impedance spectra of electroactive pseudocapacitor materials," *Journal of The Electrochemical Society*, vol. 158, no. 6, pp. 678–688, 2011.

[279] M. D. Levi and D. Aurbach, "Simultaneous measurements and modeling of the electrochemical impedance and the cyclic voltammetric characteristics of graphite electrodes doped with lithium," *Journal of Physical Chemistry B*, vol. 101, no. 23, pp. 4630–4640, 1997.

[280] F. L. Mantia, J. Vetter, and P. Novak, "Impedance spectroscopy on porous materials: A general model and application to graphite electrodes of lithium-ion batteries," *Electrochimica Acta*, vol. 53, no. 12, pp. 4109–4121, 2008.

[281] J. M. Atebamba, J. Moskon, S. Pejovnik, and M. Gaberscek, "On the interpretation of measured impedance spectra of insertion cathodes for lithium-ion batteries," *Journal of The Electrochemical Society*, vol. 157, no. 11, pp. 1218–1228, 2010.

[282] Z. He and F. Mansfeld, "Exploring the use of electrochemical impedance spectroscopy (EIS) in microbial fuel cell studies," *Energy & Environmental Science*, vol. 2, no. 2, pp. 215–219, 2009.

[283] J. Tanguy, J. L. Baudoin, F. Chao, and M. Costa, "Study of the redox mechanism of poly-3-methylthiophene by impedance spectroscopy," *Electrochimica Acta*, vol. 37, no. 8, pp. 1417–1428, 1992.

[284] J. P. Zheng, P. C. Goonetilleke, C. M. Pettit, and D. Roy, "Probing the electrochemical double layer of an ionic liquid using voltammetry and impedance spectroscopy: A comparative study of carbon nanotube and glassy carbon electrodes in $[EMIM]^+[EtSO_4]^-$," *Talanta*, vol. 81, no. 3, pp. 1045–1055, 2010.

[285] K. Kierzek, E. Frackowiak, G. Lota, G. Gryglewicz, and J. Machnikowski, "Electrochemical capacitors based on highly porous carbons prepared by KOH activation," *Electrochimica Acta*, vol. 49, no. 4, pp. 515–523, 2004.

[286] F. Lufrano, P. Staiti, and M. Minutoli, "Evaluation of nafion based double layer capacitors by electrochemical impedance spectroscopy," *Journal of Power Sources*, vol. 124, no. 1, pp. 314–320, 2003.

[287] J. D. Ferry, "Frequency dependence of the capacity of a diffuse double layer," *Journal of Chemical Physics*, vol. 16, no. 7, pp. 737–739, 1948.

[288] R. P. Buck, "Diffuse layer charge relaxation at the ideally polarized electrode," *Journal of Electroanalytical Chemistry*, vol. 23, no. 2, pp. 219–240, 1969.

[289] J. R. Macdonald, "Theory of ac space-charge polarization effects in photoconductors, semiconductors, and electrolytes," *Physical Review*, vol. 92, no. 1, pp. 4–7, 1953.

[290] J. R. Macdonald, "Electrical response of materials containing space charge with discharge at the electrodes," *Journal of Chemical Physics*, vol. 54, no. 5, pp. 2026–2050, 1971.

[291] I. Rubinstein and B. Zaltzman, "Extended space charge in concentration polarization," *Advances in Colloid and Interface Science*, vol. 159, no. 2, pp. 117–129, 2010.

[292] C. Peng, J. Jin, and G. Z. Chen, "A comparative study on electrochemical co-deposition and capacitance of composite films of conducting polymers and carbon nanotubes," *Electrochimica Acta*, vol. 53, no. 2, pp. 525–537, 2007.

[293] A. T. Chidembo, K. I. Ozoemena, B. O. Agboola, V. Gupta, G. G. Wildgoose, and R. G. Compton, "Nickel(II) tetra-aminophthalocyanine modified MWCNTs as potential nanocomposite materials for the development of supercapacitors," *Energy & Environmental Science*, vol. 3, no. 2, pp. 228–236, 2010.

[294] L. Li, H. Song, and X. Chen, "Pore characteristics and electrochemical performance of ordered mesoporous carbons for electric double-layer capacitors," *Electrochimica Acta*, vol. 51, no. 26, pp. 5715–5720, 2006.

[295] M. Inagaki, H. Konno, and O. Tanaike, "Carbon materials for electrochemical capacitors," *Journal of Power Sources*, vol. 195, no. 24, pp. 7880–7903, 2010.

[296] J. R. Macdonald, "Impedance spectroscopy: old problems and new developments," *Electrochimica Acta*, vol. 35, no. 10, pp. 1483–1492, 1990.

[297] L. A. Geddes, "Historical evolution of circuit models for the electrode-electrolyte interface," *Annals of Biomedical Engineering*, vol. 25, no. 1, pp. 1–14, 1997.

[298] R. de Levie, "On porous electrodes in electrolyte solutions: I. capacitance effects," *Electrochimica Acta*, vol. 8, no. 10, pp. 751–780, 1963.

[299] R. de Levie, "Electrochemical response of porous and rough electrodes," in *Advances in Electrochemical Science and Engineering, Vol. 6* (P. Delahay and C. Tobias, eds.), pp. 329–397, New York, NY: Interscience Publishers, 1967.

[300] H. Keiser, K. D. Beccu, and M. A. Gutjahr, "Evaluation of pore structure of porous-electrodes using measurements of impedance," *Electrochimica Acta*, vol. 21, no. 8, pp. 539–543, 1976.

[301] I. D. Raistrick, "Impedance studies of porous electrodes," *Electrochimica Acta*, vol. 35, no. 10, pp. 1579–1586, 1990.

[302] H. K. Song, Y. H. Jung, K. H. Lee, and L. H. Dao, "Electrochemical impedance spectroscopy of porous electrodes: the effect of pore size distribution," *Electrochimica Acta*, vol. 44, no. 1, pp. 3513–3519, 1999.

[303] H. K. Song, H. Y. Hwang, K. H. Lee, and L. H. Dao, "The effect of pore size distribution on the frequency dispersion of porous electrodes," *Electrochimica Acta*, vol. 45, no. 14, pp. 2241–2257, 2000.

[304] J. F. Rubinson and Y. P. Kayinamura, "Charge transport in conducting polymers: insights from impedance spectroscopy," *Chemical Society Reviews*, vol. 38, no. 12, pp. 3339–3347, 2009.

[305] I. Rubinstein, E. Sabatani, and J. Rishpon, "Electrochemical impedance analysis of polyaniline films on electrodes," *Journal of The Electrochemical Society*, vol. 134, no. 12, pp. 3078–3083, 1987.

[306] J. Tanguy, N. Mermilliod, and M. Hoclet, "Capacitive charge and noncapacitive charge in conducting polymer electrodes," *Journal of The Electrochemical Society*, vol. 134, no. 4, pp. 795–802, 1987.

[307] M. Kalaji and L. M. Peter, "Optical and electrical A.C. response of polyaniline films," *Journal of The Chemical Society, Faraday Transactions*, vol. 87, no. 6, pp. 853–860, 1991.

[308] J. Bobacka, A. Lewenstam, and A. Ivaska, "Electrochemical impedance spectroscopy of oxidized poly(3,4-ethylenedioxythiophene) film electrodes in aqueous solutions," *Journal of Electroanalytical Chemistry*, vol. 489, no. 1-2, pp. 17–27, 2000.

[309] W. Sun and X. Chen, "Preparation and characterization of polypyrrole films for three-dimensional micro supercapacitor," *Journal of Power Sources*, vol. 193, no. 2, pp. 924–929, 2009.

[310] F. C. M. Freire, G. Barbero, and M. Scalerandi, "Electrical impedance for an electrolytic cell," *Physical Review E*, vol. 73, no. 5, pp. 1–9, No. 051202, 2006.

[311] T. R. Brumleve and R. P. Buck, "Transmission line equivalent circuit models for electrochemical impedances," *Journal of Electroanalytical Chemistry*, vol. 126, no. 1-3, pp. 73–104, 1981.

[312] R. P. Buck, "Kinetics of bulk and interfacial ionic motion: Microscopic bases and limits for the Nernst-Planck equation applied to membrane systems," *Journal of Membrane Science*, vol. 17, no. 1, pp. 1–62, 1984.

[313] T. Sokalski and A. Lewenstam, "Application of Nernst-Planck and Poisson equations for interpretation of liquid-junction and membrane potentials in real-time and space domains," *Electrochemistry Communications*, vol. 3, no. 3, pp. 107–112, 2001.

[314] A. A. Moya, "Influence of dc electric current on the electrochemical impedance of ion-exchange membrane systems," *Electrochimica Acta*, vol. 56, no. 8, pp. 3015–3022, 2011.

[315] V. V. Nikonenko and A. E. Kozmai, "Electrical equivalent circuit of an ion-exchange membrane system," *Electrochimica Acta*, vol. 56, no. 3, pp. 1262–1269, 2011.

[316] J. Lim, J. Whitcomb, J. Boyda, and J. Varghese, "Transient finite element analysis of electric double layer using Nernst-Planck-Poisson equations with a modified Stern layer," *Journal of Colloid and Interface Science*, vol. 305, no. 1, pp. 159–174, 2007.

[317] J. Lim, J. Whitcomb, J. Boyda, and J. Varghese, "Effect of electrode pore geometry modeled using Nernst-Planck-Poisson-modified Stern layer model," *Journal of Computational Mechanics*, vol. 43, no. 4, pp. 461–475, 2009.

[318] R. Mills and V. M. M. Lobo, *Self Diffusion in Electrolyte Solutions: A Critical Examination of Data Compiled from the Literature*. New York, NY: Elsevier, 1989.

[319] M. Jardat, B. Hribar-Lee, and V. Vlachy, "Self-diffusion coefficients of ions in the presence of charged obstacles," *Physical Chemistry Chemical Physics*, vol. 10, no. 3, pp. 449–457, 2008.

[320] M. C. F. Wander and K. L. Shuford, "Molecular dynamics study of interfacial confinement effects of aqueous NaCl Brines in nanoporous carbon," *Journal of Physical Chemistry C*, vol. 114, no. 48, pp. 20539–20546, 2010.

[321] R. Sardenberg and J. M. A. Figueiredo, "Relationship between spatial and spectral properties of ionic solutions: The distributed impedance of an electrolytic cell," *Electrochimica Acta*, vol. 55, no. 16, pp. 4722–4727, 2010.

[322] R. P. Buck, "Diffusion-migration impedances for finite, one-dimensional transport in thin layer and membrane cells: An analysis of derived electrical quantities and equivalent circuits," *Journal of Electroanalytical Chemistry*, vol. 210, no. 1, pp. 1–19, 1986.

[323] H. Cohen and J. W. Cooley, "The numerical solution of the time-dependent Nernst-Planck equations," *Biophysical Journal*, vol. 5, no. 2, pp. 145–162, 1965.

[324] T. R. Brumleve and R. P. Buck, "Numerical solution of the Nernst-Planck and Poisson equation system with applications to membrane electrochemistry and solid state physics," *Journal of Electroanalytical Chemistry*, vol. 90, no. 1, pp. 1–31, 1978.

[325] J. R. Macdonald, "Theory of space-charge polarization and electrode-discharge effects," *Journal of Chemical Physics*, vol. 58, no. 11, pp. 4982–5001, 1973.

[326] F. Beunis, F. Strubbe, M. Marescaux, J. Beeckman, K. Neyts, and A. R. M. Verschueren, "Dynamics of charge transport in planar devices," *Physical Review E*, vol. 78, no. 1, No. 011502, 2008.

[327] G. J. Brug, A. L. G. van den Eeden, M. Sluyters-Rehbach, and J. H. Sluyters, "The analysis of electrode impedances complicated by the presence of a constant phase element," *Journal of Electroanalytical Chemistry*, vol. 176, no. 1-2, pp. 275–295, 1984.

[328] T. Pajkossy, "Electrochemistry at fractal surfaces," *Journal of Electroanalytical Chemistry*, vol. 300, no. 1-2, pp. 1–11, 1991.

[329] T. Pajkossy, "Impedance of rough capacitive electrodes," *Journal of Electroanalytical Chemistry*, vol. 364, no. 1-2, pp. 111–125, 1994.

[330] Z. Kerner and T. Pajkossy, "On the origin of capacitance dispersion of rough electrodes," *Electrochimica Acta*, vol. 46, no. 2-3, pp. 207–211, 2000.

[331] R. G. Compton and C. E. Banks, *Understanding Voltammetry*. Hackensack, NJ: World Scientific, 2007.

[332] K. Xu, "Nonaqueous liquid electrolytes for lithium-based rechargeable batteries," *Chemical Reviews*, vol. 104, no. 10, pp. 4303–4418, 2004.

[333] S. W. Lee, N. Yabuuchi, and B. M. Gallant, "High-power lithium batteries from functionalized carbon-nanotube electrodes," *Nature Nanotechnology*, vol. 5, no. 7, pp. 531–537, 2010.

[334] F. Zhao, R. C. Slade, and J. R. Varcoe, "Techniques for the study and development of microbial fuel cells: an electrochemical perspective," *Chemical Society Reviews*, vol. 38, no. 7, pp. 1926–1939, 2009.

[335] M. B. Pomfret, J. C. Owrutsky, and R. A. Walker, "In situ optical studies of solid-oxide fuel cells," *Annual Review of Analytical Chemistry*, vol. 3, pp. 151–174, 2010.

[336] I. Kovalenko, D. G. Bucknall, and G. Yushin, "Detonation nanodiamond and onion-like-carbon-embedded polyaniline for supercapacitors," *Advanced Functional Materials*, vol. 30, no. 22, pp. 3979–3986, 2010.

[337] H. R. Byon, S. W. Lee, S. Chen, P. T. Hammond, and Y. Shao-Horn, "Thin films of carbon nanotubes and chemically reduced graphenes for electrochemical micro-capacitors," *Carbon*, vol. 49, no. 2, pp. 457–467, 2011.

[338] G. Salitra, A. Soffer, L. Eliad, Y. Cohen, and D. Aurbach, "Carbon electrodes for double-layer capacitors I. relations between ion and pore dimensions," *Journal of The Electrochemical Society*, vol. 147, no. 7, pp. 2486–2493, 2000.

[339] D. Aurbach, M. D. Levi, G. Salitra, N. Levy, E. Pollak, and J. Muthu, "Cation trapping in highly porous carbon electrodes for EDLC cells," *Journal of The Electrochemical Society*, vol. 155, no. 10, pp. 745–753, 2008.

[340] R. Lin, P. Huang, J. Segalini, C. Largeot, P. L. Taberna, J. Chmiola, Y. Gogotsi, and P. Simon, "Solvent effect on the ion adsorption from ionic liquid electrolyte into sub-nanometer carbon pores," *Electrochimica Acta*, vol. 54, no. 27, pp. 7025–7032, 2009.

[341] W. G. Pell, B. E. Conway, and N. Marincic, "Analysis of non-uniform charge/discharge and rate effects in porous carbon capacitors containing sub-optimal electrolyte concentrations," *Journal of Electroanalytical Chemistry*, vol. 491, no. 1-2, pp. 9–21, 2000.

[342] J. Chmiola, C. Largeot, P. L. Taberna, P. Simon, and Y. Gogotsi, "Monolithic carbide-derived carbon films for micro-supercapacitors," *Science*, vol. 328, no. 5977, pp. 480–483, 2010.

[343] F. Béguin, K. Szostak, G. Lota, and E. Frackowiak, "A self-supporting electrode for supercapacitors prepared by one-step pyrolysis of carbon nanotube/polyacrylonitrile blend," *Advanced Materials*, vol. 17, no. 19, pp. 2380–2384, 2005.

[344] D. Hulicova, J. Yamashita, Y. Soneda, H. Hatori, and M. Kodama, "Supercapacitors prepared from melamine-based carbon," *Chemistry of Materials*, vol. 17, no. 5, pp. 1241–1247, 2005.

[345] H. A. Andreas and B. E. Conway, "Examination of the double-layer capacitance of an high specific-area C-cloth electrode as titrated from acidic to alkaline pHs," *Electrochimica Acta*, vol. 51, no. 28, pp. 6510–6520, 2006.

[346] W. Li, D. Chen, Z. Li, Y. Shi, Y. Wan, J. Huang, J. Yang, D. Zhao, and Z. Jiang, "Nitrogen enriched mesoporous carbon spheres obtained by a facile method and its application for electrochemical capacitor," *Electrochemistry Communications*, vol. 9, no. 4, pp. 569–573, 2007.

[347] B. Xu, F. Wu, R. Chen, G. Cao, S. Chen, Z. Zhou, and Y. Yang, "Highly mesoporous and high surface area carbon: A high capacitance electrode material for EDLCs with various electrolytes," *Electrochemistry Communications*, vol. 10, no. 5, pp. 795–797, 2008.

[348] T. Wang, A. Kiebele, J. Ma, S. Mhaisalkar, and G. Gruner, "Charge transfer between polyaniline and carbon nanotubes supercapacitors: Improving both energy and power densities," *Journal of The Electrochemical Society*, vol. 158, no. 1, pp. 1–5, 2011.

[349] M. Kawaguchi, A. Itoh, S. Yagi, and H. Oda, "Preparation and characterization of carbonaceous materials containing nitrogen as electrochemical capacitor," *Journal of Power Sources*, vol. 172, no. 1, pp. 481–486, 2007.

[350] M. Seredych, D. Hulicova-Jurcakova, G. Q. Lu, and T. J. Bandosz, "Surface functional groups of carbons and the effects of their chemical character, density and accessibility to ions on electrochemical performance," *Carbon*, vol. 46, no. 11, pp. 1475–1488, 2008.

[351] H. Konno, H. Onishi, N. Yoshizawa, and K. Azumi, "MgO-templated nitrogen-containing carbons derived from different organic compounds for capacitor electrodes," *Journal of Power Sources*, vol. 195, no. 2, pp. 667–673, 2010.

[352] R. Mysyk, E. Raymundo-Pinero, J. Pernak, and F. Béguin, "Confinement of symmetric tetraalkylammonium ions in nanoporous carbon electrodes of electric double-layer capacitors," *Journal of Physical Chemistry C*, vol. 113, no. 30, pp. 13443–13449, 2009.

[353] R. Mysyk, E. Raymundo-Pinero, and F. Béguin, "Saturation of subnanometer pores in an electric double-layer capacitor," *Electrochemistry Communications*, vol. 11, no. 3, pp. 554–556, 2009.

[354] J. D. Norton, H. S. White, and S. W. Feldberg, "Effect of the electrical double layer on voltammetry at microelectrodes," *Journal of Physical Chemistry*, vol. 94, no. 17, pp. 6772–6780, 1990.

[355] C. P. Smith and H. S. White, "Theory of the voltammetric response of electrodes of submicron dimensions. Violation of electroneutrality in the presence of excess supporting electrolyte," *Analytical Chemistry*, vol. 65, no. 23, pp. 3343–3353, 1993.

[356] M. Ciszkowska and Z. Stojek, "Voltammetry in solutions of low ionic strength. electrochemical and analytical aspects," *Journal of Electroanalytical Chemistry*, vol. 466, no. 2, pp. 129–143, 1999.

[357] J. Sanchez-Gonzalez, F. Stoeckli, and T. A. Centeno, "The role of the electric conductivity of carbons in the electrochemical capacitor performance," *Journal of Electroanalytical Chemistry*, vol. 657, no. 1-2, pp. 176–180, 2011.

[358] L. L. Zhang, R. Zhou, and X. S. Zhao, "Graphene-based materials as supercapacitor electrodes," *Journal of Materials Chemistry*, vol. 20, no. 29, pp. 5983–5992, 2010.

[359] M. D. Stoller, S. Park, Y. Zhu, J. An, and R. S. Ruoff, "Graphene-based ultracapacitors," *Nano Letters*, vol. 8, no. 10, pp. 3498–3502, 2008.

[360] M. van Soestbergen, P. M. Biesheuvel, and M. Z. Bazant, "Diffuse-charge effects on the transient response of electrochemical cells," *Physical Review E*, vol. 81, no. 2, No. 021503, 2010.

[361] Y.-H. Chen, C.-W. Wang, X. Zhang, and A. M. Sastry, "Porous cathode optimization for lithium cells: Ionic and electronic conductivity, capacity, and selection of materials," *Journal of Power Sources*, vol. 195, no. 9, pp. 2851–2862, 2010.

[362] A. M. Colclasure and R. J. Kee, "Thermodynamically consistent modeling of elementary electrochemistry in lithium-ion batteries," *Electrochimica Acta*, vol. 55, no. 28, pp. 8960–8973, 2010.

[363] C. Y. Wang, "Fundamental models for fuel cell engineering," *Chemical Reviews*, vol. 104, no. 10, pp. 4727–4766, 2004.

[364] P. P. Mukherjee, G. Wang, and C. Y. Wang, "Direct numerical simulation of polymer electrolyte fuel cell catalyst layers," in *Modern Aspects of Electrochemistry, No. 40* (R. White, C. Vayenas, and M. Gamboa-Aldeco, eds.), ch. 6, pp. 285–341, New York, NY: Springer, 2007.

[365] T. Berning, D. M. Lu, and N. Djilali, "Three-dimensional computational analysis of transport phenomena in a PEM fuel cell," *Journal of Power Sources*, vol. 106, no. 1-2, pp. 284–294, 2002.

[366] H. C. Yeh, R. J. Yang, and W.-J. Luo, "Analysis of traveling-wave electroosmotic pumping with double-sided electrode arrays," *Physical Review E*, vol. 83, no. 5, pp. 1–9, No. 056326, 2011.

[367] J. J. Yoo, K. Balakrishnan, J. Huang, V. Meunier, B. G. Sumpter, A. Srivastava, M. Conway, A. L. M. Reddy, J. Yu, R. Vajta, and P. M. Ajayan, "Ultrathin planar graphene supercapacitors," *Nano Letters*, vol. 11, no. 4, pp. 1423–1427, 2011.

[368] R. Greff, R. Peat, L. M. Peter, D. Pletcher, and J. Robinson, *Instrumental Methods in Electrochemistry*. Chichester, UK: Southampton Electrochemistry Group, 1985.

[369] T. Brezesinski, J. Wang, J. Polleux, B. Dunn, and S. H. Tolbert, "Templated nanocrystal-based porous TiO_2 films for next-generation electrochemical capacitors," *Journal of The American Chemical Society*, vol. 131, no. 5, pp. 1802–1809, 2009.

[370] T. Brezesinski, J. Wang, S. H. Tolbert, and B. Dunn, "Ordered mesoporous α-MoO_3 with iso-oriented nanocrystalline walls for thin-film pseudocapacitors," *Nature Materials*, vol. 9, no. 2, pp. 146–151, 2010.

[371] M. Z. Bazant, B. D. Storey, and A. A. Kornyshev, "Double layer in ionic liquids: Overscreening versus crowding," *Physical Review Letters*, vol. 106, no. 4, No. 046102, 2011.

[372] M. Galinski, A. Lewandowski, and I. Stepniak, "Ionic liquids as electrolytes," *Electrochimica Acta*, vol. 51, no. 26, pp. 5567–5580, 2006.

[373] R. Lin, P.-L. Taberna, S. Fantini, V. Presser, C. R. Pérez, F. Malbosc, N. L. Rupesinghe, K. B. K. Teo, Y. Gogotsi, and P. Simon, "Capacitive energy storage from -50 to 100 °C using an ionic liquid electrolyte," *Journal of Physical Chemistry Letters*, vol. 2, no. 19, pp. 2396–2401, 2011.

[374] S. Li, G. Feng, P. F. Fulvio, Patrick, C. Hillesheim, C. Liao, S. Dai, and P. T. Cummings, "Molecular dynamics simulation study of the capacitive performance of a binary mixture of ionic liquids near an onion-like carbon electrode," *Journal of Physical Chemistry Letters*, vol. 3, no. 17, pp. 2465–2469, 2012.

[375] R. Palm, H. Kurig, K. Tõnurist, A. Jänes, and E. Lust, "Is the mixture of 1-ethyl-3-methylimidazolium tetrafluoroborate and 1-butyl-3-methylimidazolium tetrafluoroborate applicable as electrolyte in electrical double layer capacitors," *Electrochemistry Communications*, vol. 22, pp. 203–206, 2012.

[376] P. M. Biesheuvel, Y. Fu, and M. Z. Bazant, "Electrochemistry and capacitive charging of porous electrodes in asymmetric multicomponent electrolytes," *Russian Journal of Electrochemistry*, vol. 48, no. 6, pp. 580–592, 2012.

[377] R. Zhao, M. van Soestbergen, H. H. M. Rijnaarts, A. van der Wal, M. Z. Bazant, and P. M. Biesheuvel, "Time-dependent ion selectivity in capacitive charging of porous electrodes," *Journal of Colloid and Interface Science*, vol. 384, no. 1, pp. 38–44, 2012.

[378] J. P. Valleau and G. M. Torrie, "The electrical double layer. III. modified Gouy-Chapman theory with unequal ion sizes," *Journal of Chemical Physics*, vol. 76, no. 9, pp. 4623–4630, 1982.

[379] J. Yu, G. E. Aguilar-Pineda, A. Antillon, S.-H. Dong, and M. Lozada-Cassou, "The effects of unequal ionic sizes for an electrolyte in a charged slit," *Journal of Colloid and Interface Science*, vol. 295, no. 1, pp. 124–134, 2006.

[380] D. O. Wipf, E. W. Kristensen, M. R. Deakin, and R. M. Wightman, "Fast-scan cyclic voltammetry as a method to measure rapid heterogeneous electron-transfer kinetics," *Analytical Chemistry*, vol. 60, no. 4, pp. 306–310, 1988.

[381] D. L. Robinson, A. Hermans, A. T. Seipel, and R. M. Wightman, "Monitoring rapid chemical communication in the brain," *Chemical Reviews*, vol. 108, no. 7, pp. 2554–2584, 2008.

[382] M. Perry, Q. Li, and R. T. Kennedy, "Review of recent advances in analytical techniques for the determination of neurotransmitters," *Analytica Chimica Acta*, vol. 653, no. 1, pp. 1–22, 2009.

[383] P. M. Biesheuvel, "Two-fluid model for the simultaneous flow of colloids and fluids in porous media," *Journal of Colloid and Interface Science*, vol. 335, no. 2, pp. 389–395, 2011.

[384] Z. Adamczyk and P. Warszynski, "Role of electrostatic interactions in particle adsorption," *Advances in Colloid and Interface Science*, vol. 63, no. 8, pp. 41–149, 1996.

[385] Z. Adamczyk, P. Belouschek, and D. Lorenz, "Electrostatic interactions of bodies bearing thin double-layers. 1. General formulation," *Berichte der Bunsengesellschaft für Physikalische Chemie*, vol. 94, no. 12, pp. 1483–1492, 1990.

[386] Z. Adamczyk, P. Belouschek, and D. Lorenz, "Electrostatic interactions of bodies bearing thin double-layers. 2. Exact numerical-solutions," *Berichte der Bunsengesellschaft für Physikalische Chemie*, vol. 94, no. 12, pp. 1492–1499, 1990.

[387] Z. Adamczyk, P. Belouschek, and D. Lorenz, "Electrostatic interactions of bodies bearing thin double-layers. III. Dissimilar double-layers," *Berichte der Bunsengesellschaft für Physikalische Chemie*, vol. 95, no. 5, pp. 566–573, 1991.

[388] G. M. Goldin, A. M. Colclasure, A. H. Wiedemann, and R. J. Kee, "Three-dimensional particle-resolved models of Li-ion batteries to assist the evaluation of empirical parameters in one-dimensional models," *Electrochimica Acta*, vol. 64, pp. 118–129, 2012.

[389] A. H. Wiedemann, G. M. Goldin, S. A. Barnett, H. Zhu, and R. J. Kee, "Effects of three-dimensional cathode microstructure on the performance of lithium-ion battery cathodes," *Electrochimica Acta*, vol. 88, pp. 580–588, 2013.

[390] J. C. Myland and K. B. Oldham, "Uncompensated resistance. 1. The effect of cell geometry," *Analytical Chemistry*, vol. 72, no. 17, pp. 3972–3980, 2000.

[391] I. Streeter and R. G. Compton, "Numerical simulation of potential step chronoamperometry at low concentrations of supporting electrolyte," *Journal of Physical Chemistry C*, vol. 112, no. 35, pp. 13716–13728, 2008.

[392] Z.-S. Wu, G. Zhou, L.-C. Yin, W. Ren, F. Li, and H.-M. Cheng, "Graphene/metal oxide composite electrode materials for energy storage," *Nano Energy*, vol. 1, no. 1, pp. 107–131, 2012.

[393] S. Ardizzone, G. Fregonara, and S. Trasatti, ""Inner" and "outer" active surface of RuO_2 electrodes," *Electrochimica Acta*, vol. 35, no. 1, pp. 263–267, 1990.

[394] D. Baronetto, N. Krstajić, and S. Trasatti, "Reply to "Note on a method to interrelate inner and outer electrode area" by H. Vogt," *Electrochimica Acta*, vol. 39, no. 16, pp. 2343–2494, 1994.

[395] H. Lindstrom, S. Sodergren, A. Solbrand, H. Rensmo, J. Hjelm, A. Hagfeldt, and S. E. Lindquist, "Li^+ ion insertion in TiO_2 (anatase). 2. Voltammetry on nanoporous films," *Journal of Physical Chemistry B*, vol. 101, no. 39, pp. 7717–7722, 1997.

[396] T. C. Liu, W. G. Pell, B. E. Conway, and S. L. Roberson, "Behavior of molybdenum nitrides as materials for electrochemical capacitors - comparison with ruthenium oxide," *Journal of The Electrochemical Society*, vol. 145, no. 6, pp. 1882–1888, 1998.

[397] P. Soudan, J. Gaudet, D. Guay, D. Bélanger, and R. Schulz, "Electrochemical properties of Ruthenium-based nanocrystalline materials as electrodes for supercapacitors," *Chemistry of Materials*, vol. 14, no. 3, pp. 1210–1215, 2002.

[398] K. Brezesinski, J. Wang, J. Haetge, C. Reitz, S. O. Steinmueller, S. H. Tolbert, B. M. Smarsly, B. Dunn, and T. Brezesinski, "Pseudocapacitive contributions to charge storage in highly ordered mesoporous group V transition metal oxides with iso-oriented layered nanocrystalline domains," *Journal of The American Chemical Society*, vol. 132, no. 20, pp. 6982–6990, 2010.

[399] X. Wang, G. Li, Z. Chen, V. Augustyn, X. Ma, G. Wang, B. Dunn, and Y. Lu, "High-performance supercapacitors based on nanocomposites of Nb_2O_5 nanocrystals and carbon nanotubes," *Advanced Energy Materials*, vol. 1, no. 6, pp. 1089–1093, 2011.

[400] Z. Chen, V. Augustyn, X. Jia, Q. Xiao, B. Dunn, and Y. Lu, "High-performance sodium-ion pseudocapacitors based on hierarchically porous nanowire composites," *Chemistry of Materials*, vol. 6, no. 5, pp. 4319–4327, 2012.

[401] K.-M. Lin, K.-H. Chang, C.-C. Hu, and Y.-Y. Li, "Mesoporous RuO_2 for the next generation supercapacitors with an ultrahigh power density," *Electrochimica Acta*, vol. 54, no. 19, pp. 4574–4581, 2009.

[402] H. Li, J. Wang, Q. Chu, Z. Wang, F. Zhang, and S. Wang, "Theoretical and experimental specific capacitance of polyaniline in sulfuric acid," *Journal of Power Sources*, vol. 190, no. 2, pp. 578–586, 2009.

[403] Q. Lu, Z. J. Mellinger, W. Wang, W. Li, Y. Chen, J. G. Chen, and J. Q. Xiao, "Differentiation of bulk and surface contribution to supercapacitance in amorphous and crystalline NiO," *ChemSusChem*, vol. 3, no. 12, pp. 1367–1370, 2010.

[404] E. Khoo, J. Wang, J. Ma, and P. S. Lee, "Electrochemical energy storage in a β-Na0.33v_2O_5 nanobelt network and its application for supercapacitors," *Journal of Materials Chemistry*, vol. 20, no. 38, pp. 8368–8374, 2010.

[405] M. Sathiya, A. S. Prakash, K. Ramesha, J.-M. Tarascon, and A. K. Shukla, "V_2O_5-anchored carbon nanotubes for enhanced electrochemical energy storage," *Journal of The American Chemical Society*, vol. 133, no. 40, pp. 16291–16299, 2011.

[406] Y.-H. Lee, K.-H. Chang, and C.-C. Hu, "Differentiate the pseudocapacitance and double-layer capacitance contributions for nitrogen-doped reduced graphene oxide in acidic and alkaline electrolytes," *Journal of Power Sources*, vol. 227, pp. 300–308, 2013.

[407] J. E. B. Randles, "A cathode ray polarograph part II. The current-voltage curves," *Transactions of the Faraday Society*, vol. 44, no. 5, pp. 327–338, 1948.

[408] A. Sevčik, "Oscillographic polarography with periodical triangular voltage," *Collection of Czechoslovak Chemical Communications*, vol. 13, pp. 349–377, 1948.

[409] H. Matsuda and Y. Ayabe, "Zur theorie der Randles-Sevčikschen kathodenstrahl-polarographie," *Zeitschrift für Elektrochemie*, vol. 59, no. 6, pp. 494–503, 1955.

[410] R. S. Nicholson and I. Shain, "Theory of stationary electrode polarography. single scan and cyclic methods applied to reversible, irreversible, and kinetic systems," *Analytical Chemistry*, vol. 36, no. 4, pp. 706–723, 1964.

[411] H. Farsi, F. Gobal, H. Raissi, and S. Moghiminia, "On the pseudocapacitive behavior of nanostructured molybdenum oxide," *Journal of Solid State Electrochemistry*, vol. 14, no. 4, pp. 643–650, 2010.

[412] Y. Zhang and H. Yang, "Modeling and characterization of supercapacitors for wireless sensor network applications," *Journal of Power Sources*, vol. 196, no. 8, pp. 4128–4135, 2011.

[413] P. B. Karandikar, D. B. Talange, U. Mhaskar, and R. Bansal, "Validation of capacitance and equivalent series resistance model of Manganese oxide-based aqueous super-capacitor," *Electric Power Components and Systems*, vol. 40, no. 10, pp. 1105–1118, 2012.

[414] B. E. Conway, V. Birss, and J. Wojtowicz, "Transition from "supercapacitor" to "battery" behavior in electrochemical energy storage," *Journal of The Electrochemical Society*, vol. 138, no. 6, pp. 1539–1548, 1991.

[415] P. Guillemet, T. Brousse, O. Crosnier, Y. Dandeville, L. Athouel, and Y. Scudeller, "Modeling pseudo capacitance of manganese dioxide," *Electrochimica Acta*, vol. 67, pp. 41–49, 2012.

[416] K. Somasundaram, E. Birgersson, and A. S. Mujumdar, "Analysis of a model for an electrochemical capacitor," *Journal of The Electrochemical Society*, vol. 158, no. 11, pp. 1220–1230, 2011.

[417] H. Farsi and F. Gobal, "Theoretical analysis of the performance of a model supercapacitor consisting of metal oxide nano-particles," *Journal of Solid State Electrochemistry*, vol. 11, no. 8, pp. 1085–1092, 2007.

[418] H. Farsi and F. Gobal, "A mathematical model of nanoparticulate mixed oxide pseudocapacitors; part I: model description and particle size effects," *Journal of Solid State Electrochemistry*, vol. 13, no. 3, pp. 433–443, 2009.

[419] H. Farsi and F. Gobal, "A mathematical model of nanoparticulate mixed oxide pseudocapacitors; part II: the effects of intrinsic factors," *Journal of Solid State Electrochemistry*, vol. 15, no. 1, pp. 115–123, 2011.

[420] S. Devan, V. R. Subramanian, and R. E. White, "Transient analysis of a porous electrode," *Journal of The Electrochemical Society*, vol. 152, no. 5, pp. 947–955, 2005.

[421] Z. R. Cormier, H. A. Andreas, and P. Zhang, "Temperature-dependent structure and electrochemical behavior of RuO_2/carbon nanocomposites," *Journal of Physical Chemistry C*, vol. 115, no. 39, pp. 19117–19128, 2011.

[422] Y. Liu, F. Zhou, and V. Ozolins, "Ab initio study of the charge-storage mechanisms in RuO_2-based electrochemical ultracapacitors," *Journal of Physical Chemistry C*, vol. 116, no. 1, pp. 1450–1457, 2012.

[423] V. Ozolins, F. Zhou, and M. Asta, "Ruthenia-based electrochemical supercapacitors: Insights from first-principles calculations," *Accounts of Chemical Research*, vol. 46, no. 5, pp. 1084–1093, 2013.

[424] J. Kang, S.-H. Wei, K. Zhu, and Y.-H. Kim, "First-principles theory of electrochemical capacitance of nanostructured materials: Dipole-assisted subsurface intercalation of lithium in pseudocapacitive TiO_2 anatase nanosheets," *Journal of Physical Chemistry C*, vol. 115, no. 11, p. 49094915, 2011.

[425] D. A. Tompsett, S. C. Parker, P. G. Bruce, and M. S. Islam, "Nanostructuring of β-MnO_2: The important role of surface to bulk ion migration," *Chemistry of Materials*, vol. 25, no. 4, pp. 536–541, 2013.

[426] H. Ding, K. G. Ray, V. Ozolins, and M. Asta, "Structural and vibrational properties of α-MoO_3 from van der waals corrected density functional theory calculations," *Physical Review B*, vol. 85, pp. 1–4, No. 012104, 2012.

[427] M. van Soestbergen, "Diffuse layer effects on the current in galvanic cells containing supporting electrolyte," *Electrochimica Acta*, vol. 55, no. 5, pp. 1848–1854, 2010.

[428] M. Ünlü, D. Abbott, N. Ramaswamy, X. Ren, S. Mukerjee, and P. A. Kohl, "Analysis of double layer and adsorption effects at the alkaline polymer electrolyte-electrode interface," *Journal of The Electrochemical Society*, vol. 158, no. 11, pp. 1423–1431, 2011.

[429] C. W. Wang and A. M. Sastry, "Mesoscale modeling of a li-ion polymer cell," *Journal of The Electrochemical Society*, vol. 154, no. 11, pp. 1035–1047, 2007.

[430] X. Xiao, W. Wu, and X. Huang, "A multi-scale approach for the stress analysis of polymeric separators in a lithium-ion battery," *Journal of Power Sources*, vol. 195, no. 22, pp. 7649–7660, 2010.

[431] R. Chandrasekaran, A. Magasinski, G. Yushin, and T. F. Fuller, "Analysis of lithium insertion/deinsertion in a silicon electrode particle at room temperature," *Journal of The Electrochemical Society*, vol. 157, no. 10, pp. 1139–1151, 2010.

[432] S. R. Subramanian, V. Boovaragavan, V. Ramadesigan, and M. Arabandi, "Mathematical model reformulation for lithium-ion battery simulations: Galvanostatic boundary conditions," *Journal of The Electrochemical Society*, vol. 156, no. 4, pp. 260–271, 2009.

[433] A. Frumkin, "Hydrogen overvoltage and the structure of the double layer," *Zeitschrift für Elektrochemie*, vol. 164A, pp. 121–133, 1933.

[434] W. Du, A. Gupta, X. Zhang, A. M. Sastry, and W. Shyy, "Effect of cycling rate, particle size and transport properties on lithium-ion cathode performance," *International Journal of Heat and Mass Transfer*, vol. 53, no. 17-18, pp. 3552–3561, 2010.

[435] I. V. T. amd Tapesh Joshi, K. Zaghib, J. N. Harb, and D. R. Wheeler, "Understanding rate-limiting mechanisms in $LiFePO_4$ cathodes for Li-ion batteries," *Journal of The Electrochemical Society*, vol. 158, no. 11, pp. 1185–1193, 2011.

[436] M. B. Pinson and M. Z. Bazant, "Theory of SEI formation in rechargeable batteries: Capacity fade, accelerated aging and lifetime prediction," *Journal of The Electrochemical Society*, vol. 160, no. 2, pp. 243–250, 2013.

[437] K. Nishikaw, Y. Fukunaka, T. Sakka, Y. H. Ogata, and J. R. Selman, "Measurement of $LiClO_4$ diffusion coefficient in propylene carbonate by Moir e pattern," *Journal of The Electrochemical Society*, vol. 153, no. 5, pp. 830–834, 2006.

[438] J. Xu and G. C. Farrington, "A novel electrochemical method for measuring salt diffusion coefficients and ion transference numbers," *Journal of The Electrochemical Society*, vol. 143, no. 2, pp. 44–47, 1996.

[439] D. Z. B. N. Popov and R. E. White, "Modeling lithium intercalation of a single spinel particle under potentiodynamic control," *Journal of The Electrochemical Society*, vol. 147, no. 3, pp. 831–838, 2000.

[440] T. Ohzuku, K. Sawai, and T. Hirai, "Electrochemistry of L-niobium pentoxide a lithium/non-aqueous cell," *Journal of Power Sources*, vol. 19, no. 4, pp. 287–299, 1987.

[441] M. D. Chung, J. H. Seo, X. C. Zhang, and A. M. Sastry, "Implementing realistic geometry and measured diffusion coefficients into single particle

electrode modeling based on experiments with single $LiMn_2O_4$ spinel particles," *Journal of The Electrochemical Society*, vol. 158, no. 4, pp. 371–378, 2011.

[442] R. He, S. Chen, F. Yang, and B. Wu, "Dynamic diffuse double-layer model for the electrochemistry of nanometer-sized electrodes," *Journal of Physical Chemistry B*, vol. 110, no. 7, pp. 3262–3270, 2006.

[443] Y. Liu, Q. Zhang, and S. Chen, "The voltammetric responses of nanometer-sized electrodes in weakly supported electrolyte: A theoretical study," *Electrochimica Acta*, vol. 55, no. 27, pp. 8280–8286, 2010.

[444] Y. Liu, R. He, Q. Zhang, and S. Chen, "Theory of electrochemistry for nanometer-sized disk electrodes," *Journal of Physical Chemistry C*, vol. 114, no. 24, pp. 10812–10822, 2010.

[445] A. d'Entremont and L. Pilon, "First-principles thermal modeling of electric double layer capacitors under constant-current cycling," *Journal of Power Sources*, vol. 246, pp. 887–898, 2014.

[446] X. Lang, A. Hirata, T. Fujita, and M. Chen, "Nanoporous metal/oxide hybrid electrodes for electrochemical supercapacitors," *Nature Nanotechnology*, vol. 6, no. 4, pp. 232–236, 2011.

[447] B. G. Choi, M. Yang, W. H. Hong, J. W. Choi, and Y. S. Huh, "3D macroporous graphene frameworks for supercapacitors with high energy and power densities," *ACS Nano*, vol. 6, no. 5, pp. 4020–4028, 2012.

[448] A. Laheäär, A. Jänes, and E. Lust, "$NaClO_4$ and $NaPF_6$ as potential nonaqueous electrolyte salts for electrical double layer capacitor application," *Electrochimica Acta*, vol. 82, pp. 309–313, 2012.

[449] Y. G. Wang, H. Q. Li, and Y. Y. Xia, "Ordered whiskerlike polyaniline grown on the surface of mesoporous carbon and its electrochemical capacitance performance," *Advanced Materials*, vol. 18, no. 19, pp. 2619–2623, 2006.

[450] Y.-G. Wang and Y.-Y. Xia, "Electrochemical capacitance characterization of NiO with ordered mesoporous structure synthesized by template SBA-15," *Electrochimica Acta*, vol. 51, no. 16, pp. 3223–3227, 2006.

[451] G. Wang, H. Liu, J. Horvat, B. Wang, S. Qiao, J. Park, and H. Ahn, "Highly ordered mesoporous cobalt oxide nanostructures: synthesis, characterisation, magnetic properties, and applications for electrochemical energy devices," *Chemistry - A European Journal*, vol. 16, no. 36, pp. 11020–11027, 2010.

[452] C. Yuan, X. Zhang, L. Hou, L. Shen, D. Li, F. Zhang, C. Fan, and J. Li, "Lysine-assisted hydrothermal synthesis of urchin-like ordered arrays of mesoporous $Co(OH)_2$ nanowires and their application in electrochemical capacitors," *Journal of Materials Chemistry*, vol. 20, no. 48, pp. 10809–10816, 2010.

[453] C.-L. Ho and M.-S. Wu, "Manganese oxide nanowires grown on ordered macroporous conductive nickel scaffold for high-performance supercapacitors," *Journal of Physical Chemistry C*, vol. 115, no. 44, p. 22068?2074, 2011.

[454] C. Jo, I. Hwang, J. Lee, C. W. Lee, and S. Yoon, "Investigation of pseudocapacitive charge-storage behavior in highly conductive ordered mesoporous tungsten oxide electrodes," *Journal of Physical Chemistry C*, vol. 115, no. 23, pp. 11880–11886, 2011.

[455] S. Yoon, E. Kang, J. K. Kim, C. W. Lee, and J. Lee, "Development of high-performance supercapacitor electrodes using novel ordered mesoporous tungsten oxide materials with high electrical conductivity," *Chemical Communications*, vol. 47, no. 3, pp. 1021–1023, 2011.

[456] T. Brezesinski, J. Wang, R. Senter, K. Brezesinski, B. Dunn, and S. H. Tolbert, "On the correlation between mechanical flexibility, nanoscale structure, and charge storage in periodic mesoporous CeO_2 thin films," *ACS Nano*, vol. 4, no. 2, pp. 967–977, 2010.

[457] H. Jiang, J. Ma, and C. Li, "Mesoporous carbon incorporated metal oxide nanomaterials as supercapacitor electrodes," *Advanced Materials*, vol. 24, no. 30, p. 41974202, 2012.

[458] G. Yu, X. Xie, L. Pan, Z. Bao, and Y. Cui, "Hybrid nanostructured materials for high-performance electrochemical capacitors," *Nano Energy*, vol. 2, no. 2, pp. 213–234, 2013.

[459] C. Alexander and M. Sadiku, *Fundamentals of Electric Circuits*. New York, NY: McGraw-Hill, 5th ed., 2012.

[460] C. Cagle, G. Feng, R. Qiao, J. Huang, B. G. Sumpter, and V. Meunier, "Structure and charging kinetics of electrical double layers at large electrode voltages," *Microfluidics and Nanofluidics*, vol. 8, no. 5, pp. 703–708, 2010.